



UNIVERSIDADE DE ÉVORA

Soiling in Solar Energy Conversion Technologies: Assessment and Mitigation

Ricardo Filipe Carrão da Conceição

Thesis submitted to the University of Évora
in fulfilment of the requirements for the degree of Doctor in Mechatronics Engineering and Energy
with specialization in Energy

Supervisor *Hugo Manuel Gonçalves Silva*

Supervisor *Manuel Pedro Ivens Collares Pereira*

April 14, 2019



INSTITUTO DE INVESTIGAÇÃO E FORMAÇÃO AVANÇADA



UNIVERSIDADE DE ÉVORA

Science and Technology School

Physics Department

Soiling in Solar Energy Conversion Technologies: Assessment and Mitigation

Ricardo Filipe Carrão da Conceição

Supervisors *Hugo Manuel Gonçalves Silva*
Manuel Pedro Ivens Collares Pereira

Mechatronics Engineering and Energy

Thesis

April 14, 2019

Jury

President: Doctor **João Manuel Gouveia Figueiredo**, Associated Professor with Agregation, University of Évora, Portugal.

Members:

- Doctor **Eduardo Lorenzo**, Full Professor, Polytechnic University of Madrid, Spain;
- Doctor **Ahmed Alami Merrouni**, Assistant Professor, Research Institute for Solar Energy and New Energies, Morocco;
- Doctor **Miguel Centeno Brito**, Assistant Professor, University of Lisbon, Portugal;
- Doctor Teresa Cunha Diamantino, Assistant Researcher, National Laboratory of Engineering and Geology – Laboratory of Materials and Coatings, Portugal;
- Doctor **Hugo Manuel Gonçalves da Silva**, Principal Researcher, University of Évora, Portugal.

"As a human being, one has been endowed with just enough intelligence to be able to see clearly how utterly inadequate that intelligence is when confronted with what exists."

Albert Einstein, *Letter to Queen Elisabeth of Belgium, September 1932.*

Acknowledgments

It has been a long journey until we finally got here. Yes, it is "we" not "I" since the mere existence of this thesis is only possible due to the help and incredible support, mostly during the difficult times, of my family and friends. I wish to thank from the bottom of my heart to my mother (Maria), my sister (Vera), my girlfriend (Catarina), my nephews (Francisco e Carminho) and my grandmothers (Angelica e Clotilde), for being my pillars during the elaboration of the thesis, but also my for being the pillars of my life. I am deeply grateful to my adviser, Professor Hugo Silva, which i consider a very good friend of mine. Always having new ideas, never giving up when the review of an article was not the expected and always cheering me up. I am also very thankful to Professor Hugo, since he was the one that gave me the chance to meet Professor Manuel Collares-Pereira and therefore engage in the Renewable Energies Chair. I am deeply grateful to my co-adviser, Professor Manuel Collares-Pereira, for giving me an opportunity and for believing in me and in my skills. He was an incredible support during my thesis work, helping me in so many ways, mainly in the papers. I also have to acknowledge all my co-workers, specially Francisco Tavares and Daniel Lopes. Special thanks to Professor José Mirão, from the Hercules laboratory, which allowed me to learn how to operate a Scanning Electron Microscope and also for his availability to perform measurements. I am also grateful to Anabela Rosado, from the Water laboratory, for teaching and let me use the spectrophotometer. I am very thankful to Professor Luis Narvarte, from the *Universidad Politécnica de Madrid*, for having me in the European project MASLOWATEN. A very special thanks to the University of Évora and the Institute of Earth Sciences, ICT (*Instituto Ciências da Terra*), which was my PhD scholarship host institution. This scholarship was attributed by the Portuguese Foundation for Science and Technology, FCT (*Fundação para a Ciência e Tecnologia*), without which this thesis could not be done and I have to express my sincere thanks.

Contents

List of Figures	xv
List of Tables	xix
Acronyms	xxi
Nomenclature	xxiii
Abstract	xxvii
Resumo	xxix
1 Introduction	1
1.1 Historical background	1
1.2 State of the art	7
1.3 Future perspectives	13
1.4 Motivation and previous work	14
1.5 Thesis structure	14
2 Soiling measurements in rural environment for PV	17
2.1 Introduction	17
2.2 Experiments and data	19
2.2.1 Mass accumulation	19
2.2.2 PV performance	20
2.3 Annual Soiling Characterization	22
2.4 Organic material characterization and features	25
2.4.1 SEM characterization and image processing	27

2.5	Saharan Desert Dust Event	29
2.5.1	Dust transport	29
2.5.2	Dust chemical analysis	31
2.5.3	Results	33
2.5.3.1	Mass accumulation	33
2.5.3.2	Photovoltaic performance	34
2.5.4	Modeling	35
2.6	Conclusions	37
3	Soiling measurements in rural environments for CSP	39
3.1	Introduction	39
3.2	Experimental campaign	40
3.2.1	Measurements	40
3.2.2	Soiling index	41
3.2.3	Data Processing	43
3.3	Soiling modeling	45
3.3.1	Multiple linear regression	45
3.3.2	Multiple linear regression of interaction terms	46
3.3.3	Artificial Neural Networks	49
3.3.4	Model comparison and discussion	50
3.4	Portugal-Morocco soiling measurement campaign	51
3.4.1	Results and Discussion	52
3.4.2	Effect of long-range transport of Saharan desert dust	53
3.4.3	Red rain effect	54
3.5	Conclusions	55
4	Soiling Mitigation for PV	57
4.1	Introduction	57
4.2	Irradiance and soiling modeling	59
4.2.1	Irradiance modeling	59
4.2.2	Effective irradiance model with soiling	60
4.2.3	Mass accumulation as function of the tilt angle	61
4.2.4	Transmittance ratio as function of the tilt angle	62
4.2.5	Angular loss coefficients	63
4.2.6	Algorithm flowchart	65
4.3	PV design including soiling effect	66
4.3.1	Constant tilt angle configuration	66

4.3.2	Multiple tilt angle configurations	66
4.3.2.1	Trade-off between produced energy and configuration	67
4.4	Cleaning schedule modeling	71
4.5	Conclusions	72
5	Soiling Mitigation for CSP	75
5.1	Introduction	75
5.2	Methodology	76
5.2.1	Coating production and development	76
5.2.2	Measurement setup	76
5.3	Results and discussion	78
5.3.1	Experimental results	78
5.4	SEM and image analysis	81
5.5	Cost analysis	82
5.6	Conclusions	83
6	Conclusions	85
6.1	Conclusions	85
A	Multiple tilt angle configuration table	89
B	Knowledge developed for the work in the thesis - 1	93
B.1	Introduction	93
B.2	Methodology	95
B.3	Results	96
B.4	Discussion	102
B.5	Conclusions	104
C	Knowledge developed for the work in the thesis - 2	107
C.1	Introduction	107
C.2	Measurement campaign	109
C.3	Desert Dust Transported into Southern Portugal	111
C.4	Potential Gradient	115
C.4.1	Daily analysis	115
C.4.2	Robust lowess smoothing	120
C.4.3	Wavelet analysis	120
C.5	Dust charge model	122
C.6	Conclusions	126

List of Figures

1.1	Soiling studies evolution [1].	2
1.2	Clarence Kemp's Batch Solar Water Heater advertisement.	3
1.3	Archimedes feat representations: (a) Archimede's mirror burning roman ships. Wall painting by Giulio Parigi, in 1600, at Uffizi Gallery, Florence; (b) Ceramic panel in the Physics room of the <i>Colégio Espirito Santo</i> at the University of Évora.	4
1.4	Bell Lab advertisement of PV panel with battery storage.	6
1.5	Global installed solar power capacity, in Megawatts (MW), between 2000 and 2015 [2].	7
1.6	Soiling studies performed in 2016, adapted from [3]: (a) for PV; (b) for CSP.	8
1.7	Dust deposition factors [4].	9
1.8	Cleaning methods, adapted from [4].	10
1.9	Coatings mode of action: (a) Hydrophilic; (b) Hydrophobic.	11
1.10	Robotic cleaning: (a) GEKKO, from Serbot AG; (b) SunPower Oasis, from SUNPOWER; (c) HECTOR, from SENER; (d) PARIS, from SENER.	12
1.11	Electrodynamic screen schematic, adapted from [5].	13
1.12	Water stress level by country using Business-As-Usual scenario [6] for 2040.	14
1.13	PV and CSP potential regions: (a) PV; (b) CSP.	15
2.1	Glass coupon supports: (a) glass tree in PECS; (b) glass sample support in Elaia; (c) PECS soiling experiment.	21
2.2	Soiling ratio and rates.	23
2.3	Environmental measurements: (a) Rain; (b) Aerosol optical depth.	24
2.4	Mass accumulation on 30° tilted glass sample.	25
2.5	Annual pollen trends in Lisbon (Portugal) from 2007 to 2010, adapted from [7].	26
2.6	Main types of pollen from glass sample SEM: (a) <i>Arecaceae</i> ; (b) <i>Pinaceae</i> ; (c) <i>textitQuercus</i> sp; (d) <i>textitPoaceae</i>	27

2.7	SEM images: (a) April 2017; (b) July 2017.	28
2.8	NASA VSIIR dust event true image colours: (a) 20 th February; (b) 21 st February; (c) 22 nd February; (d) 23 rd February.	30
2.9	HYSPLIT air masses trajectories: (a) 20 th February; (b) 21 st February; (c) 2 nd February; (d) 23 rd February.	31
2.10	PECS glass samples: (a) N6 rain drop with dust; (b) SEM of N6 glass rain drop; (c) Elaia glass sample SEM; (d) EDS of the zoomed structure.	32
2.11	PECS soiling experiment results: (a) Mass accumulation; (b) AOD; (c) SR index; (d) Precipitation.	34
2.12	Environmental parameters and modeling from January to April 2017: (a) Air and dew point temperature; (b) Wind speed and direction; (c) Mass accumulation modeling; (d) SR modeling.	36
3.1	Measuring instrumentation: (a) TraCS and SOLYS2; (b) Dylos DC1100 Pro; (c) WindMaster Pro; (d) Meteorological station.	41
3.2	Soiling index and precipitation from June 2017 to May 2018: (a) Soiling index; (b) Precipitation.	42
3.3	Calculation process schematic.	43
3.4	Environmental parameters: (a) $PM_{0.5-2.5}$; (b) VWS ; (c) T ; (d) RH	44
3.5	Predictors effects between: (a) $PM_{0.5-2.5}$ and VWS ; (b) $PM_{0.5-2.5}$ and RH ; (c) VWS and RH ; (d) T and RH	47
3.6	Three dimensional scatter plot of predictors and output.	48
3.7	ANN architecture.	49
3.8	ANN predictions and target output.	50
3.9	Measuring instrumentation: (a) TraCS at REC; (b) TraCS at GEP.	51
3.10	Dirtiness index and precipitation: (a) at PECS; (b) at GEP.	53
3.11	Barcelona supercomputing center dust forecasts: (a) for 21 th April at midnight; (b) for 21 th April at 6 a.m	54
3.12	TraCS mirror at PECS after long-range transport of Saharan desert dust	54
3.13	Red rain event effect: (a) TraCS mirror in a clean state; (b) TraCS mirror after red rain event.	55
4.1	Irradiance components scheme.	59
4.2	Mass accumulation as function of the tilt angle for each month (data retrieved in 2017 at PECS).	62
4.3	Transmittance ratio as function of mass accumulation (weighted data retrieved in 2017 at PECS and transmittance data retrieved at the Water Laboratory, University of Évora).	63
4.4	Coefficients and angular losses: (a) a_r ; (b) c_2 ; (c) L_a ; (d) L_d	64
4.5	Algorithm flow chart. Two processes are considered: calculation of the irradiance on the tilted plane (left side) and the soiling implementation (right side). The effective irradiance, G_{eff} , and the effective energy, E_{eff} , are then calculated.	65
4.6	Effective energy for: (a) clean scenario; (b) soiled scenario.	67

4.7	UNISTRUT Service Company movable PV frame.	68
4.8	Profitability index for : (a) 2 tilt angles; (b) 3 tilt angles; (c) 4 tilt angles; (d) 5 tilt angles.	70
4.9	Profitability window for two cases, including different energy prices, for: (a) 2017; (b) 2050.	71
4.10	Cleaning schedule as a function of soiling. Blue dots represent the clean scenario, red squares represent the soiled scenario, light blue vertical lines depict the cleaning period and black diamonds represent the energy loss between the clean and soiled scenarios.	72
5.1	Measurements setup: (a) TraCS; (b) Modified glass tree.	77
5.2	Schematic view of the measured areas in the mirror: the uncoated part of the sample is the left side (areas 1 and 2); the coated part is the right side (areas 3 and 4).	77
5.3	Soiling index of the coated and uncoated sides of the mirror samples for: (a) 0° tilt; (b) 45° tilt.	78
5.4	Uncoated and coated sides of the horizontal mirror a few days after the first cleaning: (a) Uncoated; (b) Coated.	79
5.5	Relation between relative humidity and soiling index for the 45° tilted mirror.	80
5.6	Box plot of all the soiling indexes.	81
5.7	SEM pictures of the uncoated and coated parts of the mirrors: (a) uncoated 0°; (b) coated 0°; (c) uncoated 45°; (d) coated 45°.	82
B.1	Ceilometer backscatter as function of height for the entire campaign, 17 to 21 June 2015.	96
B.2	Measurements made from 17 to 21 June 2015 campaign: (a) High-frequency potential gradient; (b) Air temperature; (c) Global horizontal irradiance; (d) Aerosol optical depth (The black dots in the panels represent 1-h averaged values).	98
B.3	(a) Spectrogram of the high-frequency potential gradient from 17 to 20 June 2015; (b) Inset showing a 1-h zoom of the spectral peak for the 19 June, starting around 1000 UTC; this shows the particularly complex pattern of the peak. (c) Inset showing the correspond <i>HFPG</i> values for the inset on (b). The coloured arrows in (c) and (d) mark the same moments in both the spectra and data.	100
B.4	(a) Standard deviation of high-frequency potential gradient (σ_{PG}); (b) Richardson number (Ri); (c) Surface sensible heat flux (SHF); (d) Turbulent kinetic energy (TKE).	101
C.1	Geographic location of the three sites used for measurements of atmospheric electric potential gradient and HYSPLIT backward trajectories for Evora, Amieira and Beja: (a) Backward trajectories for 15 th July 2014; (b) Backward trajectories for 16 th July 2014; (c) Backward trajectories for 17 th July 2014; (d) Backward trajectories for 18 th July 2014 (red trajectories correspond to particles arriving at altitudes of 2 km, blue ones to 2.5 km and green ones to 3 km. The white rectangle represents the zoom-in appearing in the upper-panel).	110
C.2	Aerosol optical depth, at 440 nm, Angstrom Exponent and Attenuated backscatter profiles measured at Évora during July 2014: (a) Aerosol optical depth at 440 nm and Angstrom Exponent measured at Évora during July 2014; (b) Attenuated backscatter profiles from CALIOP aboard of CALIPSO for the dawn of 18 th July (The inset shows the satellite path along which the profile was taken).	112
C.3	BSC-DREAM8b maps of total dust load (g/m^2) for: (a) 15 th July 2014; (b) 16 th July 2014; (c) 17 th July 2014; (d) 18 th July 2014; (e) Vertical dust profiles in which the black profile corresponds to 15 th July and the fading grey runs from the 16 th to 18 th July.	114

C.4	Daily variation of the PG for the ALEX2014 campaign at BEA station. The thick black lines in the plots represent the lowess smoothed mean daily FW PG for the all campaign. The dust event starts on 16 th July and ends on the 17 th July (highlight by dark blue rectangles). Dark red rectangles mark the day before and after the dust event.	116
C.5	Daily variation of the PG for the ALEX2014 campaign at AMI station. The thick black lines in the plots represent the lowess smoothed mean daily FW PG for the all campaign. The dust event starts on 16 th July and ends on the 17 th July (highlight by dark blue rectangles). Dark red rectangles mark the day before and after the dust event.	117
C.6	Daily variation of the PG for the ALEX2014 campaign at EVO station. The thick black lines in the plots represent the lowess smoothed mean daily FW PG for the all campaign. The dust event starts on 16 th July and ends on the 17 th July (highlight by dark blue rectangles). Dark red rectangles mark the day before and after the dust event.	118
C.7	Number of local minima of the PG daily curves, marked with red dots, and relative Std (%), marked with blue dots, respectively for: (a) BEA; (b) AMI; (c) EVO.	119
C.8	PG at BEA: (a) raw data (back solid line represents a robust lowess smoothing); (b) wavelet periodogram (1-hour averaged). The vertical dashed line in both panels represents the 16 th July 2014 desert dust event. Gaps correspond to missing data.	121
C.9	PG at AMI: (a) raw data (back solid line represents a robust lowess smoothing); (b) wavelet periodogram (1-hour averaged). The vertical dashed line in both panels represents the 16 th July 2014 desert dust event. Gaps correspond to missing data.	121
C.10	PG at AMI: (a) raw data (back solid line represents a robust lowess smoothing); (b) wavelet periodogram (1-hour averaged). The vertical dashed line in both panels represents the 16 th July 2014 desert dust event. Gaps correspond to missing data.	122
C.11	Schematic diagram of the charge model to explain the observations: (a) diagram for clean aerosol conditions; (b) diagram for a desert dust event.	123

List of Tables

2.1	Soiling rates and statistical parameters.	22
2.2	SEM image parameter analysis.	29
3.1	Soiling index rates and associated statistical parameters.	43
3.2	Statistical parameters of models.	50
3.3	Daily and extrapolated monthly dirtiness rates at PECS and GEP.	53
4.1	Monthly mean mass accumulation statistics (data retrieved in 2017 at PECS).	61
4.2	Comparison between tilt angle shift (in magnitude) between present work and [8], for a constant tilt angle in a soiled scenario.	66
5.1	Soiling rates of the different mirror sides between events.	79
5.2	Difference between initial mirrors' reflectance.	80
5.3	Average area of organic material in the mirror samples.	81
A.1	Optimum tilt angles, effective energy and gain comparison between different configurations for the respective periods. The first column in Table A.1 has all the possible combinations of configurations (e.g. 1 angle, 2 angles) with the tilt angles for both soiled and clean scenarios, β_C and β_S , on column two and three, respectively. The fourth and fifth columns correspond to the respective periods for each of the optimum tilt angles in each configuration, for clean and soiled scenarios, respectively. The sixth and seventh columns correspond to the effective energy in each configuration, for both clean and soiled models, respectively. The eighth column corresponds to the effective energy gain for each soiled configuration regarding the soiled fixed one.	89
B.1	Daily correlation coefficients and the respective p -values in parentheses for the five days of the campaign relating standard deviation of the high-frequency potential gradient (σ_{PG}) with, (a) Richardson number (Ri), (c) near-surface sensible heat flux (SHF), (d) turbulent kinetic energy (TKE)	102

Acronyms

AE	<i>Angström Exponent</i>
AERONET	<i>AErosol RObotic NETwork</i>
ALEX	<i>ALqueva hydro-meteorologica EXperiment</i>
AOD	<i>Aerosol Optical Depth</i>
BIPV	<i>Building Integrated Photovoltaics</i>
BSC	<i>Barcelona Supercomputing Center</i>
CALIOP	<i>Cloud-Aerosol Lidar with Orthogonal Polarization</i>
CALIPSO	<i>Cloud-Aerosol Lidar and Infrared Pathfinder Satellite Observation</i>
CAPEX	<i>Capital Expenditure</i>
CSP	<i>Concentrated Solar Power</i>
DNI	<i>Direct Normal Irradiance</i>
DREAMS	<i>Dust Characterisation, Risk Assessment, and Environment Analyser on the Martian Surface</i>
DW	<i>Disturbed-Weather</i>
ECMWF	<i>European Centre for Medium-Range Weather Forecasts</i>
EDS	<i>Energy Dispersive Spectroscopy</i>
FW	<i>Fair-Weather</i>
GDAS	<i>Global Data Assimilation System</i>
GEC	<i>Global Electric Circuit</i>
GEP	<i>Green Energy Park</i>
GHI	<i>Global Horizontal Irradiance</i>
HFPG	<i>High-Frequency Potential Gradient</i>
HYSPLIT	<i>Hybrid Single-Particle Lagrangian Integrated Trajectory</i>
IRESN	<i>Institut de Recherche en Energie Solaire et Energies Nouvelles</i>
I-V	<i>Current-Voltage</i>

- LCOE** *Levelized cost of energy*
- LFC** *Linear Fresnel Collector*
- LIDAR** *Light Detection And Raging*
- MASLOWATEN** *MArket uptake of an innovative irrigation Solution based on LOW WATer-ENergy consumption*
- MENA** *Middle East and North Africa*
- mc-Si** *Multicrystalline-Silicon*
- MicroARES** *Micro Atmospheric Radiation and Electricity Sensor*
- MLR** *Multiple Linear Regression*
- MLRIT** *Multiple Linear Regression with Interaction Terms*
- MSE** *Mean Squared Error*
- NASA** *National Aeronautics and Space Administration*
- NEX-GDDP** *NASA Earth Exchange Global Daily Downscaled Projections*
- NCEP** *National Centers for Environmental Prediction*
- NOAA** *National Oceanic and Atmospheric Administration*
- OPEC** *Organization of Petroleum Exporting Countries*
- OPEX** *Operation Expenses*
- PBL** *Planetary Boundary Layer*
- PECS** *Parque de Ensaio de Coletores Solares*
- PG** *Potential Gradient*
- PTC** *Parabolic Trough Collector*
- PV** *Photovoltaic*
- REC** *Renewable Energies Chair*
- RMSE** *Root Mean Squared Error*
- SCD** *Space Charge Density*
- SEM** *Scanning Electron Microscope*
- SR** *Soiling Ratio*
- STC** *Standard Test Conditions*
- STE** *Solar Thermal Energy*
- SURFEX** *SURFace EXternalisée*
- TraCS** *Tracking Cleanliness System*
- VIIRS** *Visible Infrared Imaging Radiometer Suite*

Nomenclature

AOD Aerosol Optical Depth

A_D Sample average particle area

a_r Angular loss coefficient

$adjr^2$ Adjusted determination coefficient

CP Capex variation

CAPEX Capital expenditure

E_{eff} Monthly effective irradiance

E_{soiled} Soiled scenario effective irradiance

E_{clean} Clean scenario effective irradiance

F_d Potential gradient under dusty layer

F_c Potential gradient for fair-weather days

F' Potential gradient between bottom of dusty layer and Earth surface

G Irradiance in the PV plane

G_0 Irradiance at STC conditions (1000 W/m^2)

G_{eff} Effective irradiance on tilted plane

g Gravity acceleration

H Heaviside function

he_+ Positive space charge height height

he_- Negative space charge height height

HFPG High-frequency potential gradient

I_{SC} PV module short-circuit

$I_{\text{SC}}^{\text{soil}}$ Soiled PV module short-circuit

$I_{\text{SC}}^{\text{soil},0}$ Soiled PV module short-circuit, in clean state, in STC conditions

- I_{SC}^{clean} Cleaned PV module short-circuit
- $I_{SC}^{clean,0}$ Cleaned PV module short-circuit in STC conditions
- I_b^r Reflected irradiance from the mirror
- I_b Direct Normal irradiance
- I_{coll} Total irradiance on tilted plane
- $I_{bn} \cos(\theta)$ Tilted plane direct normal irradiance component
- $I_d \left(\frac{1+\cos\beta}{2} \right)$ Tilted plane sky-diffuse component
- $I_h \rho_g \left(\frac{1-\cos\beta}{2} \right)$ Tilted plane ground reflected component
- I_{bn} Beam irradiance
- I_d Diffuse irradiance
- I_h Global horizontal irradiance
- J_z Air-Earth current density
- L_b Direct irradiance component angular loss factor
- L_d Diffuse irradiance component angular loss factor
- L_a Albedo irradiance component angular loss factor
- M_A Monthly mass accumulation
- $m_a(t)$ Mass accumulated at a certain time
- $m(t)$ Mass at a certain time
- $m(0)$ Initial mass of the cleaned glass
- N_T Tilt angle annual changes
- n_+ positive ion concentration
- n_- negative ion concentration
- O_D Organic material average diameter
- OA_{PNR} Particle ratio between organic and all material
- OA_{AR} Area ratio between organic and all material
- $OPEX$ Operational expenditure
- OP Opex variation
- P_{max} PV module maximum power output
- P_{max}^{soil} Soiled PV module maximum power output
- $P_{max}^{soil,0}$ Soiled PV module maximum power output in clean conditions
- PR Performance ratio
- P_W Profitability window
- PI Profitability index

P_A Profitability area

$PM_{0.5-2.5}$ Particulate matter

r^2 Coefficient of determination

$Rain$ Precipitation

RH Relative humidity

Ri Richardson number

SR Soiling Ratio index for PV

S_R Soiling Rates for PV

$SR_{I_{SC}}$ Soiling Ratio index based on PV short-circuit

$SR_{P_{max}}$ Soiling Ratio index based on PV maximum power output

SY Annual PV specific yield

SHF Surface sensible heat flux

T Air temperature

t Time

T_{soil} Soiled PV cell temperature

T_0 Temperature at the reference conditions (25°C)

T_{clean} Cleaned PV cell temperature

th_+ Positive space charge density thickness

th_- Negative space charge density thickness

TKE Turbulent kinetic energy

VWS Vertical wind speed

WS Wind speed

z Atmospheric height

α PV module short-circuit temperature correction coefficient

β Tilt angle

β_S Soiled PV module tilt angle

β_C Clean PV module tilt angle

ε_0 Vacuum permittivity

γ PV module power temperature correction

λ Soiling index for CSP

$\Delta\lambda$ Difference between soiling index between consecutive days

ω Hour angle

Ω_0 Background contribution to soiling arising from particles not detected by AOD

ρ_0 Clean mirror maximum weighted reflectance

ρ_g *Ground albedo coefficient*

$\cos(\theta)$ *Angle between beam irradiance and the surface normal*

δ *Declination*

ϕ *Latitude*

τ_r *Normal incidence transmittance ration*

τ_{soiled} *Soiled glass transmittance*

τ_{clean} *Clean glass transmittance*

θ_v *Virtual potential temperature*

σ_{PG} *High-frequency potential gradient standard deviation*

σ_t *Air electric conductivity*

$\Delta\sigma_t$ *Air electric conductivity variation*

ζ *Space charge density*

ζ_d *Space charge density on the bottom of dusty layer*

Abstract

Soiling, the process of particle deposition onto surfaces, has been studied since the 40's. Initially, it was studied as a physical process, including types of adhesion forces, and later its effect on performance of solar energy conversion technologies was analyzed, such as in photovoltaics and concentrated solar power. This thesis approaches the problem from a cause-effect point of view and how it can be mitigated. Soiling is characterized, mineral and chemically, using a Scanning Electron Microscope. Polycrystalline photovoltaic modules deposition rates are retrieved and related to environmental parameters, as well as, to long-range Saharan desert dust transport, a non-local phenomenon. Attention is also given to Spring, where atmospheric pollen concentration enhances soiling. The effect of soiling on the photovoltaic optimum tilt angle, for fixed and multiple angles, is studied along with a simple economic analysis. Cleaning schedules, for a desired system efficiency, are calculated based on annual soiling. Mirror soiling, related to concentrated solar power technologies, is also analyzed. Soiling rates are calculated and interlinked with environmental parameters such as air temperature, relative humidity, particulate mater concentration and vertical wind speed. From a collaboration with the *Institut de Recherche en Energie Solaire et Energies Nouvelles* Morocco, an insightful study is made comparing soiling effect between Portugal and Morocco. A passive cleaning method, impregnated anti-soiling coating, is tested. Comparison between coated and uncoated mirrors is done to evaluate its performance and conclude if it stands as a possible tool to reduce water consumption in cleaning solar harvesting technologies.

Keywords: Solar Energy, Conversion Technologies, Soiling, Modeling, Mitigation

Resumo

Sujidade em Tecnologias de Conversão de Energia Solar: Avaliação e Mitigação

A sujidade, o processo de deposição de partículas em superfícies, tem sido estudada desde os anos 40. Inicialmente, começou a ser estudada como um processo físico, incluindo tipos de forças de adesão, e mais tarde o seu efeito no desempenho de tecnologias de conversão de energia solar, como na tecnologia fotovoltaica e e de concentração. Esta tese aborda este problema de um ponto de vista causa-efeito e como pode ser mitigado. A sujidade é caracterizada, mineral e químicamente, usando um Microscópio Eletrónico de Varrimento. As taxas de deposição em módulos fotovoltaicos policristalinos são calculadas e relacionadas com parâmetros ambientais, tal como com o transporte de longo alcance de areia do deserto do Sahara, um fenómeno não local. Também é dada atenção à Primavera, onde a concentração de pólen na atmosfera aumenta a sujidade. O efeito da sujidade no ângulo de inclinação fotovoltaico óptimo, para ângulos fixos e múltiplos, é estudado juntamente com análises económicas. Calendários de limpeza, para uma eficiência de sistema desejada, são calculados com base em dados anuais de deposição de partículas. A sujidade em espelhos, relacionada com as tecnologias de energia solar concentrada, é também analisada. As taxas de deposição são calculadas e relacionadas com parâmetros ambientais, tais como temperatura do ar, humidade relativa, concentração de partículas e velocidade vertical do vento. A partir de uma colaboração com o *Institut de Recherche en Energie Solaire et Energies Nouvelles* Marrocos, fez-se um estudo esclarecedor, comparando o efeito da sujidade entre Portugal e Marrocos. Um método passivo de limpeza, revestimentos impregnados anti-sujidade, é testado. A comparação entre espelhos revestidos e não revestidos é realizada para avaliar o seu desempenho e concluir se é um método importante para alcançar uma redução no consumo de água na limpeza de tecnologias de energia solar.

Palavras chave: Energia Solar, Tecnologias de Conversão, Sujidade, Modelação, Mitigação

1

Introduction

1.1 Historical background

Soiling, defined as particle deposition onto surfaces, reduces solar energy conversion technologies performance through transmission, reflection and absorption losses. This thematic has been under studied since the 40s, please see Fig. 1.1. The first known soiling study appeared in 1942, during World War II, and concerned solar thermal technology. Part of the list of the insightful papers and researchers (in the sense that they realized soiling could be a problem for solar energy harvesting technologies) include: Hottel and Woertz [9], with the study made in 1942 in Boston, where a 4.7% reduction in performance was found in solar-thermal collectors; Dietz with his work in 1963 [10], found that glass samples could loose $\approx 5\%$ in transmittance due to soiling; Hamberg and Tomlinson [11] conducted a study in 1971, also in U.S.A, using artificial soiling to test the effect in solar absorptance. After these visionaries work, Garg [12] conducted the first known soiling study in India in 1974, where the effect of soiling on glass transmittance for different tilt

angles was carried out. Undoubtedly, these works are of vital importance, however there are many more researchers in this field to be recognized. Most of the initial studies were made in U.S.A and later, due to solar energy availability in specific regions of the globe and research investment in solar energy, soiling studies started to become abundant in Middle East and Northern Africa (MENA) regions.

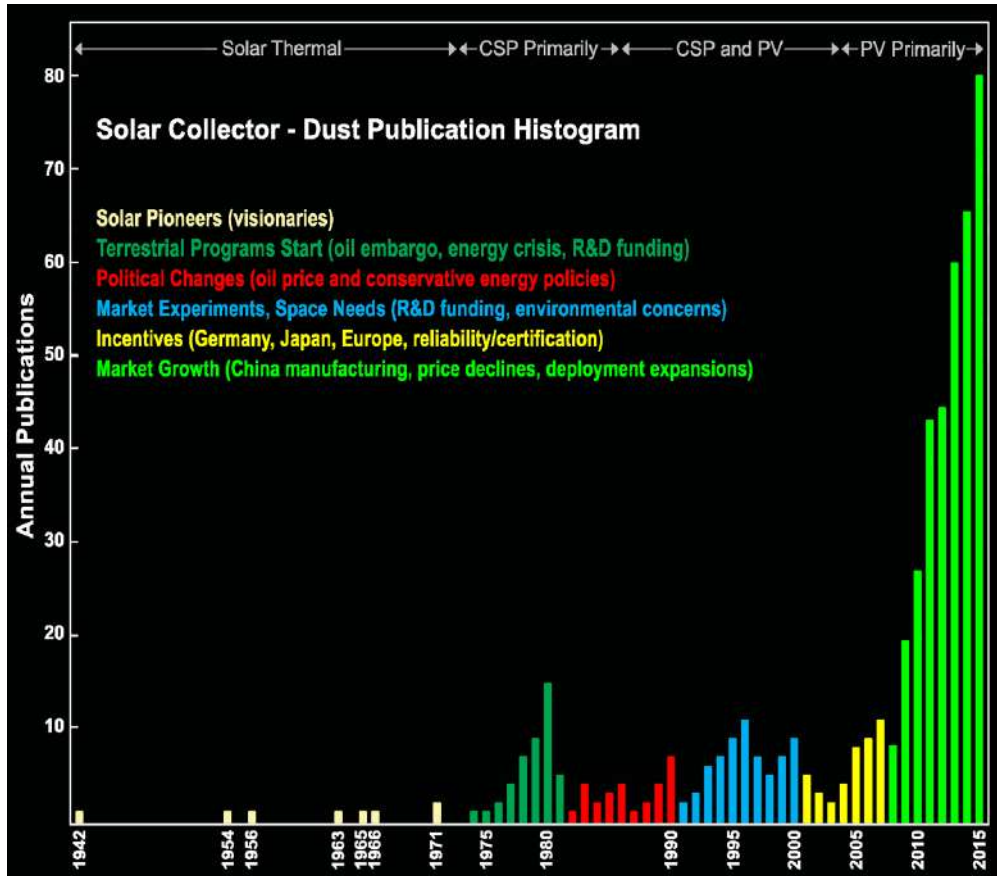


Figure 1.1: Soiling studies evolution [1].

To give a full perspective on the evolution of soiling studies throughout time, particularly on solar-thermal energy (STE), photovoltaic (PV) and concentrated solar power (CSP) technologies, it is necessary to explain how these technologies evolved, the energy policies and research direction at the time, because they are closely related to the evolution of soiling studies, as it will be shown.

Perhaps, the beginning of marketable STE technology was in 1891, when Clarence Kemp's Batch Solar Water Heater was presented [13], please see Fig. 1.2. By 1909 William Bailey invented the first thermosyphon system, which allowed the hot water to circulate without a pump, an improvement to Kemp's invention. This system was mostly commercialized in California and Florida [13]. During the 30s, solar water heating was already a mature and spread technology, while PV and CSP were just giving their first steps, as it will be shown next. In fact, it can be seen in Fig. 1.1, that the initial research on soiling was on solar-thermal technology, from the 40s to the 70s. This is due to the fact that this was the only solar energy conversion technology that was actually on the market. At that time, this was the more interesting

technology to study soiling effect. After solar-thermal, the next target technology working on soiling effect was CSP.

Climax Solar-Water Heater

UTILIZING ONE OF NATURE'S GENEROUS FORCES

THE SUN'S HEAT

{ Stored up in Hot Water for Baths,
Domestic and other Purposes.

Price Of No. 1 Heater for
1892 Reduced to \$15 Net



**GIVES HOT WATER at all HOURS
OF THE DAY AND NIGHT.**

NO DELAY.

FLOWS INSTANTLY.

NO CARE. NO WORRY.


ALWAYS CHARGED.

ALWAYS READY.

**THE WATER AT TIMES
ALMOST BOILS.**

Price, No. 1, \$25.00

This Size will Supply sufficient
for 3 to 8 Baths.



OUTLET INLET

CLARENCE M. KEMP, BALTIMORE, MD.

Advertisement for the Climax solar water heater, 1892. The price of this, Kemp's smallest unit, had just dropped from \$25 to \$15.

Figure 1.2: Clarence Kemp's Batch Solar Water Heater advertisement.

The ideas behind CSP come from remote times, for example, the idea of using mirrors to concentrate light, in particular to burn wood. Whether it is a myth or not, it is attributed to Archimedes, a greek mathematician, in 214-212 B.C., the idea of concentrating the sun's energy to burn an enemy fleet [14], please see Fig. 1.3a. Two millennia later, in 1973, Dr. Loannis Sakkas proved that this could be attainable (web.mit.edu). Using seventy bronze-coated mirrors to focus the sun's energy on a plywood silhouette of a Roman galley attached to a rowboat about 48 meters away, it was possible to set it on fire. The Archimedes feat is part of the ceramic panel in the Physics room of the *Colégio Espirito Santo* at the University of Évora, please see Fig. 1.3b.

In 1866, August Mouchout used parabolic trough collectors (PTC) to run the first solar steam engine ever built [15]. At the end of the XIX century, a portuguese inventor, Father Himalaya [16], worked on the topics of solar energy concentration, producing highly original concentrators, which culminated with the *pireheliophoro*, winner of the Grand Prix at St. Louis World Fair in 1904. In 1913, the first PTC plant technology was built in Meady [17], Egypt, by Frank Schuman an American inventor and entrepreneur. Linear Fresnel collector (LFC) technology was first designed and built by Giovanni Francia in 1963 in Genoa [18], Italy, however, it was only tested a year late in Lacédémone-Marseilles facility, France, due to the



(a)



(b)

Figure 1.3: Archimedes feat representations: (a) Archimede's mirror burning roman ships. Wall painting by Giulio Parigi, in 1600, at Uffizi Gallery, Florence; (b) Ceramic panel in the Physics room of the *Colégio Espírito Santo* at the University of Évora.

cooperation with Marcel Perrot. The first solar tower power demonstrator was built in Sicily, Italy [19], in 1965. Stirling/dish systems prototypes were tested from 1982 to 1985 [20] in California.

At the beginning of the XX century the only marketable solar energy conversion technology was STE, as referred before, which explains the fact that the first soiling papers were performed on this technology. After STE, also CSP started to have developments and demonstrators, but it was not commercialized, which led to a delay in the study of environmental effects, like soiling, in such technology's performance. It should be pointed that most of the first CSP demonstrators were built in Europe and North Africa like Schuman's demonstrator, which was unfortunately shut down in 1915 due to the beginning of World War I and the introduction of fossil fuels, a trend followed by other plants. Actually, both World Wars, as well as, fossil fuels implementation, reduced the investment in renewable energies research, and therefore soiling related studies throughout the last decades. One can conjecture that if both World Wars had never happen, experiments like Schuman's demonstrator would not be stopped and possibly CSP could be a much more

deployed technology today.

On the other hand, the oil embargo in the 70s from the OPEC (Organization of Petroleum Exporting Countries), as a supposed retaliation to the western countries support of Israel [21], in the Yom Kippur War, led to a shift in energy policies. Because of supply and demand imbalance, U.S.A, as well as other countries, turned their attention to solar energy technologies again. However, since solar thermal systems were supported by the federal government, abundant on the market and cheaper compared to PV systems, PV research and subsequent manufacturing cost decrease did not happen during this period. In fact, since there were already CSP testing platforms deployed in regions such as MENA and Asia [22], where soiling is more concerning, studies of particle deposition effect started to be performed on this technology and not on PV.

During the 80s, after the oil embargo ended, Ronald Reagan (advocate of nuclear energy) was elected president of the U.S.A. There was a complete change in the energy policies again, leading to less funding for solar energy technologies development and therefore less soiling related publications. After this renewable energy development "embargo" due to political decisions, PV soiling studies became frequent. To understand how this new line of research appeared, it is vital to understand how PV technology evolved.

PV technology is based on the photoelectric effect, discovered in 1839 by Edmond Becquerel [23] and explained much later by Albert Einstein in 1905 [24], which won the Nobel prize for this work in 1921. The first solar cell, using selenium, was created by Charles Fritts in 1883 [25], however it had low efficiency $\approx 1\%$ and an expensive manufacturing process; for those reasons, it was not commercially viable. Only in 1954, after the discover of semiconductors, Bell Telephone Laboratories (Bell Labs in New Jersey, U.S.A), developed silicon cells [26], initially with 4% and then with 6% efficiency, please see Fig. 1.4. This was a significant achievement, since silicon was (and still is) the base for the electronic industry, however there was no way, at that time, to compete with the low price of fossil fuels.

During the 50s and 60s, due to U.S.A. space race, there was a boost in PV cells research by the National Aeronautics and Space Administration (NASA), as this technology was considered an important power source for space and satellite equipments. Thus, there is no surprise in noting that this renewable energy was initially used on space purposes and not on Earth applications. PV cells were very expensive, but this did not matter in space applications. Indeed during this period the priority of countries like U.S.S.R and U.S.A. was to be the first to land on the moon. Curiously, at that time, interest on dust deposition was substantially raised, because moon dust is significantly electrified and stick to the astronauts space suits and equipment. Solutions to repeal dust were proposed, like the electrostatic curtains [27] that are now being considered for solar energy systems on Earth.

During the 90s, due to market initiatives, like the "one million solar roofs" in the U.S.A. and "one thousand roofs" in Germany and the successes of space exploration with PV introduction not only in satellites [1], but also as a power source for rovers, and the increasing concern with climate change, a greater interest in PV technology along with the effect of soiling on its performance has arisen. It is very



Something New Under the Sun. It's the Bell Solar Battery, made of thin discs of specially treated silicon, an ingredient of common sand. It converts the sun's rays directly into usable amounts of electricity. Simple and trouble-free. (The storage batteries beside the solar battery store up its electricity for night use.)

Bell System Solar Battery Converts Sun's Rays into Electricity!

Bell Telephone Laboratories invention has great possibilities for telephone service and for all mankind

Ever since Archimedes, men have been searching for the secret of the sun.

For it is known that the same kindly rays that help the flowers and the grains and the fruits to grow also send us almost limitless power. It is nearly as much every three days as in all known reserves of coal, oil and uranium.

If this energy could be put to use — there would be enough to turn every wheel and light every lamp that mankind would ever need.

The dream of ages has been brought closer by the Bell System Solar Battery. It was invented at the Bell Telephone Laboratories after

long research and first announced in 1954. Since then its efficiency has been doubled and its usefulness extended.

There's still much to be done before the battery's possibilities in telephony and for other uses are fully developed. But a good and pioneering start has been made.

The progress so far is like the opening of a door through which we can glimpse exciting new things for the future. Great benefits for telephone users and for all mankind may come from this forward step in putting the energy of the sun to practical use.

BELL TELEPHONE SYSTEM 

Figure 1.4: Bell Lab advertisement of PV panel with battery storage.

important to note that due to high soiling on the rovers PV system and the reasons referred before, research on cleaning methods began to take off. During this active decade for PV technology, there was, nevertheless, a continuation on CSP studies, since large plants were constructed during the 80s and 90s [21] (e.g. "Solar 1" and "Solar 2" facilities in the Mojave desert, California).

In the beginning of 2000, due to feed-in tariffs in European countries, and system buy-down subsidies in countries like Japan, there was a considerable market expansion and further research in solar technologies, specially on PV. After China started PV cells mass production, there was a considerable cost reduction and a breakthrough occurred on PV technology. This had two consequences: PV technology achieved a mature and low price state, resulting in market expansion; due to this expansion, investigation on soiling was urged on how it decreases systems' performance, as well as, development of cleaning methods to reduce operation

costs. Unfortunately, CSP did not follow the same expansion, in terms of installed capacity compared to PV, since cost reductions could not be achieved at the same rate, please see Fig. 1.5, a trend that is now changing with the use of thermal energy storage [28], cheaper than electrical storage.

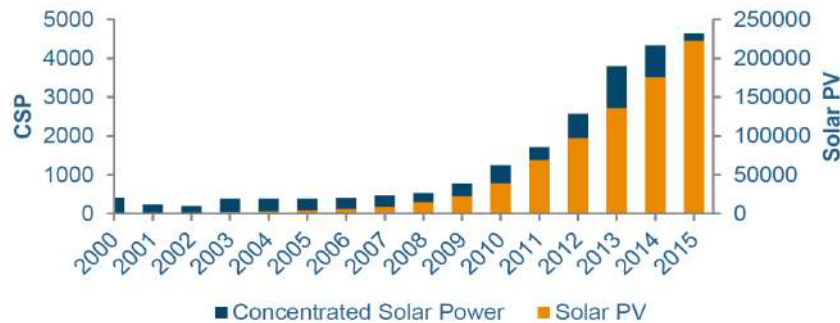


Figure 1.5: Global installed solar power capacity, in Megawatts (MW), between 2000 and 2015 [2].

In summary, this section emphasizes the impact that political decisions, as well as, special events like global armed conflicts, exert on the renewable energies development and therefore on soiling research. There is undoubtedly a strong relation between these factors.

1.2 State of the art

In present days, soiling research, both in PV and CSP technologies, has gained a major role in solar energy systems. However, the type and amount of studies performed for each technology is different, please see Fig. 1.6. However, many aspects can be shared among the two, since PV modules commonly have glass covers and CSP mirrors are surface glass based, most of the time. Besides the fact that there is more research in PV, there is also a higher diversity among those studies, which is expected since PV research has been growing a lot in the last two decades. On both technologies, nevertheless, there are areas where the focus has been higher; these are: (1) dependency on climate zones, as geographic regions; (2) modeling and simulation; (3) mitigation and cleaning. Regarding the area of interest (1), it is related to the measurement of soiling effect and its geographic dependence, e.g. [29, 30, 31]. It should be noted that some of the contributions presented in this thesis [32, 33] are within this area of study. These studies are usually the first to be made, since the initial objective is to characterize the region in terms of what type of soiling exists (size, shape and chemical analysis of deposited particles), as well as, soiling rates. This allows to have an idea on how the environmental conditions, mainly, dry and wet periods, affect particle deposition and therefore soiling effect. This area of interest is inherently connected to particle physical and chemical properties. Having this type of information allows for more complex studies, like the ones within the area of interest (2). Certainly, it is important to develop models able to forecast soiling. In this way, it would be possible, for instance, to develop cleaning schedules for a solar plant or, in the case of PV, calculate a corrected optimum tilt angle taking soiling into account, which will be introduced in Chapter 4. The area of

interest (3) comes as a consequence of the other two, besides the fact that it is a research topic driven by NASA [34]. Having an idea on the type of soiling and its annual trends, as well as, the ability to predict it, are all factors that can contribute to a better design of a cleaning method or mitigation techniques with the potential to reduce maintenance costs. One of these passive techniques comprises the anti-soiling coatings, which are also part of the present work and are introduced in Chapter 5. In terms of state of the art, these are the most interesting domains of soiling research.

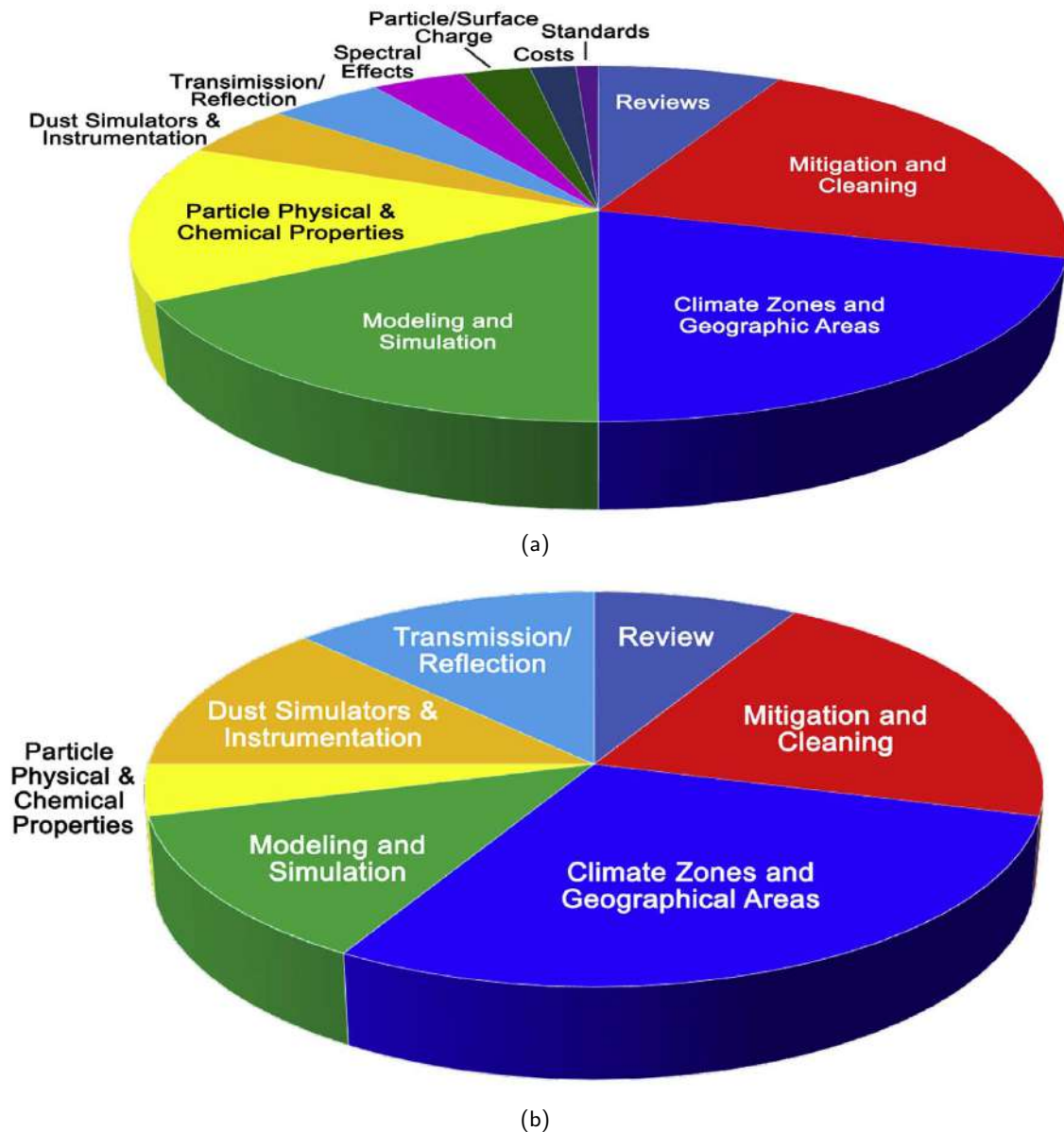


Figure 1.6: Soiling studies performed in 2016, adapted from [3]: (a) for PV; (b) for CSP.

The area of interest (1), which is the one to which more soiling studies have been dedicated and still many are being published [35, 36]. This area is related to soiling measurements and the understanding of soiling effects depending on the geographical area. It is known that the amount of soiling and how it is spread on the surfaces (homogeneously or non-homogeneously) is geographical and time dependent, which

means soiling will vary from site to site. This fact is easily understandable, since different locations have different climates; which implies different meteorological conditions, mainly temperature, relative humidity, rain, wind speed and direction [37], that affect the way particles adhere to surfaces [38]. Moreover, different locations also have different types of particles suspended in the atmosphere; which also might have a different impact on how and to what extent the irradiance entering the panels will be reduced [39, 40]. Even neighbor locations may have different types and amounts of soiling, depending if they are or not close to a specific source of particles, e.g. factories, airports and roads, among others [29]. Even though, most of those studies were done in or near to desert areas (where soiling is a major problem [41] and where there is high solar energy availability), there are other locations with considerable potential for solar energy usage that also need attention regarding soiling; as will be shown, Portugal (Southern Europe) is one of those cases. This country is one of the best to deploy solar energy harvesting technologies in Europe [42]; its southern region has annual availabilities of global horizontal irradiance that can go up to approximately 1900 kWh/m² (around 2200 kWh/m² for direct normal irradiance), [43]. With such availability, it is expected that solar energy conversion technologies, such as PV and CSP, will be very common in Portugal in the future, which makes soiling an interesting and very important factor to be taken into account. Moreover, according to NASA Earth Exchange Global Daily Downscaled Projections (NEX-GDDP) [44, 45], in 2100 this region might have higher air temperatures than at the present time and it may rain less frequently, but with more intensity. These are negative projections regarding soiling, since if they become a reality, there will be more time for particles to build up on the surfaces, leading to an increased soiling over time. Moreover, if climate follows this trend, Southern Portugal and Spain will become semi-arid regions, which can also lead to an increase of particles suspended in the atmosphere that are able to deposit, because vegetation acts as a particle retainer and obstacle [46].

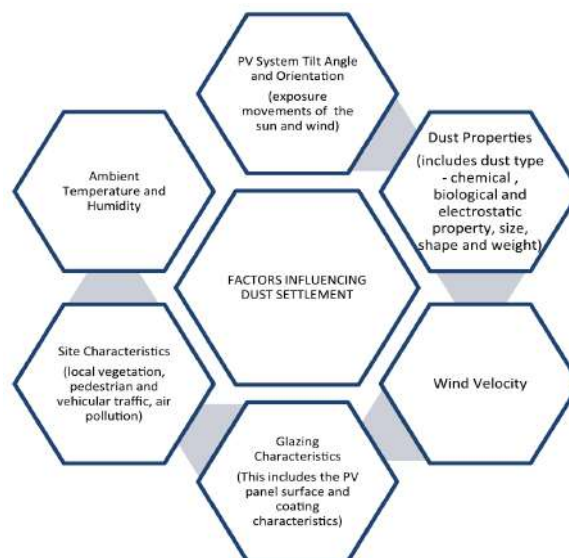


Figure 1.7: Dust deposition factors [4].

The area of interest (2) is closely connected to power production and elaboration of cleaning schedules

[47, 48]. If one knows how much soiling there will be in the next day or week, one may be able to manage, for instance, battery charge/discharge strategies taking into account the soiling effect in the incident irradiance. From a different perspective, the simulations and forecasts can be used to elaborate cleaning schedules, because the owner knows ahead in time what energy could possibly be lost. Most of the state of the art methods, include artificial neural networks (ANN) [49, 50], since they are typically used for very complex problems without analytic or empirical solutions. In the past few years ANNs have been applied in different fields related to solar energy, like irradiance forecasts [51], PV plants power output prediction [52], among others. Since atmospheric processes are very complex, due to the relation between multiple variables, and also due to solar energy conversion technologies characteristics, please see Fig. 1.7, ANNs have been used because of their ability to identify complex non-linear relationships. The author thinks that ANNs will be of great help in the future, in very different areas, and will probably solve many problems that otherwise could not be solved.

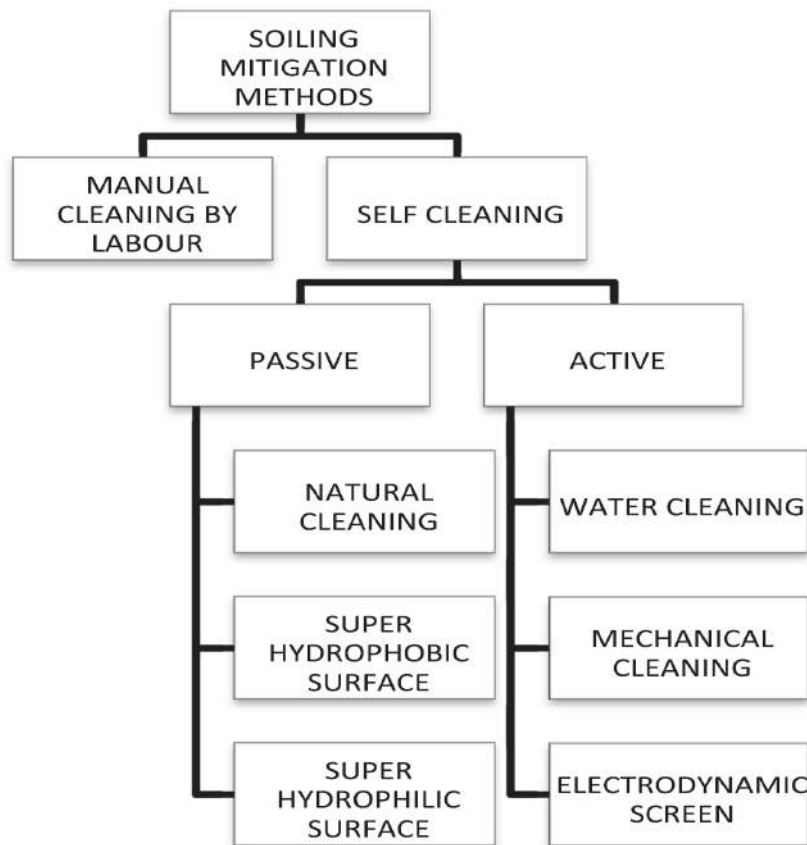


Figure 1.8: Cleaning methods, adapted from [4].

Going now into the details of soiling mitigation, area of interest (3), cleaning is the most common tool. In fact, manual cleaning is the more frequent method to clean soiling, whether it is from surfaces of solar energy conversion technologies or any other surface like skyscraper's windows and indoor particle deposition. This method is reliable, since it allows to remove any contaminant, including bird droppings and cemented dust. However, if not done properly this method can lead to surface scratching and abrasion,

which can therefore deteriorate the surface optical characteristics [4]. Moreover, it represents substantial costs, depending on how many times the surfaces need to be cleaned during the year.

Self-cleaning methods are the ones, as the name implies, where there is no need for human intervention, which reduces maintenance costs. These methods can be passive or active. Passive methods are the ones where no energy is spent for cleaning, as well as, other tools and fluids related to cleaning. These methods can be split in two different groups: natural cleaning (e.g. rainfall); anti-soiling coatings (e.g. super-hydrophobic or super-hydrophilic). The most promising of these methods is the use of anti-soiling coatings, where besides being anti-static, the dust does not adhere so much to the surface, they also have hydrophobic or hydrophilic characteristics. Super-hydrophobicity, turns the surface water repellent, which means that water will form almost spherical drops on the surface and then roll down, dragging soiling on the way [4]. Super-hydrophilicity, on the other hand, makes the water spread on the surface enabling it to go underneath the contaminants and wash them away [4, 36]. Nevertheless, it should be noted that the referred technologies need water to achieve higher cleaning performance.

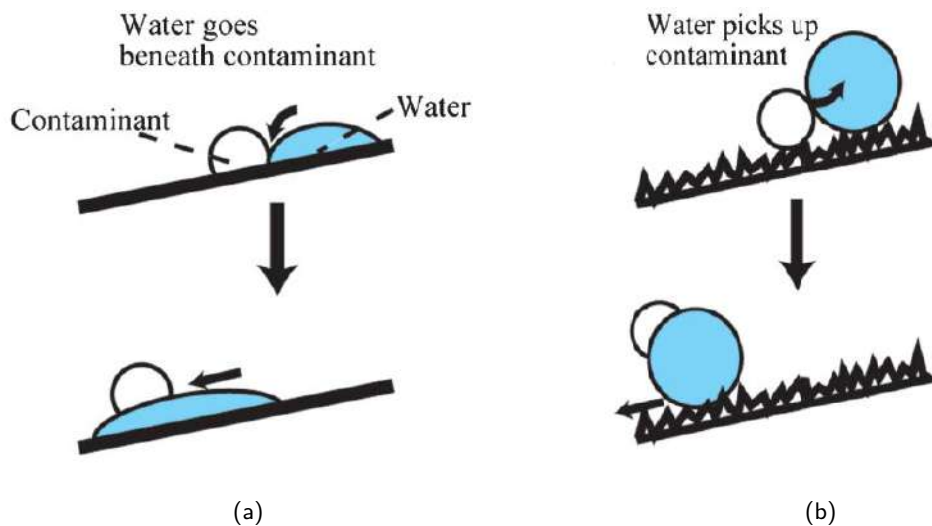


Figure 1.9: Coatings mode of action: (a) Hydrophilic; (b) Hydrophobic.

Active methods are the ones where energy must be spent to perform cleaning. Static non-pressurized systems, are simple to use and normally have a surfactant added to the water, to maximize the cleaning efficiency. However, methods like this tend to use a reasonable amount of water, so it is not indicated for regions where water is a scarce element, e.g. deserts, where most CSP plants are located.

Mechanical cleaning concerns all type of methods where there are moving parts, whether it is horizontal or vertical. Cleaning robots that move over a PV string or a CSP line are within this category. They are usually equipped with a wiper or brush and use water and/or compressed air. These methods have revolutionized the cleaning methods. They are self-powered, usually by a dedicated PV module and storage, they are fast and efficient.

This is a growing market, as new robotic systems are being developed and one of the most promising

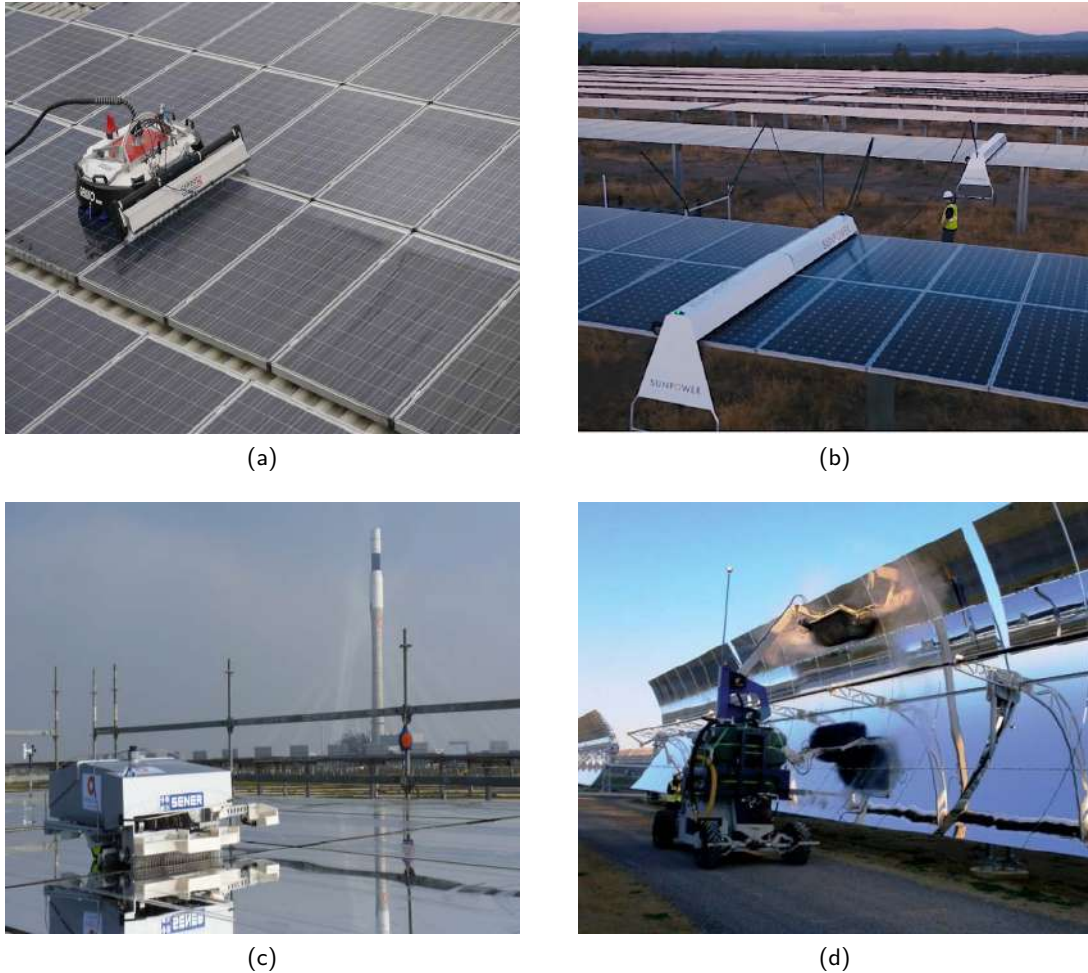


Figure 1.10: Robotic cleaning: (a) GEKKO, from Serbot AG; (b) SunPower Oasis, from SUNPOWER; (c) HECTOR, from SENER; (d) PARIS, from SENER.

systems is the use of ultrasonic piezoelectric transducers and a very small amount of fluid, normally water, where cavitation is induced. As a result of cavitation, which consists of bubble formation within the medium, these implode creating micro-jets at high velocity and temperature; the micro-jets ultimately clean the surfaces. There is one particular method, developed by TEKNIKER that was presented in SolarPACES 2017 (the article has not been published yet); it states that it consumes 600 times less water than conventional methods and enables for a total recovery of mirror reflectance.

Another important method includes the Electrodynamic screens, which consist on a set of parallel electrodes located on a transparent substrate, which is printed on a PV module surface [53]. The electrodes are powered by a two or three phase system, creating a traveling wave, which transports the charged particles to the end of the electrodes. According to [54], neutral particles will gain charge in the process due to dielectrophoresis process within the particle or by inducted charging of conducting particles. This method was shown to be very promising for dry deposition, with an efficiency over 90% and an energy consumption of 1 Wh/m^2 per cleaning cycle and zero water consumption [55]. However, it has been reported in literature a power loss of $\approx 15\%$ due to the following aspects: the cover is not completely transparent, ineffectiveness

in removing small particles ($\leq 5 \mu\text{m}$) [56] and it can only be used in dry conditions.

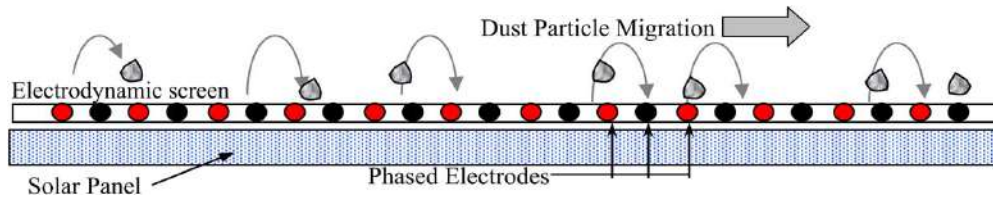


Figure 1.11: Electrodynamic screen schematic, adapted from [5].

1.3 Future perspectives

Currently, most of the existing soiling studies are PV related, however CSP plants deployment took off around 2007 with Spain leading the way. As seen in Fig. 1.5, CSP installed capacity is increasing and it is expected to increase more in the future. Nevertheless, knowledge on the effect of soiling on PV technology is greater than it is on CSP. Considering both these projections, it is expected that, in the next few decades, an increase in CSP soiling studies.

There is an inherent problem with cleaning, which is the use of a cleaning agent, like water. Probably, anti-soiling coatings can increase the periods between cleanings, due to their anti-static characteristic, and so reduce the water consumption. The development of zero water consumption methods can also be an interesting path to follow, however the author thinks that it is impossible to achieve the same level of cleanliness without the use of a liquid agent. The most viable option is to develop cleaning methods that have a higher cleaning performance than the ones existing today, but with a lower water consumption. According to the Water Resource Group projections [6], by 2040 the water demand will surpass the water supply in several countries. For this reason, it is important to adopt different mentalities and policies. This also means that water consumption for cleaning purposes also needs to be rethought. In Fig. 1.12, it is represented the water stress level, which means the ratio of withdrawals to available water, projection by country for 2040. The areas that will experience extreme high levels of water stress include Asia, Northern Africa, Southern Europe, Australia and some regions of the American continent. In Fig. 1.13, it can be observed the areas with highest potential for PV and CSP production. It is seen that there is a very close connection between the regions where in the future there will be extreme water stress levels and the best regions to deploy PV and CSP technologies. It should be noted that in some of these regions there are already working plants, e.g. Morocco.

The author thinks, without a doubt, that surface cleaning methods will receive much more attention in the future. Not only because it is an interesting subject by itself, but also because there is the need to clean the solar energy conversion technologies, since they are and will be located in desert or near-desert regions; where particle deposition is higher. More importantly, there will be the need to develop optimized methods for cleaning, since it is expected for these areas extreme water stress levels.

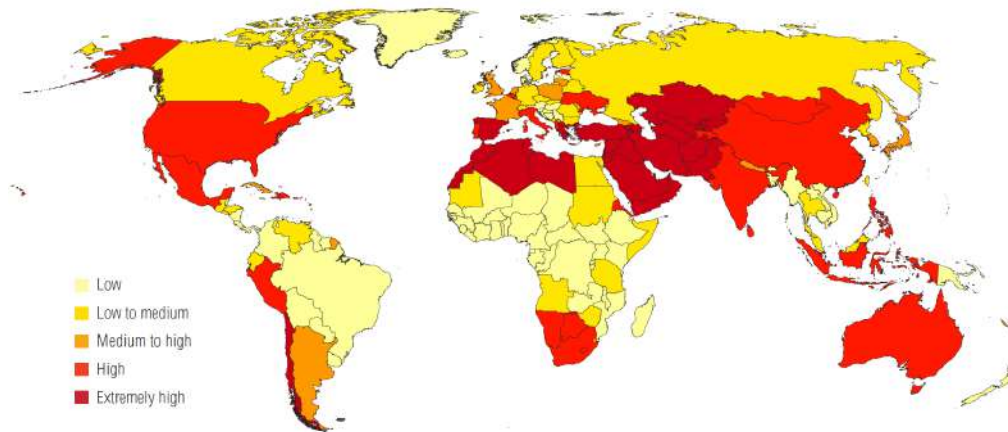


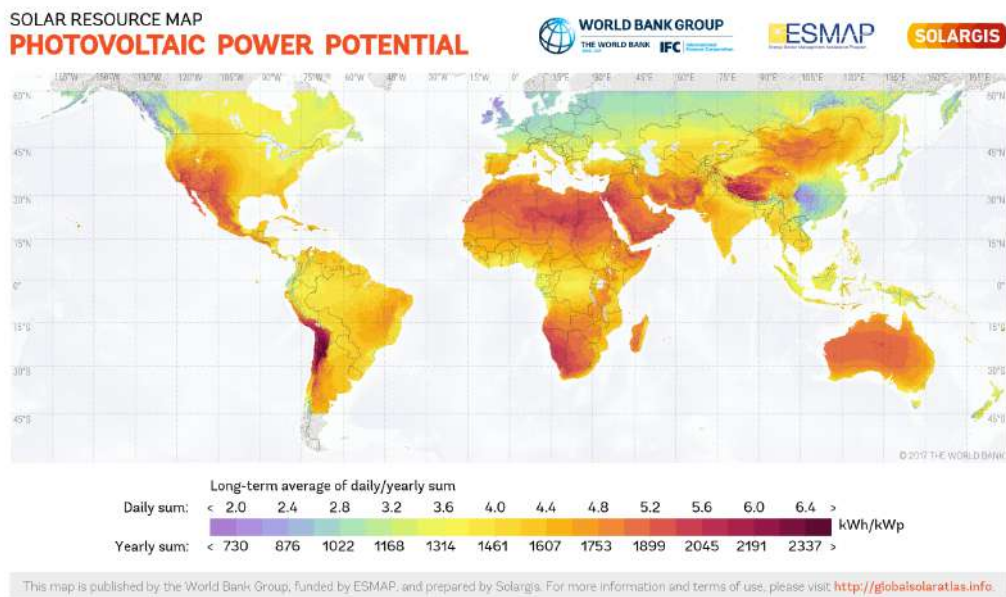
Figure 1.12: Water stress level by country using Business-As-Usual scenario [6] for 2040.

1.4 Motivation and previous work

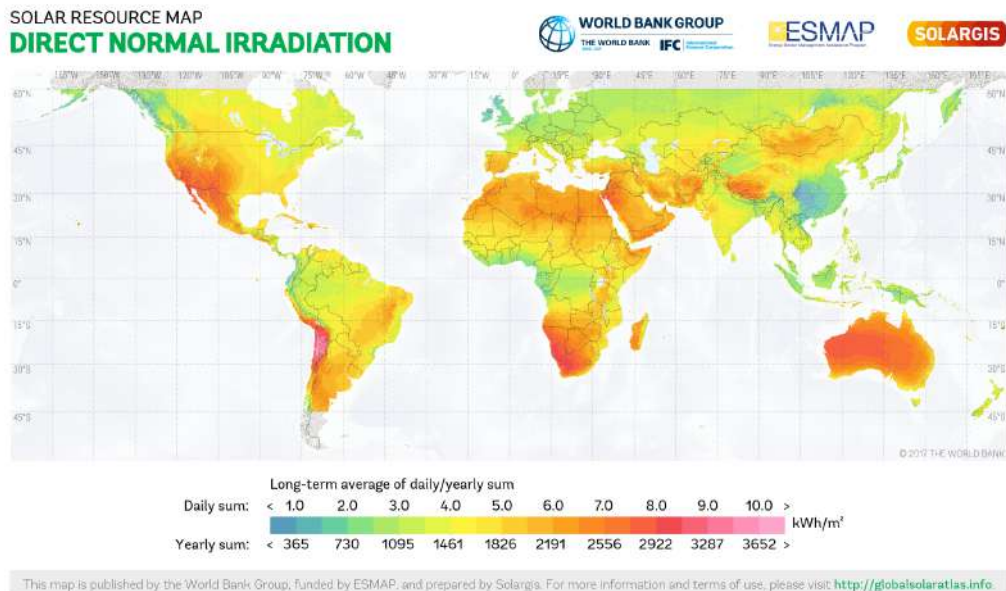
This thesis is, in part, a continuation of the author's Master Degree work, which is based on pollution estimations based on the atmospheric electric field measurements [57, 58, 59, 60, 61]. These previous works have enabled the author to acquire knowledge concerning atmospheric processes and particles, which can be consulted in Appendix B and C. These tools have enabled an easier introduction to soiling, as well as, to provide background for particle deposition mechanisms, e.g. turbulent deposition [58]. This work can be seen as the particle effect not on the atmosphere, but on the performance of solar energy conversion technologies. The idea of soiling research in this region came to help future CSP and PV plants regarding the quantitative effect of soiling on those technologies. As a matter of fact, for the author's best knowledge, no soiling study was ever published for this location. Along with this fact, this work attends to be ahead of time, by studying soiling effect for future plants and to be among the first to have a quantitative analysis on soiling for agricultural regions. The study is done in Alentejo region in Southern Portugal (details are given in the next section). The assessment part of this study is important to characterize the region in terms of soiling and for comparison with other locations, which allows to quantify the particle deposition severity level. However, mitigation techniques and methods are also an important part of this work. Majorly, because this is one of the driest regions of Portugal, which implies a reasonable water consumption, namely for cleaning, which is not a priority for water usage. Anti-soiling coatings (which are water free) and PV panel tilt angle modification, are part of the research performed and documented in this thesis. The two major topics covered in this work, besides the reasons invoked before, were set to account for water reduction techniques.

1.5 Thesis structure

The thesis is structured as follows: Chapter 2 includes soiling assessment research in PV, and within this scope are presented an annual analysis and characterization (visual/chemical) of the type and effect of



(a)



(b)

Figure 1.13: PV and CSP potential regions: (a) PV; (b) CSP. SOLARGIS is acknowledge, please consult: <https://solargis.com/maps-and-gis-data/download/world/>.

soiling on PV effect, local pollen emission and long-range transport of Saharan dust to Portugal and their respective effect on PV. Chapter 3 deals with soiling in CSP, using a TraCS (Tracking Cleanliness System) to quantify the soiling effect on a plain mirror during an entire year, from 2017 to 2018. This Chapter also contains a joint study between the Renewable Energies Chair (REC) and the *Institut de Recherche en Energie Solaire et Energies Nouvelles* (IRESEN) to compare soiling effect among Portugal and Morocco. In Chapter 4, mitigation techniques for PV are modeled. Anti-soiling coatings, for CSP, are tested and presented in Chapter 5. Chapter 6 includes the discussion and conclusions about all research topics presented

in the thesis. Both Appendices B and C, include work done in the path towards this thesis, as well as, background knowledge obtained for the work in this thesis.

The work done led to the following publications:

Journal publications:

- R. Conceição, H.G. Silva, J. Mirão, M. Gostein, L. Fialho, L. Narvarde, M. Collares-Pereira, Saharan dust transport to Europe and its impact on photovoltaic performance: A case study of soiling in Portugal, *Sol. Energy*. 160 (2018) 94–102.
- R. Conceição, H.G. Silva, J. Mirão, M. Collares-Pereira, Organic Soiling: The Role of Pollen in PV Module Performance Degradation, *Energies*. (2018) 1–13.
- R. Conceição, H.G. Silva, M. Collares-Pereira, CSP mirror soiling characterization and modeling, *Sol. Energy Mater. Sol. Cells*. 185 (2018) 233–239.
- R. Conceição, H.G. Silva, L. Fialho, F. Lopes, M. Collares-Pereira, PV system design with the effect of soiling on the optimum tilt angle, *Renew. Energy*. 133 (2019) 787–796.
- D. Lopes, R. Conceição, H. G. Silva, J. Mirão, G. Pérez, E. Araanzabe, M. Collares-Pereira, Evaluating the effect of an anti-soiling coating on the reduction of CSP mirrors dirtiness, *Solar Energy* (2019). Submitted.
- R. Conceição, H. Silva, A. Bennett, R. Salgado, D. Bortoli, M. Costa, and M. Collares Pereira, High-Frequency Response of the Atmospheric Electric Potential Gradient Under Strong and Dry Boundary-Layer Convection, *Boundary-Layer Meteorol.* (2017) 166:69.
- H. G. Silva, F. M. Lopes, S. Pereira, K. Nicoll, S. M. Barbosa, R. Conceição, S. Neves, R. G. Harrison, M. Collares Pereira, Saharan dust electrification perceived by a triangle of atmospheric electricity stations in Southern Portugal, *J. Electrostat.* 84 (2016) 106–120.

Conferences:

- R. Conceição, A. Merrouni, D. Lopes, A. Alae, H. G. Silva, E. Bennouna, M. Collares-Pereira, A. Ghennioui, A Comparative Study of Soiling on Solar Mirrors in Portugal and Morocco: Preliminary Results for the Dry Season, *SolarPACES*, (2018). Accepted for publication. This paper has been invited for an oral presentation, which was delivered by Dr. Ahmed Merrouni in SolarPACES 2018.

2

Soiling measurements in rural environment for PV

2.1 Introduction

Soiling on solar harvesting technologies, namely in PV systems, has been intensively studied in the past few decades; since it induces severe performance losses on such systems by reducing the incoming irradiance, through reflection, scattering and absorption [12, 39, 62]. This implies that the systems do not work at their fullest capability [63]. As a consequence, frequent cleaning of the systems is required, which represents an important slice on the cost of the electricity being produced. Moreover, soiling is not only a local [32], but also a seasonal phenomenon and for that reason, if operational costs are to be reduced, a proper characterization of it is needed. This has been done extensively in the literature, but mostly focused on desert regions [64, 65, 66], which have high irradiance values and significant problems with dust deposition, namely mineral and not organic.

However, everyday new PV and CSP plants are being deployed around the world and the tendency is to have more of them in the future, due to not only due to fossil fuels extinction, but also to decarbonize the economy and preserve the planet. Naturally PV in those also suffers from soiling, not only from local sources but also transported from remote ones [32]. One country in Europe that certainly is going to grow the use of solar technologies is Portugal, due to its high irradiance availability [42]. With this in mind, studies of soiling in this region are very important for future plants.

Environmental variables, like rain and aerosol optical depth (AOD), contribute to explain the observed soiling ratio (SR) during the period of the measuring campaign, November 2016 to October 2017, showing how both variables shape the evolution of the SR metrics. These variables are considered of vital importance for soiling deposition and removal, since rain is the main natural cleaning agent and AOD is used as a proxy for particle concentration in the atmosphere. Note also that the absence of rain allows for particles to build up on top of surfaces increasing the soiling and consequently decreasing PV module performance.

Although most soiling work considers dust to be the main soiling agent, it is restricted to mineral particles such as desert dust [67, 68], the first part of this Chapter is focused mainly on an annual soiling analysis for the measurement location, reported for the first time, as well as, the soiling rates that develop during periods without rain, which are then related to the environment, through AOD, SEM imagery and image processing and the role of organic soiling on the PV module performance. In this context, Alentejo (where the measurements were performed, Évora - $38^{\circ}34'0.01''$ N; $7^{\circ}54'0.00''$ W) is an ideal location for this type of study, since this is the region with the highest pollen concentration in Portugal [69]. Pollen concentration is expected to increase in the next few decades in Europe [70], and that may imply more organic soiling in the future and this is one more reason to study its impact on PV. Besides, studies of organic soiling are very scarce for, making it an excellent study opportunity. For organic particle deposition, EDS cannot be used since the composition is mainly carbonic and no conclusions can be taken. For this purpose, Elsa Caeiro, from the Portuguese Society of Aerobiology (*Sociedade Portuguesa de Aerobiologia*) using the SEM images obtained, was able to identify some of the organic material deposited.

The second part of this Chapter is related to the impact of long-range Saharan dust transport. One event happened in February and another in March 2017, and their effect on the performance of photovoltaic flat panels is reported as a case study of soiling. Through satellite images, dust coming from North Africa was detected, while using the Hybrid Single-Particle Lagrangian Integrated Trajectory (HYSPPLIT), specific origin locations of the dust were found. Dust accumulated on glass coupons deployed in Southern Portugal, Évora and Alter do Chão, was analyzed by Scanning Electron Microscopy (SEM) and Energy Dispersive Spectroscopy (EDS). Mass accumulation on those coupons was weekly measured with a microbalance and related with environmental parameters, such as AOD and rain, through a proposed empirical model. Performance measurements took place at Évora using mc-Si PV flat panels and an I-V curve tracer to get two parameters: maximum output power and short-circuit current. It was found that the first dust event led to decreases in the maximum output power of $\approx 8\%$ and in the short-circuit current of $\approx 3\%$, while the second event led to a decrease of $\approx 3\%$ in both parameters. A relation between PV performance and mass

accumulation was explored.

Saharan desert dust storms are a significant source of dust, that frequently reach Portugal (around 4-5 major events per year) [71], bringing quantities of dust that significantly influence the performance of PV systems, as will be shown. In fact, during this study a major Saharan desert dust storm took place on 20th- 24th February 2017, in which a large amount of dust was swept up into a low pressure system over North Africa, leading to the transportation of a dust cloud over Portugal. Significant soiling was detected and it was derived mainly not from local particles, but from the ones with very far away origin. Though with less intensity, another dust event occurred on March 2017 from 14th-16th and it is also documented here. This work points towards the fact that not only local environment affects soiling, but it shows instead that long-range dust transport (from a process developed thousands of kilometers away) can also influence soiling and the PV performance on a far away region. This work uses the mentioned Saharan desert events as a case study to highlight the importance of these phenomena in the energy production of the region and also the need to develop mitigation tools, e.g., proper dust storm forecasts or the use of active and passive cleaning mechanisms.

2.2 Experiments and data

Soiling measurements took place at two rural locations in Southern Portugal (Alentejo): Évora at *Plataforma de Ensaios de Colectores Solares* (PECS), from REC [72], which was used for both parts of this Chapter, and Alter do Chão in a 200 ha olive tree property of Elaia group, which was only used for the second part of this Chapter. These locations have the following coordinates: Évora - 38°34'0.01" N; 7°54'0.00" W and Alter do Chão - 39°12'3.39" N; 7°39'37.09" W. The last location is part of a larger soiling experiment of the European project MArkET uptake of an innovative irrigation Solution based on LOW WATER-ENERgy consumption (MASLOWATEN funded by Horizon 2020, contract number 640771). The MASLOWATEN project, in which REC participates, is led by *Universidad Politécnica de Madrid* and its objective is to use high power PV pumping systems for productive agriculture irrigation consuming zero conventional electricity and achieving less water consumption.

2.2.1 Mass accumulation

SINA high transmittance solar glass coupons, from Interfloat Corporation, were left outdoors in two experimental setups. In PECS, the experimental setup consists of 25 coupons, with 11 cm length 9 cm width and 3.2 mm thickness at approximately 1.5 m height from the ground, with 6 samples per geographical direction (North, East, South and West) in 15° inclination steps and one completely horizontal on the top, following the idea in [73], as shown in Fig. 2.1a. For clarity, N6 and E6 are the designations used for the glass coupons oriented towards North and East with 15° inclination regarding the horizontal position, respectively. In Elaia a single glass coupon was deployed on a single-axis tracking PV system, approximately

1.5 m above the ground, in a structure that replicates the usual PV module assembly glass-metal frame, see Fig. 2.1b. Weekly mass measurements were done to all 25 samples at PECS and monthly SEM and EDS measurements were done to selected coupons from PECS and Elaia. Mass was obtained using a Bosch SAE 80/200 microbalance model. The mass uncertainty, 0.17 mg, was determined from several measurements of a clean reference glass. The objective is to study the mass accumulation density on the glass coupons and relate it with the environmental conditions as well as to characterize the accumulated soiling. Mass accumulation density on week t , $m_a(t)$, is determined by subtracting, from the measured mass at that week, $m(t)$, the initial mass of the clean glass, $m(0)$, dividing it all by the sample area:

$$m_a(t) = \frac{m(t) - m(0)}{Area}. \quad (2.1)$$

No cleaning is done to the glass during the experiment and only environmental action (e.g., rain) can act towards reducing the mass accumulated on the coupons.

2.2.2 PV performance

The testing campaign, related to the evaluation of the PV performance, is depicted in Fig. 2.1c. It shows two mc-Si PV flat panels of the same model FTS-220P, manufactured by Fluitecnik. The current-voltage (I-V) characteristic curves were obtained with a Eurotest PV Lite MI 3109 manufactured by Metrel. On these PV modules, one was manually cleaned before each I-V curve tracing and the other was kept unclean since the beginning of the experiment. Three I-V curves were obtained for each module. The measurements were only performed in clear sky, near solar noon, and the tracker was always set perpendicular to the sun when performing the measurements. When not performing measurements, the panels are set facing south and tilted approximately 34° from the horizontal. This is done to represent what would be the approximate position of a real fixed system, optimized for this location. This experiment is fundamentally based on [74], with one main difference: measurements are not taken continuously, so the number of points which contribute to the calculations is smaller.

The soiling ratio index, mathematically defined as SR , is calculated by comparison of the short-circuit current (I_{SC}), which is denoted $SR_{I_{SC}}$ and the maximum power output (P_{max}), denoted $SR_{P_{max}}$ of the two photovoltaic panels. The main difference noted in [74] is the fact that when soiling is homogeneous both metrics give similar results, but when the soiling is not homogeneous, calculating the soiling ratio based on the short circuit current can give either an underestimated or overestimated result, comparing it what was actually lost in power output. The reason for this is the fact that non-uniform soiling distorts the I-V curve in such a way that in some cases it changes considerably the I-V maximum power point. In mathematical terms, $SR_{I_{SC}}$ and $SR_{P_{max}}$ are calculated through Eq. 2.2, Eq. 2.3 and Eq. 2.4:

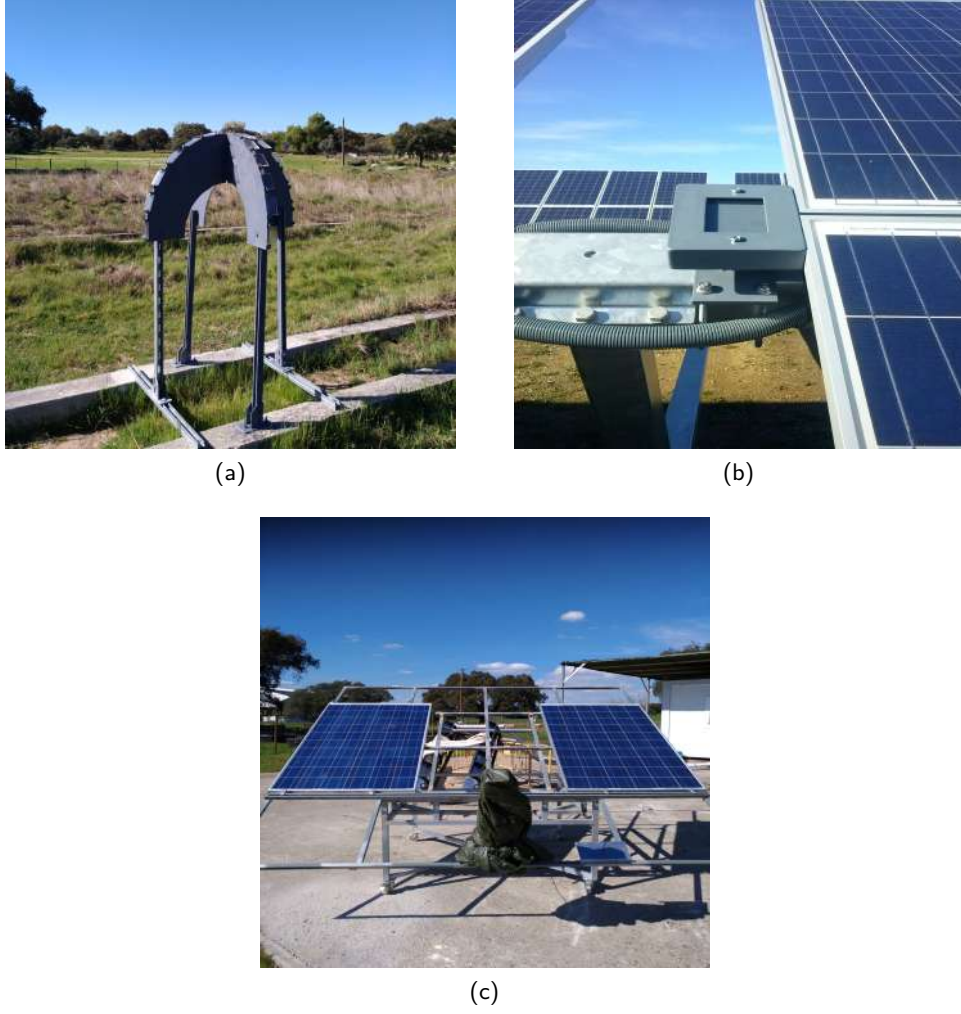


Figure 2.1: Glass coupon supports: (a) glass tree in PECS; (b) glass sample support in Elaia; (c) PECS soiling experiment.

$$SR_{I_{SC}} = \frac{I_{SC}^{soil}}{I_{SC}^{soil,0} [1 + \alpha(T_{soil} - T_0)] (G/G_0)}, \quad (2.2)$$

where I_{SC}^{soil} is the short-circuit current of the soiled PV panel, $I_{SC}^{soil,0}$ is the short-circuit current of the soiled PV at clean condition in standard test conditions (STC), α is the short-circuit temperature correction coefficient, T_{soil} is the cell temperature of the soiled panel, T_0 is the temperature at reference condition (25°C), G is the irradiance in the PV plane and G_0 the irradiance at STC conditions (1000 W/m²).

$$SR_{P_{max}} = \frac{P_{max}^{soil}}{P_{max}^{soil,0} [1 + \gamma(T_{soil} - T_0)] (G/G_0)}, \quad (2.3)$$

where P_{max}^{soil} is the maximum power of the dirty PV panel, $P_{max}^{soil,0}$ is the maximum power at clean condition and γ is the maximum power temperature correction coefficient. For the calculation of the irradiance in the

PV plane, the clean module is used:

$$G = G_0 \frac{I_{SC}^{clean} [1 + \alpha(T_{clean} - T_0)]^{-1}}{I_{SC}^{clean,0}}, \quad (2.4)$$

where I_{SC}^{clean} is the short-circuit current of the clean PV panel, $I_{SC}^{clean,0}$ is the short-circuit current at clean condition in Standard Test Conditions (STC) and T_{clean} is the cell temperature of the cleaned panel.

2.3 Annual Soiling Characterization

An annual series of soiling data for the region under study is reported here for the first time, with data ranging from November 1st, 2016 to October 31st, 2017, as presented in Fig. 2.2. Soiling rates, mathematically defined as $S_R \approx d(SR)/dt$, between periods without rain are shown as red dashed lines in this figure. To explain the observed soiling ratio and the respective soiling rates, rain is also added to the study, see Fig. 2.3a and aerosol optical depth data, see Fig. 2.3b. Rain as the main cleaning agent is very important, as well as the AOD, proxy of particle concentration in the atmosphere. There are five evident cases in Fig. 2.2: two long-range desert dust transportation events, one in February (denoted in Fig. 2.2 as F. Event) and other in March (denoted as M. Event), with both events documented in the previous section, and three periods where the lack of rain, denoted as SPR, S_1 and S_2 , which led to a linear decrease in both SR metrics, marked with the red dashed line.

Table 2.1: Soiling rates and statistical parameters.

	SPR	S_1	S_2
S_R (%/month)	4.1	1.9	1.6
r^2	0.97	0.97	0.94
RMSE	0.0013	0.0007	0.0008

During Fall and Winter, because of frequent rain, soiling cannot accumulate in significant amounts on the glass surfaces, yielding SR metrics close to 1 as expected. The first major soiling event was in February, F. Event, where a major quantity of Saharan dust was transported to Southern Europe, mainly Portugal and Spain [32], leading to a decrease of $\approx 8\%$ in $SR_{P_{max}}$. The second one was in March, M. Event, although with less intensity led to a decrease of $\approx 3\%$ in both SR metrics. During Spring, mainly April, denoted as SPR, there was an absence in rain, which allowed for organic material (confirmed below with complementary measurements to be mostly pollen) to deposit on the PV glass surfaces, leading to a decrease of 4.1% in both metrics, see Table 2.1. Note that since the soiling rates are per month, that also means that at the end of the month the losses are the same as the loss rates, since at the beginning of every event the panels were clean. However, heavy rain in the first part of May, was able to remove the accumulated soiling. In

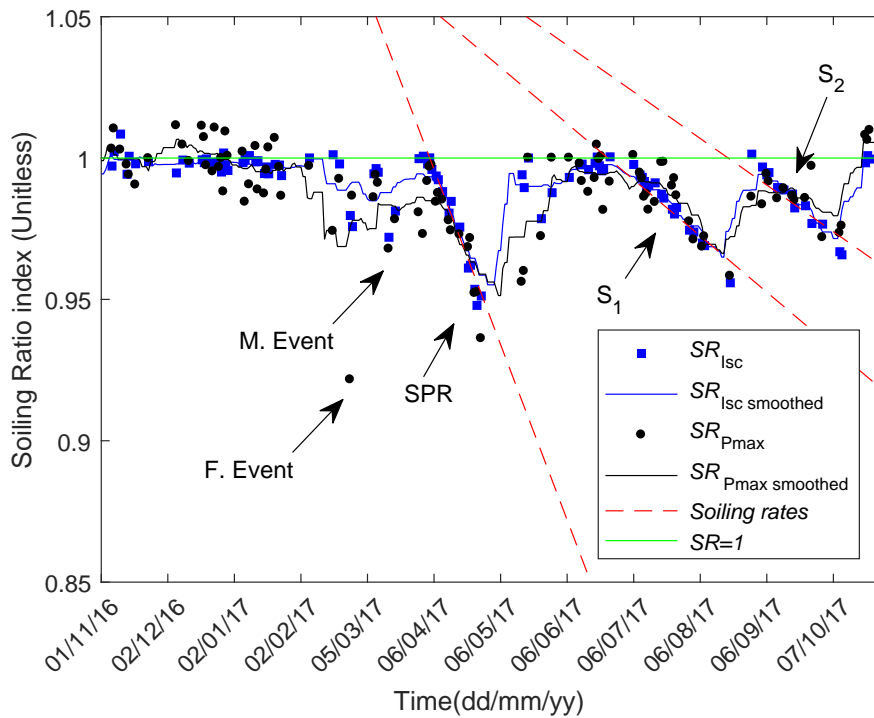


Figure 2.2: Soiling ratio and rates.

June maintenance was done to the PV tracker and because of that the PV panels were cleaned, which resulted in two weeks without data coinciding with some rain. During July, the period denoted by S_1 , due to the scarce rain, soiling was able to settle, leading to a decrease of 1.9%. In August (vacation period) there was less data points and at the end of the month. There was then a rainy day, which cleaned the PV panels, returning both metrics close to one. Due to the continued lack of rain during September, particles accumulated over the surface leading to a decrease of 1.8%. After a heavy rain period in the beginning of October the SR metrics recovered near to unity.

Analysis shows that, the February dust event is responsible for the highest loss registered, however during Spring, due to an increase of organic material, reveals itself as the second most important soiling case. Moderate March dust event comes in third, hand in hand with the soiling rates developed during Summer.

SR metrics decay were smoothed, due to the noisy data derived from the reduced amount of data points, [74]. In statistical terms, the values of r^2 , for the linear decay of the SR metrics, are presented on Table 2.1; they are all above 0.9, which represent very high correlation values while, RMSE values always bellow 0.002. This fact ensures that not only the soiling rates are close to being linear, but also they enhance confidence on the results obtained for the SR.

Note that in Fig. 2.3b, AOD data is in red and the smoothed data in black, which serves the purpose of being able to visualize the trends in AOD. It can be seen that the highest AOD was in February, due to

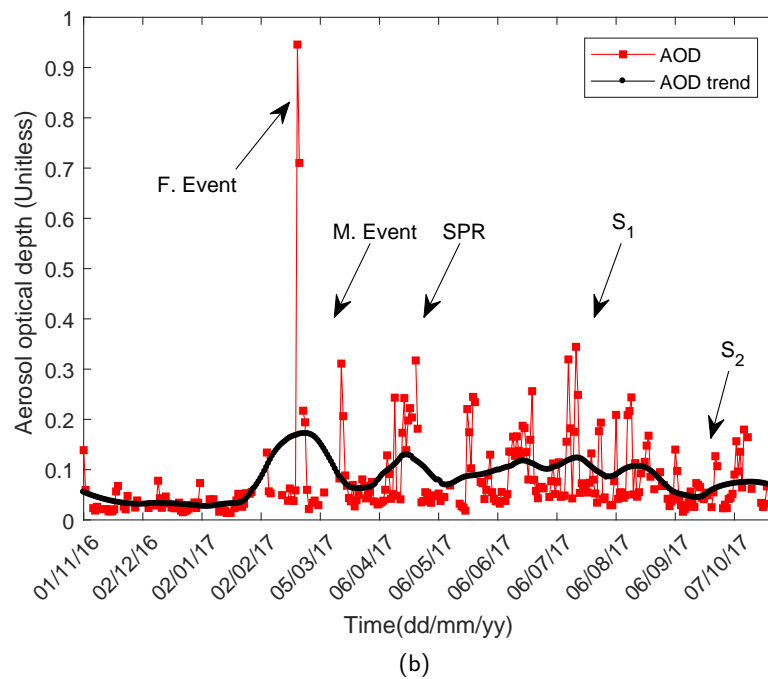
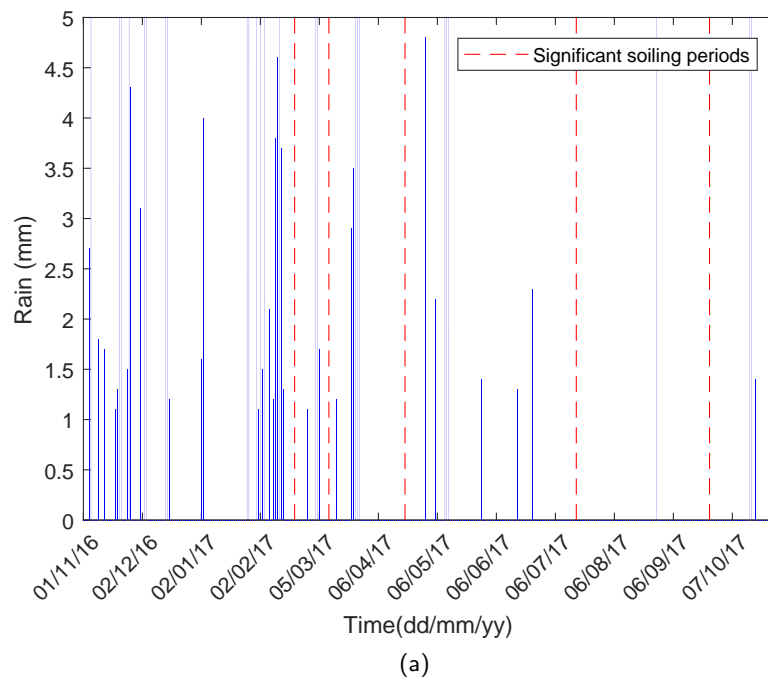


Figure 2.3: Environmental measurements: (a) Rain; (b) Aerosol optical depth.

the large dust event, while lower values are in March when the event with less intensity took place. After that, a peak in April can be seen, which is due to the increase in organic material in the atmosphere, with a more or less constant trend during the Summer, until it starts to decay from September on. However as stated before, due to rain in May, maintenance in June, lack of data and high rain at the end of August, soiling was only able to develop during Summer. If these exceptions are ignored, it can be concluded that

the soiling rates follow the same trend as the AOD and lack of rain. As a consequence, it means that the AOD is working as particle concentration proxy. Higher AOD values, means there are more particles in the atmosphere, which increases the probability of a particle to be deposited on the surface, leading to higher PV performance losses. For further proof, see Fig. 2.4, where m_a represents the mass accumulation on the 30° tilted glass sample. Note that fast dust events are not well represented by this particular glass probably probably due to the glass tree architecture. However, for periods without rain and continuous particle deposition it relates very well with AOD and SR metrics.

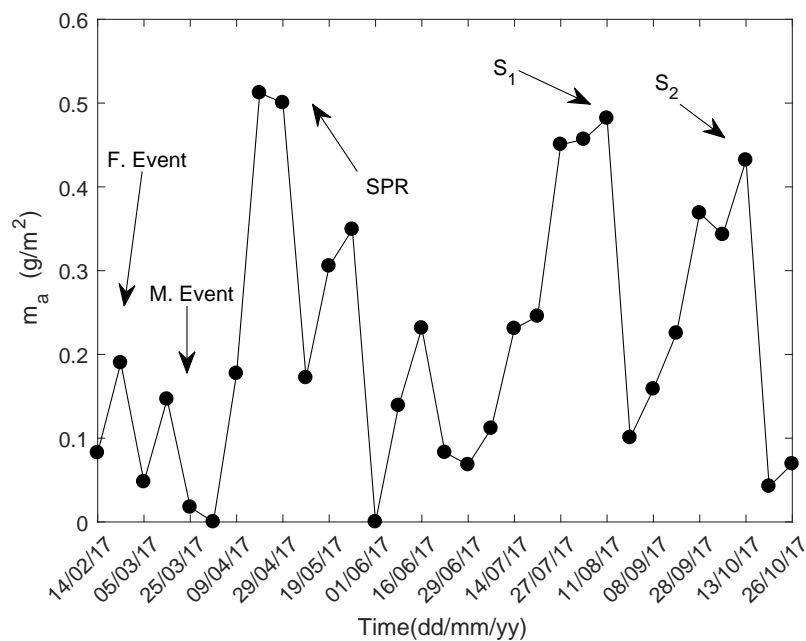


Figure 2.4: Mass accumulation on 30° tilted glass sample.

It can be seen that the mass accumulation is higher during April, then July and lastly during September. This corroborates not only the soiling rates results, but also the use of AOD to explain such phenomena. Note again that due to maintenance the glasses had to be clean in the beginning of June, that is the reason why the mass accumulation is zero on that period.

As seen in the data of Fig. 2.2 and Table 2.1, if the rain is scarce during the Spring, the organic material (namely pollen, as shown below) may induce very high soiling levels, even higher than mineral material. In the next section a descriptive analysis is given on the type of soiling found in SEM images from April and July.

2.4 Organic material characterization and features

Organic material has been out of the scope of most of the known soiling studies, since their are absent or in very low quantities in desert areas, where most studies were and are still being done. However Portugal

is one of the places in Europe, which is not only affected by desert dust, e.g. Saharan long dust transport, but also by high amounts of pollen, mostly during Spring. More specifically, the region of Alentejo is the one with the highest pollen concentration in Portugal as described in [69]. The type of pollen in higher concentrations belong to the family of *Gramineae*, *Oleaceae*, *Fagaceae*, *Pinaceae*, *Cupressaceae*, *Platanaceae*, and *Urticaceae*, according to [75]. It is known that the locations far from the ocean coast and situated more to the south of the country are the ones with more pollen concentration. From [75] it is also known that pollen counts can roughly go from 3000 grains/m³ in January to 40000/m³ in May. Assuming that most of pollen species follow the trend of low values at night to high values towards the afternoon [76], there is a potential problem, since dew that forms during the night can hold pollen during the beginning of the day, while it did not evaporate yet. However, there are some types of pollen, that have their maximum concentration during the night [77], and following the same logic, can also cause higher deposition in PV panels, if they get trapped by the dew water.

Also from 2007 to 2009, for some of the pollen species referred before, total pollen count was calculated, in the city of Lisbon [7] and normalized, which can be seen in Fig. 2.5. It is assumed that the trends in Évora and Lisbon are similar, mainly because there are not far apart (around 100 km). However, Évora should have substantially higher pollen count values. It can be seen that from January to April/May, the tendency is to have an increasing amount of pollen, which then starts to decay until the end of the year. The fact that April has the highest concentration of pollen, together with the lack of rain can lead to a harsh decrease in the PV performance, corroborating what was seen before, Fig. 2.2.

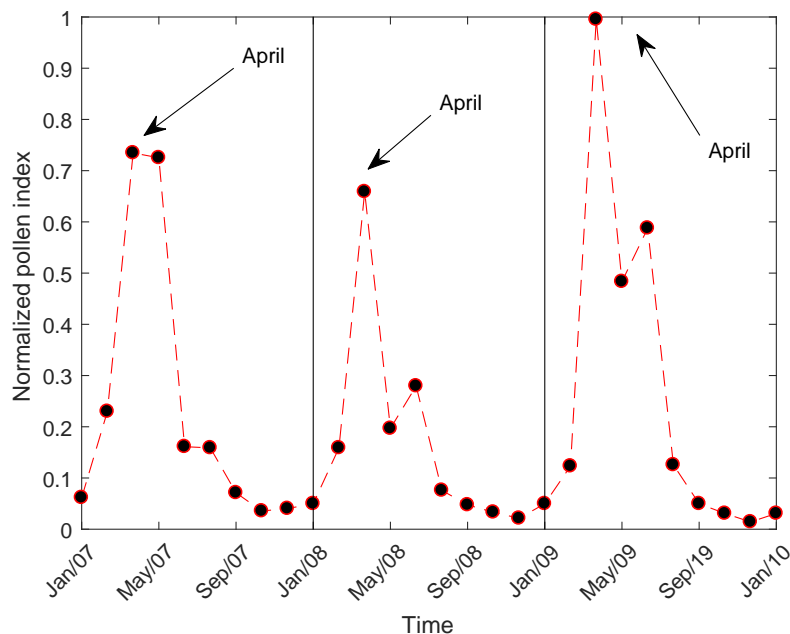


Figure 2.5: Annual pollen trends in Lisbon (Portugal) from 2007 to 2010, adapted from [7].

In spite of the already high pollen concentration, the prediction for the future is that the concentration of some species of pollen will increase, see [78], this could make pollen (as a soiling agent), even more

important in the future. This is reinforced by NASA NEX-GDDP for 2100, predicting less frequent rain for Portugal. If it indeed becomes a reality, it may not only be possible that soiling will have more time to build up on surfaces, but also the amount could be higher (mainly during the Spring), which will eventually result in higher losses than the ones shown here.

2.4.1 SEM characterization and image processing

In order to have a deeper insight into what kind of organic and mineral material gets deposited on PV surface, SEM and EDS measurements were made to the central glass sample (with zero tilt angle) on the glass tree shown in Fig. 2.1a. The organic material found in the SEM was mainly pollen, which is shown in Fig. 2.6.

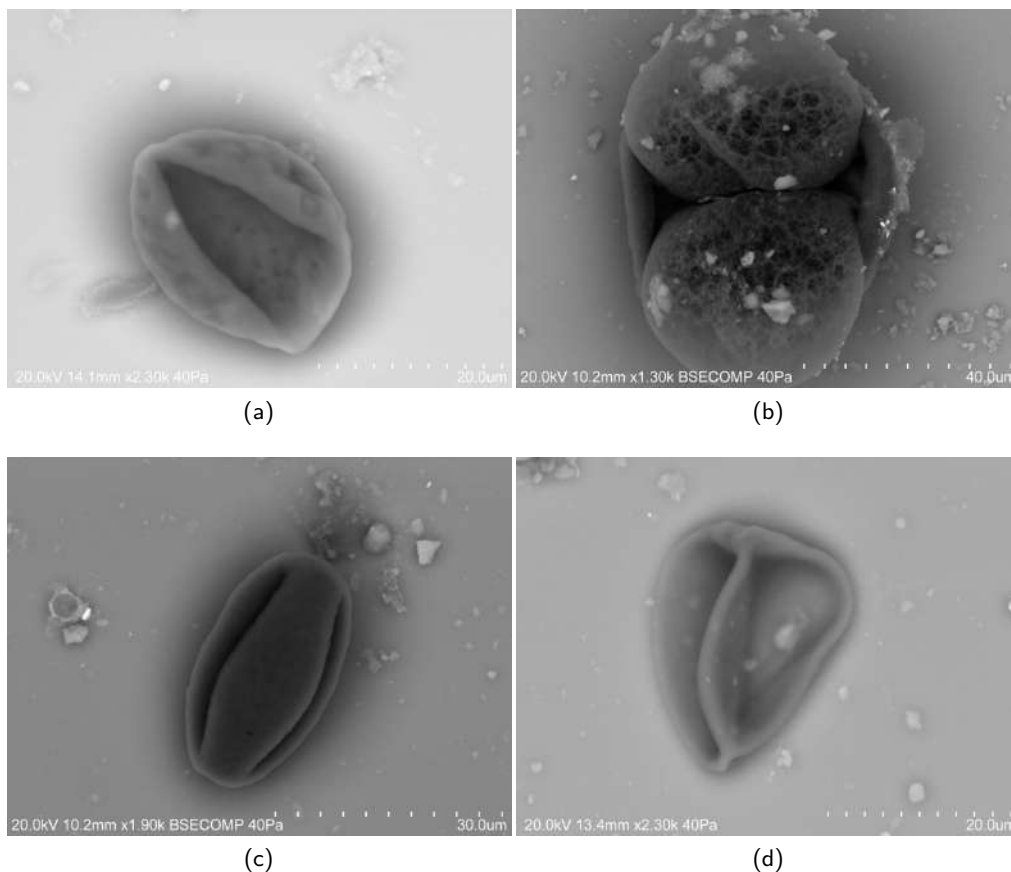
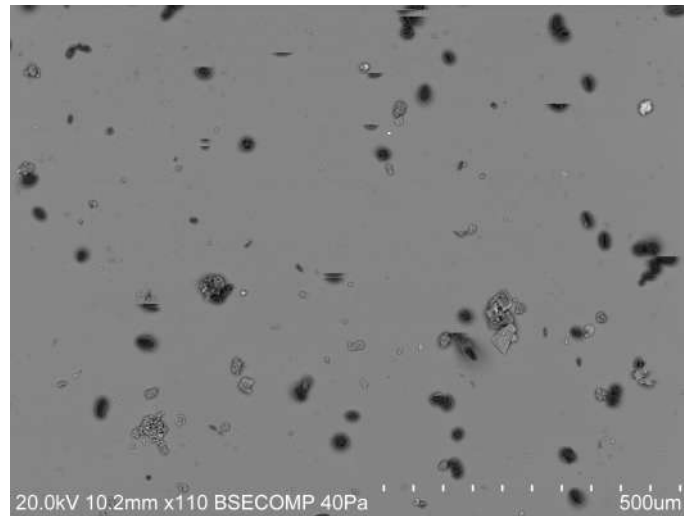


Figure 2.6: Main types of pollen from glass sample SEM: (a) Arecaceae; (b) Pinaceae; (c) *Quercus sp*; (d) Poaceae.

Different species were found, as the Arecaceae in Fig. 2.6a, Pinaceae in Fig. 2.6b, *Quercus sp* in Fig. 2.6c and Poaceae in Fig. 2.6d. From image observation, it can be seen that these pollen species tend to be geometrically spherical or elliptical. It can also be seen that they tend to be around 20 to 30 μm diameter, if assumed spherical. For a better understanding of how the pollen affected PV performance during the Spring and Summer the following SEM images are shown, one taken at April and other at July with the

same magnification, in Fig. 2.7.



(a)



(b)

Figure 2.7: SEM images: (a) April 2017; (b) July 2017.

Using ImageJ, which is an open source image processing program (<http://imagej.net>), the following characteristics of the organic material, as well as all the material in the SEM images were found, see Table 2.2. The variable O_D corresponds to the average diameter of the organic material (in black on the SEM images), A_D is the average diameter of all the particles detected in the image, OA_{PNR} is the ratio percentage between the organic and all material present in the image, in terms of particle count, while OA_{AR} is the ratio in percentage (in terms of area) between the organic and all material in the image. It should be noted that it is very difficult to analyze such images and there is uncertainty associated with it. A more precise method is needed and this analysis is only for a general characterization that needs to be deepened.

The organic material, which are essentially pollen, namely *Quercus sp*, have $\approx 20 \mu\text{m}$ diameter, which is in line with the size of that species in Fig. 2.6c. When considering all the material in the sample, organic and mineral, the diameter drops to $\approx 14.5 \mu\text{m}$, which is expected, since mineral soiling tends to be smaller than

Table 2.2: SEM image parameter analysis.

	April	July
O_D (μm)	20.5	19.3
A_D (μm)	14.4	14.9
OA_{PNR} (%)	33.8	4.1
OA_{AR} (%)	40.3	6.5

pollen. In April, 33.8% of the particles present are organic material, while in July only 4.1%. This illustrates the difference, considering the number of particles, between these two different seasons in terms of soiling. Regarding the percentage ratio of area occupied by organic particles, 40.3% of the area occupied by all particles is occupied by organic soiling in April, while in July only 6.5%. From this data, it can be concluded, that organic material, namely pollen, deposits on surfaces during the Spring at higher concentrations and due to its higher diameter it has relatively more impact than mineral soiling (smaller particles). Moreover, it can be happening that pollen instead of just depositing directly over the glass surface, it is also depositing over the mineral matter. Instead of the radiation passing just the mineral or pollen layer, it also has to pass, in certain areas, both the pollen and mineral layer.

2.5 Saharan Desert Dust Event

2.5.1 Dust transport

True-colour images taken by the Visible Infrared Imaging Radiometer Suite (VIIRS) instrument aboard the National Oceanic and Atmospheric Administration (NOAA)/NASA Suomi NPP satellite, please see Fig. 2.8, show the February 2017 Saharan desert dust event. The low pressure system caused the transport of dust to Portugal and brought particles from the Saharan region to the locations where the experiments were ongoing. As a consequence of particle transportation, a dust cloud covered the sky resulting in very high AOD values, exceeding the threshold in [79] for desert dust events by almost 10 times.

Just considering this, it is clear that it was a major event, since when small events happen the AOD values are much lower [60]. This was the case for the second event that occurred latter on March 2017. Nevertheless, NASA images did not allow the precise identification of the dust plume geographic point of origin and to obtain this information, the HYSPLIT modelling system [80] was used for the trajectory analysis, see Fig. 2.9. Backward trajectories were calculated from the Global Data Assimilation System (GDAS) used by the National Centers for Environmental Prediction (NCEP), [81], data with 0.5° by 0.5° latitude-longitude resolution. Trajectories were calculated every 2 hours for a time frame of 48 hours and the altitude at the desired location was set to 500 meters, which is enough for particle dry deposition or for it to be brought down by rain, in a process denoted as wet deposition. The different colors represent the

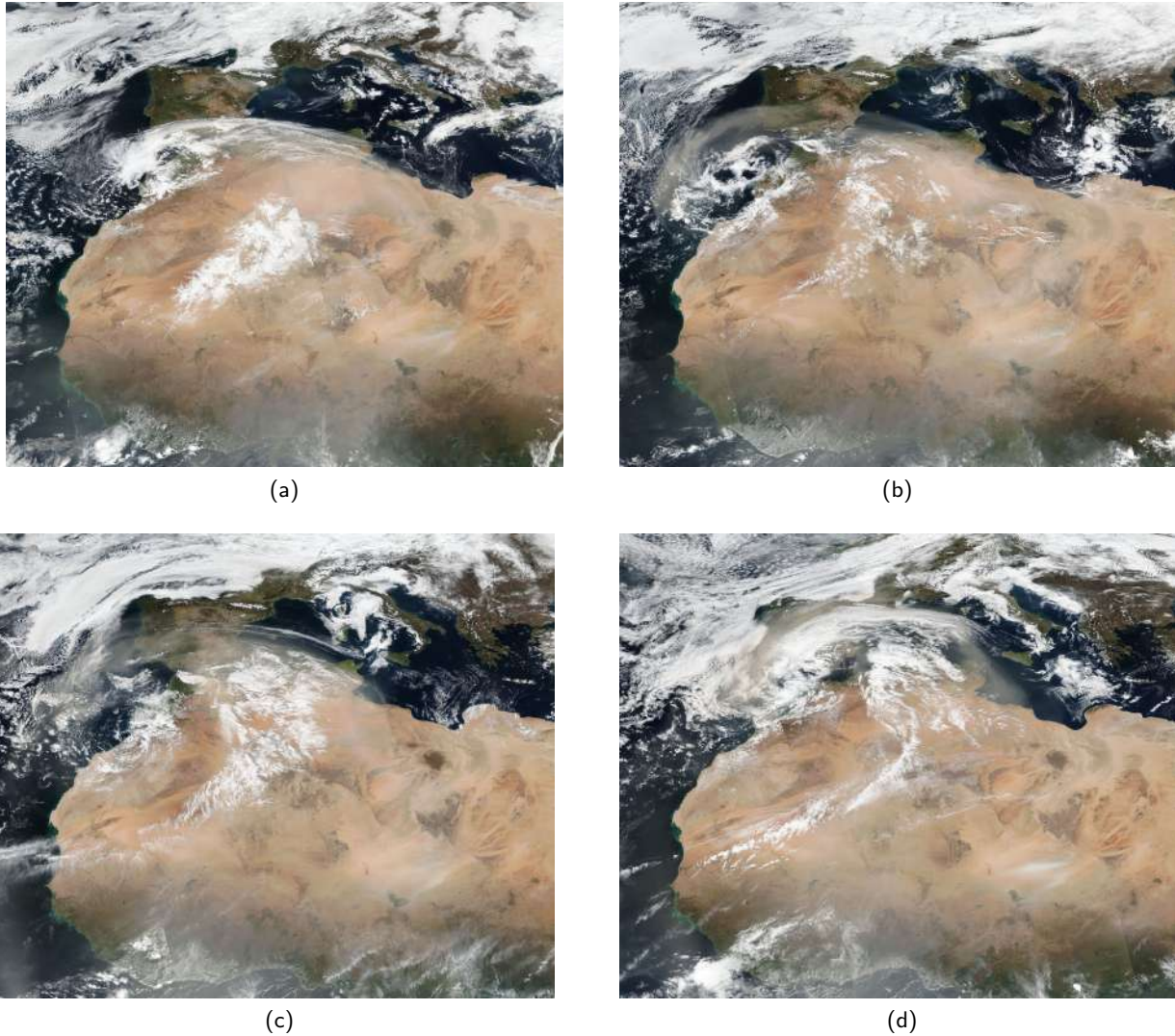


Figure 2.8: NASA VSIIR dust event true image colours: (a) 20th February; (b) 21st February; (c) 22nd February; (d) 23rd February.

different trajectories starting at each time step, although there are different trajectories with the same color since there are too many trajectories for the HYSPLIT color palette. From HYSPLIT analysis it is possible to conclude that dust plumes came mainly from Northern Mali, Algeria and Tunisia (all part of the Sahara desert), crossed the Mediterranean sea and reached Southern Europe.

To have further information on the amount of dust and the altitude at which the dust plume arrived at the experimental locations, the Barcelona Supercomputing Center (BSC) forecasts [82, 83], were analyzed (not shown). For the February event, the 21st was the day with the highest concentration, reaching approximately $900 \mu\text{g}/\text{m}^3$ at 3 km altitude; in the next two days the concentration decreased until it reached background values on the third day. On the March event, the 15th had lower concentration values of $250 \mu\text{g}/\text{m}^3$ again at 3 km altitude; the dust concentration decreased in the following days. According to data available in [84], background atmospheric aerosol load in May, in the region where both sites are

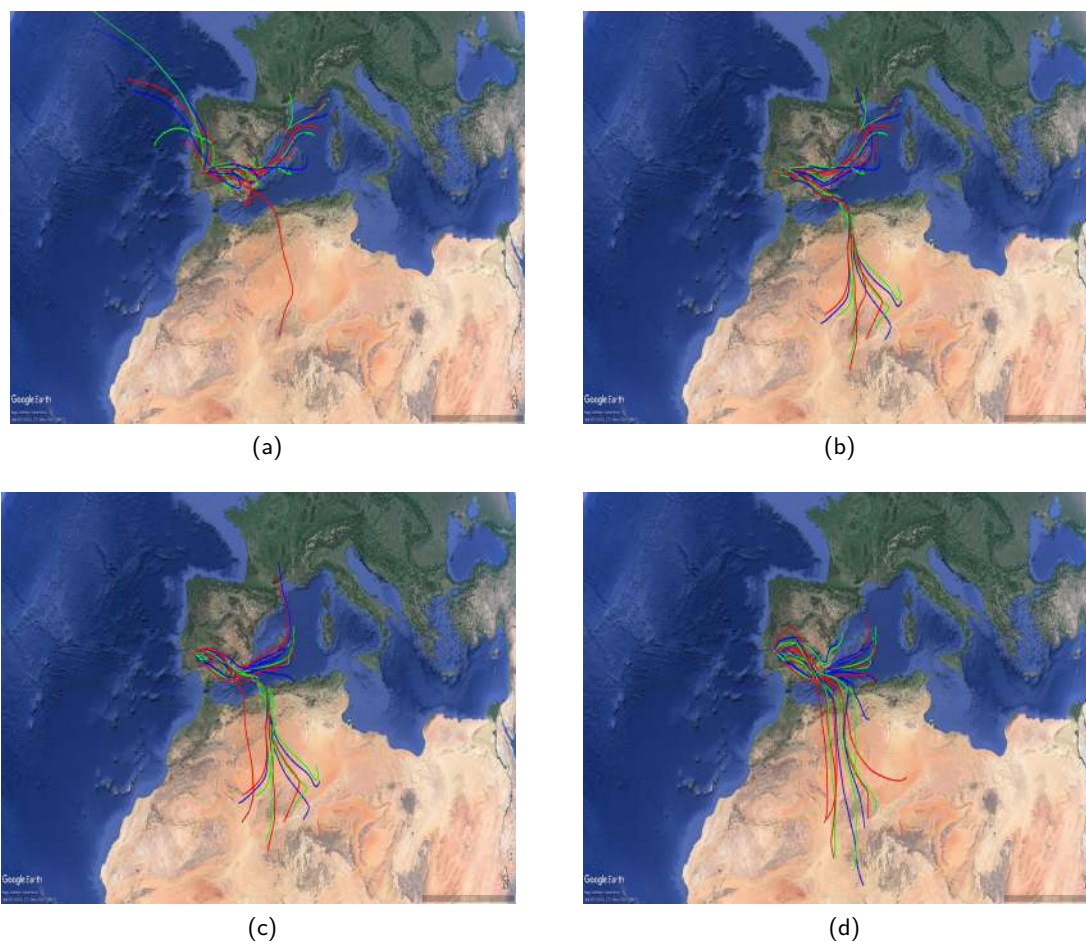


Figure 2.9: HYSPLIT air masses trajectories: (a) 20th February; (b) 21st February; (c) 22nd February; (d) 23rd February.

located, is around $20 \mu\text{g}/\text{m}^3$, but for February and March it is expected to be even less, since in May pollen concentration in the atmosphere increases, escalating the aerosol load. Thus, these forecasts show a 45 fold increase relative to background values on the February event, while in the March event there was a 5.25 fold increase, illustrating the clear difference between these two events.

2.5.2 Dust chemical analysis

The particles from the February dust event were deposited on the glass coupons in PECS, Fig. 2.1a, and in Elaia, Fig. 2.1b. Two glass coupons from PECS, N6 and E6, were collected from the setup on the 22nd February, at the beginning of the dust break. N6 glass had multiple 'mud' drops, both visible under naked eye (Fig. 2.10a) and backscattered electron SEM (Fig. 2.10b). These were due to light rain contaminated with Saharan dust precipitated during the night of 21st February. The E6 glass coupon did not show the same drops, but it will be important for comparison between Saharan dust and local dust previously deposited on the glasses. The Elaia glass was collected on the 23rd February. The three were analyzed on the 25th February using SEM-EDS. It is assumed that the areas which were chosen to make

the SEM-EDS analysis are representative of the entire glass surfaces. For the Elaia glass coupon, Fig. 2.10c, it could be stated that it is probably composed by aluminosilicates (AS) and halite (NaCl). The AS are characteristic of desert areas, such as Sahara [85, 86] and the NaCl probably resulted from the evaporation of sea spray collected by the dust plume while traveling over the Mediterranean sea [87] and dragged together with the plume.

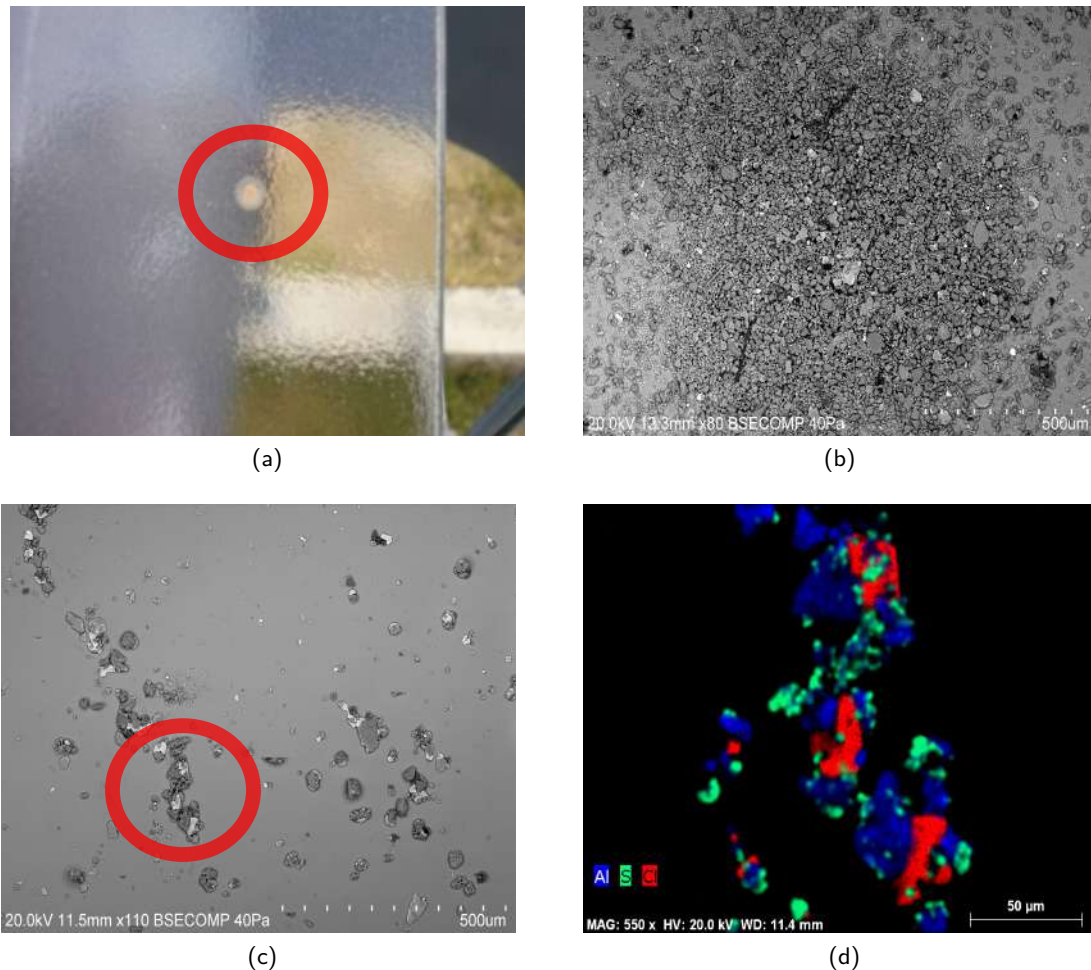


Figure 2.10: PECS glass samples: (a) N6 rain drop with dust; (b) SEM of N6 glass rain drop; (c) Elaia glass sample SEM; (d) EDS of the zoomed structure.

The SEM image, Fig. 2.10c, shows particles of different sizes agglomerated. From the EDS analysis, Fig. 2.10d, and corresponding multi-point analysis, it is seen that large particles, in red, could correspond to NaCl. For PECS, the E6 sample (less affected by the dust event) showed what could possibly be AS, but also quartz (SiO_2) and calcite (CaCO_3), while N6 (with the 'mud' drop) showed the possibility of quartz, iron oxides (Fe_xO_x), calcite, gypsum ($\text{CaSO}_4 \cdot 2\text{H}_2\text{O}$), and rutile (TiO_2). Another important fact is that E6 glass had most particles spread and not agglomerated like the one from Elaia and N6, possibly indicating agglomeration during the dust plume transport by particle collision. Regarding the dust point of origin, HYSPLIT points towards the Southern Algeria and Northern Mali crossing Northern Algeria and Tunisia. Following the procedure in [85], weight percentage (wt.%) ratios of $(\text{Ca}+\text{Mg})/\text{Fe}$ were calculated, since

they can serve as indicators to differentiate locations for the Saharan dust. For Elaia the value 1.89 was found, while for PECS, E6 and N6, the values were 3.21 and 2.23, respectively. Corresponding values for origin locations, [85], are in the range 0.62-2.08. While for N6 and Elaia there is a reasonable agreement with the literature values, for E6 (which did not get hit by mud drops) the values are higher, probably due to the influence of local particle composition.

2.5.3 Results

2.5.3.1 Mass accumulation

The top-horizontal glass coupon at PECS in the week before the February event had a mass of 76.78376 g, at the event its mass was 76.79432 g and a week after 76.78388 g. Note that these values are the result of the mean measurement of the glass three times. This corresponds to an increase in the accumulated mass of almost $\approx 1067 \text{ mg/m}^2$; this is the highest mass accumulation during one week detected in all the campaign (except for bird drops). The Elaia sample weighed 76.96808 g right after the event, while cleaned it weighed 76.96410 g; which corresponds to an increase in mass accumulation of only $\approx 402 \text{ mg/m}^2$, a decrease of 665 mg/m^2 in relation to PECS. This difference can be related to the location, since the glass sample at Elaia is surrounded by olive trees and by the 140 kWp PV plant (part of MASLOWATEN), while in PECS is a wide open experimental facility; both trees and the PV panels can work as a barrier to the dust brought from afar explaining the lower mass accumulation in Elaia when compared to PECS. Nevertheless in the scenario of such intense soiling events, these barriers tend to have little effect, especially in the February event, in which most of the dust was brought down by rain; affecting equally both installations. Moreover, for March dust event the PECS glass mass was 76.78410 g the week before the event, 76.78669 g at the week of the event and 76.78306 g the week after the event, corresponding to an increase of $\approx 367 \text{ mg/m}^2$. At Elaia, the sample was only measured on the 9th April; this was a week with a high pollen concentration according to the *Rede Portuguesa de Aerobiologia* (Portuguese Network of Aerobiology). The mass measured was 76.97520 g; which regarding the measurement from February's event corresponds to an increase of $\approx 720 \text{ mg/m}^2$. This increase is certainly not only due to the dust event (it rained after that), but due to the pollen concentration. The olive trees which acted as a barrier in the February event, were at that moment at the blossoming stage, being an active source of pollen, visible in posterior SEM images (April 2017) of the analyzed samples. Regarding the aerosol optical thickness, mathematically defined as *AOD*, representing the integrated extinction coefficient over a vertical column of unit cross section, is represented in Fig. 2.11a for the 870 nm wavelength, which is the one usually used to identify situations as dust events [79]. It can be seen that the two dust events, one in February and the other in March, have different *AOD* amplitudes. The February event has the highest one as expected, since the atmospheric particle concentration was higher. These measurements were taken at the University of Évora campus in the city center (about 8 km away from PECS) and it also evidences that high *AOD* values on April are due to higher pollen concentration.

2.5.3.2 Photovoltaic performance

In Fig. 2.11c, both SR metrics, $SR_{I_{SC}}$ in red dots and $SR_{P_{max}}$ in black dots, are presented; the corresponding lines evidence the general data trend. It highlights both dust events intermediated by rain, Fig. 2.11d, and April with basically no rain. Pollen influence on PV performance is shown in Fig. 2.11b, which will be addressed next.

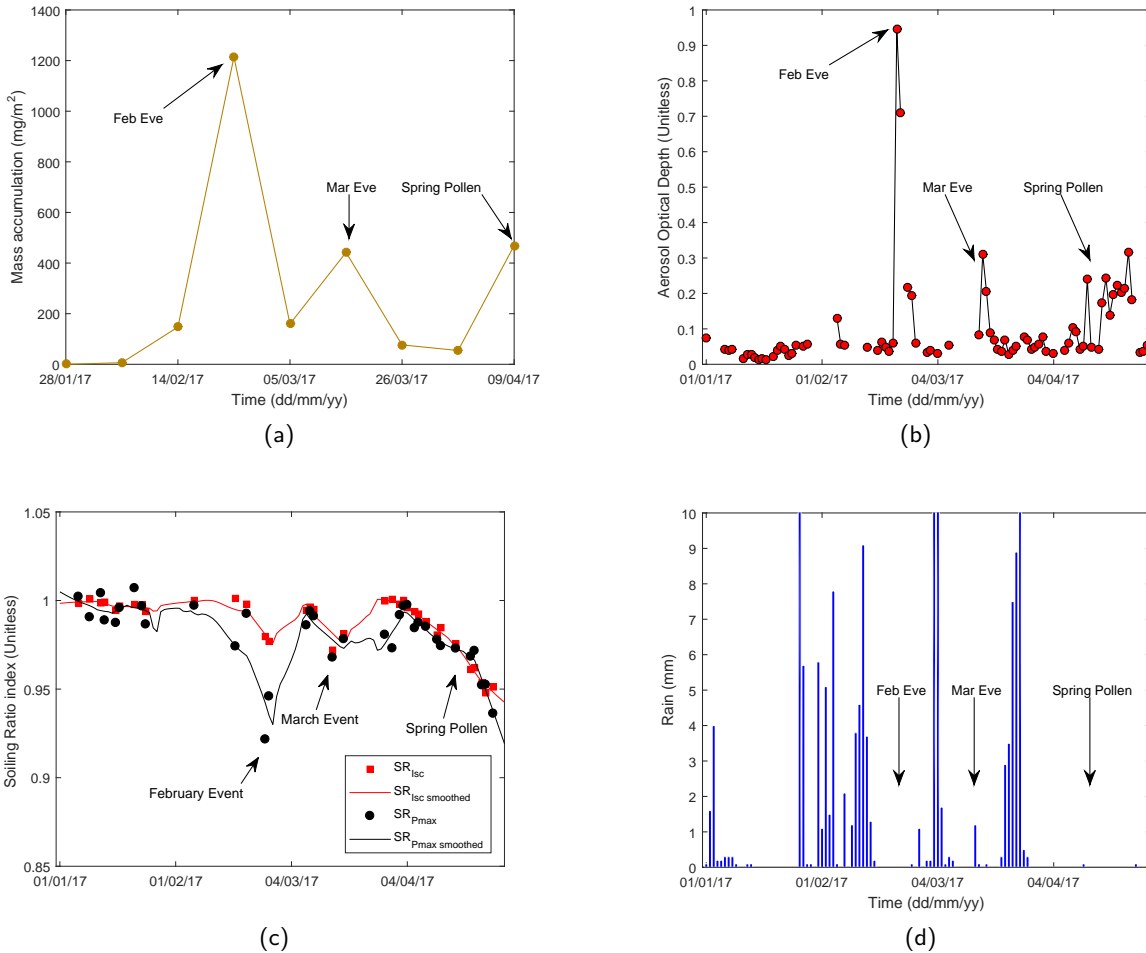


Figure 2.11: PECS soiling experiment results: (a) Mass accumulation; (b) AOD; (c) SR index; (d) Precipitation.

Apart from these facts, when soiling is absent it is expected that both metrics have values close to one (not exactly one due to experimental errors and second order effects, [88]); which is what happens here. More importantly, on the 25th February a significant decrease of 8% was obtained in the PV modules maximum power output and a decrease of only 3% in the short-circuit current. The reduction difference is due to the non-uniform particle deposition [89] on the glass of the PV modules; as it was caused by light rain during the 21st February night. This points to $SR_{P_{max}}$ being more accurate metric for soiling; as noticed by [74]. Most importantly, it warns the significant impact that dust events can have on the PV energy yield, mainly, taking into account that 4 – 5 major dust events tend to occur per year [71]. During

the period of 14th-16th March, another event took place, but it was far less significant than the February event, mainly because the dust concentration and event duration were lower, as concluded from the BSC vertical profiles forecasts. Despite this fact, it had an effect of $\approx 3\%$ decrease in both $SR_{I_{SC}}$ and $SR_{P_{max}}$, indicating homogeneous soiling. Soiling homogeneity may have been achieved through dry deposition and favorable atmospheric conditions and/or condensation during the night period.

2.5.4 Modeling

To detail the SR metrics plot performed at PECS, Fig. 2.11c, an environmental parameter analysis is required, and for that, the most important variables regarding soiling are represented in Fig. 2.12. The dew point temperature in Fig. 2.12a, calculated with Magnus formula and NOAA parameters, indicates when the conditions for condensation to form are met. It can be seen from Fig. 2.12a that those conditions exist on most nights and from further site observations, it can be stated that condensation is frequent, mainly during the first two months of the year. As stated in [90], dew can help clean the surfaces and that along with frequent precipitation leads to SR constantly close to unity, however frequent humid/dry cycles like dew at night and high temperatures during the day may enhance the cementation process. With the air temperature rising and relative humidity lowering towards the summer, the probability for dew to form and for rain diminishes. In April, grains of pollen have time to build up on top of the PV modules leading to a decrease in both SR metrics; that is why it is very important to take into account not only the dust events but also pollen. Regarding wind speed Fig. 2.12b, the red horizontal line represents the 8 m/s limit hourly mean data (this value is usually used, see [91], to define fair-weather conditions in atmospheric sciences). The higher the wind speed the more deposition will occur [92], which is in line with the general dust sedimentation model developed in [93]. Since there is no clean-cut air velocity threshold or limit to state at which point particle deposition can be greatly increased, the 8 m/s limit is used. From the data, it was calculated the amount of points which are below this limit and the value obtained was 99.6%. That together with precipitation and dew, forms a scenario not prone to soiling. Another important variable is the wind direction, inset in Fig. 2.12b. The wind did not have a dominant direction during the campaign. Nevertheless, previous observations indicated that dominant winds were from the North-East quadrant, which may increase soiling, since there is an active quarry a few kilometers east of PECS. Further studies (not presented here) were also performed to check if there was any variation from nocturnal winds to diurnal ones, but the same pattern was found on both situations.

Additionally, it is possible to relate m_a (connected to the PV performance degradation) with the environmental parameters rain, mathematically defined as *RAIN*, and *AOD*. The horizontal top glass at the PECS experiment was chosen to this study. Since m_a is measured almost every week, this time period is used to calculate total *RAIN* and mean *AOD* for each measurement point; this last variable is not sampled regularly and only during day time and in the absence of clouds/precipitation. Note that the variable *RAIN* corresponds to the sum of the precipitation during a given week. Ideally, particle counter measurements

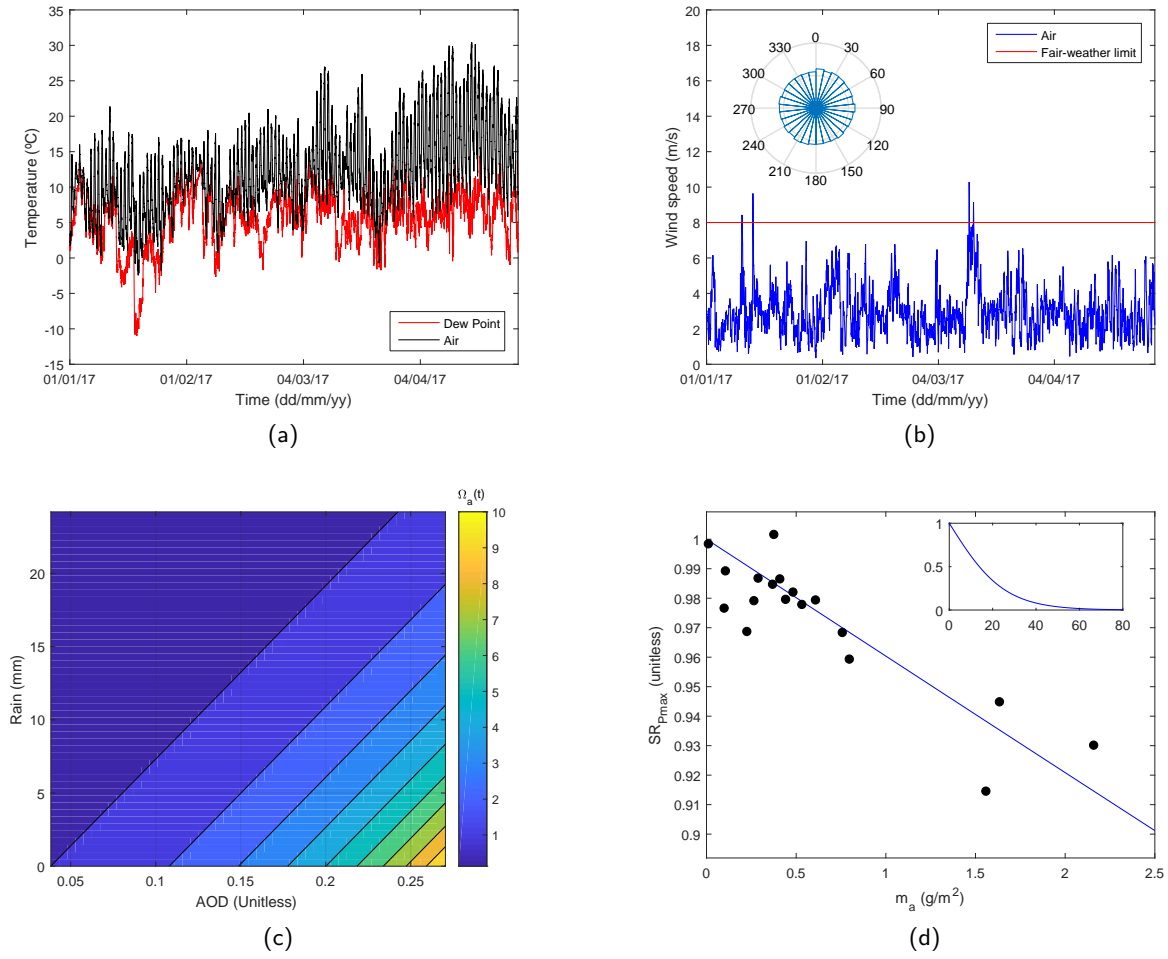


Figure 2.12: Environmental parameters and modeling from January to April 2017: (a) Air and dew point temperature; (b) Wind speed and direction; (c) Mass accumulation modeling; (d) SR modeling.

should be more appropriate than AOD , but no such equipment was available at the time. In these conditions, an empirical model is proposed to relate AOD and $RAIN$ of a given week t with the ratio of the m_a for that week with the previous one, as expressed by:

$$\Omega_a(t) = \frac{m_a(t)}{m_a(t-1)} = \Omega_0 \exp[\omega_1 AOD(t) - \omega_2 RAIN(t)], \quad (2.5)$$

where, $\Omega_0 = 0.6833$ with 95% confidence bounds (0.4692, 0.8974) (unitless), $\omega_1 = 9.948$ with 95% confidence bounds (8.664, 11.230) (unitless) and $\omega_2 = 0.0868$ with 95% confidence bounds (0.0119, 0.1559) (mm^{-1}). Taking into account a complete series (without bird drops) this model fits well the data, see Fig. 2.12c: $r^2=0.95$ and adjusted $r^2=0.95$; indicating that both variables are contributing to the model, while the RMSE is 0.772. For the AOD a positive exponential is applied, while for the $RAIN$ a negative one is used. Moreover, Ω_0 represents the background contribution to soiling arising from particles not detected by the AOD measurements. A more accurate analysis would, in fact, need to take particle size distributions into

account. Furthermore, the model respects two important asymptotic limits, which are: $\lim_{RAIN \rightarrow \infty} \Omega_a = 0$ and $\lim_{AOD \rightarrow \infty; RAIN \rightarrow 0} \Omega_a = \infty$. Although these limits will never be reached, they are in line with the most basic idea behind soiling, which is: if there is rain and low concentration of particles in the atmosphere, the amount of deposition will be low; however, if the amount of rain is low and the amount of particles is high, the deposition will increase. It should be stated that the use of a small time frame, like the one used here, contributes to the stability of the model. Using a larger time frame may result in a certain loss of sensitivity of the model, because the values and periodicity of *AOD* and *RAIN* for larger time periods may ruin any possible relation. To complete the analysis, a simple model was used to relate m_a with the $SR_{P_{max}}$, (for both homogeneous and non-homogeneous soiling), and can be seen in Fig. 2.12d. It is given by Eq. 2.6:

$$SR_{P_{max}}(m_a) = \frac{2}{1 + \exp(m_a/m_0)}. \quad (2.6)$$

For this model, Fig. 2.12d, a $r^2=0.7$ (with the same adjusted r^2) was obtained, with a characteristic mass: $m_0 \approx 12.61 \text{ g/m}^2$ with 95% confidence bounds (10.40, 14.81). This model represents a steep descending in $SR_{P_{max}}$ at the beginning until it stabilizes resembling transmittance measurements [94]. Actually, the model estimates near zero $SR_{P_{max}}$ values with a critical mass density m_c around 75 g/m^2 , Fig. 2.12d inset; which is in line with literature values [94] for glass transmittance losses. Similarly to the previous model this empirical relation captures the essential asymptotic behaviors: $\lim_{m_a \rightarrow \infty} SR_{P_{max}} = 0$ and $\lim_{m_a \rightarrow 0} SR_{P_{max}} = 1$, these are the completely soiled and completely clean limits, respectively.

2.6 Conclusions

The first part of this Chapter, besides showing an entire year of SR measurements also reveals that organic soiling can have a significant importance on the decrease of PV performance. It provides in depth insight in terms of deposited particle characterization. It describes the content, shape and size of particles that build up on the top of surfaces with visual and chemical analysis, which can help in future studies for soiling modeling/prediction, since these characteristics are perhaps the most important ones to characterize soiling at microscopic scales. Soiling rates have been calculated and compared for different seasons of the year and highlight how Spring and periods without rain can impact solar harvesting technologies. During Spring, besides the mineral soiling that can be deposited, also pollen at high concentration in the atmosphere lead to PV module performance decrease. Furthermore, the periods without rain allow for the particles to build up, increasing the soiling over time, resulting in higher losses along that period. Due to this fact, it is possible to distinguish several soiling rates along the year. Soiling rates were analyzed together with rain (the main cleaning agent) and AOD as a proxy for particle concentration, showing a good agreement. SEM imagery helped in the detection of organic soiling, namely pollen, which deposited on the PV modules increasing the background soiling seen during Summer, which led to a greater module

performance degradation. Note that the data may be helpful to determine cleaning schedules and for modeling purposes for future PV plants in the region, as it was done in Chapter 4.

The results presented in the second part of this Chapter demonstrate several important points: (i) particles from a remote origin have a significant role in soiling and it shows that soiling is not only a consequence of local phenomena; (ii) the need to forecast long-range dust transport and its impact; (iii) soiling rate may not be always linear, as some prediction models assume; (iv) exponential empirical models describe well the relation of mass accumulation and the environmental parameters. Note that more data points are needed to assess the model robustness, and to test data from locations with other climates, to see if the model holds; however this is a preliminary model and its potential resides in the fact of using only two variables. This part clearly shows the negative effect of the Saharan dust events on the Southern Iberian peninsula (thousands of kilometers away from from point of origin), with a significant decrease in the production of photovoltaic energy due to soiling and significant economic effects on solar energy installations (especially in low rain seasons). It also highlights the need for the development of low-cost soiling mitigation tools like anti-soiling coatings.

The work in this Chapter resulted in the following publications:

- R. Conceição, H.G. Silva, J. Mirão, M. Gostein, L. Fialho, L. Narvarte, M. Collares-Pereira, Saharan dust transport to Europe and its impact on photovoltaic performance: A case study of soiling in Portugal, *Sol. Energy*. 160 (2018) 94–102.
- R. Conceição, H.G. Silva, J. Mirão, M. Collares-Pereira, Organic Soiling: The Role of Pollen in PV Module Performance Degradation, *Energies*. (2018) 1–13.

3

Soiling measurements in rural environments for CSP

3.1 Introduction

The rural region of Évora, Alentejo, Portugal, was under study regarding the effect of soiling in PV technology in the previous Chapter. The most severe seasons for soiling were identified [33], as well as, occasional non-local effects [32]. However, there was the same lack of studies regarding the effect of soiling in CSP, as there were for PV on this region or other similar rural areas, which provides a unique research opportunity. The direct effect of soiling in PV production is easier to investigate than in any CSP technology, due to its intrinsic simplicity. This is one of the reasons why CSP soiling studies are more scarce. It should be noted that measurements of mass accumulation and transmittance/reflectance losses on glass/mirror samples (in a static position, which is usual) can be used as in PV technology related results. However,

a more realistic CSP study, might require samples to move throughout the day, to simulate the tracking associated with such systems. Despite of this, there are interesting studies about CSP soiling [95, 96, 97, 98]. Additionally, a higher soiling impact is expected in CSP than PV, due to the fact that light goes twice through the soiling layer, which can lead to more scatter and therefore less useful irradiance, specially given the small acceptance angles of the concentrators. In fact, soiling will modify the light path, not only when it reaches the mirrors, but also as it exits them and also increase the internal reflections within the glass. Overall, this process will result in a soiling effect which is 5 to 10 times worst than in PV [99].

This Chapter includes a full year of soiling effect in mirror's reflectance, as well as, the development of soiling prediction models using three different methods: (i) linear, (ii) linear with interaction terms and (iii) neural networks. The prediction of soiling has been shown to be very difficult, mainly because it is a very complex atmospheric process, which usually needs to take into account many environmental parameters. The analysis starts with a linear relationship to assess variable's trends. A linear regression is also tested with interaction terms to check if there is any relation between the output and interlinked predictors. However, since the process may be very complicated to solve explicitly, a neural network with 1 hidden layer was designed and the optimum number of neurons calculated through a similar process as in [100]. The objective is not only to try to find different models that fit the data well and can serve as prediction models, but also to evaluate possible trends and relations between the variables, which can be explained from a physical point of view.

Moreover, the last part of this Chapter presents the fruitful results of a collaboration between REC and IRESEN regarding the study of soiling effect in CSP. Considering the fact that Southern Portugal and Northern Africa are locations with high irradiance, and that Morocco has already started building large CSP plants (such as Noor complex in Ouarzazate), it is essential to investigate soiling effect on mirror's specular reflectance in both countries. The locations where this study is made are: PECS, Portugal ($38^{\circ}34'0.01''$ N; $7^{\circ}54'0.00''$ W); Green Energy Park (GEP), Morocco ($32^{\circ}12'0.00''$ N; $7^{\circ}94'0.00''$ W). It is worth mention that it is not only Morocco that can suffer from Saharan desert dust events, since long-range dust transport creates problems in Portugal [32], as seen in the previous Chapter. This study can be seen as the beginning of a comprehensive research regarding CSP soiling, namely for flat mirrors in CSP plants, like in Tower and Fresnel ones (since the measurement methodology is based in a flat mirror, as it will be shown afterwards).

3.2 Experimental campaign

3.2.1 Measurements

Measurements of soiling effect on the mirror's reflectance were performed using a TraCS from CSP Services (Germany) mounted on a SOLYS 2 sun tracker, from Kipp & Zonen (Holland, uncertainty $\leq 2\%$ for pyrhelimeter hourly values); vertical wind speed was retrieved using a WindMaster Pro 3-Axis Anemometer

from Gill Instruments (UK, uncertainty $\leq 1.5\%$ RMS); particulate matter measurements were taken with a DC1100 Pro from Dylos Corporation (U.S.A., uncertainty $\leq 10\%$); temperature, relative humidity and precipitation were measured at a nearby meteorological station (≈ 750 m) with a Thermo-Hygrometer (Thies Clima, Germany, with uncertainty $\leq 3\%$ for relative humidity and 0.5°C for temperature) and a Tipping Bucket Rain gauge from RM Young (USA, uncertainty $\leq 2\%$), respectively. Below, in Fig. 3.1, are presented the instruments referred before:

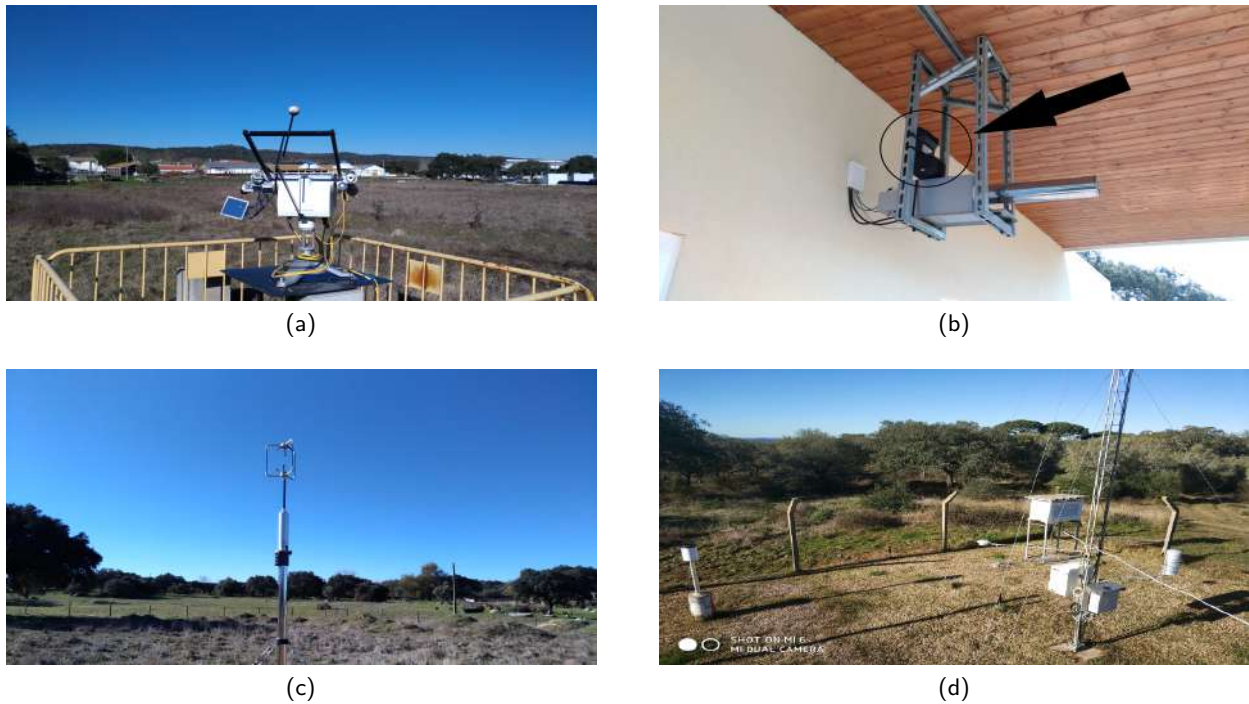


Figure 3.1: Measuring instrumentation: (a) TraCS and SOLYS2; (b) Dylos DC1100 Pro; (c) WindMaster Pro; (d) Meteorological station.

It should be noted that soiling effect is calculated through comparison between the direct normal irradiance, I_b , and the irradiance measured by a second pyrhelimeter, I_b^r , reflected by the TraCS's mirror [101, 102]. This mirror is rotating and performs a full revolution every 10 minutes and due to the fact that sun spectrum is variable throughout the day, daily means were calculated using data around solar noon. This process will be explained afterwards.

3.2.2 Soiling index

The measurement campaign started in June 2017 and lasted until the May 2018. The mirror was cleaned at the beginning of every month from June to August and then left untouched, due to the start of the raining season. During Summer, cleaning was performed to avoid soiling saturation, above which no measurements could be done.

The soiling index, λ , here defined as the normalized ratio between the reflected direct normal irradiance,

I_b^r , from the mirror and measured direct normal irradiance, I_b . The soiling index is represented in Fig. 3.2a and given by:

$$\lambda = 1 - \frac{\rho}{\rho_0}, \quad (3.1)$$

where $\rho = \frac{I_b^r}{I_b}$. The parameter ρ_0 corresponds to the maximum weighted reflectance measured with the mirror cleaned. This value was calculated by the manufacturer after a series of tests and represents the clean scenario mean reflectance.

The outcome of Eq. 3.1 is a null value in the absence of soiling, and as the particle deposition increases the soiling index also increases.

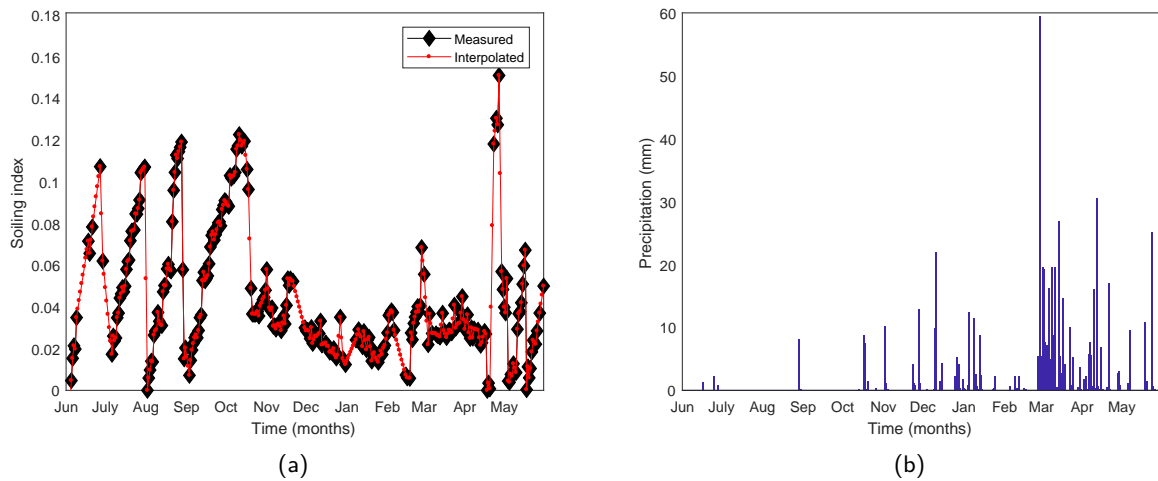


Figure 3.2: Soiling index and precipitation from June 2017 to May 2018: (a) Soiling index; (b) Precipitation.

The effect of manual cleaning done to the mirror until September can be observed. It should be noted that the results derived from cleaning are not always the same, probably due to improper cleaning, as well as, slight changes in mirror positioning, which can influence the irradiance that strikes the pyrheliometer. However, for this study, relative values are more important than absolute ones, since the soiling of the next day will be compared to the previous one.

Regarding the data, it is seen that Summer is indeed the worst season for soiling; perhaps an exception should be made for Spring, when high soiling values were also detected for PV technology [33]. However in this case, there was also long-range transport of a Saharan desert dust event. Later, in November and December, after rain and dew formation has been detected regularly (more than during Summer), λ recovered to low values. Statistical data associated with the soiling rates are presented in Table 3.1. Winter and the beginning of Spring show low soiling values as expected, due to frequent and severe raining, however it should be noted that without manual cleaning, it is extremely hard to recover the initial reflectance of the mirror. It is pointed that during April and May there were also manual cleanings performed, due to the

collaboration with IRESEN.

Table 3.1: Soiling index rates and associated statistical parameters.

	Jun	Jul	Aug	Sep
λ (%/month)	13.3	8.8	11.5	8.8
r^2	0.956	0.986	0.927	0.953
RMSE (%)	0.009	0.003	0.01	0.006

3.2.3 Data Processing

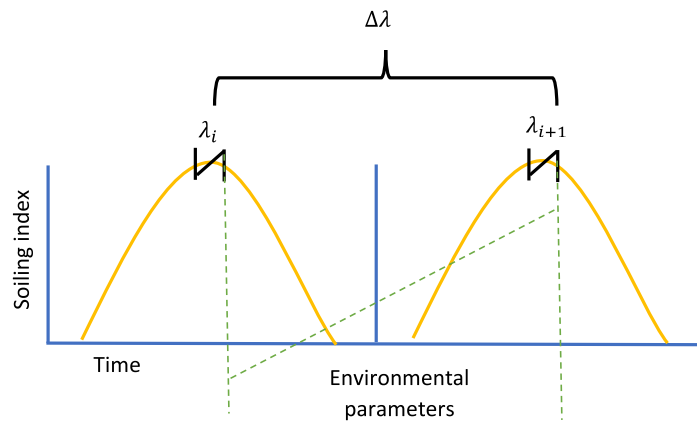


Figure 3.3: Calculation process schematic.

Daily means were calculated following the schematic in Fig. 3.3. Two different days are represented, where the yellow curve corresponds to typical TraCS measurements. The mean of the soiling index of the day before is represented by λ_i , while for the next day it is given by λ_{i+1} and it is calculate around solar noon, represented by the black lines. The difference between the previous day and the next day is represented by $\Delta\lambda$, see Eq. 3.2.

$$\Delta\lambda = \lambda_{i+1} - \lambda_i \quad (3.2)$$

This parameter represents an increase of soiling from one day to the following, if it is positive, and a reduction of soiling, if it is negative. Particulate matter values, $PM_{0.5-2.5}$, correspond to a 24-h mean, from 14h of the previous day to the next day, as well as, vertical wind speed, VWS . Air temperature, T , and relative humidity, RH , are a result of the mean from 9h of the previous day until 6h of the next day, see Fig. 3.3. Since $PM_{0.5-2.5}$ measurements have no RH compensation, all $PM_{0.5-2.5}$ values (minutely scale) corresponding to RH above 65 % were removed, which implies that for some nights there are possibly no data for a few hours. To characterize the night period, both T and RH were used, which are also important for dew formation phenomenon, as well as, hygroscopic growth [103]. Periods with precipitation were removed, since it is seen that it has a cleaning effect and the interest here is to study other environmental

parameters that are possibly interlinked with soiling effect.

Environmental parameters are presented in Fig. 3.4. It can be seen that the particulate matter, in Fig. 3.4a, which represents particulate matter between 0.5 and 2.5 μm , is rather constant throughout the campaign, excluding peaks towards Fall, which are due to agricultural activities (more intensive during that season). The parameter VWS , present in Fig. 3.4b, is mostly negative, pointing downwards, and with higher intensity during Summer compared to Fall, which likely indicates higher strong and dry convection [58]. It should be noted that VWS corresponds to the vertical component of the air direction, which means that its positive velocity means pointing upwards while a negative value means pointing downwards. During Summer, T , presented in Fig. 3.4c, is higher compared to other seasons, as expected, while RH , presented in Fig. 3.4d, has high values during the whole campaign, however what is observed from Summer to Fall is the fact that these tend to increase in frequency, which is understandable, since Summer days are drier.

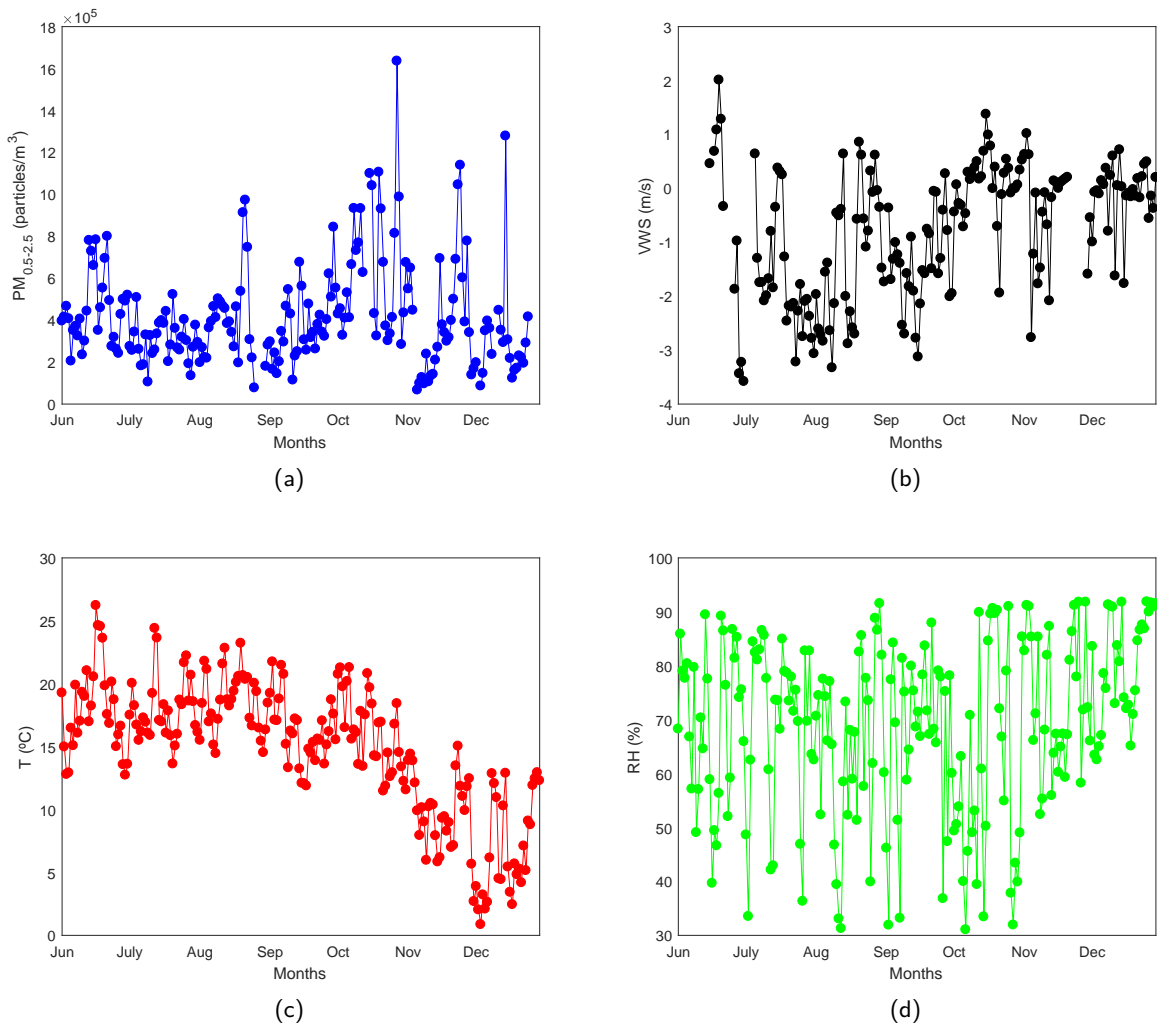


Figure 3.4: Environmental parameters: (a) $PM_{0.5-2.5}$; (b) VWS ; (c) T ; (d) RH .

3.3 Soiling modeling

3.3.1 Multiple linear regression

The data for this model and the subsequent models is always the same. The mean of the environmental parameters that will be related with $\Delta\lambda$, for the different models, is derived, as referred before.

A stepwise regression method was used, which is based in adding/removing terms in a relation between predictors in order to achieve to maximize some criterion. The criterion used for adding or removing terms is the Adjusted R-Squared, $adjr^2$, since the r^2 will always increase if more related terms are added.

The inputs, for all models, are: $PM_{0.5-2.5}$, $PM_{0.5}$ (which stands for particulate matter above $0.5\ \mu\text{m}$), VWS , T and RH . The output $\Delta\lambda$ of the multiple linear regression (MLR) model is given by:

$$\Delta\lambda = \beta_0 + \beta_1 X_1 + \beta_2 X_2 + \dots \beta_n X_n \quad (3.3)$$

The stepwise method begins with only a constant term (intercept) and follows towards a linear model, testing combinations of variables and finalizes with the one that maximizes the $adjr^2$. For this particular model, only four inputs provide such combination: $PM_{0.5-2.5}$, VWS , T , and RH . Such model has the following statistical parameters: $r^2=0.150$, $adjr^2=0.121$ and $RMSE=0.0045$. The corresponding equation for these predictors is shown in Eq. 3.4. The fact that $PM_{0.5}$ is not chosen as a variable that contributes to the model, has two causes: the mutual correlation of $PM_{0.5}$ and $PM_{0.5-2.5}$, which excludes one of these variables from the relation; smaller particles have a higher scattering effect than large ones [95].

$$\Delta\lambda_{MLR} = \beta_0 + \beta_1 PM_{0.5-2.5} + \beta_2 RH + \beta_3 T + \beta_4 VWS \quad (3.4)$$

Increased relative humidity has a positive impact on the output, which was also detected in [104]. This can be explained by the fact that hygroscopic growth starts to take place for high values of relative humidity [105, 103], which increases the water content of some aerosol species, making them more prone to settling [106]. Two different reasons may also exist which are: if the relative humidity is high enough there can be dew formation, which can trap particles more easily through capillary forces [107], however if the amount of dew formed is very high, it is more likely to clean the surface; if there is no dew formation but there is an excess of water molecules aggregated to particles, that may enhance the electrostatic adhesion to surface since water molecules are bipolar.

Higher air temperatures are also connected to more soiling. In this context, higher air temperatures are connected to Summer days, while lower values are connected to Fall. As seen in Fig. 3.2a, soiling is higher during Summer and so is the temperature, which means that this output and input are seasonally connected. This matter will be discussed afterwards. Vertical wind speed has a positive effect on soiling,

which means that enhances it when pointing downwards, increasing particle deposition.

As expected, such linear model is not complex enough to explain how these variables may be related with the loss/gain of soiling from one day to the other. Such model has been studied by others [108, 104], with a $r^2=0.167$, which is a similar value to the one found here. However, it should be noted that Guo and co-workers obtained this value using 10 variables, which means that using only 4 would certainly lead to a lower r^2 .

3.3.2 Multiple linear regression of interaction terms

Previous analysis shows that using a simple linear model is not enough to explain $\Delta\lambda$ and most likely the predictors are connected to each other, since dust deposition and re-suspension are processes that may depend on such combinations. A multiple linear regression with interaction terms (MLRIT) is now considered as follows:

$$\Delta\lambda = \beta_0 + \beta_1 X_1 \beta_2 X_2 + \dots \beta_n X_n \beta_{n-1} X_{n-1} \quad (3.5)$$

The stepwise method is exactly the same as for the MLR with the same criterion, which yields the Eq. 3.6:

$$\Delta\lambda_{MLRIT} = \beta_0 + \beta_1(PM_{0.5-2.5} \times VWS) + \beta_2(PM_{0.5-2.5} \times RH) + \beta_3(VWS \times RH) + \beta_4(RH \times T) \quad (3.6)$$

However, the variables that maximize MLRIT are the same that do so for MLR, these no longer contribute independently to the output. Such model has the following statistical parameters: $r^2=0.279$, $adjr^2=0.228$ and $RMSE=0.0042$. This model has a higher r^2 and $adjr^2$ and lower RMSE than MLR model, as expected. The improvement of r^2 from MLR to MLRIT, near the double, shows the importance of interaction terms and the failure of simple linear models. Interaction terms have real physical meaning in the description of soiling, for instance, the interaction between $PM_{0.5-2.5}$ and VWS highlights the enhancement in soiling found at high levels of particulate matter and downward moderate winds.

It should be noted that r^2 value for MLRIT is close to the ones in [48] for an artificial neural network with one hidden layer having 5 neurons. More on neural networks will be discussed afterwards.

Figure 3.5 represents the scatter plots (colors representing intensities of $\Delta\lambda$), of the interaction variables presented in Eq. 3.6. It should be noted that all circles within Fig. 3.5 contain more than 50% of the points corresponding to $\Delta\lambda > 0.008$, which statistically ensures that these areas are the ones with the highest

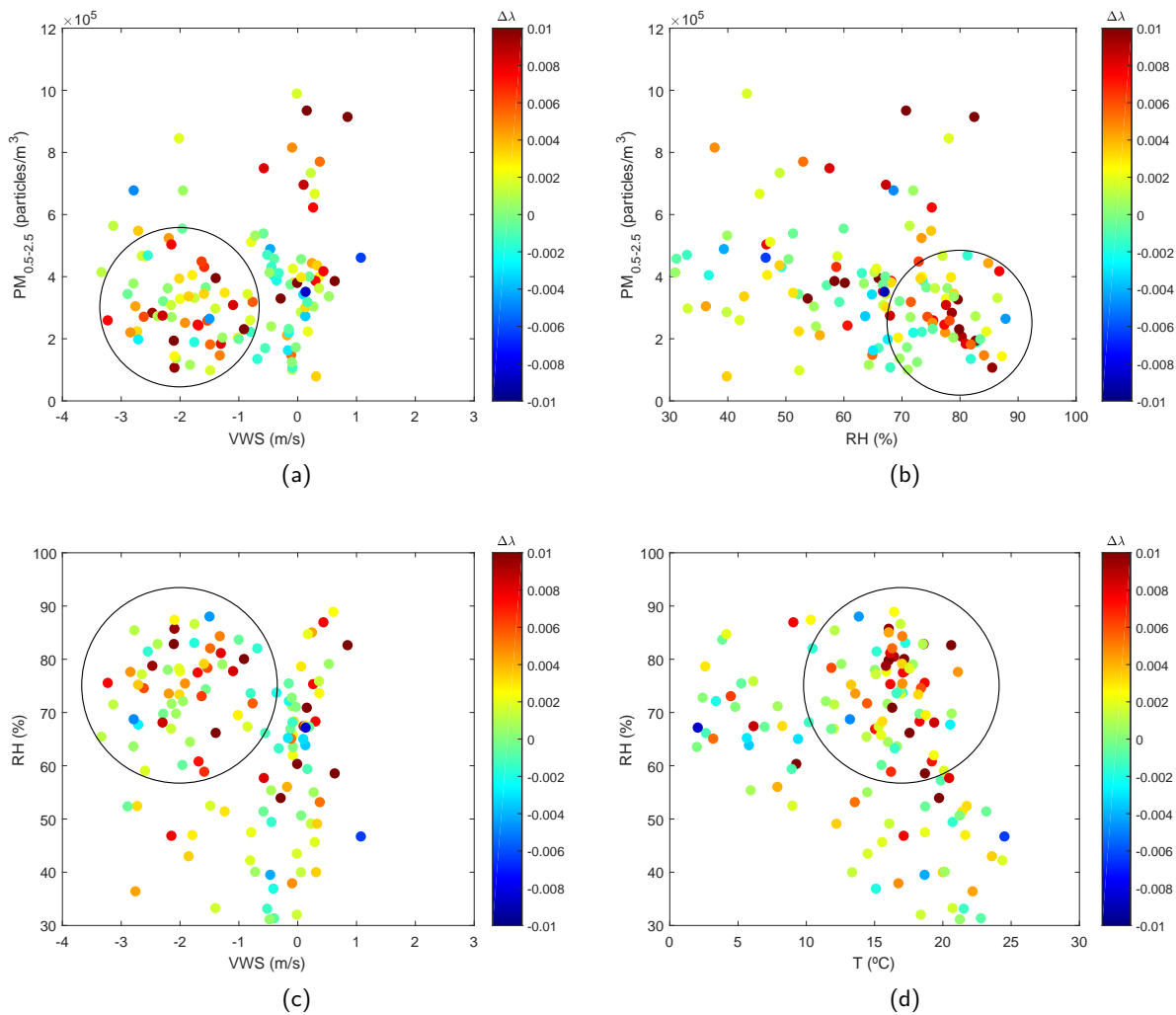


Figure 3.5: Predictors effects between: (a) $PM_{0.5-2.5}$ and VWS ; (b) $PM_{0.5-2.5}$ and RH ; (c) VWS and RH ; (d) T and RH .

concentration of points representing situations where soiling increased from one day to the next.

It can be observed, in Fig. 3.5a, that most of the points corresponding to a substantial increasing in soiling are connected to downwards winds (magenta circle), however if there are more particles and the wind is blowing upwards (at a very low velocity) there can also be deposition, which demonstrates the importance of particle concentration. In Fig. 3.5b, it can be seen that higher relative humidity is related to more deposition, as referred before, through an increased particle size and subsequent deposition [106], due to an increased electrostatic attraction or possible minimal dew formation, which allows for particles to be easier retained.

From Fig. 3.5c, it can be seen that the combination of downwards wind and high relative humidity may lead to higher particle deposition and consequently performance loss. Wind blowing downwards, together with possible particle hygroscopic growth enhances particle deposition (through increased particle adhesion).

It can be seen that even for very low downward and upward winds there is deposition. This means that relative humidity is an extreme important factor, in this case, for soiling enhancement.

Figure 3.5d shows a very interesting combination, which is that high air temperatures and relative humidity are somehow connected to increased soiling. This situation is probably representing what happens during Summer (when most of the times the soiling increased from day-to-day), when there may exist moderate temperatures and relative humidity. What can be possibly happening is during Summer there are normally higher temperatures compared to Fall, while there are more nights with higher relative humidity on Fall compared to Summer. This way, dew does not form so frequently during Summer, or it forms but at minimal amounts and dries faster, which can increase particle deposition, while during Fall, lower temperatures and possibly more frequently dew formation in larger amounts will not dry that fast, allowing surface cleaning. For higher clarity, the 3D scatter plot in Fig. 3.6 can be observed.

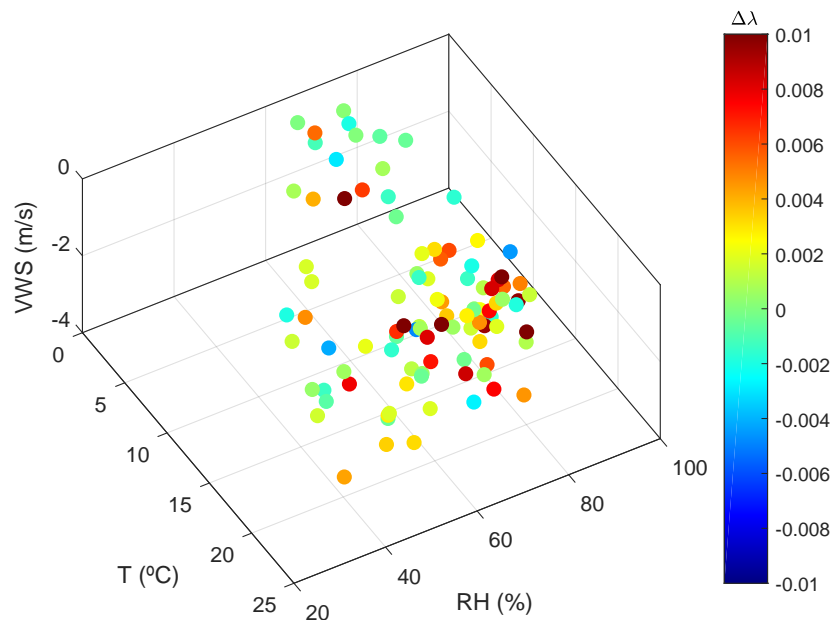


Figure 3.6: Three dimensional scatter plot of predictors and output.

The upward wind data points were removed from the plot for better visualization. It is observed that most of the points related to a decrease of $\Delta\lambda$ are located in the bottom right corner, which corresponds to higher temperatures and relative humidity and moderate values of downwards wind speed. This summarizes what has been stated before in terms of environmental parameters.

It should be noted that MLRIT explains better the variation of the output, however it yields a poor result. It is known that this is a very complex problem to solve, however this study is important, because it shows unknown trends in the data and between variables, which can help in the future other researchers to achieve an analytic solution. Next section will treat this problem with neural networks to access their potential in this field.

3.3.3 Artificial Neural Networks

ANNs have been vastly used in the last decade with different scopes [50, 49, 109], due to its potential to deal with highly complex problems, for which there is not yet an analytical solution. This seems to be one of those problems, where only trends could be understood on the data (which is also important). A single layer perceptron, see Fig. 3.7, is tested, which is a neural network with only one hidden layer. For more information on neural networks see [110].

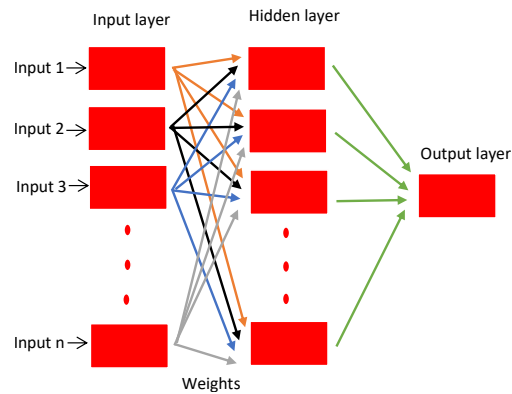


Figure 3.7: ANN architecture.

The training algorithm chosen was the Levenberg-Marquardt [111]. To find the optimum number of neurons in each hidden layer, the dataset was divided in two: one for designing purposes (90% of the data) and the other for calculating the mean square error (MSE) of those designs. The maximum number of neurons tested was 10, to avoid overfitting. Each design was tested 10 times [100] and MSE (the chosen performance index) calculated each time, using the testing dataset. The design with the lowest MSE was selected, to improve generalization for new data. For the hidden, layer a sigmoid function was selected, while for the output layer a linear one was used. It should be noted that inputs and outputs of ANN are the same as in for MLR and MLRIT. The results comparing the targets with the output from ANN are shown in Fig. 3.8.

Due to the lack of more extensive data series and additional variables in the model, like turbulence and confirmation of dew formation, it was not possible to increase the explained variability of the problem. Nevertheless, this is a fast process and gives better results than linear models. If there is not an analytic solution for this problem, ANN appears to be a promising tool, although there is the need of finding all the variables that somehow contribute to the solution.

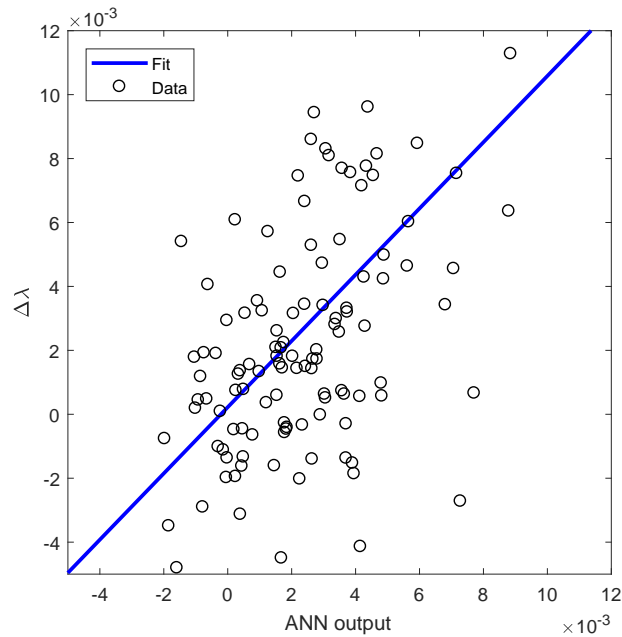


Figure 3.8: ANN predictions and target output.

3.3.4 Model comparison and discussion

It can be observed in Table 3.2 the statistical parameters chosen to evaluate the goodness of the fit for the different models.

Table 3.2: Statistical parameters of models.

	MLR	MLRIT	ANN
r^2	0.150	0.279	0.629
RMSE	0.0045	0.0042	0.0037
MSE	2.03e-5	1.78e-5	1.40e-05

From the most simple to the more complex model, it is stated an increase in r^2 and a decrease in both RMSE and MSE is shown, as expected. The simpler models, MLR and MLRIT, besides their low ability to explain the variability in the data, are important for a fundamental study in terms of basic relations and trends between the predictors and the output. MLRIT is important, because it shows how the predictors can be interlinked with each other and the effect on the output. ANN on the other hand do not serve to study the physical meaning behind the data, but it is instead a tool that can be used to solve complex problems. It was not possible to achieve higher r^2 values, although they are higher than the ones found, for instance, in [104]. Possibly more data points are required, for instance, to increase ANN learning skill, using more examples, but also because there are more variables that need to be introduced, like knowing exactly when dew and very light rain occurred, which can be very important for both cleaning or soiling increase, while atmospheric turbulence and convection may also play a role, as well as other variables. The

time-scale, in which the variables and output is calculated, is related to the results, so there is a need for a deeper study of these topics.

3.4 Portugal-Morocco soiling measurement campaign

The methodology is based on the use of a TraCS system as done in Section 3.2, measuring apparatus for PECS and GEP are shown in Fig. 3.9. It compares I_b , measured by the pyrhelimeter towards the sun, with the irradiance reflected by the mirror to the second pyrhelimeter, I_b^r . It is then possible to calculate the dirtiness index, λ , to obtain an estimation of the soiling effect on the reflectance, as in Eq. 3.1. Therefore, if $\lambda = 0$, it means that there is no soiling affecting the mirror's reflectance, while $\lambda = 1$ implies a maximum soiling effect. Manual cleaning is performed every two weeks on both sites, to avoid soiling saturation, mostly in Morocco, and bird dropping effects, which otherwise cannot be controlled. It is worth mentioning that the pyrhelimeters, on both sites, are cleaned daily, except on weekends.

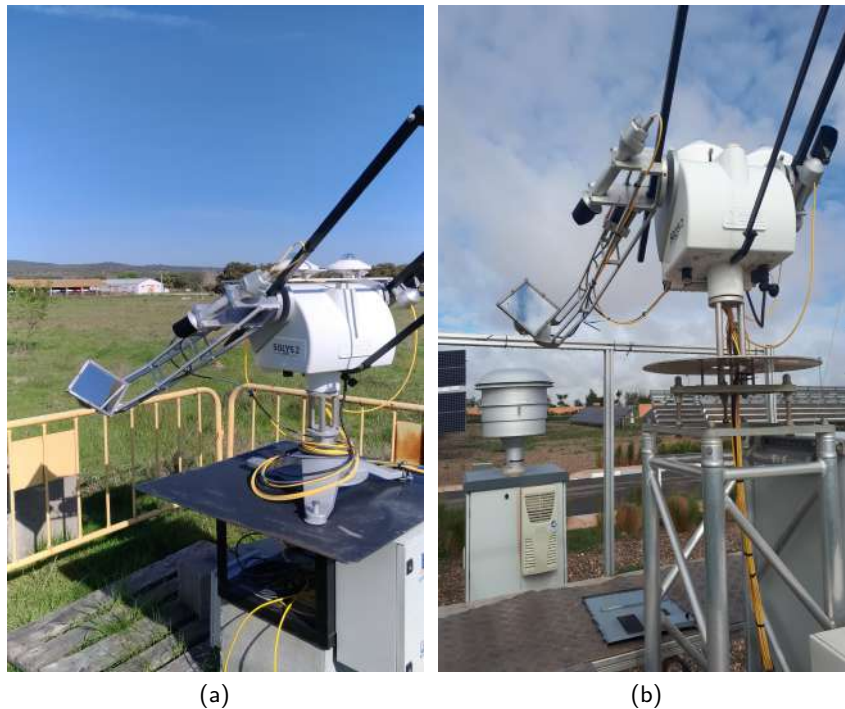


Figure 3.9: Measuring instrumentation: (a) TraCS at REC; (b) TraCS at GEP.

Moreover, besides the maintenance protocol, the quality control check procedure and algorithm flow to process the data are presented next:

- Remove values higher than 1 and lower than 0 from the TraCS data (which is already the ratio between the reflected and direct normal irradiance).
- Remove values which correspond to direct normal irradiance values lower than 400 W/m^2 and higher than 1380 W/m^2 from the TraCS data.

- Remove minutely values over and under 1 standard deviation from the respective daily mean from the TraCS data.
- Remove days which have less than 60 minutes of data.
- Calculate ρ_0 for each time the mirror is cleaned and use that value for the next weeks, until it is cleaned again.
- Calculate λ .
- There will be days that due to clouds/bird drops events were removed using the filters referred before. For better readability (if it is assumed a linear increase/decrease of the soiling), the data is linearly interpolated.

3.4.1 Results and Discussion

The first results, as plotted in Fig. 3.10, show that the λ values in Morocco are much higher than the ones found in Portugal by a factor of approximately 3. This is expected, since GEP is located near the largest desert of the world, the Sahara Desert, which contributes to higher air particle concentration, compared to PECS, and therefore can lead to higher particle deposition and harsh soiling effect on solar energy conversion technologies. In PECS, except for the case of long-range dust transport and rain (discussed below), the soiling effect behavior is similar between cleanings. The cleanings were performed every two weeks, except for June, where it was performed with a delay of 5 days. It should be note that there was a day with high precipitation during May, however it was an event in the afternoon, lasted for an hour and the wind was blowing mainly from the North (data not shown). Since the TraCS system follows the sun and that during that period the mirror was facing Southwest, the cleaning was not significant. For Morocco, according to the measurements, λ values generally float between 0.2 and 0.25 after two weeks of mirror exposition without cleaning. Besides, if a specific phenomenon happens, like red rain, these values can be much higher, like in the 24th of April and the 3rd of August, where the measured λ are of 0.46 and 0.27 respectively. These λ values can be considered huge, as they correspond to a reflectance drop of 36.1% and 15.6% from the initial mirror reflectance. The red rain phenomenon will be discussed in detail in the following sections.

Values of λ between two weeks, for PECS during the Summer, usually reaches approximately 0.06. This value was calculated based on the λ mean values at the end of every two weeks. If this value is divided by the number of days in two weeks, it gives approximately 0.004 per day, which is denominated as daily dirtiness rate. This value may seem low, but if no cleaning is done, and if one assumes that particle deposition will keep increasing with this constant rate, this value can achieve 0.12 after a month, which is denominated as extrapolated monthly dirtiness rate. This parameter is extrapolated from the λ values after two weeks. Such soiling level will drastically influence CSP performance. For GEP, there is, in a two weeks period, a dirtiness index around 0.22, which is approximately 0.015 per day (more than 3 times the value

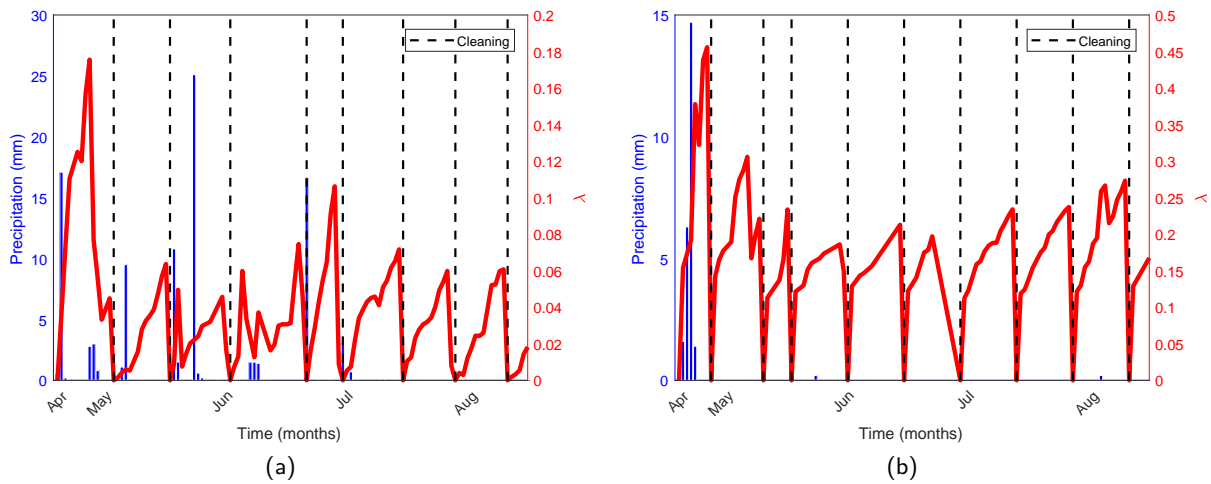


Figure 3.10: Dirtiness index and precipitation: (a) at PECS; (b) at GEP.

for PECS). If the same logic is applied, as before, after a month if no cleaning is performed, the dirtiness index can achieve around 0.44, which is an extremely high value. This value can be even higher if a dust storm and/or a red rain event happens. The results mentioned before are summarized in Table 3.3.

Table 3.3: Daily and extrapolated monthly dirtiness rates at PECS and GEP.

	PECS	GEP
Daily dirtiness rate (%)	0.4	1.5
Extrapolated monthly dirtiness rate (%)	12	44

3.4.2 Effect of long-range transport of Saharan desert dust

Saharan desert dust events have an impact in Portugal, if long-range transport of such events reaches it. On the 21st of April 2018, one of such events started to take place and ended around 24th of April 2018. BSC forecasts depicted its occurrence, see Fig. 3.11. The long-range Saharan desert dust event reached Portugal and caused an important drop on the mirrors optical efficiency. It was the highest drop registered during the campaign for Portugal, approximately 0.18. Barcelona Super Computing forecasts are used to access the difference on the effect on both sites, see Fig. 3.11. In PECS it can be seen the effect of such event in Fig. 3.12.

Since GEP is closer to the dust source than PECS, it is only natural that the number of particles reaching it is higher. For this event, which happened between 21st to 24th April (although the dust deposition may occur over several days after the event due to dust suspension/re-suspension), BSC forecasts show a dust load around 6.4 g/m², which is a very high value, while for PECS is in the range between 1.6 and 3.2 g/m², which at most, is half the dust load forecasted for GEP’s location. During the transport, dust will eventually deposit over time, leading to a reduced dust load. GEP registered a loss around 0.45, while PECS, due to this event, had a loss of approximately 0.18. It is very interesting to note that between both regions, during

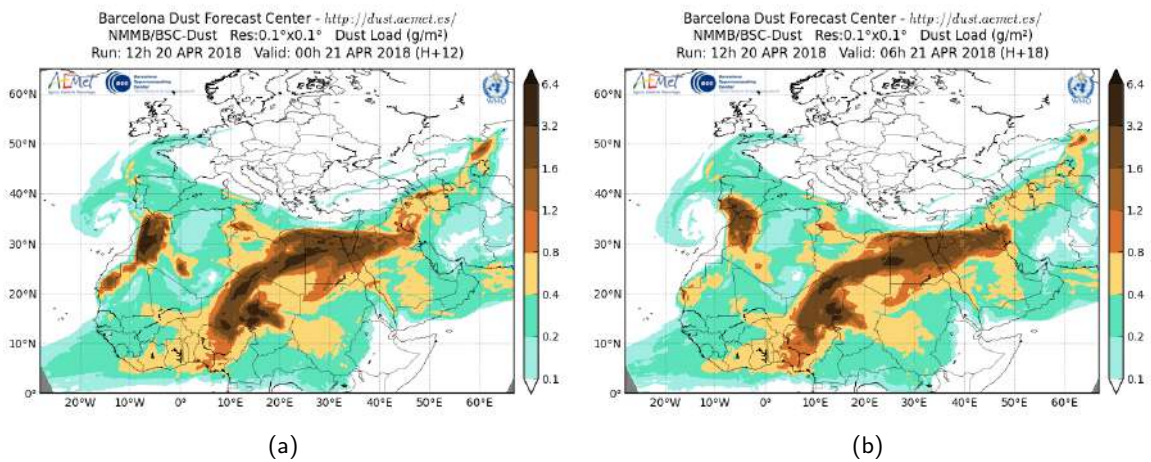


Figure 3.11: Barcelona supercomputing center dust forecasts: (a) for 21st April at midnight; (a) for 21st April at 6 a.m

the desert dust event and in normal conditions, it seems to exist a factor of approximately 3 between soiling effect in Portugal and Morocco.



(a)

Figure 3.12: TraCS mirror at PECS after long-range transport of Saharan desert dust.

Nevertheless, independently of the location, Saharan desert dust events have a very harsh event on mirror's reflectance, higher than on PV [32]. Dust forecasts may become very important for cleaning strategies in the future and thus for the electricity market.

3.4.3 Red rain effect

One of the major concerns for solar plants operators are the red rain events [112]. Red rain is a phenomenon that happens when a small amount of rain event occurs during a dust loaded atmosphere. This leads to the drop of dust particles on the mirror surface that agglomerate and stick strongly on it (please

see Fig. 3.13), which results in a considerable reflectance drop. Indeed, as it can be seen from Fig. 3.10b, the reflectance measured on the 24th of April was around 66.2% which represent a drop of 27.8% from the mirror's initial reflectance and a drop of 19.7% in only one day. This phenomenon happens after the coincidence of two events: a high dust load in the atmosphere from the 21st to the 24th of April, causing dust transportation from Northern Africa to Europe, and a small rainfall of 1.4 mm in the night-early morning of the 23rd and 24th of April.



Figure 3.13: Red rain event effect: (a) TraCS mirror in a clean state; (b) TraCS mirror after red rain event.

Reflectance is not the only issue with red rain, mitigation can be a strong problem for the plants operating and maintenance crews. In fact, cleaning the mirrors after red rain events require a lot of water, and associated labor, to enhance their optical efficiency which results in higher maintenance costs. This is also concerning, since MENA regions are usually associated with water scarcity.

3.5 Conclusions

This Chapter contributes to enrich knowledge on the effect of soiling in the loss of reflectance of mirrors, which is connected to CSP technologies, and most specific to Fresnel and tower, since the reflectors are flat or nearly so. It should be noted that many more studies have been done regarding PV and therefore the effect of soiling in glass transmittance. That underscores the need for more studies of this kind. It should also be noted that this is the first time, to the author best knowledge, dealing with TraCS data and relating it with environmental parameters. It was possible to observe well defined soiling rates during Summer, as expected, and make a comparison between them and the ones from a PV system, as well as to detect trends between soiling increase/decrease and environmental behavior. Soiling prediction was also made using artificial neural networks, however better results can be obtained if more data, variables and different time-scales are used.

The last part of this Chapter presents preliminary results of the comparison of soiling measurements in Portugal and Morocco. The two countries have good prospects for CSP implementation and thus, soiling needs to start being accounted for. As expected, Morocco is found to have substantially more soiling,

with daily dirtiness rates of approximately 1.5% in comparison to Portugal, with just approximately 0.4%. Nevertheless, both sites were affected by a Saharan desert dust storm, attaining dirtiness index of 0.18 and 0.45 respectively, for Portugal and Morocco. Moreover, it was shown how Morocco can be drastically affected with a dust storm followed by a red rain event, which highlights the need for mitigation techniques and cleaning mechanisms. The use of forecast tools for such events in the management and operation of CSP plants was discussed and perhaps, in the future, they will be useful for mitigation techniques. Moreover, new cleaning mechanisms, spending less water than the ones existing today, need to be developed, since both Portugal and Morocco are countries that may experience or are already experiencing high-water stress levels [113], namely in the areas that have potential for CSP plants implementation. Future work of this collaboration will be centered in a long term assessment of soiling effect on both locations, including Spring effect, when the concentration of pollen and other organic soiling is higher on the atmosphere [33].

The work in this Chapter resulted and will result in the following publications:

- R. Conceição, H.G. Silva, M. Collares-Pereira, CSP mirror soiling characterization and modeling, *Sol. Energy Mater. Sol. Cells*. 185 (2018) 233–239.
- R. Conceição, A. Merrouni, D. Lopes, A. Alae, H. G. Silva, E. Bennouna, M. Collares-Pereira, A. Ghennioui, A Comparative Study of Soiling on Solar Mirrors in Portugal and Morocco: Preliminary Results for the Dry Season, *SolarPACES 2018*. Accepted for publication.

4

Soiling Mitigation for PV

4.1 Introduction

As shown in Chapter 2, a decrease of $\approx 8\%$ in power output has been observed [32] in Southern Portugal, showing how soiling can significantly influence solar energy plants operations, even in non-desert regions, and with worse effects in concentrated solar power technologies [114].

Adding soiling to the cell-temperature effect, will determine a significant performance decrease from the expected nominal performance. One approach to reduce soiling effect is the use of anti-soiling coatings [63], however these still need to be further researched. Thus, the available and reliable way to handle soiling nowadays, is to regularly clean the affected surfaces, especially in regions where the number of particles in the atmosphere is exceptionally high, allowing to reduce considerably the system's performance. Currently, the only viable cleaning option for PV panels (or glass surfaces in general) is through manual cleaning or automated robots. If solar plants are economically able to afford expensive robotic solutions, then soiling

becomes a minor problem. However, for PV plants that are not able to support the cost of such technology or for smaller plants and private owners without an easy access to the PV system (e.g. roof installation), designing the system to take into account the local soiling would be significantly valuable. This would reduce cleaning tasks and would also increase energy production.

The first objective of the present Chapter is to study the optimum tilt angle considering soiling, focusing in the maximization of energy production, taking into account the soiling effect in the absence of cleaning schedules, as this is still not a widely studied subject. To develop such model, several aspects are considered. Firstly, measured data is required as an input variable for the in-situ model, particularly solar irradiance measured at ground-level (if available, it should be used instead of satellite data). Secondly, dust deposition should be considered as function of the tilt angle, which is also a local feature [115]; for instance, dew, turbulence, wind speed and direction, can modify the amount of particle deposition [116]. Thirdly, it is necessary to have transmittance measurements of the PV glass covered with soiling accumulated on site, since the same number of different types of particles can lead to different transmittance losses [117]. These models are then introduced in a general model of irradiance considering soiling, enabling an estimation of their effects on PV plants.

Another objective is to calculate multiple soiled tilt angle configurations throughout the year, which can be deployed using movable frames, and can range from 2 to 12 tilt angles per year, simultaneously studying the effect of soiling on the energy production of these configurations compared to a fixed structure. Moreover, it is presented a method considering the comparison between dirty and clean scenarios, allowing the PV system owner to determine the best periodicity to perform scheduled cleaning.

This topic has still not been fully developed and for that matter literature concerning advances in the effects of soiling in PV systems is still scarce [8, 118]. The approach used in [8] is based on the dependency of soiling with the tilt angle. However, in such study, particle deposition is assumed to be constant for all months, which is an unrealistic scenario, due to the seasonal variability of precipitation and other environmental conditions. The present work explores soiling on a monthly basis, since soiling variability is one of the most important aspects of particle deposition. Furthermore, multiple tilt angle configurations are explored in order to include the annual irradiance and soiling variability, as well as, an economic analysis to determine the optimum configuration. It should be mentioned that the approach used by Lu and Hajimirza [118] has valuable meaning, since it is based on panel length and friction coefficients. However, such analysis is different from the one presented here, since it is performed with respect to the solar zenith angle, which implies a 2-axis tracking. Similarly, the work carried out by Xu and co-workers [8], does not include a multiple tilt angle analysis, a resulting economic analysis and does not explore the development of cleaning schedules, as shown here.

The present Chapter aims to demonstrate how soiling can be mitigated by changing the tilt angle of the PV modules, for both constant and multiple tilt angles throughout the year. Moreover, for multiple annual configurations, it is necessary to take into account the annual variation of particle deposition and irradiance

and, for that matter, an economic analysis is performed to maximize profitability. Finally, a different use for the approach developed in this work is presented: the derivation of cleaning schedules, for any given loss of system performance.

The remainder of this Chapter is structured as follows: Section 4.2 explains how the irradiance and soiling were processed and modeled; Section 4.3 presents an analysis of optimum tilt angles from a fixed to a 12-tilt angle configuration, to determine the best potential configuration relatively to the fixed one; Section 4.4 uses the model to determine the PV panels cleaning schedule, defining the yearly cleaning period when losses surpass a certain threshold; final conclusions and remarks are summarized in Section 4.5.

4.2 Irradiance and soiling modeling

4.2.1 Irradiance modeling

This subsection describes how irradiance on a tilted plane, β , is modeled. The total irradiance on a tilted surface, I_{coll} , is composed of direct, $I_{\text{bn}} \cos(\theta)$, sky-diffuse, $I_d \left(\frac{1+\cos\beta}{2} \right)$, and ground reflected components, $I_h \rho_g \left(\frac{1-\cos\beta}{2} \right)$, as depicted in Fig. 4.1. It should be noted that I_{bn} , I_d and I_h represent the beam, diffuse and global horizontal irradiance, respectively.

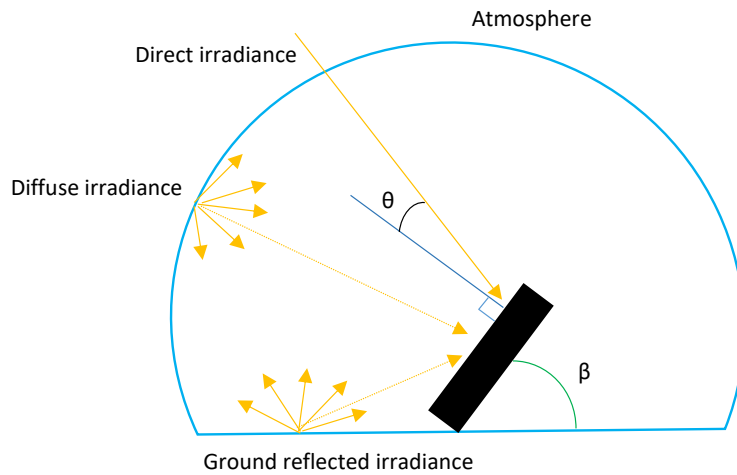


Figure 4.1: Irradiance components scheme.

The total irradiance can be mathematically described [119] as shown in Eq. 4.1:

$$I_{\text{coll}} = I_{\text{bn}} \cos(\theta) + I_d \left(\frac{1 + \cos\beta}{2} \right) + I_h \rho_g \left(\frac{1 - \cos\beta}{2} \right), \quad (4.1)$$

where $\cos(\theta)$ is the angle between the beam irradiance and the surface normal, β is the tilt angle of the surface with the ground (please see Fig. 4.1) and ρ_g is the ground albedo coefficient. The direct irradiance component is obtained using simple geometry, while the diffuse component is determined with the Liu-Jordan

isotropic model [120, 121] and the albedo component through the classic isotropic approach. The variable $\cos(\theta)$ can be calculated straightforward using spherical geometry, as given by Eq. 4.2:

$$\cos \theta = \cos(\delta) \cos(\phi - \beta) \cos(\omega) + \sin(\delta) \sin(\phi - \beta), \quad (4.2)$$

where δ , ϕ and ω are the declination, latitude and hour angle, respectively. Regarding the ground reflected irradiance, there is a lack of a robust database for ρ_g , since in-situ measurements are non-existing. However, the typical approach to overcome this is to consider $\rho_g=0.2$, [119] and thus, calculations concerning the ground reflected irradiance were performed using this value as reference.

Solar irradiance data was taken from PVGIS [122], despite the fact that local data is available for all of the above irradiance components, except for albedo, to highlight the general application of the method. Typical meteorological days were used in the analysis.

4.2.2 Effective irradiance model with soiling

For the effective irradiance that reaches the PV panels on a given tilt angle β , the model described in [123] is used, as shown by Eq. 4.3:

$$G_{\text{eff}} = \tau_r \left[(1 - L_b) I_{\text{bn}} \cos(\theta) + (1 - L_d) I_d \left(\frac{1 + \cos \beta}{2} \right) + (1 - L_a) I_h \rho_g \left(\frac{1 - \cos \beta}{2} \right) \right], \quad (4.3)$$

where τ_r is the normal incidence transmittance ratio for soiled and clean glass PV cover, while L_b , L_d and L_a are angular loss factors for direct, diffuse and albedo components, respectively. The variable τ_r is calculated through Eq. 4.4, as follows:

$$\tau_r = \frac{\tau_{\text{soiled}}}{\tau_{\text{clean}}}, \quad (4.4)$$

while angular loss factors from [123] are calculated as follows, in Eq. 4.5 – 4.7:

$$L_b = \frac{\exp\left(-\frac{\cos \theta}{a_r}\right) - \exp\left(-\frac{1}{a_r}\right)}{1 - \exp\left(-\frac{1}{a_r}\right)}, \quad (4.5)$$

$$L_d = \exp\left[\frac{-c_1}{a_r} \left(\sin \beta + \frac{\pi - \beta - \sin \beta}{1 + \cos \beta}\right) - \frac{c_2}{a_r} \left(\sin \beta + \frac{\pi - \beta - \sin \beta}{1 + \cos \beta}\right)^2\right], \quad (4.6)$$

$$L_a = \exp \left[\frac{-c_1}{a_r} \left(\sin \beta + \frac{\beta - \sin \beta}{1 - \cos \beta} \right) - \frac{c_2}{a_r} \left(\sin \beta + \frac{\beta - \sin \beta}{1 - \cos \beta} \right)^2 \right], \quad (4.7)$$

where c_1 is a constant, c_2 a coefficient obtained from a least square fit and a_r is the angular loss coefficient. The angular loss factor for the direct irradiance component corresponds to the ratio between transmittance with a certain incidence angle and transmittance with normal incidence. Both diffuse and albedo angular loss factors are calculated solving two integrals that consider the contribution of each solid angle unit incident on the PV module (assuming an isotropic distribution of diffuse and albedo components).

4.2.3 Mass accumulation as function of the tilt angle

To account for the effect of soiling on the tilt angle, it is necessary to infer the dependency of mass accumulation with the tilt angle itself. The data needed to model such dependency was obtained using the setup and method described in Sub-Section 2.2.1, Fig. 2.1a . This glass tree is able to provide several tilt angles configurations, ranging from 0° to 90° at 15° steps. In this analysis, only the south glasses were taken into account, since that is the typical azimuth of installed PV systems.

Mass accumulation measurements were performed with a micro-balance (Bosch SAE 80/200). The weight of each glass sample was measured at the end of every week, while the respective monthly means were calculated thereafter. Assuming exponential mass functions of the type $M_A(\beta) = p_1 \exp(p_2\beta)$, monthly dependencies on the tilt angle, $M_A(\beta)$, were then calculated, see Table 4.1. Due to missing periods of data during the months of December and January, the corresponding $M_A(\beta)$ functions were set equal to the value found for November, as it was found to be the month with less soiling (February is not considered in this assumption since there was a severe and unusual Saharan desert dust event). Additionally, November is a month within the rainy season and, therefore, a reduction in the amount of soiling is expected to occur.

Table 4.1: Monthly mean mass accumulation statistics (data retrieved in 2017 at PECS).

Months										
	F	M	A	M	J	J	A	S	O	N
r^2	0.97	0.91	0.95	0.98	0.90	0.91	0.994	0.995	0.99	0.91
RMSE	0.01	0.02	0.18	0.01	0.01	0.03	0.02	0.01	0.02	0.02

Mass accumulation functions can be seen in Fig. 4.2, with Spring and Summer months showing higher soiling, as expected, mainly due to the lack of precipitation. In particular, during April, the highest soiling occurs due to the increase in organic soiling, namely pollen deposition [33]. As shown in Fig. 4.2, the soiling effect with the tilt angle is approximately exponential in all cases, although the data was smoothed to eliminate bird dropping effects on mass accumulation. The statistical values obtained are summarized in Table 4.1, where all values of r^2 are above 0.9 (with the majority of them above 0.95) and a RMSE consistently below 0.02, corresponding to reliable approximations.

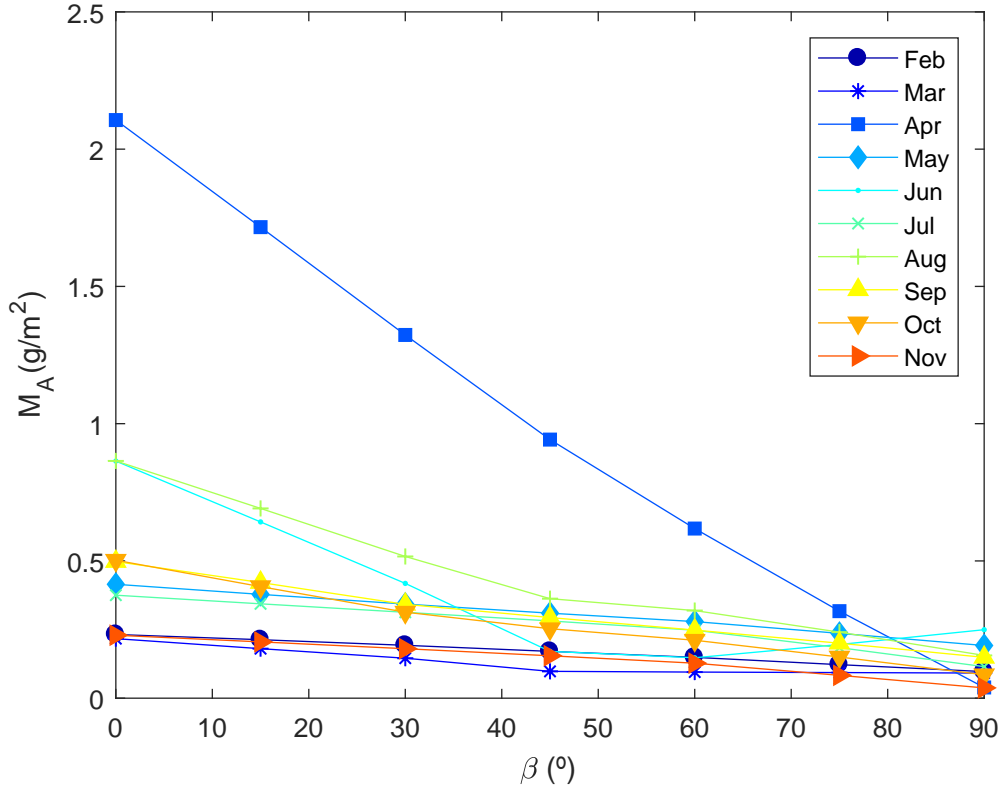


Figure 4.2: Mass accumulation as function of the tilt angle for each month (data retrieved in 2017 at PECS).

4.2.4 Transmittance ratio as function of the tilt angle

In order to model the relation of transmittance ratio with the tilt angle, mass accumulation data was related to the transmittance ratio between dirty and clean glasses. This leads to a linear least square fit that can be obtained through Eq. 4.8:

$$\tau_r(M_A) = b_1 M_A + 1, \quad (4.8)$$

where $b_1 = -0.2545 \text{ m}^2/\text{g}$. Previous studies, for instance [115], have used an exponential model instead of a linear one. However, no high transmittance loss regimes, such as those in desert regions, are present in this data set, justifying the use of a linear fit. Since this is the case for typical urban and rural environments in Europe, the focus of the present work is given to a linear model instead of an exponential one (see Fig. 4.3), where high correlations (r^2) can be obtained.

With both $\tau_r(M_A)$ and $M_A(\beta)$, it is possible to estimate the transmittance ratio as a function of β and $\tau_r(\beta)$ from Eq. 4.8, for each month, as follows in Eq. 4.9.

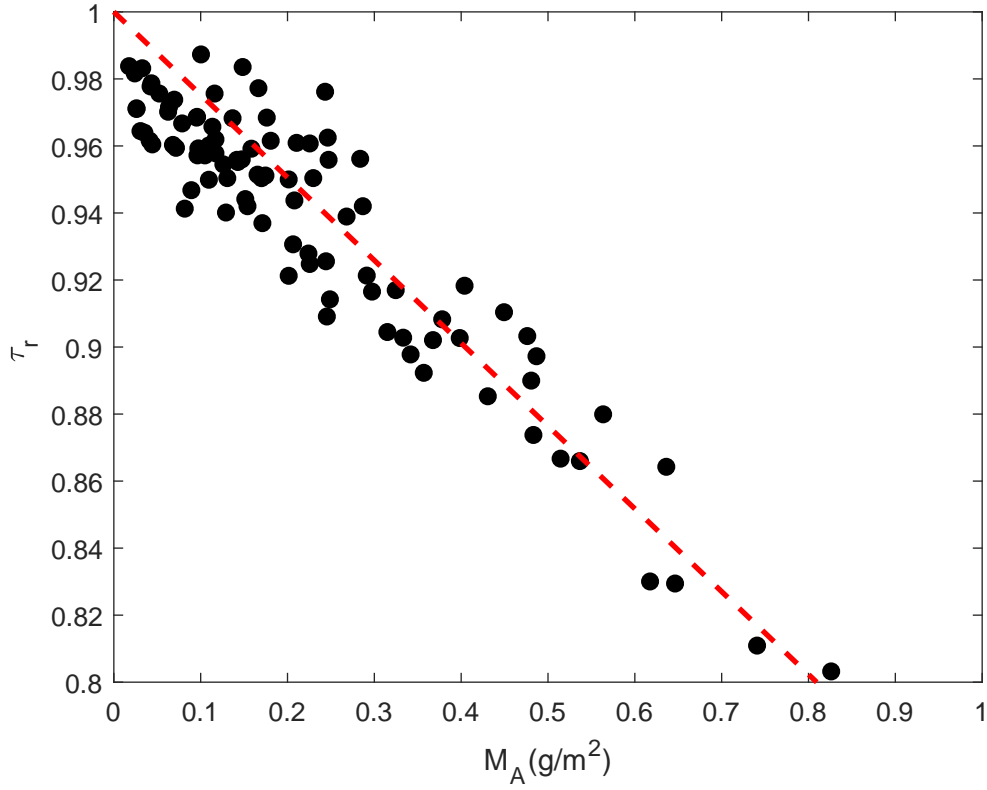


Figure 4.3: Transmittance ratio as function of mass accumulation (weighted data retrieved in 2017 at PECS and transmittance data retrieved at the Water Laboratory, University of Évora).

$$\tau_r(\beta) = b_1[p_1 \exp(p_2\beta)] + 1 = b_1p_1 \exp(p_2\beta) + 1 \quad (4.9)$$

4.2.5 Angular loss coefficients

The angular loss coefficient, a_r , in Eq. 4.5 – 4.7, has a dependency on the transmittance ratio, $a_r(\tau_r)$. Such relation is assumed to be linear and can be obtained through Eq. 4.10, with data fitting as in [124]:

$$a_r(\tau_r) = d_1\Delta\tau + d_2, \quad (4.10)$$

where $d_1 = -1.23$ and $d_2 = 1.403$, with a r^2 of 0.997. Taking into account that in the present model τ_r is dependent on β , it implies that:

$$a_r(\beta) = a_r[\tau_r(\beta)], \quad (4.11)$$

thus, alternatively to Eq. 4.10, a_r can be represented simply by its β dependency, as shown in Eq. 4.12.

$$a_r(\beta) = d_1[b_1p_1 \exp(p_2\beta) + 1] + d_2. \quad (4.12)$$

The coefficient c_2 is also dependent on the a_r , as described in [123], therefore a similar process was used, as shown in Eq. 4.13:

$$c_2(a_r) = f_1a_r + f_2, \quad (4.13)$$

where $f_1 = 0.5$ and $f_2 = -0.154$, with a r^2 of 0.99, and, as in a_r , its β dependency can be presented as:

$$c_2(\beta) = f_1d_1[b_1p_1 \exp(p_2\beta) + 1] + d_2 + f_2 \quad (4.14)$$

In Fig. 4.4 both a_r and c_2 coefficients are presented, as well as, the albedo and diffuse loss factors:

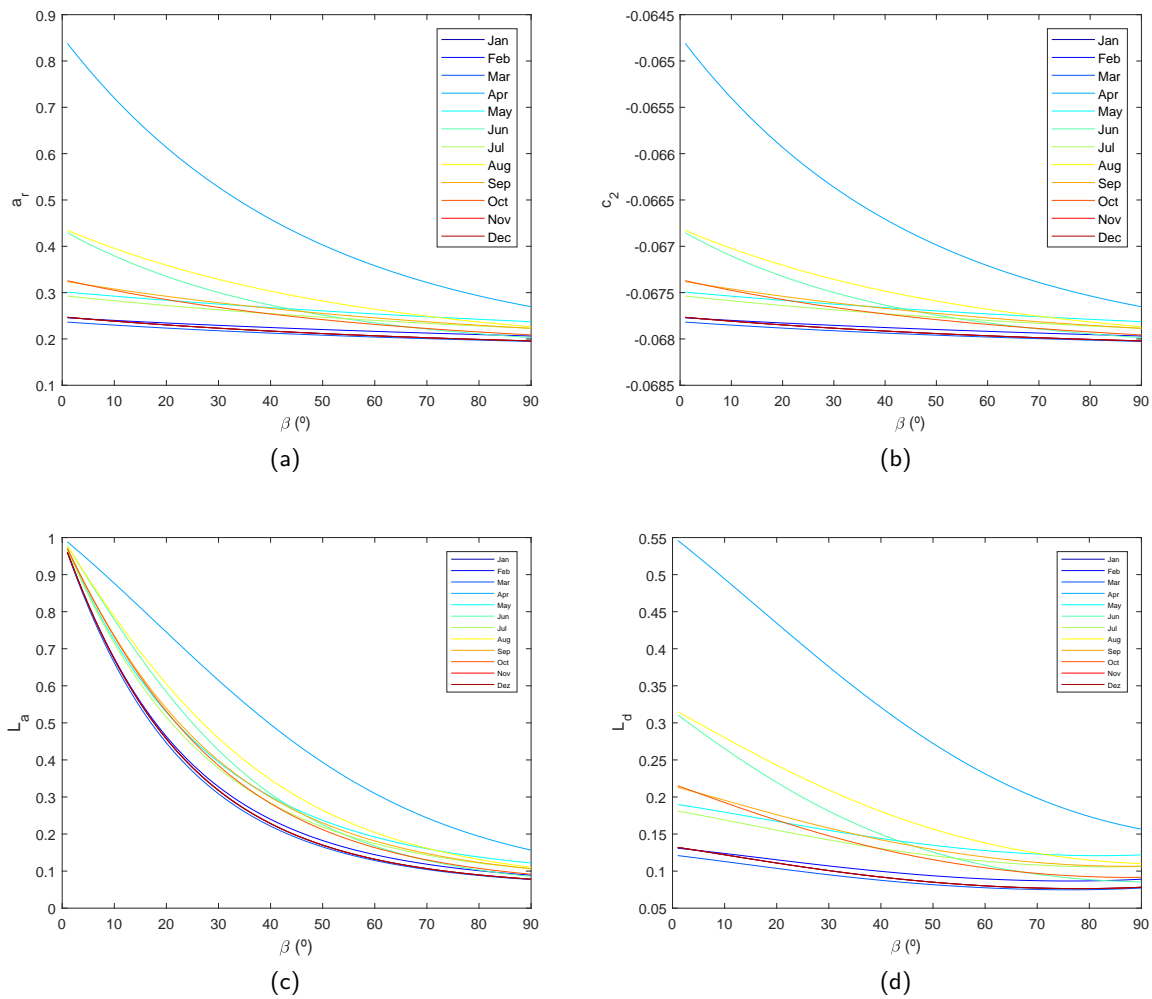


Figure 4.4: Coefficients and angular losses: (a) a_r ; (b) c_2 ; (c) L_a ; (d) L_d .

4.2.6 Algorithm flowchart

Consequently, for the analysis previously described, all variables depend only on β , on a monthly basis, which allows for Eq. 4.6 to be calculated considering the angle of incidence, θ , and the tilt angle, β . For a clearer description of the process, a flowchart is presented below (see Fig. 4.5).

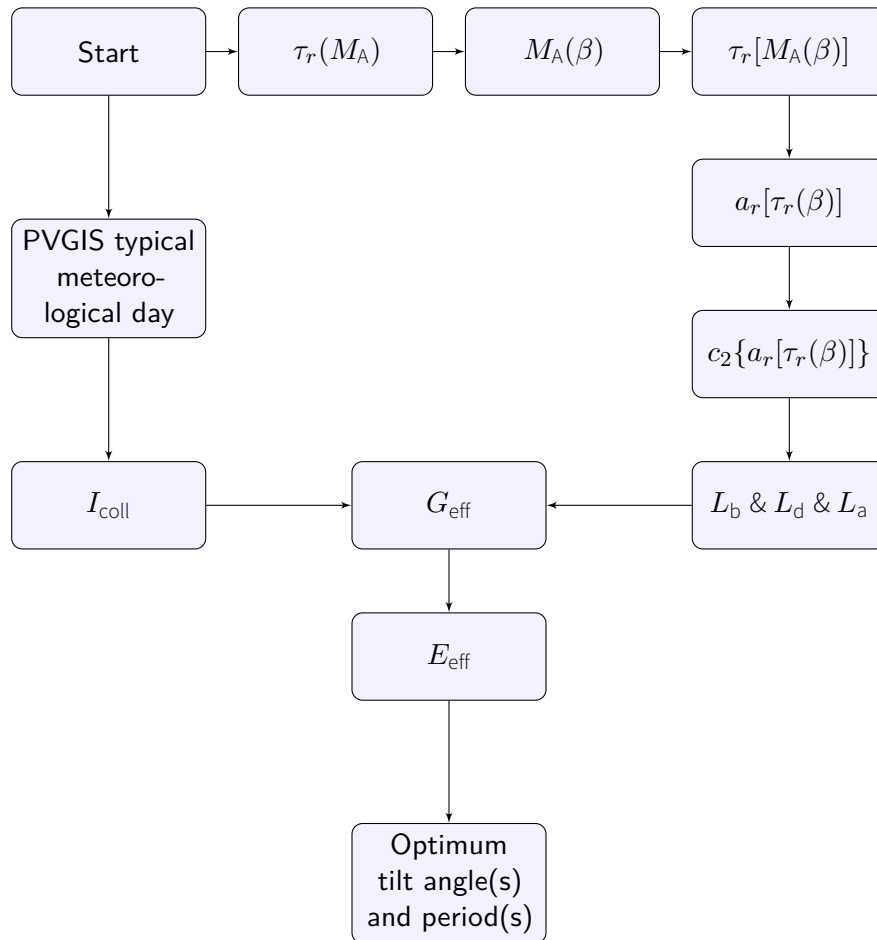


Figure 4.5: Algorithm flow chart. Two processes are considered: calculation of the irradiance on the tilted plane (left side) and the soiling implementation (right side). The effective irradiance, G_{eff} , and the effective energy, E_{eff} , are then calculated.

The algorithm presents two processes running in parallel: the calculation of the tilted plane irradiance, I_{coll} , (considered here as the process on the left side) and the soiling implementation (considered here as the process on the right side). With the effective irradiance, G_{eff} , being calculated for each month through Eq. 4.3 and the effective energy, E_{eff} , obtained by multiplying G_{eff} with the number of days of the respective month, the effective energy can then be calculated for different periods and tilt angles. For instance, if a bi-annual tilt angle configuration is preferred, then every combination of two periods within a year is calculated for every tilt angle (with 1° steps) and then, the respective periods that maximize the annual energy production are chosen.

4.3 PV design including soiling effect

4.3.1 Constant tilt angle configuration

As previously explained, the objective of this work is not only to calculate the effective irradiance on the PV plane with soiling, but also to help the design of improved static and quasi-static systems including a realistic soiling model. The static case is useful, for instance, for small PV producers, small domestic rooftop PV systems, small PV plants or Building Integrated Photovoltaics (BIPV), which may be in locations of difficult access. Such situations demand a system designed to include the soiling effect, as it will be discussed in detail, further in this Chapter.

For a constant optimum tilt angle configuration, which is the most common setup due to higher maintenance and operational costs associated with traditional tracking systems, there is a shift of 6° in the tilt angle. This value is substantially higher when compared with other estimations [8]. In Table 4.2, for comparison purposes, it is depicted the tilt angle shift, in magnitude, obtained in [8] and in this work, for a constant tilt angle. It should be noted that the values obtained in [118] are dependent on the solar zenith, which can direct the analysis to a full and not manual tracking, as studied here, and for that reason it is not considered in the present analysis.

Table 4.2: Comparison between tilt angle shift (in magnitude) between present work and [8], for a constant tilt angle in a soiled scenario.

	Present work	Xu and co-workers
Tilt angle shift ($^\circ$)	6	0.17

This analysis may be helpful for small PV installations, where it can be difficult to perform cleaning tasks. Such technique allows the modules to be tilted considering soiling effects *a priori*, reducing cleaning needs, while maximizing the energy production. It should be noted that the optimum tilt angle for the clean model is 34° on the test site coordinates, which is identical to the one obtained with PVGIS for the same location. This highlights a high correlation between the present model and the PVGIS algorithm for the optimum angle results. From a clean to a soiled scenario, the optimum tilt angle shift not only depends on local soiling, but on irradiance as well. The trade-off between these two variables is what dictates such shift.

4.3.2 Multiple tilt angle configurations

The previous analysis is relevant for static systems, which are currently the most common ones. This Chapter also intends to show how quasi-static systems, considering a set of different tilt angles throughout the year, can have their design enhanced considering soiling effect and therefore allowing a power production maximization. In Table A.1, at the appendix section, results from 1 to 12 tilt angles per year, with and without soiling, are shown. It is also observed that increasing the system flexibility with respect to the tilt, more energy can be produced, as expected. Values of R_{SS} , i.e. the percentage ratio between the annual

effective energy of a specific configuration and the constant tilt one, ranges from $\approx 3.2\%$ for a bi-annual tilt configuration to $\approx 4.3\%$ for a 12 tilt angle configuration. Another conclusion is that periods for soiled scenarios may be different from the clean ones. Therefore, an optimum tilt angle for scenarios with soiling is different in value and also has different operation periods for each tilt angle. Interestingly, above 5 annual tilt angles, no significant increase in the effective energy is observed. This will be further discussed in detail.

The results for the clean scenario, in Table A.1, show that the optimum tilt angle for a multiple tilt configuration throughout the year is higher in Winter-Autumn and lower in Spring-Summer, as expected, due to the sun's elevation. However, if soiling is considered, the optimum tilt angle changes, as well as, the operating periods for each tilt angle (compared to the constant angle setup). It should be noted that, due to higher soiling levels in April and June, the soiled model increases the tilt angle relatively to the clean model, in order to maximize energy production during these periods. To increase the reliability of the soiled model predictions additional years of soiling data are needed. Soiling and irradiance have inter-annual variations and can change significantly from site to site. Consequently, it is also recommended the use of several years of soiling data.

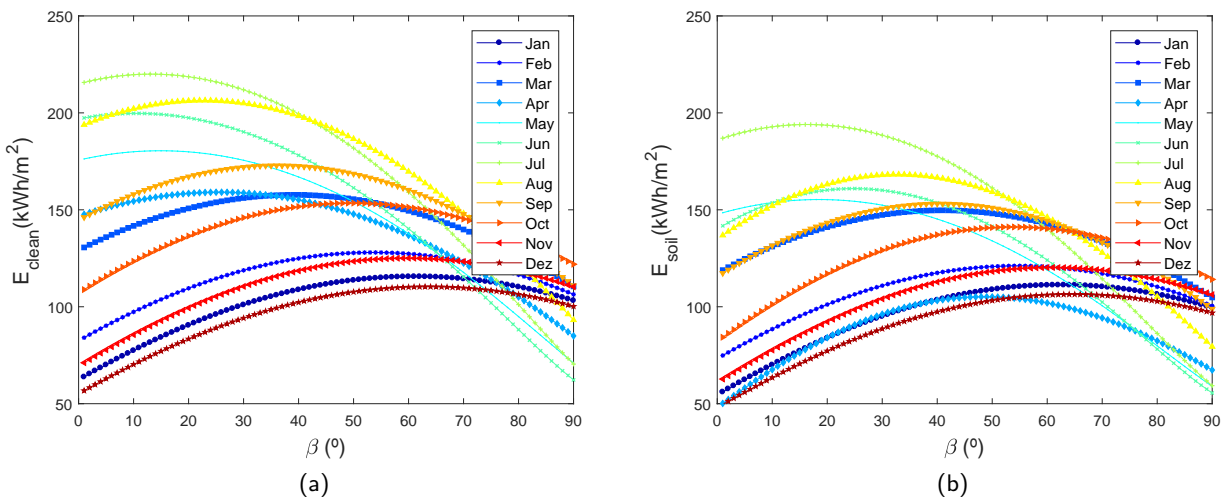


Figure 4.6: Effective energy for: (a) clean scenario; (b) soiled scenario.

In Fig. 4.6, the effective energy as function of β , with and without soiling for every month, is depicted. Results show a shift on the optimum tilt angle from lower to higher values regarding the clean and soiled scenarios. This transition is related to the fact that soiling is higher at lower tilt angles, causing the increase of the optimum tilt angle in order to reduce the soiling effect.

4.3.2.1 Trade-off between produced energy and configuration

To maximize energy production, it is important to determine the best system configuration; for that matter, some effort is required to change the PV system tilt angle, increasing maintenance and operation

costs (*OPEX*). The system can be installed with movable frames for easier tilt changes (commercially existing nowadays), for instance the one in Fig. 4.7, from UNISTRUT Service Company (www.unistrutusa.com):



Figure 4.7: UNISTRUT Service Company movable PV frame.

These systems are not automatic, however they are less expensive and do not require maintenance, being easy to install and use. Such systems constitute an option providing an optional and practical way to implement the methods discussed in this work.

In order to choose the best configuration, the capital expenditures (*CAPEX*), mathematically defined as $CAPEX$, and operating expenses (*OPEX*) mathematically defined as $OPEX$, of a 1 MWp plant with constant tilt was considered. The respective data was gathered from the 2017 European Photovoltaic Technology and Innovation Platform [125]. A 25-year period analysis was then performed, which is a common period for the operation of PV plants. Considering a fixed frame, the $CAPEX$ was taken to be $\approx 800 \text{ €}/\text{kWp}$ and $OPEX \approx 15 \text{ €}/\text{kWp}$. The $CAPEX$ and $OPEX$ for any of the other configurations, with movable frames, are set as a percentage increase of their values for a fixed structure. The variables CP and OP represent the percentage increase of $CAPEX$ and $OPEX$, respectively. It should be noted that N_T represents the number of times that the tilt angle is changed. The energy price, represented by the variable kWh_p , was retrieved from OMIE's website (www.omel.es) and was set as $5.5 \text{ c€}/\text{kWh}$, while an average performance ratio, PR , of 0.82 was considered for this region (above the 0.8 commonly used), since soiling effect is already present in the annual effective energy calculated. It is assumed that annual PV specific yield, SY , in kWh/kWp , is equal to the product of the annual effective energy by the PR . Multiplying this by the energy cost, the income, and taking the $CAPEX$ and $OPEX$ to represent full cost, a profitability index, PI , was created to evaluate the difference between all configurations with respect to the fixed one (see Eq. 4.15). It should be noted that, these calculations are performed for a 25-year period with a $CAPEX$ and $OPEX$ variation for every multiple tilt angle configuration.

$$PI = A_{\text{conf}} - B_{\text{fixed}}, \quad (4.15)$$

where:

$$A_{\text{conf}} = \sum_{j=1}^{25} SYkWh_p - (CAPEX + CP + OPEX + N_{TOP})$$

$$B_{\text{fixed}} = \sum_{j=1}^{25} SYkWh_p - (CAPEX + OPEX)$$

For simplicity reasons, in Fig. 4.8 a representation of Eq. 4.15 is only shown for 2, 3, 4 and 5 tilt angles. A triangular area can be observed, denominated profitability area, P_A , which is common for all figures. It should be noted that, all figures, including the ones not presented, depict a profitable area, even for low variation values of $CAPEX$ and $OPEX$, such as 0.1%, which may not be a realistic result. Moreover, it can be observed from Fig. 4.8, that an increase in the number of tilt angles along the year leads to an increase in the $OPEX$ and $CAPEX$ variation, for which there can be profit. This is expected, since changing tilt angles can increase costs, but at the same time, it is compensated by the increase in the energy production. The area where more profit can be made is the one for which the variation of both $CAPEX$ and $OPEX$ is close to zero, which may not be realistic. In order to find the optimum configuration, a parameter was created to relate profitability area with the sum of the profitability index of that same area, denominated weighted profitability, P_W , as calculated through Eq. 4.16:

$$P_W = \frac{\iint_A PI \, dx \, dy}{P_A} \quad (4.16)$$

In order to evaluate the sensitivity of this index to energy prices, several values were considered, as shown in Fig. 4.9. According to the chosen criterion, results show that the optimum configuration, is the 4 tilt angle one. Adding more tilt angles throughout the year does not increase substantially the weighted profitability. It should be noted that the optimum configuration is independent of the energy price, except for very low values, which is to be expected, since the gain becomes meaningless. It can also be noticed that the weighted profitability decreases with the energy price reduction, considering that the energy production, relatively to the fixed configuration, is not compensated by low energy prices. Predicted values of $CAPEX$ and $OPEX$ for 2050 from [125] are used in Fig. 4.9b. For the same energy price, the weighted profitability window is larger, mainly because the predicted values of $CAPEX$ and $OPEX$ will be lower than the ones in 2017.

This analysis shows that in the future, and under current conditions, it may be even more profitable to have a PV plant with movable frames instead of a fixed installation. Nevertheless, it is stated that this is a

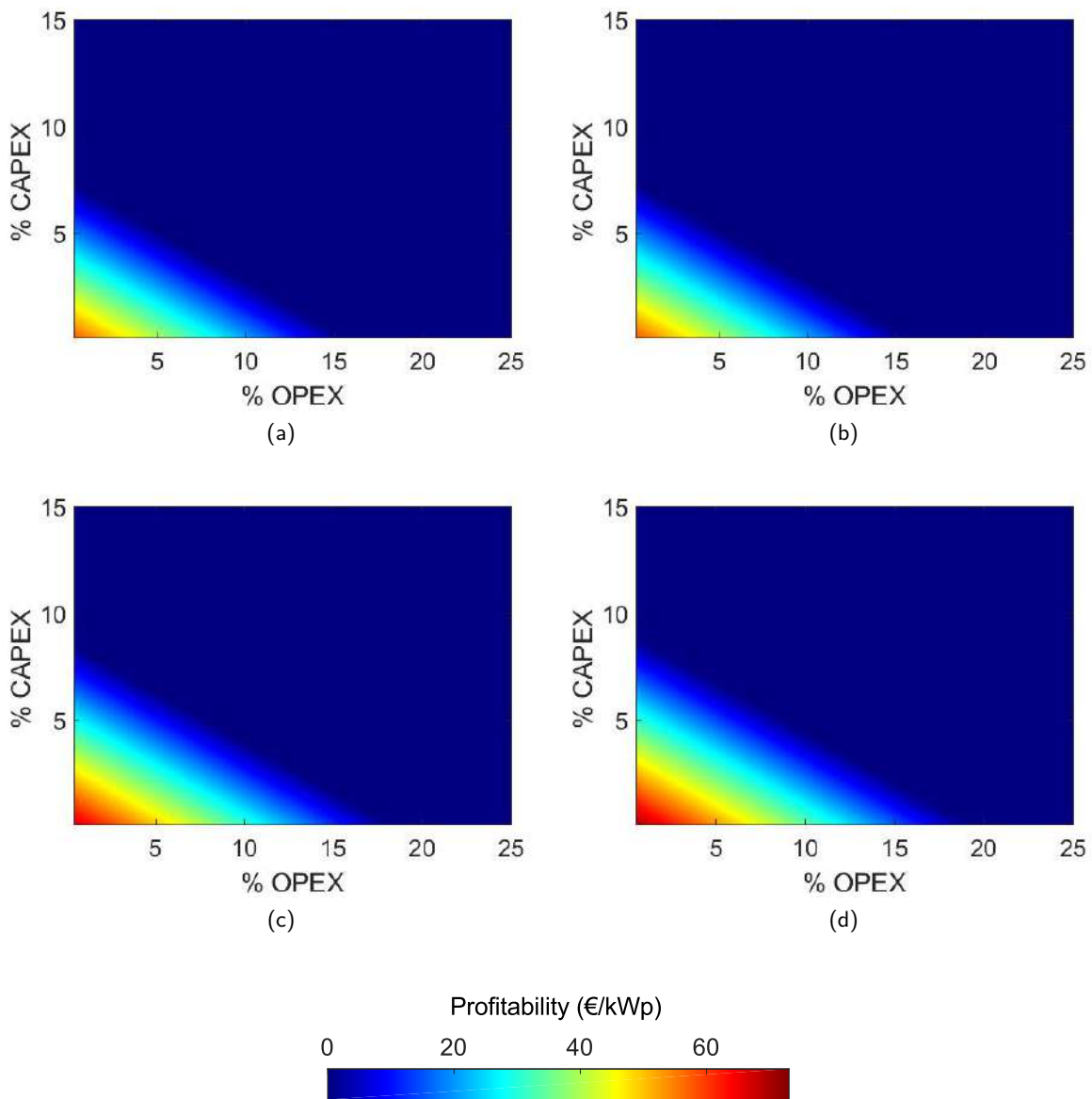
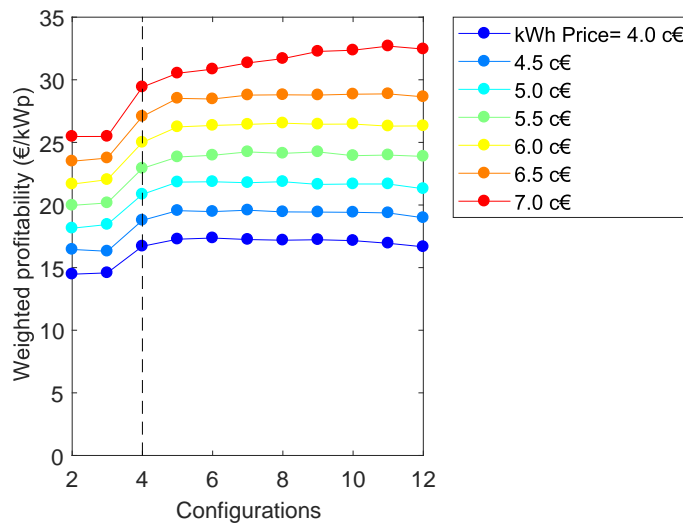
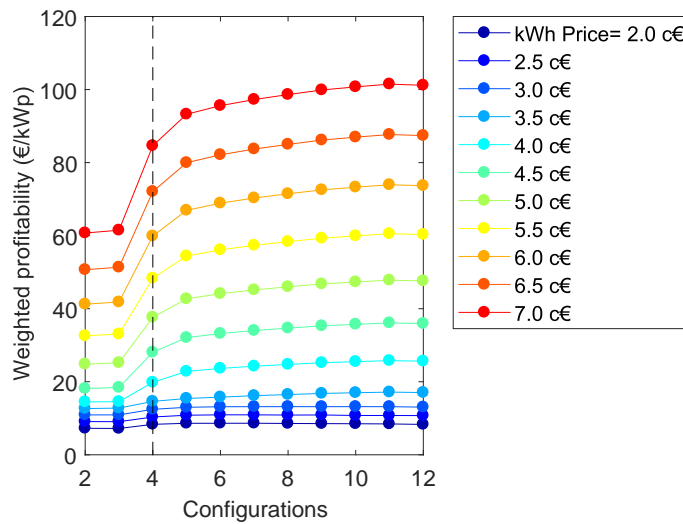


Figure 4.8: Profitability index for: (a) 2 tilt angles; (b) 3 tilt angles; (c) 4 tilt angles; (d) 5 tilt angles.

simple analysis and therefore, larger data sets should be considered when a more robust economic analysis is taken into account.



(a)



(b)

Figure 4.9: Profitability window for two cases, including different energy prices, for: (a) 2017; (b) 2050.

4.4 Cleaning schedule modeling

Many PV system owners may not have the economic capacity to invest in a movable system or either the know-how to design their systems *a priori* considering soiling effect. However, to ensure maximum efficiency, it is necessary to know the optimum cleaning schedule. In this context, the energy production evolution of both clean and soiled models for the same tilt angle and a specific configuration was determined, as shown in Fig. 4.10:

When considering the particular case for this location, the results for the energy production with constant tilt angle throughout the year, see Fig. 4.10, demonstrate, for instance, that if a loss higher than 5% in the energy produced is not desired, a periodic cleaning from April to September should be carried out. Other

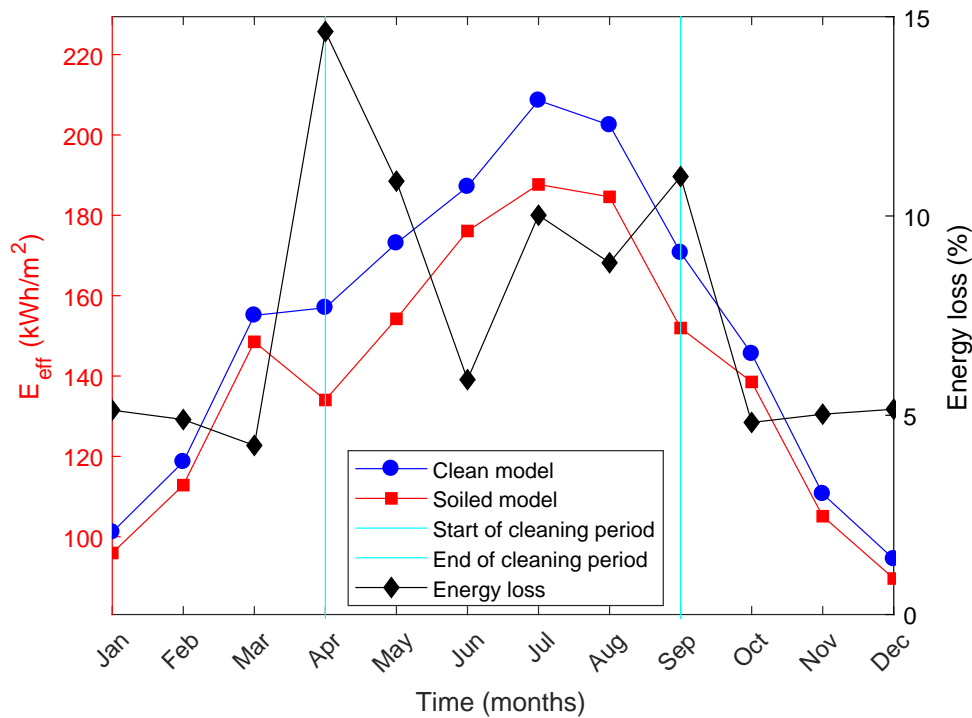


Figure 4.10: Cleaning schedule as a function of soiling. Blue dots represent the clean scenario, red squares represent the soiled scenario, light blue vertical lines depict the cleaning period and black diamonds represent the energy loss between the clean and soiled scenarios.

thresholds can be chosen, as desired, and respective cleaning periods can be determined.

4.5 Conclusions

The present Chapter includes a modified effective irradiance model (i.e. local soiling was introduced with several constants being recalculated and the method used to achieve other objectives) with the particle deposition effect using in-situ soiling data. This allowed the inclusion of soiling effect in the determination of the tilt angle, optimizing the energy production, improving from models only considering irradiance. This approach created the opportunity to calculate the optimum tilt for a static system designed to ignore cleaning tasks (or at least to reduce them), while maximizing its energy output. Moreover, the model was also used to calculate multiple optimum tilt angle designs to maximize the annual energy output, which can be performed using simple movable frames and also taking into account that no cleaning will be performed. For large PV plants, it could be interesting to increase the energy production with a quasi-static system using movable tilt angle frames, rather than 2-axis or 1-axis tracking systems, usually associated with higher maintenance costs and higher downtime due to lower reliability. Considering the tilt angle moving costs, energy production and with the consequent economic analysis, the optimum design for a multiple tilt angle configuration along the year was found. The established model was also used as a method to define a

cleaning schedule, i.e. the identification of necessary cleaning periods to achieve a desired efficiency range. It should be noted that generalization to other locations is feasible and that larger data sets of soiling are needed in order to increase the model robustness.

The work in this Chapter resulted in the following publication:

- R. Conceição, H.G. Silva, L. Fialho, F. Lopes, M. Collares-Pereira, PV system design with the effect of soiling on the optimum tilt angle, *Renew. Energy* 133 (2019) 787–796.

5

Soiling Mitigation for CSP

5.1 Introduction

According to the National Renewable Energy Laboratory (NREL), a 5% decrease in the specular reflectance may lead to a drastic increase of 5% in the levelized cost of energy (LCOE) [126]. Therefore, the development of anti-soiling coatings to decrease soiling is needed, especially in arid regions where this effect is more severe. With that objective in mind, the WASCOP project brought together RIOGLASS (a Spanish CSP mirror manufacturer) and IK4-TEKNIKER (a Spanish R&D institute) to develop a new type of anti-soiling coating. It is both hydrophilic and photo-catalytic, which has the particularity of having a longer durability in relation with common coatings presented in the literature [127], thus it has good prospects to reach the market in a few years' time-scale. To that end, substantial experiments need to be performed on the coating performance, including different regions of the globe with potential for CSP implementation. In this context, the experimental facilities of PECS, in which this thesis was done, represent

an excellent opportunity to test the coatings under an agricultural environment and using the methodology here developed in [114]. It is the objective of this Chapter to evaluate the effectiveness of anti-soiling coating for CSP mirrors in this area to cut down maintenance costs due to cleaning, observing how frequently the mirrors need to be cleaned under normal circumstances, but also after long-range transport of Saharan desert dust [32]. A simple economic analysis will be made to explore possible scenarios for the use of these coatings. The manuscript is organized as follows: in Section 5.2 it is explained the methodology used; in Section 5.3 it is described the experimental results and their discussion is presented; in Section 5.4 it is summarized the content of this Chapter, as well as, the final conclusions and remarks.

5.2 Methodology

5.2.1 Coating production and development

It should be noted that the entire paragraph is quoted from the RIOGLASS and IK4-TEKNIKER companies. The anti-soiling coating presented in this Chapter is titania-based in the anatase form. It should be noted that the entire paragraph is a quote from the supracited companies. It is initially applied in liquid form over the glass. Once deposited, a conventional heat treatment on the glass allows the formation of a chemical covalent bond between the coating and the glass, resulting in a highly durable and homogeneous dense coating, which shows anti-soiling properties due to its hydrophilic behavior [128]. To evaluate the coating efficiency, 300×100 mm glass samples were partially coated (half of the sample coated and half of the sample uncoated) by spray-coating and were then thermally treated. The reflective layer was deposited afterwards in the back side of the glass. The coating thickness is in the range of 100-150 nm. The coating has photocatalytic properties being capable of degrading different pollutants. The hydrophilicity of the TiO₂ surface is induced by UV-irradiation and was measured using a goniometer after 24 hours of UV exposure, being the contact angles 13° for the coated reflector and 45° for the uncoated reflector.

5.2.2 Measurement setup

Measurements of soiling effect on the mirror's reflectance were performed using a TraCS mounted on a SOLYS 2 sun tracker, as shown in Fig. 5.1a, in PECS. This an agricultural area, very suitable for soiling studies, especially during summer when the agricultural activities are more intense, as seen in previous Chapters [129]. Moreover, two mirrors were fixed in a soiling setup oriented towards south, as shown in Fig. 5.1b, which is an adaptation of the glass tree shown in Chapter 2. These mirrors have been divided in half: the left side with a simple mirror, without coating, and the right side with a mirror embedded with RIOGLASS anti-soiling coating. The mirrors were installed in two positions: one horizontal and the other tilted at 45° to evaluate the coating anti-soiling properties with inclination. The measurements started on May 2018 and lasted until September 2018. This period corresponds to the dry period of the year, when

most of CSP production would take place along with very low precipitation.



Figure 5.1: Measurements setup: (a) TraCS; (b) Modified glass tree.

Measurements of both mirrors' reflectance were performed in four different positions. These positions were kept the same throughout the experiment, because of the size of the mirrors and for comparison reasons. A total of eight positions (four for each mirror) were analyzed. This allows different positions of each side of the mirrors to be analyzed, allowing a better characterization of the mirrors' reflectance loss. In the 45° tilted mirror positions (1) and (4) are the ones on the lower side of the mirror, allowing the study of particle slip in the mirror. The uncoated part of the sample is the left side and the coated part is the right side, as shown in Fig. 5.2.

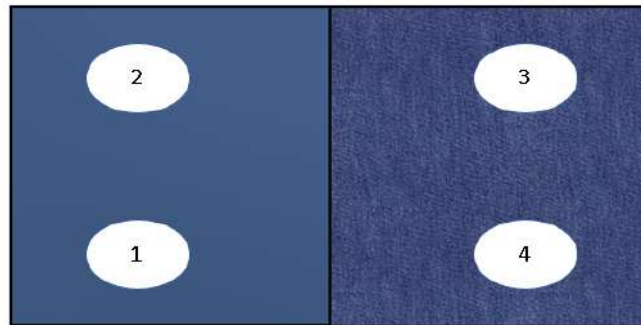


Figure 5.2: Schematic view of the measured areas in the mirror: the uncoated part of the sample is the left side (areas 1 and 2); the coated part is the right side (areas 3 and 4).

The TraCS compares the irradiance reflected to a pyrheliometer by the mirrors with the DNI measured by a second pyrheliometer [114]. This type of measurement allows the loss of reflectance, due to soiling, to be evaluated with the solar irradiance which has the advantage of perceiving its spectral content (which commercial portable reflectometers do not), but has the disadvantage that measurements can only be made in clear-sky days. It should be noted that soiling effect is calculated in the same way as it was in Chapter 3, please see Eq. 3.1.

5.3 Results and discussion

5.3.1 Experimental results

As it can be observed from Fig. 5.3, in the initial days of the experiment, the coated samples are associated with lower soiling index values, and the coated part of the mirror with 45° tilt shows the lowest value, presenting a soiling index below 0.05, until the first episode of rain. This shows the good catalytic properties of the coated mirrors in the absence of cleaning and, the very low value in the 45° tilted mirror means that particles adhesion to the mirror is probably reduced due to the action of gravity. From the figure, it is also seen that episodes of rain decrease the overall value of soiling in uncoated mirrors almost every time, whereas for the coated mirrors, this only happens once (for the 45° after simulated rain), while in the rest of the cases the value stays almost the same or even higher. However, it must be considered that measurements were only made a few days after the rain events, meaning that accumulation of particles was already significant. This could be due to the hydrophilic properties of the mirror, agglomerating particles.

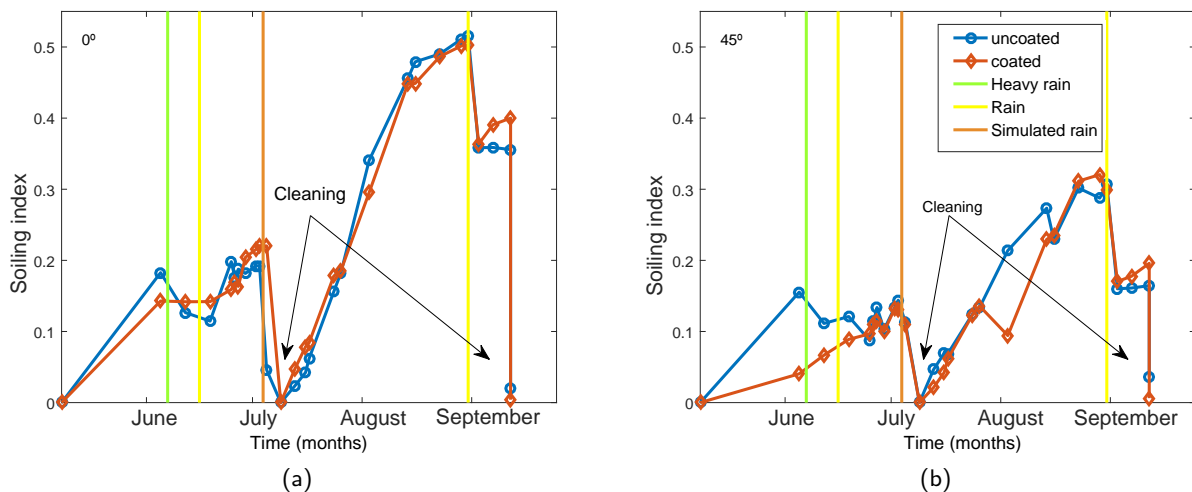


Figure 5.3: Soiling index of the coated and uncoated sides of the mirror samples for: (a) 0° tilt; (b) 45° tilt.

After the first cleaning, the 0° tilted coated mirror seems to divert from its initial behavior of lower soiling indexes than the uncoated. Large amounts of particles were observed on this side, likely because of the hydrophilic properties of the anti-soiling coating and the fact that particles will not slip due to gravity, but are instead pulled towards the glass (since it is horizontal), as shown in Fig. 5.4. Moreover, air humidity and the water accumulated in the morning onto the mirrors can be a factor to explain this behavior, transporting the particles to the hydrophilic coating, since there is no inclination in the mirror. In the 45° tilted mirror, the behavior of both coated and uncoated mirrors is similar to the one seen on the initial days of the experiment, because of the photocatalytic properties of the mirror.

In the beginning of July, an episode of rain contaminated with dust from Saharan desert dust [114] took place. The values dispersed a lot and it is harder to evaluate the differences in optic behavior between



Figure 5.4: Uncoated and coated sides of the horizontal mirror a few days after the first cleaning: (a) Uncoated; (b) Coated.

coated and uncoated mirrors, mainly due to the non-uniform distribution of soiling. One of the phenomena that can cause this, is the deposition of particles swept by rain contaminated with the Saharan desert dust in agglomerates, meaning that certain areas of the mirrors have greater amounts of particles than others. As a consequence, it is difficult to have reliable measurements in both coated and uncoated mirrors. Still, this episode shows that the coatings tend to be inefficient in terms of contaminated rain, as water acts as the deposition agent and not the cleaning agent.

In the following days of the experiment, from July until the end of August, the region suffered a severe heat wave, with temperatures over 40°C and high amounts of dust particles in the air, almost resembling an arid climate characteristic of Northern African countries [130]. This, together to low relative humidity, led to an increase of the soiling index rising from 0.2 to almost 0.45 in just one month of exposition, where the soiling rates per day are shown in Table 5.1. Two periods were considered for this, period 1 from installation until the first measurement and period 2 from the first cleaning until the second episode of rain.

Table 5.1: Soiling rates of the different mirror sides between events.

	Period 1 (%/day)	Period 2 (%/day)	r^2 (Period 2)	RMSE (Period 2)
Uncoated 0°	0.65%	1.10%	0.9580	0.0458
Uncoated 45°	0.55%	0.56%	0.9512	0.0256
Coated 0°	0.51%	1.02%	0.9721	0.0346
Coated 45°	0.14%	0.60%	0.9506	0.0275

To evaluate the effect of morning dew, the relative humidity, RH , between midnight and 6 a.m was used, since this tends to be the most humid period of the day and when it is common to happen dew formation. In Fig. 5.5, a comparison between the soiling index for the coated and uncoated sides of the 45° tilted mirror are shown and it should be noted that the only considered measurements were the ones where measurements were taken in two consecutive days.

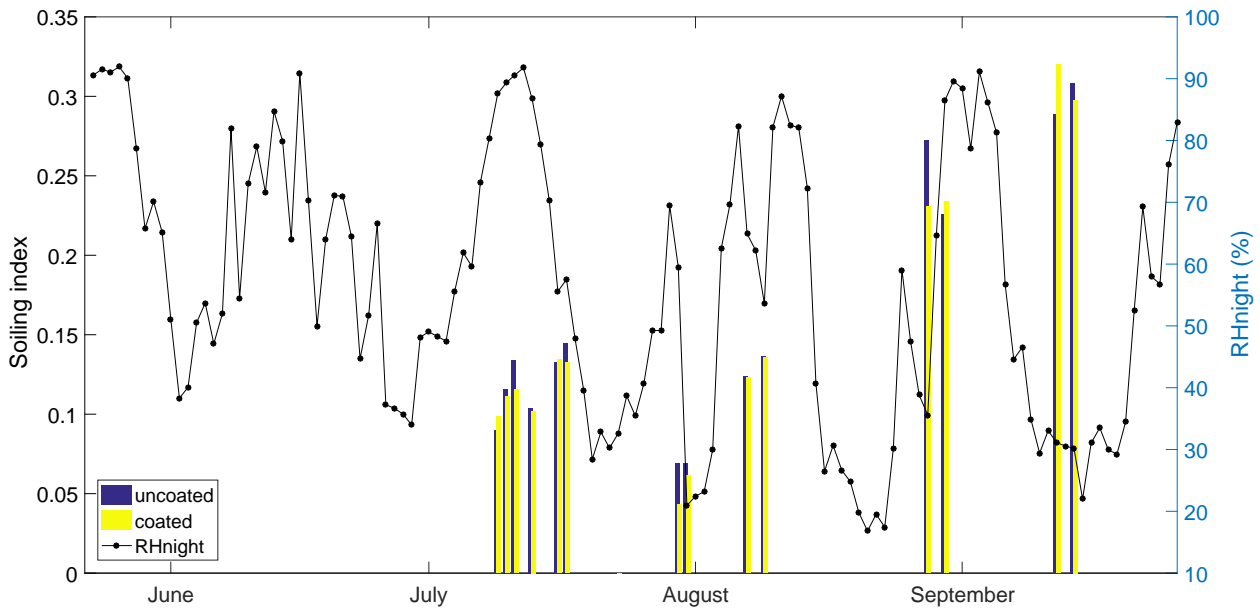


Figure 5.5: Relation between relative humidity and soiling index for the 45° tilted mirror.

During July, higher relative humidity during the night led to a reduction of the soiling index. On this month, dew formation was observed in the mirror, allowing the cleaning in the 45° tilted mirror due gravity and therefore particle washing. After this relative humidity peak, a reduction of the relative humidity in the night led to an increase in the soiling index. Throughout August, lower relative humidity led to a steadier, but higher increase of soiling index results. After the heat wave, in August, and the increase of relative humidity during night, between August and September, a decrease in the soiling index was observed in the uncoated side of the mirror and the values maintained constant for the coated side. The soiling rate was lower after this period until September. However, more data is needed to fully understand the effect of the relative humidity during the night and therefore dew formation.

After the second episode of rain, that occurred in September, there is a significant decrease of the soiling index in both mirrors, something that did not happened before. This could have happened due to the high number of particles already in the mirror, favoring the cleaning process with rain. Moreover, in the last cleaning, showed in Fig. 5.3, which was performed on the 26th of September, it can be seen that the soiling index does not reach zero. The comparison of the reflectance between the second measurement with the mirrors cleaned and the first, show a reflectance loss, as show in Table 5.2. However, more tests need to be performed to understand if this behavior is maintained or if it was caused by the way the cleaning was done.

Table 5.2: Difference between initial mirrors' reflectance.

β	Uncoated	Coated
0°	2.1%	0.4%
45°	3.7%	0.6%

By the data analyzed in the box plot, shown in Fig. 5.6, it is clear that the results for the 45° tilted

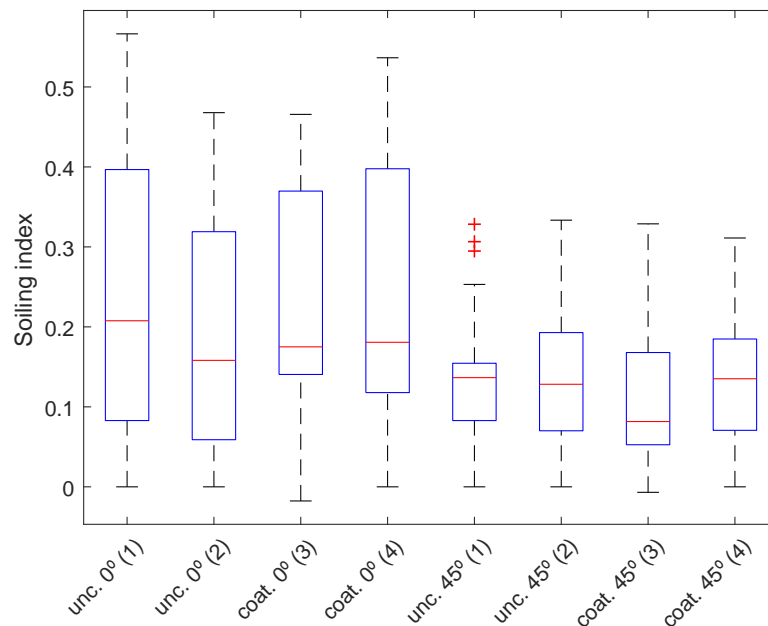


Figure 5.6: Box plot of all the soiling indexes.

mirror are less prone to variations and the position (3) for this mirror is the one that has the lower overall average results. This is the position on the upper side of the 45° tilted mirror, showing the positive effect of the anti-soiling coating in sweeping the particles by gravity, keeping overall the mirror clean.

5.4 SEM and image analysis

To evaluate and try to quantify the amount and type of particles that adhere to the mirrors, SEM analysis was made. In Fig. 5.7, SEM pictures show certain areas in the different mirrors. The pictures were taken from random locations of each mirror, not covering the whole sample. Two coated mirrors and two uncoated mirrors were exposed and allowed to accumulate soiling under the same conditions as the ones presented in the previous results.

- The pictures were taken in mid-September, from the mirrors accumulating particles since mid-June.
- It is visible that the mirror with 0° tilt presents higher number of particles in comparison with the 45° tilted mirror.

Table 5.3: Average area of organic material in the mirror samples.

β	Uncoated organic material average area (μm^2)	Coated organic material average area (μm^2)
0°	346.3	88.6
45°	401.6	293.0

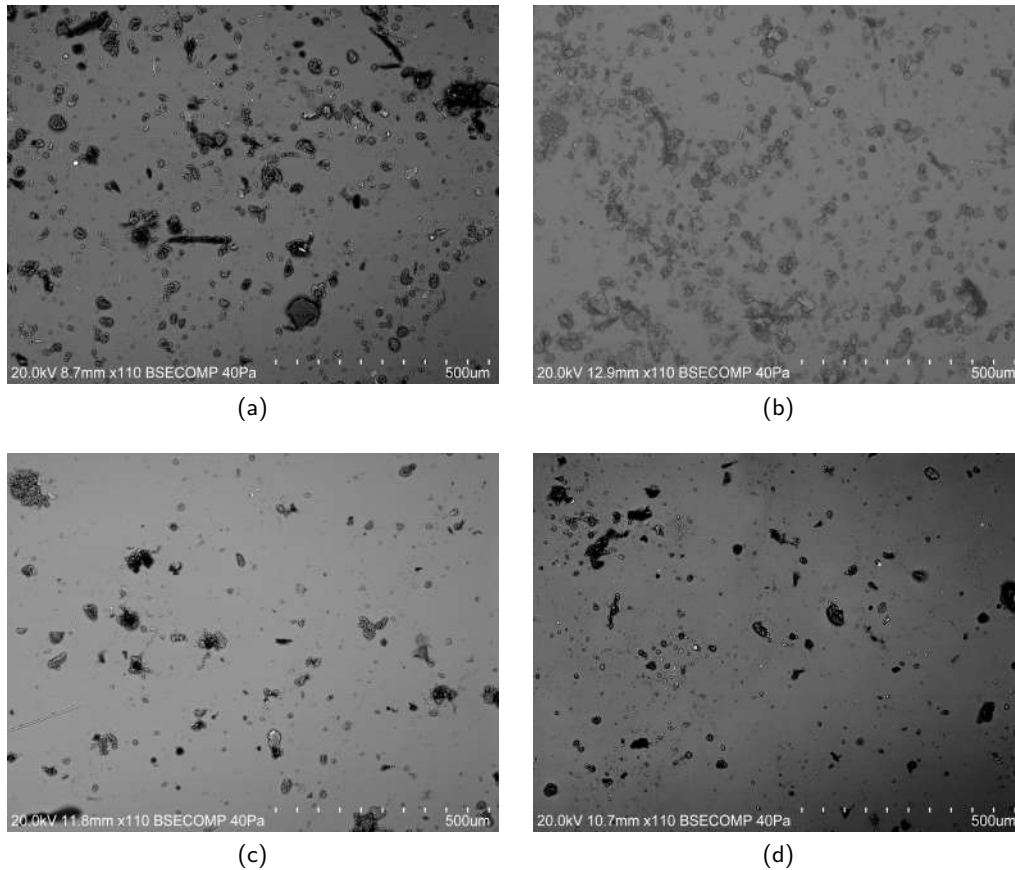


Figure 5.7: SEM pictures of the uncoated and coated parts of the mirrors: (a) uncoated 0°; (b) coated 0°; (c) uncoated 45°; (d) coated 45°.

From Table 5.3, it is clear that the uncoated sides of the mirrors for both positions have the highest average organic particle area. Although the pictures were taken from random places in the samples, a pattern can already be seen, especially for the 0° tilted mirror where the uncoated side has an average particle area almost four times the coated side. The photocatalytic properties of the mirror can be the cause of this phenomena, where the organic particles in the coated mirrors are being degraded. However, it should be noted that this analysis was performed using ImageJ, which can have high uncertainty, so this results should be only used for a general approach. Moreover, a more detailed analysis should be performed and during more time to assess the performance of such coatings.

5.5 Cost analysis

To evaluate the effect of the anti-soiling coating in the final energy cost-reduction at a plant scale, a cost analysis was performed. DNI data from was gathered from TraCS meteorological station in herdade da Mitra, Évora, to estimate the yearly amount of available solar energy. The study presented in this Chapter was performed for an Andasol I type plant with 510 120 m² solar field aperture area and an 16% solar-to-electricity efficiency. DNI values lower than 400 W/m², set as the critical value for CSP production,

and higher than 1000 W/m², which is usually the maximum obtained for this location, were removed. It is shown in Eq. 5.1, the expected loss between the uncoated and coated mirrors.

$$\Delta C = \Delta\lambda \times \eta_{solar-energy} \times E_{available} \times C_{energy}, \quad (5.1)$$

where $\Delta\lambda$ is the difference of soiling index between coated and uncoated mirrors (45° tilted plane) with a value of 1.3%, $\eta_{solar-energy}$ is the correspondent solar-to-electricity efficiency, while $E_{available}$ is the annual available energy for the solar field and C_{energy} is the energy price, which was assumed to be 11 c€/kWh for solar thermal energy. Since the soiling measurements only took place between May and September, an average $\Delta\lambda$ was calculated and this value was assumed constant for the whole year calculation. A loss of almost 252 545 € was obtained for only one year, meaning that even with regular cleaning, for a period of 10 years running, almost 2.5 M€ are expected to be lost due to soiling.

In the future a deeper analysis of the particles that adhere to the mirrors will be made, covering the year, to have a better perception on how coatings' performance behave with different environmental conditions.

5.6 Conclusions

In this Chapter, the effect of rain for coated samples is not so substantial in reducing soiling as in the uncoated ones, thus, regular cleaning is recommended. However, more experiments need to be done during the rainy season to evaluate this characteristic. After cleaning, the 45° tilted mirror with coating shows the lowest value for the soiling index, especially position (3), meaning the RIOGLASS anti-soiling coating should work very well for tilted platforms, due to the photocatalytic properties. This coating also appears to wear off less than the uncoated mirrors, being more durable and allowing a better mirror reflectance recovery after 4 months of exposure. However, more experiments need to be performed to evaluate this phenomena. The amount of soiling in the agricultural area of Herdade da Mitra in Évora is not very significant, but still affect the mirrors' reflectance, especially in the hot Summer days, resembling almost the climate of Northern African countries. When the soiling index is higher, environmental factors such as air humidity and morning dew are very relevant in the deposition and agglomeration of particles and should be taken into account for the soiling effect. A simple economic analysis shows that this coating can be an upgrade to the existing cleaning passive technologies increasing profitability.

The work in this Chapter will result in the following publication:

- D. Lopes, R. Conceição, H. G. Silva, J. Mirão, G. Pérez, E. Araanzabe, M. Collares-Pereira, Evaluating of the effect of an anti-soiling coating on the reduction of CSP mirrors dirtiness, Solar Energy (2019). Submitted.

6

Conclusions

6.1 Conclusions

This Chapter summarizes the results obtained in the entire work, as well as, final remarks about the topics discussed. The author has committed in his PhD. thesis to study the soiling effect in both PV and CSP technology. Concerning these topics, Chapter 2 contains information not only about soiling effect due to two different types of events (long-range transport of Saharan dust and spring), but also a complete yearly analysis of soiling effect on PV technology. Modeling was also carried out, always with the purpose of understanding how environmental parameters, like relative humidity, wind speed, air temperature, among others, influence particle deposition and therefore affect PV performance.

In Chapter 3, a similar procedure used for PV was employed for CSP, resulting a full year campaign, in which soiling effect in a plain mirror was studied. As in the Chapter 2, not only soiling effect was studied, but soiling rates and modeling, as well. Furthermore, the beginning of a collaboration between REC and

IRESEN, which represents a significant advance in terms of soiling studies, is another achievement presented in this thesis and for the future. Usually, these studies are done for a single location, but to be able to compare two sites, using the same instruments, methodology and having the opportunity to deepen the understanding of Saharan desert dust events, is beyond expectation.

Regarding mitigation techniques, Chapter 4 presents an algorithm which has been used and extended to understand how soiling can modify the regular used optimum tilt angle for PV, which is usually calculated based on irradiance. The results show that modifying this angle can lead to better PV performance without cleaning or, at least, reducing the cleaning needs. Moreover a multiple tilt angle analyses was performed with soiling included, to check how many position throughout the year should be used to achieve maximum power production. An economic analysis was also carried out to complete the multiple tilt angle study, in which the best configuration is chosen based on a trade-off between energy produced and capital invested.

Following the same logic, a mitigation technique was also studied for CSP, namely for Fresnel and Tower, due to the plain mirror used in Chapter 5. The initial objective was to use simple anti-soiling coatings, which usually are sold as sprays. However, there was a unique opportunity to test an imbued coating in the mirror, from an industrial partner, Rioglass, which is one of the world biggest producers of mirrors for CSP applications. This study was also using the TraCS sensor, as well as, the glass tree shown in Chapter 2 with some modifications. It was observed that these coatings can be a tool to reduce soiling, however they usually need some water so their hydrophobic/hydrophilic capacities can produce the desire effect. Nevertheless, more tests need to be performed in order to evaluate its performance during the rainy season, compared to uncoated mirrors.

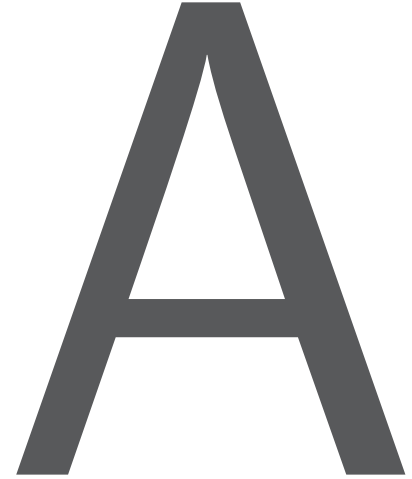
This thesis includes everything the author has proposed himself to and more. From a engineering and field working point of view, the objectives were also fulfilled. From the designs of the glass tree in AutoCAD, to its construction and field deployment, as well as, field work with I-V curve trace, PV modules, Sun Tracker, TracS installation, data logger and data pre-processing, processing and post-processing, the author has gained invaluable skills.

From a scientific point of view, the author counts with already several publications since its Master degree thesis. During the period, which includes the thesis preparation and elaboration, the author counts with 9 peer reviewed articles, in which 8 are presented in this thesis (2 of them in the appendix). Besides the importance of these studies for the region and country, which for the author best knowledge are the first, they were published in recognized and renowned journals like *Solar Energy*, *Solar Energy Materials and Solar Cells*, *Energies* and *Renewable Energies*. Besides these scientific work, the author has also participated in other publications, which are out of the scope of this thesis, such as:

- F. Carapau, P. Correia, L.M Grilo, R. Conceição, Axisymmetric motion of a proposed generalized non-Newtonian fluid model with shear-dependent viscoelastic effects, *Int. J. Appl. Math.* 47 (2017) 361–372.

- F. Carapau, R. Conceição, Three-Dimensional Velocity Field for Blood Flow Using the Power-Law Viscosity Function, *WSEAS: Transactions for Heat and Mass Transfer*, 12 (2018) 35–48.
- F. Lopes, R. Conceição, T. Fasquelle, H. G. Silva, R. Salgado, P. Canhoto, M. Collares-Pereira, Short-term Forecasts of DNI from the Integrated Forecasting System (ECMWF) for Optimized Operation Strategies of a Central Receiver System, *Appl. Energy*, (2019), under review.
- F. Lopes, R. Conceição, H. G. Silva, R. Salgado, P. Canhoto, M. Collares-Pereira, Predictive Value of Short-term Forecasts of DNI for Solar Energy Systems Operation, *SolarPACES* (2018), accepted for publication.

The author hopes that his contributions for this field will be important and useful for Solar Energy in the present and in the future.



Multiple tilt angle configuration table

Table A.1: Optimum tilt angles, effective energy and gain comparison between different configurations for the respective periods. The first column in Table A.1 has all the possible combinations of configurations (e.g. 1 angle, 2 angles) with the tilt angles for both soiled and clean scenarios, β_C and β_S , on column two and three, respectively. The fourth and fifth columns correspond to the respective periods for each of the optimum tilt angles in each configuration, for clean and soiled scenarios, respectively. The sixth and seventh columns correspond to the effective energy in each configuration, for both clean and soiled models, respectively. The eighth column corresponds to the effective energy gain for each soiled configuration regarding the soiled fixed one.

Nº tilts	β_C (°)	β_S (°)	Month _C	Month _S	E_{eff}^C (kWh/m ²)	E_{eff}^S (kWh/m ²)	R_{SS} (%)
1	34	40	1-12	1-12	1843	1617	-
2	51	52	1-3 & 9-12	1-4 & 9-12	1911	1670	3.2
	17	24	4-8	5-8			

APPENDIX A. MULTIPLE TILT ANGLE CONFIGURATION TABLE

3	50	51	1-3	1-4	1912	1671	3.3
	17	26	4-8	5-9			
	51	59	9-12	10-12			
4	50	51	1-3	1-4	1918	1679	3.8
	17	20	4-8	5-7			
	36	36	9	8-9			
	57	59	10-12	10-12			
5	57	58	1-2	1-2	1922	1682	4.0
	39	45	3	3-4			
	17	20	4-8	5-7			
	36	36	9	8-9			
	57	59	10-12	10-12			
6	57	58	1-2	1-2	1926	1683	4.1
	32	45	3-4	3-4			
	13	20	5-7	5-7			
	23	36	8	8-9			
	36	54	9	10			
	57	63	10-12	11-12			
7	57	58	1-2	1-2	1928	1684	4.1
	39	45	3	3-4			
	26	20	4	5-7			
	13	33	5-7	8			
	23	41	8	9			
	36	54	9	10			
	57	63	10-12	11-12			
8	57	58	1-2	1-2	1928	1685	4.2
	39	45	3	3-4			
	26	22	4	5-6			
	13	16	5-7	7			
	23	33	8	8			
	36	41	9	9			
	50	54	10	10			
	62	63	11-12	11-12			

9	61	58	1	1-2	1928	1685	4.2
	54	41	2	3			
	39	49	3	4			
	26	22	4	5-6			
	13	16	5-7	7			
	23	33	8	8			
	36	41	9	9			
	50	54	10	10			
	62	63	11-12	11-12			
10	61	58	1	1-2	1928	1686	4.2
	54	41	2	3			
	39	49	3	4			
	26	18	4	5			
	15	25	5	6			
	12	16	6-7	7			
	23	33	8	8			
	36	41	9	9			
	50	54	10	10			
	62	63	11-12	11-12			
11	61	62	1	1	1928	1686	4.3
	54	55	2	2			
	39	41	3	3			
	26	49	4	4			
	15	18	5	5			
	12	25	6-7	6			
	23	16	8	7			
	36	33	9	8			
	50	41	10	9			
	60	54	11	10			
	64	63	12	11-12			

12	61	62	1	1	1929	1687	4.3
	54	55	2	2			
	39	41	3	3			
	26	49	4	4			
	15	18	5	5			
	10	25	6	6			
	13	16	7	7			
	23	33	8	8			
	36	41	9	9			
	50	54	10	10			
	60	61	11	11			
	64	65	12	12			

B

Knowledge developed for the work in the thesis - 1

B.1 Introduction

Atmospheric electricity has been suggested as a promising tool for studying convection in the planetary boundary layer (PBL), e.g. [131, 132, 133]. The key concept in this context is the turbulent transport of space charge [134], where space charge is defined as the difference between positive and negative charge carriers, usually divided into two categories: small ion clusters and charged aerosols. As the small ion clusters (with sizes around 10 nm) have higher electric mobility, it is usual to consider them as the most important charge carriers in the atmosphere [135]. Thus, space charge density (ζ) is normally simplified to:

$$\zeta = n_+ + n_-, \quad (\text{B.1})$$

where n_+ and n_- are the concentrations of positive and negative small ion clusters, respectively. When an excess of negative ions occurs, ζ is negative and negative values of the atmospheric electric potential gradient (PG^1) are measured [60], while in the case of an excess of positive ions, positive values are observed. This makes potential gradient sensitive to the turbulent transport of space charges; these are, in fact, responsible for short-term potential gradient fluctuations (in the frequency range from ≈ 0.01 to ≈ 10 Hz), e.g., [132, 137]. It is important to mention that potential gradient is a result of the global electric circuit (GEC), being charged in shower clouds and thunderstorm active regions and discharged in poorly conductive fair-weather regions, (e.g., [138, 139]). In this way, GEC imposes a vertical electrical current between the ionosphere and the Earth's surface, generating the steady-state potential gradient through Ohm's Law. Therefore, GEC dynamics generates a global variation of the potential gradient that has its most recognized feature in the Carnegie curve [140]. In contrast, processes occurring within the PBL tend to have a local influence on the potential gradient. An example of this is the effect of anthropogenic pollution, which tends to increase the potential gradient by ion scavenging of pollutant aerosols [59]. Even so, scarce co-located observations of the PBL and electric parameters have been reported. One such account was made in [141], where for the first-time co-located measurements of clouds and aerosols (using a laser cloud-base recorder) and the potential gradient (using a field-mill) were performed. Nevertheless, potential gradient measurements were taken at 1 Hz, which is insufficient to capture a complete signature of turbulent processes (occurring up to 100 Hz, [142]). Another important reference can be found in [132], who combined a very well instrumented campaign (an array of eight potential gradient sensors, a sodar and meteorological measurements) with numerical modelling to show that dynamic and stability conditions of the PBL influence turbulent space-charge flows and the formation of electrostatic structures. In addition, they showed that generation of short-period electrostatic pulsations (in the range 0.001 to 1 Hz) occurs during the transition from stable to convective conditions in the PBL. This observation is in line with previous work, which showed that the sunrise perturbation of the potential gradient (referred to as the sunrise effect) was due to upward convective transport of accumulated positive space charge (electrode layer) in the surface layer during the night [143]. Recently, in [144], the authors went further by measuring high resolution vertical charge profiles at Alqueva, southern Portugal, and concluded that, after sunrise, the evolution of the charge profiles was consistent with the fact that charged ultra fine aerosols were lifted upwards by convection.

In this context, the present study aims, for the first time, to combine PBL backscatter measurements with high-frequency potential gradient (HFPG) measurements taken at 100 Hz, to infer the effect of strong and dry convection on the high-frequency potential gradient response. In fact, measuring and analyzing potential gradient at frequencies above 1-10 Hz (historically used sample rates) entails various challenges, such as the difficulty of storing the large amount of data generated, and most importantly the contamination due to the electric grid noise². Records were made during a five-day campaign during the summer of 2015

¹Potential gradient is related to the vertical component of the atmospheric electric field, E_z , by the relation, $PG = -E_z$, to guarantee positive values for potential gradient in fair-weather conditions as defined in [136]. The fair-weather days are selected for cloudiness < 0.2 , wind speed < 5 m s⁻¹, and the absence of fog or precipitation.

²Inspection of the signal spectra at least up to ≈ 50 Hz, meaning it is needed to measure at least ≈ 100 Hz.

in southern Portugal (nearly 100 km from Alqueva reservoir, [144]) in an electromagnetic quiet region. Besides backscatter and HFPG measurements, meteorological and AOD measurements were made. The campaign coincided with dry and strongly convective days.

B.2 Methodology

The observation station is in the centre of Évora (38.567 559° N, 7.911 411° W) with approximately 50 000 inhabitants, located in southern Portugal. The major sources of pollutants are due to anthropogenic activity (mainly traffic). Background pollution levels at the site are low (discussed below) in comparison to levels observed in a large metropolis, which produce a significant signature on the potential gradient records, e.g. [59]. Measurements were made during a summer campaign from 17 to 21 June 2015. The field-mill used, model JCI 131F shown in [145] and manufactured by Chilworth UK, was installed at the University of Évora campus (at 2 m height) with a few trees and two buildings in its surroundings (approximately 50 m away). The instrument was calibrated in December 2013 and recent work reveals a flat spectral response up to frequencies of approximately 100 Hz [146]. This fact makes the device suitable for the study of high-frequency electrical phenomena. The ceilometer used is a Vaisala CL31 instrument, installed at the same site, which operates using a pulsed laser of 910 nm wavelength and monostatic optical configuration enabling accurate results at low altitudes [147]. The ceilometer uses a lidar technique to determine the backscatter coefficients obtained from the signals returned by atmospheric scatter interacting with the collimated beam of near-infrared radiation emitted by the laser device equipping the instrument. The backscatter profile is determined with a vertical resolution of 10 m between the surface and roughly 7.5 km height, every 10 s. The CL31 instrument allows simultaneous detection of up to three layers of clouds. A Cimel CE-318 sun photometer, included in the AErosol RObotic NETwork (AERONET) network [148], was used for spectral AOD measurements, which represent the solar radiation extinction due to aerosol loading in the atmospheric column. Two wavelengths were used: 870 nm (A_{870}) and 440 nm (A_{440}). Air temperature was retrieved (every min) using a thermo-hygrometer (Thies Clima) and wind speed with a switching anemometer (Vector Instruments) both at 2-m height. GHI was measured using an Eppley pyranometer (model 8-48) and 10-min averages recorded. Finally, note that local summer time in the measurements location corresponds to UTC+1.

The experimental observations are complemented by simulations of the non-hydrostatic Meso-NH [149] atmospheric model v5.3 at 3-km horizontal resolution for the days of the campaign, over a domain of 102×130 grid points centred approximately at Évora. Initial and boundary conditions were obtained from the European Center for Medium-Range Weather Forecasts (ECMWF) operational analysis, updated every 6 hours. The deep convection is assumed to be explicitly resolved, but an eddy diffusivity with Kain-Fritsch scheme for shallow convection [150] was used and turbulence parametrized using the one-dimensional scheme of Cuxart et al. (2000). The fluxes between the surface and the atmosphere are computed using the SURFEX (*Surface Externalisée*) [151] and the ECOCLIMAP v2.0 [152] models updated by [153] for

southern Portugal.

It should be noted that this type of subject within atmospheric processes, time is usually represented in military hours and the same approach is used in this Appendix.

B.3 Results

The backscatter images retrieved by the ceilometer for the five-day campaign, 17 to 21 June 2015, are presented in Fig. B.1; apparently, days 17 to 19 June have almost no clouds or fog above the ceilometer. The wind speed < 5 m/s (Fig. B.2c) and global horizontal irradiance suggests almost clear skies (Fig. B.2d); this confirms the fair-weather criterion on those days. In contrast, day 20, and more so, 21 June appear to be contaminated by clouds, as observed in both backscatter and global horizontal irradiance (Fig. B.1 and Fig. B.2c, respectively). Moreover, all days of the campaign presented strong and dry convection confirmed by the ceilometer data, corresponding to intense convection that led to high PBL tops, above approximately 2 km (please see Fig. B.1). The low-level increased backscatter from aerosol (including those swelled by water moisture) present under the nocturnal inversion can be seen around 0000-0600 UTC and then 2100-0000 UTC. Sunrise initiates convection in the period of 0600-0800 UTC and develops during the following 2 h to form a strong and dry convective boundary layer, between 1000-2000 UTC. The PBL height reaches its maximum around 1500 UTC and starts to decrease around 1800 UTC; after 2000 UTC, the depth of the layer with high aerosol concentration is less than 1 km.

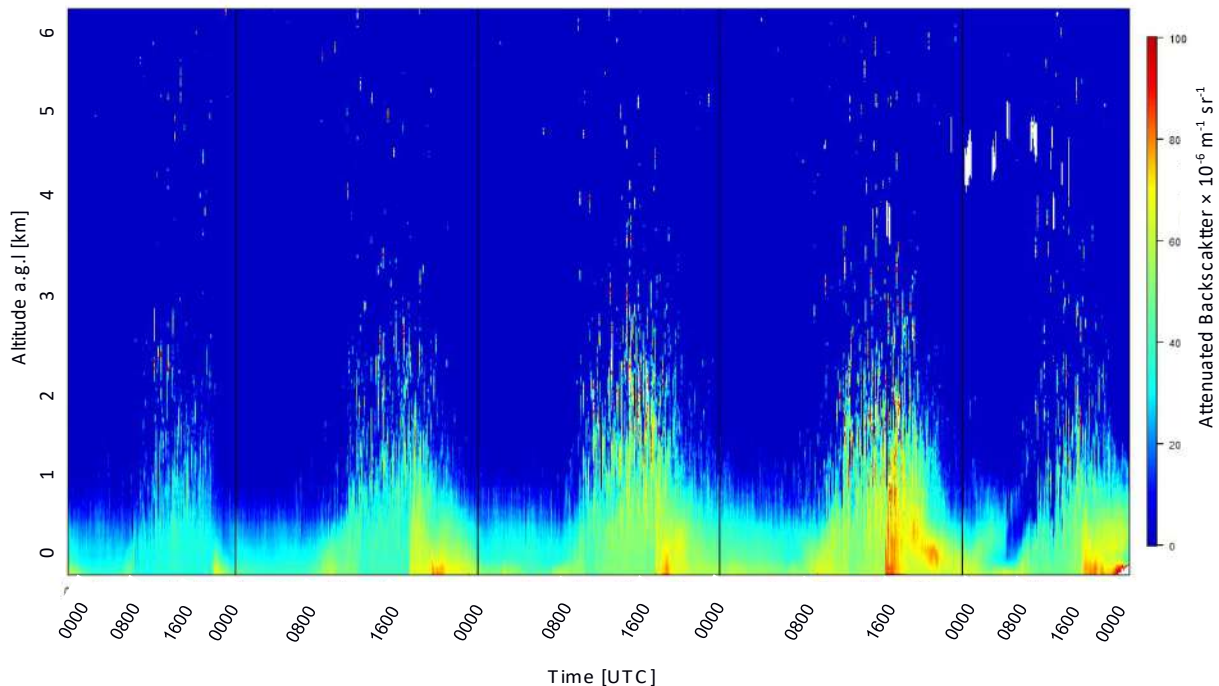
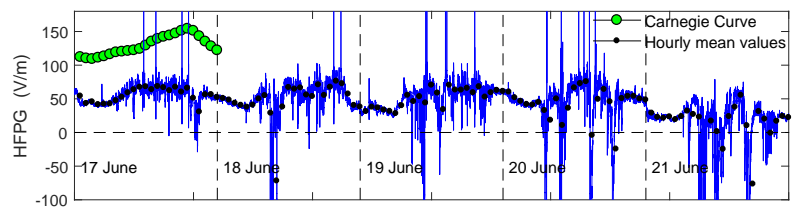
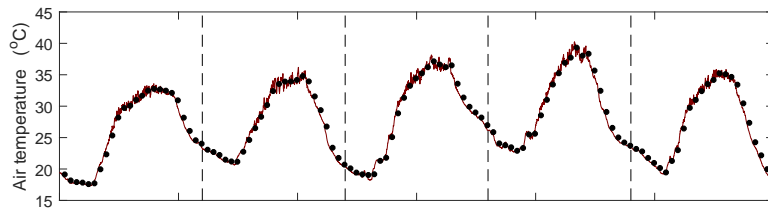


Figure B.1: Ceilometer backscatter as function of height for the entire campaign, 17 to 21 June 2015.

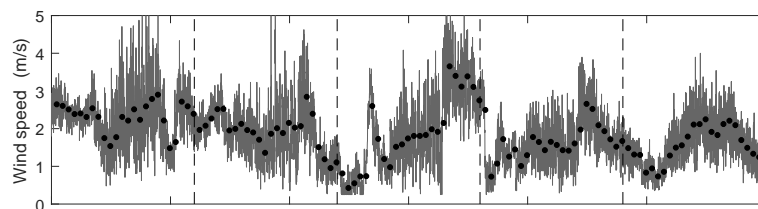
The measurements presented in Fig. B.2 for all the campaign, tend to behave in a remarkably similar way throughout this period. Coloured lines show raw data and the dots represent 1-h averages to highlight the daily behaviour of the five variables. In Fig. B.2a the HFPG taken at 100 Hz is shown, and it can be inferred that this varies essentially between 0 and 100 V/m; which is the normal range in Portugal in the absence of thunderstorms and/or heavy pollution [57]. Significant fluctuations, both positive and negative, appear during the day, namely between 0800-2000 UTC, corresponding to the period where the mixed layer is most active (please see Fig. B.1) and space-charge transport is more significant. As expected, the HFPG has its higher characteristic values around 1700-1800 UTC due to the well-known GEC planetary thunderstorm charging mechanism [138]. Green dots show the Carnegie curve, which indicates that the potential gradient is in phase with this reference curve when considering 1-h averages (black dots on Fig. B.2a). Hourly variations of the potential gradient show a broad minimum between 0200-0600 UTC and a broad maximum between 1600-2000 UTC, suggesting that the GEC is the primary driver for the daily evolution of the potential gradient. Lower potential gradient values at Évora station as compared with the Carnegie curve are attributed to the ionization from natural radioactivity that increases the electric conductivity of the air and reduces the potential gradient. Such ground-generated ionization is present at land stations (as is the case of Évora) and absent over the sea. Discussion on potential gradient deviations from the Carnegie curve can be found in [154]. The air temperature, T (Fig. B.2b) at Évora has the expected behaviour for clear-sky summer days at Évora, an increasing trend is observed around sunrise after approximately 0600 UTC, reaching a plateau, with approximately 2°C variability from 1500 until 1800 UTC, from which it starts to decrease coinciding with the PBL collapse. The air temperature, T reaches a maximum of approximately 35-40°C at low relative humidity (approximately 20 %, not shown) at 1500 UTC. In terms of wind speed, W_s (Fig. B.2c), reflects closely the PBL processes underway; a local W_s minimum is observed at approximately 0600 UTC, around sunrise, followed by a systematic increase through the day. In the late afternoon, approximately 1800 UTC, a sharp increase is found in the wind speed, probably associated with the arrival of the sea breeze from the west coast and the collapse of the convective PBL. After this maximum, W_s starts to decrease. The W_s remains below 5 m/s throughout the campaign. As mentioned above, global horizontal irradiance (Fig. B.2d) indicates almost clear skies from the 17 to 20 June, while 21 June appears to be contaminated by clouds. The daily evolution of the AOD for the two reference wavelengths considered (440 and 870 nm) is shown in Fig. B.2e, showing that AOD tends to increase in the morning, while remaining approximately stable during the rest of the day. As these measurements require sunlight, no records exist during the night (where a decrease in AOD is expected). It is also seen that AOD generally increases during the campaign, having an approximately constant value on the last day, 21 June. The increase in AOD values could relate to an increase in the surface aerosol load because of convection, in combination with other factors that transport aerosols aloft. These values are above the range of values for clean aerosol conditions, as defined by criteria in [79]: $A_{870} < 0.04$ and $A_{440} < 0.12$. Nevertheless, according to the same authors AOD values are consistent with a continental aerosol regime, characterized by $A_{440} < 0.3$ and represent typically 75 % of summer days. This fact excludes the influence of any significant aerosol event, such as forest fires or Saharan dust storms [60].



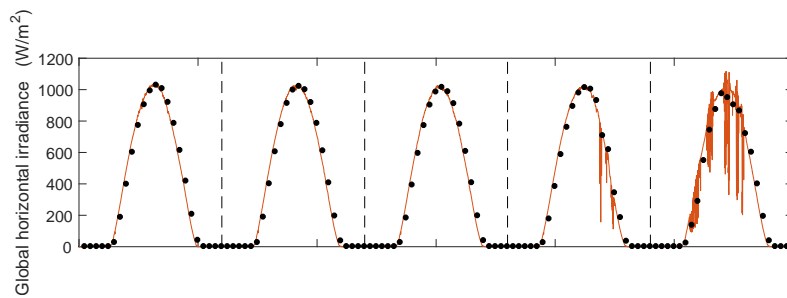
(a)



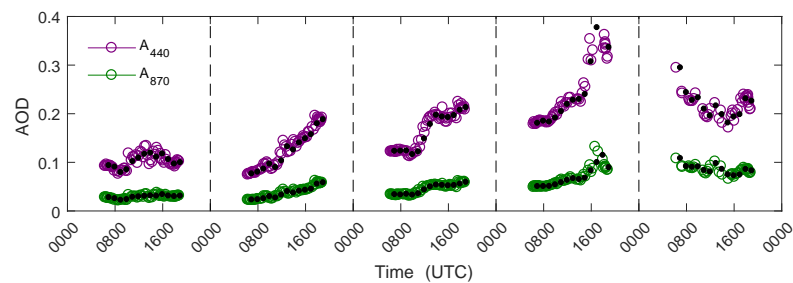
(b)



(c)



(d)



(e)

Figure B.2: Measurements made from 17 to 21 June 2015 campaign: (a) High-frequency potential gradient; (b) Air temperature; (c) Wind speed; (d) Global horizontal irradiance; (e) Aerosol optical depth (The black dots in the panels represent 1-h averaged values).

Spectrograms in Fig. B.3 were made using 10-sec data bins (corresponding to 1000 potential-gradient values) of HFPG with an overlap of 2 sec. On the one hand, persistent horizontal signals at approximately 50 Hz are due to the contamination from the electric grid and the constant narrow band signals around 20-30 Hz are likely to be aliased harmonics from the electric grid. No evidence of the typical frequencies corresponding to Schumann resonances can be seen, probably due to insufficient sensitivity resulting from the small aperture area of the field-mill. On the other hand, similar vertical features (for example, the spikes around 0800 UTC) are observed in the five days of the campaign, but highlighted on some days more than others, which requires further inspection, see below. It is expected that certain high-frequency excitations derived from turbulent transport of space charge occurs [155], chiefly during PBL strong and dry convection, as in the present case. Generically, it can be seen at approximately 0800 UTC, 1500 UTC and 2000 UTC that there is an increase of frequencies being excited across the accessible bands (approximately 0.01 to 50 Hz). The 1500 UTC excitation appears to be the strongest, opening the possibility for the existence of a relation between HFPG excitations and turbulence due to strong and dry convection observed during the campaign. To clarify the nature of the spectral transient peaks just mentioned, an inset to the figure is included in Fig. B.3, inset b, in which the spectrogram is zoomed around the spectral peak for 19 June, starting around 1000 UTC. The zoom shows the particularly complex pattern of the peak with a duration of almost 1 hour, and is incompatible with an impulsive source of noise, e.g., an electrical discharge, a rapid fluctuation on the electric grid, or even a fast bird passage. Moreover, the spikes in the spectrogram coincide with systematic negative excursions of the potential gradient, while positive ones tend not to contribute to those spectral transients. This coincidence can be confirmed in the inset c in Fig. B.3, which presents the same HFPG raw data with which the zoomed spectra of the inset b were produced. The colored arrows mark the same moments in both the spectra and the data; very good agreement is found. The observed trend points to the fact that these spectral spikes arise from the HFPG response to environmental perturbations, rather than due to erroneous data points. A more detailed analysis of the HFPG variability is considered.

In Fig. B.4a, the dashed black lines represent the standard deviation calculated for 30-min data bins (corresponding to approximately 180.000 values) of the 100-Hz potential gradient (σ_{PG}). The solid blue line represents data trends obtained through a locally weighted second-degree polynomial regression model, a robust loess smoothing at 5%, from 1-h averaged standard deviation of the potential gradient. All days of the campaign have high variability; in some cases, surpassing 150 V/m. Moreover, Fig. B.4a shows the gross tendency seen in the spectrograms. There is an increase of the standard deviation of the potential gradient after approximately 0800 UTC, reaching a maximum at approximately 1000 UTC, and at approximately 1600 UTC a local minimum occurs, with the standard deviation decreasing after the 1800 UTC maximum. The 21 June 2015 is slightly different from this tendency. To further relate the observed standard deviation of the potential gradient with convection, three parameters have been considered from the Meso-NH model for the days of the campaign: Richardson number (Ri), surface sensible heat flux (SHF), and the near-surface turbulent kinetic energy (TKE). Ri was calculated using

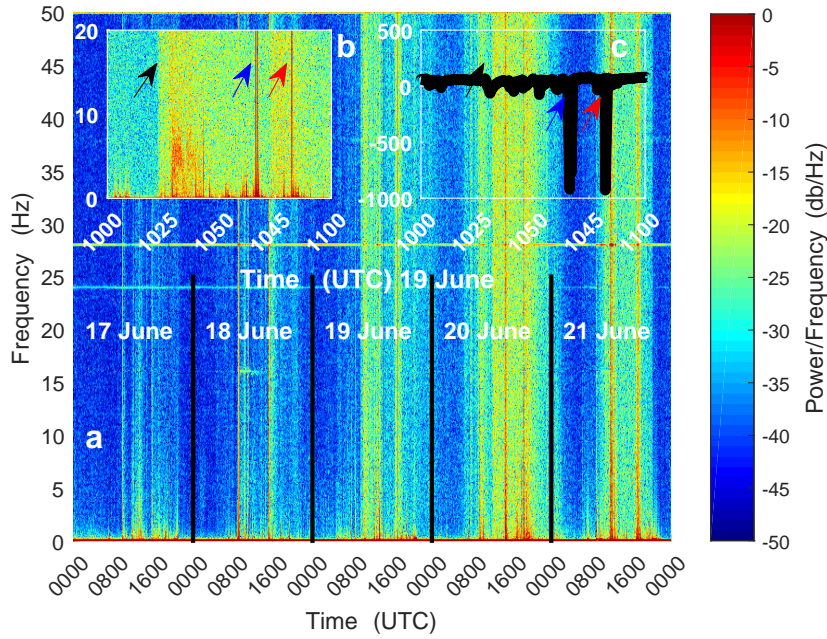
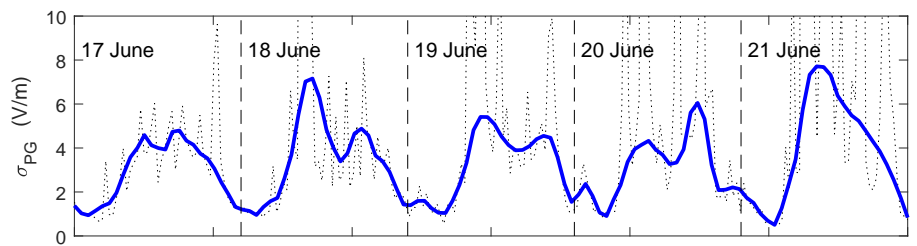


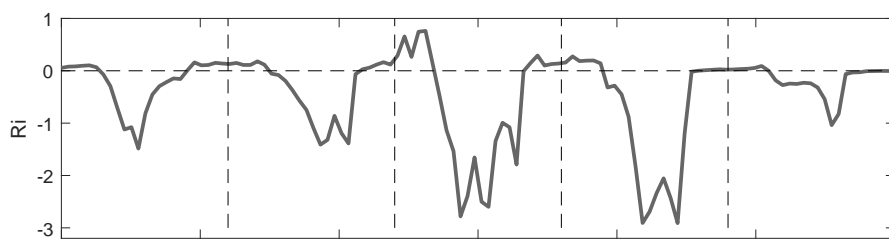
Figure B.3: (a) Spectrogram of the high-frequency potential gradient from 17 to 20 June 2015; (b) Inset showing a 1-h zoom of the spectral peak for the 19 June, starting around 1000 UTC; this shows the particularly complex pattern of the peak. (c) Inset showing the correspond *HFPG* values for the inset on (b). The coloured arrows in (c) and (d) mark the same moments in both the spectra and data.

$$Ri = gz \frac{\theta_v(z) - \theta_v(0)}{0.5 [\theta_v(z) + \theta_v(0)] V^2(z)}, \quad (\text{B.2})$$

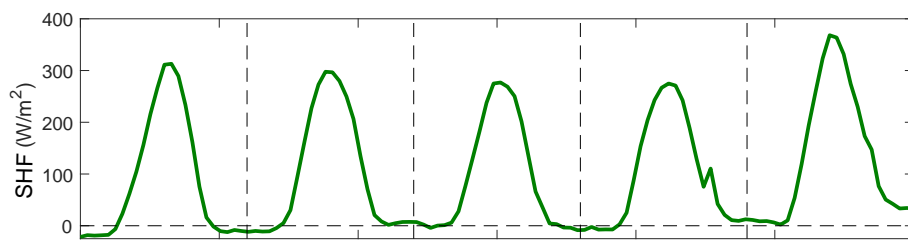
where z is the height of the first atmospheric level, g is the acceleration due to gravity, $\theta_v(z)$ and $\theta_v(0)$ are the virtual potential temperature at z and at the surface, respectively; $V(z)$ is the wind speed at z . As expected, the simulated Ri becomes negative during the morning (please see Fig. B.4b), indicating an unstable surface layer around noon, more pronounced on 19th and 20th, corresponding to days with weaker winds. During the periods of very negative Ri , convective transport in the surface layer is buoyancy driven. The evolution of the simulated SHF is shown in Fig. B.4c, where SHF can be interpreted as an indicator of the convective transport in the surface layer. At approximately 1500 UTC, SHF is at its maximum for all days of the campaign, implying that vertical velocity is a maximum too. As a matter of fact, SHF values show that convection commences at 0800 UTC, has a maximum at approximately 1500 UTC, and decreases until 2000 UTC; consistent with previous discussion on backscatter, please see Fig. B.1. SHF values are similar for 17 to 20 June, having higher values on the 21 June, probably due to the presence of stronger winds, even under a less thermal unstable environment (less negative Ri). The analyzed Meso-NH model TKE at the lowest atmospheric level (closest to the surface) is shown represented in Fig. B.4d. Its evolution follows that of SHF , showing that during the present case study the buoyant production of TKE predominates. However, Fig. B.4d also shows an increase in TKE in the late afternoon due to an increase in wind speed and wind shear.



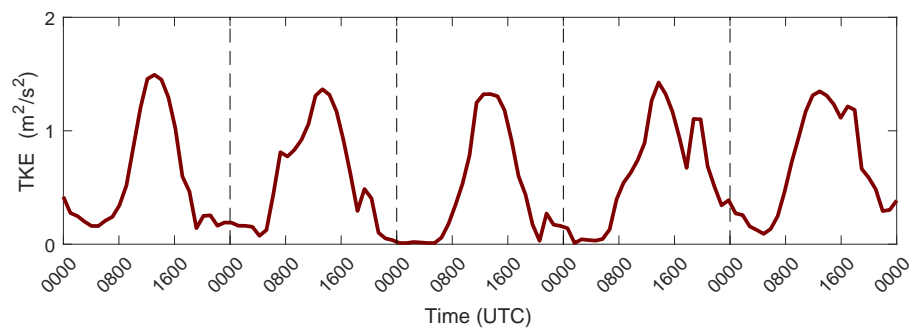
(a)



(b)



(c)



(d)

Figure B.4: (a) Standard deviation of high-frequency potential gradient (σ_{PG}); (b) Richardson number (Ri); (c) Surface sensible heat flux (SHF); (d) Turbulent kinetic energy (TKE).

To quantify the relation between the HFPG excitations, the standard deviation of the potential gradient represented in Fig. B.4a, and the simulated parameters related with convection, Pearson correlations were calculated for these parameters. The results are presented in Table B.1, where the standard deviation of the potential gradient generally correlates better with *SHF* and *TKE* than with *Ri*. A tendency for lower correlation values on the 20 June and higher on the 21 June is found for the standard deviation of the potential gradient, and both *SHF* and *TKE*, while for the standard deviation of the potential gradient and *Ri* the lower absolute value is observed on 18 June and the higher absolute values on the 19 June (dominated by thermal convection). Moreover, the fact that both *SHF* and *TKE* have higher absolute correlation values with the standard deviation of the potential gradient than *Ri* implies that the HFPG variability is sensitive to convection independent of its origin. This is especially apparent on 21 June, characterized by turbulence from both thermal and dynamical mechanisms, but still with the higher correlation between the standard deviation of the potential gradient and *SHF*, please see Fig. B.1. In fact, from the evolution of the daily relation of these two parameters, it can be appreciated that there is an increase (decrease) in the Pearson correlation with increased (decreased) convection. Correlation is especially high on 21 June (the day with more intense convection) reaching approximately 0.94 (p -value < 0.0001), confirming the association between HFPG and PBL convection. In line with these results, the same tendency is observed for the correlations of the standard deviation of the potential gradient and *TKE* and on 21 June, it reaches approximately 0.9241 (p -value < 0.0001); which further demonstrates the close association between these two parameters.

Table B.1: Daily correlation coefficients and the respective p -values in parentheses for the five days of the campaign relating standard deviation of the high-frequency potential gradient (σ_{PG}) with, (a) Richardson number (*Ri*), (c) near-surface sensible heat flux (*SHF*), (d) turbulent kinetic energy (*TKE*)

Correlation coefficients (p-value)	17 June	18 June	19 June	20 June	21 June
$\sigma_{PG} - Ri$	-0.6150 (0.001)	-0.5590 (0.005)	-0.7176 (<0.0001)	-0.6150 (0.001)	-0.5980 (0.002)
$\sigma_{PG} - SHF$	0.7979 (<0.0001)	0.7637 (<0.0001)	0.7183 (<0.0001)	0.6094 (<0.0001)	0.9448 (<0.0001)
$\sigma_{PG} - TKE$	0.7410 (<0.0001)	0.6848 (<0.0001)	0.7324 (<0.0001)	0.6422 (<0.0001)	0.9241 (<0.0001)

B.4 Discussion

Low-level increased backscatter from aerosol present under the nocturnal inversion is seen on our observations around 0000-0600 UTC and at 2100-0000 UTC (Fig. B.1) and the stable conditions prevent significant turbulence, giving low variability in HFPG (Fig. B.4a), consistent with positive *Ri* (Fig. B.4b). Sunrise initiates significant turbulence near to surface due to convection (Fig. B.4c), leading to the formation of a convective boundary layer, which gradually grows into the residual layer of the previous day, breaking

through it in the late morning, see Fig. B.1. At this stage, the near-surface space charge (atmospheric ions and charged aerosols), increasing during the night, ascend from the surface and trigger the largest pulse of space charge of the day, with significant positive-to-negative HFPG spikes around 1000 UTC (Fig. B.2a). Such spikes are also revealed by the broadband (up to 50 Hz) excitation of frequencies on HFPG spectrogram (Fig. B.3) and a considerable increase in the standard deviation of the potential gradient (Fig. B.4a). An increase in *SHF* values is observed at a similar time, reinforcing a link between the negative HFPG spikes and convection initiation. This process can be explained essentially by the elevation and erosion of the nocturnal electrode layer [156] under the influence of convection, in which the rapid upward displacement of negative space charge within the convective plumes reduces the potential gradient considerably in relation to its typical value for this time of the day (approximately 50 V/m).

Space charge is then transported by numerous convective plumes throughout the day, producing an increased standard deviation of the potential gradient (Fig. B.4a). Around 1500 UTC the convective process is at its maximum as can be seen by the backscatter data (Fig. B.1) and confirmed by both *SHF* and *TKE* values (Fig. B.4c and Fig. B.4d, respectively). At such time, all surface space charge should be aloft and being transported to higher altitudes (above 1 km); space charge would essentially be composed of easily transported small cluster ions. This implies that the space charge might form an elevated layer in which charge distribution changes rapidly from positive to negative, causing significant positive-to-negative fluctuations in the HFPG (Fig. B.2a) associated with the initial development of convective plumes over the site. Such fluctuations would generate HFPG spectra excitations (Fig. B.3) and increase the standard deviation of the potential gradient (Fig. B.4a). The charge variability should then be associated with the translation of eddies containing different space-charge densities, but displacement of an elevated charge layer due to large eddies (thermal plumes) could also account for variability, although at longer periods of several seconds to minutes. After undergoing considerable mixing, the space-charge gradient will reduce, thereby reducing the relative intensity of charged eddies, and older space-charge parcels may recombine. Recombination, masking from space-charge parcels of different polarities and a weakening space-charge gradient, reduces the overall contribution of turbulent space charge to the potential gradient measured at the surface, weakening the HFPG fluctuations (Fig. B.2a).

After this, around 1800 UTC, air temperature starts to decrease (Fig. B.2b) and such reduction initiates the collapse of the PBL (Fig. B.1); confirmed by the reduction in the *SHF* values (Fig. B.4c). During this process, which lasts approximately 2 hours, air circulation in the lower levels of the PBL increases and aerosols being transported in that circulation increase the PBL backscatter of those levels (Fig. B.1). Air circulation also increases turbulent transfer of near-surface space charge and consequently negative spikes appear again in the HFPG (Fig. B.2a). This is reflected in excitations in the HFPG spectra (Fig. B.3) and may explain the observed local maximum of the standard deviation of the potential gradient around 1800 UTC (Fig. B.4a).

Stability increases after sunset, around 2000 UTC (Fig. B.4b), and at the same time the convective boundary layer collapses; *SHF* values are inverted from positive to negative (Fig. B.4c). This process

reduces the convective space charge and aerosol transport, while increasing relative humidity causes the aerosols to swell and become more confined to the surface. This can be seen by increased low altitude backscatter (Fig. B.1). The extinction of convective transport at 2000-0000 UTC results in a reduction of the standard deviation of the potential gradient and TKE (Fig. B.4a and Fig. B.4b, respectively).

To the authors best knowledge, this is the first time it is proposed the occurrence of a quiet HFPG variability period between the disequilibrium in the turbulent eddy structure, early in the day, as the boundary layer grows and, at the end of the day, as sensible heat flux is removed. It must be highlighted that 17 to 19 June 2015 are working days (Wednesday to Friday, respectively), while 20 and 21 June 2015 are non-working days (Saturday and Sunday, respectively). Though a bit more perturbed by clouds, similar results were observed for the non-working days in comparison to the working ones. The fact that all days show similar behaviour implies that these observed phenomena were not significantly influenced by anthropogenic activities occurring mainly during the working days (e.g., space charges emitted by vehicle gas exhaustion). No lightning activity was detected in the region, excluding thunderstorms as a source of HFPG.

B.5 Conclusions

The influence of strong and dry convection within the PBL on high-frequency fluctuations of the potential gradient is assessed using co-located measurements of PBL backscatter, meteorological parameters, and 100-Hz recorded potential gradient, as well as the numerically simulated Ri , SHF and TKE quantities using the Meso-NH atmospheric model v5.3. The results are consistent with the hypothesis that, under strong and dry convection, HFPG variability is closely associated with convective processes within the PBL. This is supported by the fact that the beginning and the end of strong convective layers show very good agreement with HFPG variability. Fair correlations are also found between the standard deviation of the potential gradient and Ri and significant correlations are found between the standard deviation of the potential gradient, SHF and TKE , corroborating the proposed link. HFPG variability during this investigation was not expected to be strongly influenced by anthropogenic factors. Atmospheric convection plays a decisive role on particle deposition, which is a major problem for solar energy plants, as soiling of the panels produces a substantial reduction in the plant efficiency [95, 37]. Future work should focus on the understanding of particle rise and deposition due to convection, using HFPG variability as a convection proxy.

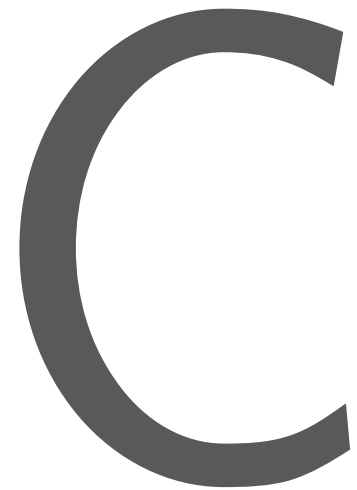
The work in this appendix resulted in the following publication:

- R. Conceição, H. Silva, A. Bennett, R. Salgado, D. Bortoli, M. Costa, and M. Collares Pereira, High-Frequency Response of the Atmospheric Electric Potential Gradient Under Strong and Dry Boundary-Layer Convection, *Boundary-Layer Meteorol.* (2017) 166:69.

It should be noted that in this work, a study about atmospheric variables and their relation to convection

was made, which made easier to study environmental effects on soiling, which is a matter within the following publications presented in this thesis:

- R. Conceição, H.G. Silva, J. Mirão, M. Gostein, L. Fialho, L. Narvarte, M. Collares-Pereira, Saharan dust transport to Europe and its impact on photovoltaic performance: A case study of soiling in Portugal, *Sol. Energy*. 160 (2018) 94–102.
- R. Conceição, H.G. Silva, M. Collares-Pereira, CSP mirror soiling characterization and modeling, *Sol. Energy Mater. Sol. Cells*. 185 (2018) 233–239.



Knowledge developed for the work in the thesis - 2

C.1 Introduction

Dust storms have been receiving significant attention in the past decades (e.g., [157]), among different roles, because of their impact on the planetary radiative forcing and its relevance to the Earth's climate. Though little information has been collected on dust electrification (e.g. [158, 159]), the interest has been raised recently due to its importance in two main areas: energy systems and planetary exploration. In the former, dust electrification can have technological importance since it is of great usefulness in the development of automatic electrostatic dust particle removal for solar energy systems, as it was used on NASA's lunar missions [160]. This technological improvement on Earth will permit the increase of the efficiency of solar energy systems while reducing water consumption in the cleaning activities of these systems

[161]. In the latter, the understanding of Martian dust devil electrification [162] is expected to be boosted by the ExoMars mission [163], which has deployed this year two payloads: Dust Characterisation, Risk Assessment, and Environment Analyser on the Martian Surface (DREAMS) and Micro Atmospheric Radiation and Electricity Sensor (MicroARES); these measuring instruments are expected to further contribute to the understanding of these phenomena on Mars. In fact, the ExoMars team is using Saharan dust storms as a way to comprehend Mars dust storms [164]. Those authors found evidence that the atmospheric electric field influences the dust-lifting process; dependent on the mineralogical composition of the dust and the atmospheric relative humidity [164]. Moreover, it is reported in [165] the electrification of haboobs in the Sahelian belt of West Africa. Measurements were made in the (source) region where the storms developed and significant electric perturbations were found only under heavy dust loads (high concentration of large sized particles) exhibiting in most of the occurrences strong and negative unipolar electrification (absolute electric fields of $\approx 1\text{-}10$ kV/m). These observations are similar to Kamra's measurements [166], in which the author states that most of the dust storms dominated by clay minerals tend to produce negative space charges in the source region. Nevertheless, debate still exists on either the negative electrification comes from clay minerals (dust) or quartz minerals (sand), [165].

Many open questions also exist on the way space charge generated in the source region behaves under long-range transport. In principle, only small particles (e.g., clay particles with size ranges from 1 to $10\ \mu\text{m}$) can be transported and according to previous observations of negative clay electrification, negative perturbations in the electric fields would have to be found away from the source region. Even so, the work of Reiter and co-authors [167] seems to contradict this. The author has shown that during a Saharan dust outbreak that reached the Zugspitze Peak (Germany), a positive space charge density (SCD) at ≈ 3 km altitude was formed two times larger than in normal clean conditions. Tropospheric LIDAR measurements showed that the dust layer was co-located with the space charge density around ≈ 3 km and chemical aerosol analysis showed that sand particles were dominant with significant increased concentrations of SiO_2 and Al_2O_3 . More recently, balloon-borne charge measurements of Saharan dust layers (up to 4 km) have been made in the Cape Verde Islands, where Saharan dust outbreaks are frequently transported to. The experiment depicted a maximum absolute charge density of ≈ 25 pC/m³ [168]. From background conductivity considerations any dust charge generated during lofting in the source region should have decayed long before reaching Cape Verde [168] and consequently no long-range electrification would be observable. For that reason, the authors argued that a possible mechanism to explain long-range dust charging was due to the vertical air-Earth electric current, imposed by GEC, flowing through the atmospheric electric conductivity gradient inside the dust layer [169]. The atmospheric electric conductivity gradient is a consequence of small ion scavenging by dust particles, in which the ion-particle attachment process charges dust particles (with low electrical mobilities) that significantly decrease electric conductivity ([159]) and generates the conductivity gradient. In principle, the action of the air-Earth current would then create a positive space charge at the top of the dust layer and a negative space charge would be generated by mirror charges, forming a bipolar charge distribution. The overall charge of the dust layer would be a result from the net charge of this bipolar distribution.

Previous work on the long-range dust electrification has been focused on a single measuring site where PG was recorded (e.g., [170]). Nevertheless, recent efforts in atmospheric electricity concern the development of arrays of PG field-mills in large time (≈ 1 hour) and space scales (≈ 100 km), as it is the case of the network installed in South America [154] and the one under development in Europe (COST Action 15211: Atmospheric Electricity Network). The existence of such networks raises the possibility of coordinated PG measurements to track atmospheric phenomena such as smoke plume transport, known to affect PG measurements [57]. In this context, an experiment was conceived and undertaken during the ALqueva hydro-meteorological EXperiment (ALEX2014): alex2014.cge.uevora.pt. The experiment consisted on the installation of three similar PG field-mills, in Southern Portugal, forming a triangular array that allowed the recording of PG time series during a three-month period, from June to August 2014. This period corresponds to the summer season in the northern hemisphere and represents a unique opportunity to perform such an experiment due to two main reasons: the frequency of occurrences of fair-weather days and the occurrences of isolated Saharan dust outbreaks transported over Africa to the measuring region (e.g. [171]; [172]). The use of arrays of sensors instead of single sensors allows regional perturbations to be distinguished from local ones and, contrary to previous thoughts on this matter, present efforts seem to encourage their use. The present work contributes to that view, adding to it the separation of short time-scale phenomena (below 1-day), more prone to local influences, e.g. cloud passage, and mid time-scale phenomena (above 1-day), more sensible to regional process, e.g. pollution.

This work is organized as follows: Section 2 describes the experimental setup, Section 3 outlines the Saharan dust event of July 16th-17th 2014; Section 4 presents the PG measurements during the ALEX2014 campaign; Section 5 discusses the results and a formulation is derived to reinforce the observations; and in Section 6 main conclusions along with recommendations for future work are given.

C.2 Measurement campaign

An equilateral triangle is formed by three JCI field-mills [145, 146], separated by nearly 50 km from each other, forming a triangular array of about ≈ 1000 km² in Southern Portugal (Fig. C.1a).

The geographic location of the three sites in which measurements of PG were conducted are: Évora (EVO) at 38.50 N, 7.91 W; Amieira (AMI) at 38.27 N, 7.53 W and Beja Airbase (BEA) at 38.07 N, 7.93 W. The EVO and BEA sites follow almost a North-South alignment, whilst AMI is more deviated to the East and is settled approximately in the mid-way of the other two sites. The EVO station is situated in the center of the city of Évora (≈ 50 000 inhabitants), where major sources of pollutants are due to anthropogenic activity such as traffic, heating (winter) and cooling (summer) air systems. In EVO, a JCI 131 was installed in the University of Évora campus (at 2 m height) with few trees and two University buildings in its surroundings (≈ 50 m away). The instrument was calibrated in 2012 and has been operating since 2005. The AMI station is located on the shoreline of the Southern part of the Alqueva reservoir (currently



(a)



(b)



(c)



(d)



(e)

Figure C.1: Geographic location of the three sites used for measurements of atmospheric electric potential gradient and HYSPLIT backward trajectories for Evora, Amieira and Beja: (a) Geographic location of the three sites used for measurements of atmospheric electric potential gradient; (b) Backward trajectories for 15th July 2014; (c) Backward trajectories for 16th July 2014; (d) Backward trajectories for 17th July 2014; (e) Backward trajectories for 18th July 2014 (red trajectories correspond to particles arriving at altitudes of 2 km, blue ones to 2.5 km and green ones to 3 km. The white rectangle represents the zoom-in appearing in the upper-panel).

one of the largest man-made lake in western Europe), set upon a hill approximately 30 m above the lake water level, with low vegetation in its surroundings [173]. The BEA station is located further south on an air base in the outskirts of the small city of Beja ($\approx 40\,000$ inhabitants). In AMI and BEA two identical field-mills JCI 131F were used and installed as well at 2 m height above the ground. Measurements in the three sites were made every second and 1-minute average values recorded. A quality control criterion for the raw data was used, and values within the precision threshold of the field-mills ($\approx |1|$ V/m) were rejected. This allows the removal of values that correspond to equipment malfunction and/or maintenance, such as when a field-mill stops operating but the data logger continues to record.

The characterization of the aerosol conditions in the region was based on the AERONET station located at EVO. An automatic sun tracking photometer (CIMEL CE-318-2) is operated to measure aerosol optical depth at several wavelengths in the range of 340-1640 nm. AOD is a measure of the solar radiation extinction due to the aerosol load present in the atmospheric column; more details can be found in [148]. The spectral dependence of the optical depth defines the Angstrom Exponent (AE) based on the ideas developed by Angström in [174]. AE provides information on the size distribution of the aerosol population (i.e., aerosol fine and coarse modes relative proportion). When coarse particles are in large proportion in the aerosol population, AE tends to be low, i.e., lower than 1. AOD and AE data can be retrieved from the AERONET webpage: aeronet.gsfc.nasa.gov

Finally, solar radiation curves (technical definition being global horizontal irradiance, GHI) were measured in EVO station with a 10 minutes rate using an Eppley pyranometer (model 8-48).

C.3 Desert Dust Transported into Southern Portugal

It is shown in Fig. C.1b to Fig. C.1e a set of HYSPLIT backward trajectories for the 15th, 16th, 17th and 18th July 2014, respectively. HYSPLIT can be found here: ready.arl.noaa.gov; details of the theory behind the model can be found in [80]. Red trajectories correspond to particles arriving at altitudes of 2 km, blue ones to 2.5 km and green ones to 3 km. These altitudes are selected according to the typical altitudes at which Sahara desert dust arrives at Southern Portugal [172]. Four day backward trajectories ending at 12 UTC were considered for the three days. The most important feature in these figures is the transition from Eastward trajectories on the 15th July, bringing clean air from the Atlantic Ocean, to Southward trajectories on the 16th-17th July, bringing dust from the western part of Sahara Desert. The 16th-17th July backward trajectories are persistently over Moroccan territory, in the western part of the Sahara Desert, which triggered the transport of dust towards the Iberian Peninsula. On the 18th July a reverse transition occurs and the Southward trajectories become Eastward trajectories as they were on the 15th July.

In Fig. C.2a the aerosol optical depth and Angstrom Exponent measured at Évora station. The measurements show a clear signature of dust on 16th-17th July, with a visible increase in the atmospheric turbidity (AOD increases from normal background levels of ≈ 0.1 to ≈ 0.3), and low wavelength dependence

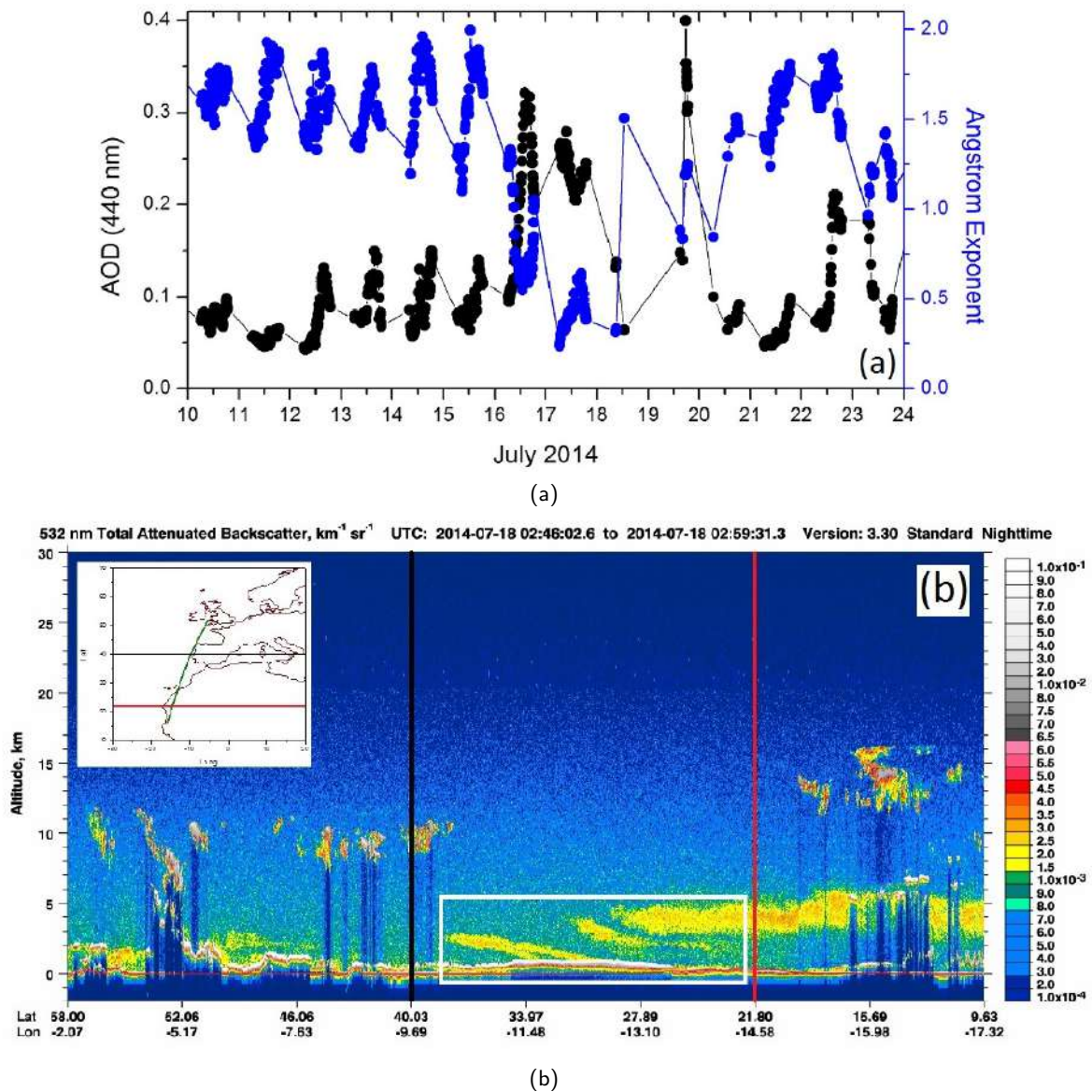


Figure C.2: Aerosol optical depth, at 440 nm, Angstrom Exponent and Attenuated backscatter profiles measured at Évora during July 2014: (a) Aerosol optical depth at 440 nm and Angstrom Exponent measured at Évora during July 2014; (b) Attenuated backscatter profiles from CALIOP aboard of CALIPSO for the dawn of 18th July (The inset shows the satellite path along which the profile was taken).

(AE decreases from typical values of ≈ 2 to ≈ 0.2), e.g. [171]. The combination of sun-photometer measurements and backward trajectories makes it clear that dust is present over the region under analysis. Satellite information was also retrieved from the Cloud-Aerosol Lidar and Infrared Pathfinder Satellite Observation (CALIPSO) satellite borne lidar, Cloud-Aerosol Lidar with Orthogonal Polarization (CALIOP) [175], data available at: eosweb.larc.nasa.gov. The CALIOP total attenuated backscatter (532 nm) profile for the dawn of 18th July is shown in Fig. C.2b. The respective depolarization profile (not shown here) confirms that these aerosols are of dust type. The inset shows in green the satellite path, the horizontal black line is above the latitude where the PG sensors were located and the red one points roughly the region

where the satellite path crosses the western part of the Sahara desert (the satellite path passes nearly 200 km westward of the array location). The backscatter profiles of the intersection points between the black and red lines with the satellite path are marked by black and red vertical lines, respectively, in the main picture. The figure shows the profile of the dust (evidenced by a greenish color on the depolarization ratio plots) along the satellite path on the western part of the Sahara desert at latitudes that go from $\approx 28^\circ$ to $\approx 18^\circ$. This confirms the discussion on the backward trajectories in which the dust is brought aloft at the western part of the Sahara. It is worth mentioning that the heights of the dust shown by CALIPSO are consistent with the heights shown in the trajectory plots.

Maps and dust profiles from the BSC-DREAM8b model (Dust REgional Atmospheric Model) based on the Barcelona Supercomputing Center are shown in Fig. C.3. Detailed description of the model can be found in the literature [176, 177, 178], whereas the data is freely available on the project webpage: bsc.es/projects/earthscience/BSC-DREAM/. The successive maps for 15th-18th July are shown between Fig. C.3a and Fig. C.3d, respectively, demonstrating that dust loads of $\approx 0.5 \text{ g/m}^2$ start to develop in the western part of the Saharan desert on the 15th July. The dust loads in that part of the desert increased on the following two days: 16th-17th July; then started to spread northeastwards towards Portugal. According to the model the dust outbreak reaches the location of the PG sensors on the 16th July, around 12 UTC, in agreement with the AERONET measurements shown in Fig. C.2a. On the 17th July the dust covers practically all Iberia with dust loads lower than $\approx 0.25 \text{ g/m}^2$. The following day, 18th July, shows that the dust load in the western part of Sahara desert continues to increase in certain regions ($\approx 1.5 \text{ g/m}^2$), although the dust is no longer over Portugal in the region of the PG sensors. The model dust profiles shown in Fig. C.3e confirms this point of view, with the height of the dust layer typically extending from the surface up to 3 km. On the 15th and 18th July there is effectively no dust and on the 16th July a dust layer develops from 0.5 km in altitude up to 2.5 km, whereas on the 17th July the dust layer profile goes from 1 km to 3 km. On both days the maximum dust load is estimated to be $\approx 50 \text{ }\mu\text{g/m}^3$ – therefore a relatively weak desert dust outbreak. An interesting remark is the fact that the maximum diffuse solar radiance (technically diffuse horizontal irradiance, DHI) for EVO on the dust event days (16th-17th July) was $\approx 200 \text{ W/m}^2$, twice the value for 15th July, probably additional confirmation of the presence of the desert dust plume.

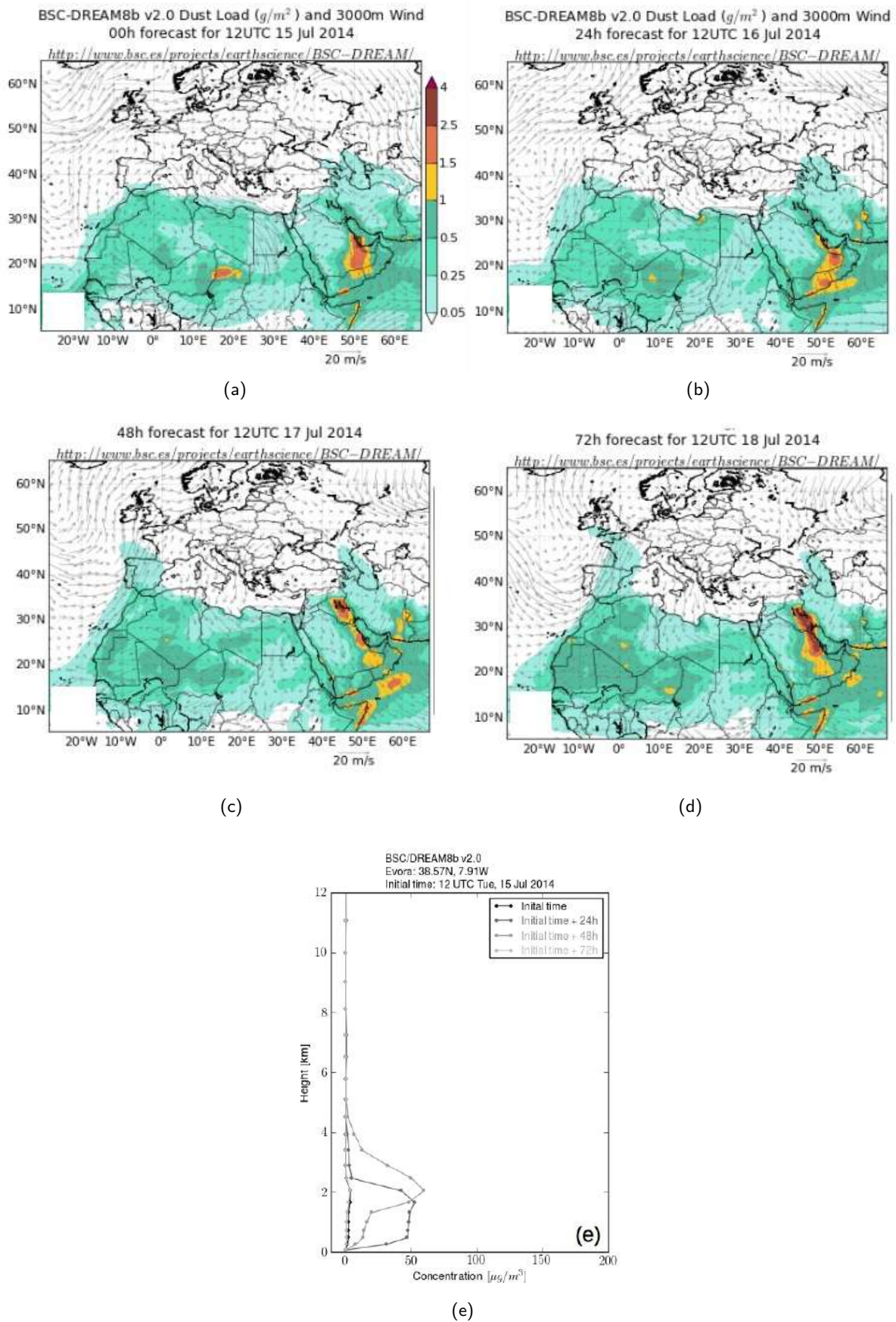


Figure C.3: BSC-DREAM8b maps of total dust load (g/m²) for: (a) 15th July 2014; (b) 16th July 2014; (c) 17th July 2014; (d) 18th July 2014; (e) Vertical dust profiles in which the black profile corresponds to 15th July and the fading grey runs from the 16th to 18th July.

C.4 Potential Gradient

This section intends to evidence PG perturbations, on 16th-17th July, as a result of the presence of the Saharan dust over Southern Portugal. If such perturbations are proved to be unique to the desert dust event, these might be interpreted as evidences of the long-range desert dust electrification and a model can be discussed (in the next section) to explain the observations. Three analyses are made to that end: (i) A daily analysis of the PG data for the three stations; (ii) A robust lowess (locally weighted linear regression) smoothing of the PG data for the three stations; (iii) A wavelet analysis over the 1-hour averaged PG data for the three stations.

C.4.1 Daily analysis

To examine possible short time-scale (below 1 day) effects of the Saharan dust on the PG measurements (as retrieved by the triangle of sensors), the daily variation in PG for each of the three sites is represented in Fig. C.4, Fig. C.5 and Fig. C.6, respectively for BEA, AMI and EVO. Dark blue rectangles mark the days of the dust event, 16th-17th of July, and the first and second dark red rectangles mark the day before, 15th July, and after the event, 18th July, respectively. The thick black lines in the plots represent the lowess smoothed mean daily variation (i.e., the mean daily cycle with a lowess curve superimposed) of the FW PG for the entire ALEX2014 campaign in the respective stations (used as comparison). A reference GHI curve was obtained by lowess smoothing the mean daily variation of six undisturbed GHI curves (7th to 12th July); correlation of the reference curve with the GHI curves for each day permitted the selection of Disturbed-Weather (DW) days, having correlations below 0.99, and Fair-Weather (FW) days, with correlations equal or above 0.99. This criterion could be calibrated with cloud cover data and a given cloud cover attributed to a given correlation, nevertheless, such procedure is out of the scope of the present manuscript. The indication of DW and FW appears in the lower-right corner of the PG panels in Fig. C.4, Fig. C.5 and Fig. C.6. It should be said that 16th-17th of July (the days of the dust event) appear to be FW days, what should rule out clouds or other disturbed meteorological phenomena as the cause for the possible PG perturbations on those days.

Moreover, BEA station data, Fig. C.4, shows that PG on the 15th July tends to follow the mean daily behaviour, as expected for a FW day, and a similar tendency occurs on the 16th July, despite the beginning of the dust event. On the 17th July, the day in which the dust event is fully developed (as confirmed by the AE in Fig. C.2a) evident perturbations on the PG take place between 8 and 10 UTC, in which the PG oscillates approximately around ± 200 V/m. Such sharp inversions are rare on FW days, as it is the case, and are usually attributed to cloud passage on DW conditions. In fact, similar oscillations are found in BEA, but for DW days, e.g., on the 23rd June and 29th July. The only FW day in which the PG perturbations resemble those of the dust event, 17th July, occur on the 28th July, in which the PG inversion goes down to approximately -120 V/m, but no oscillations are found. The unusual behavior of the PG supports the

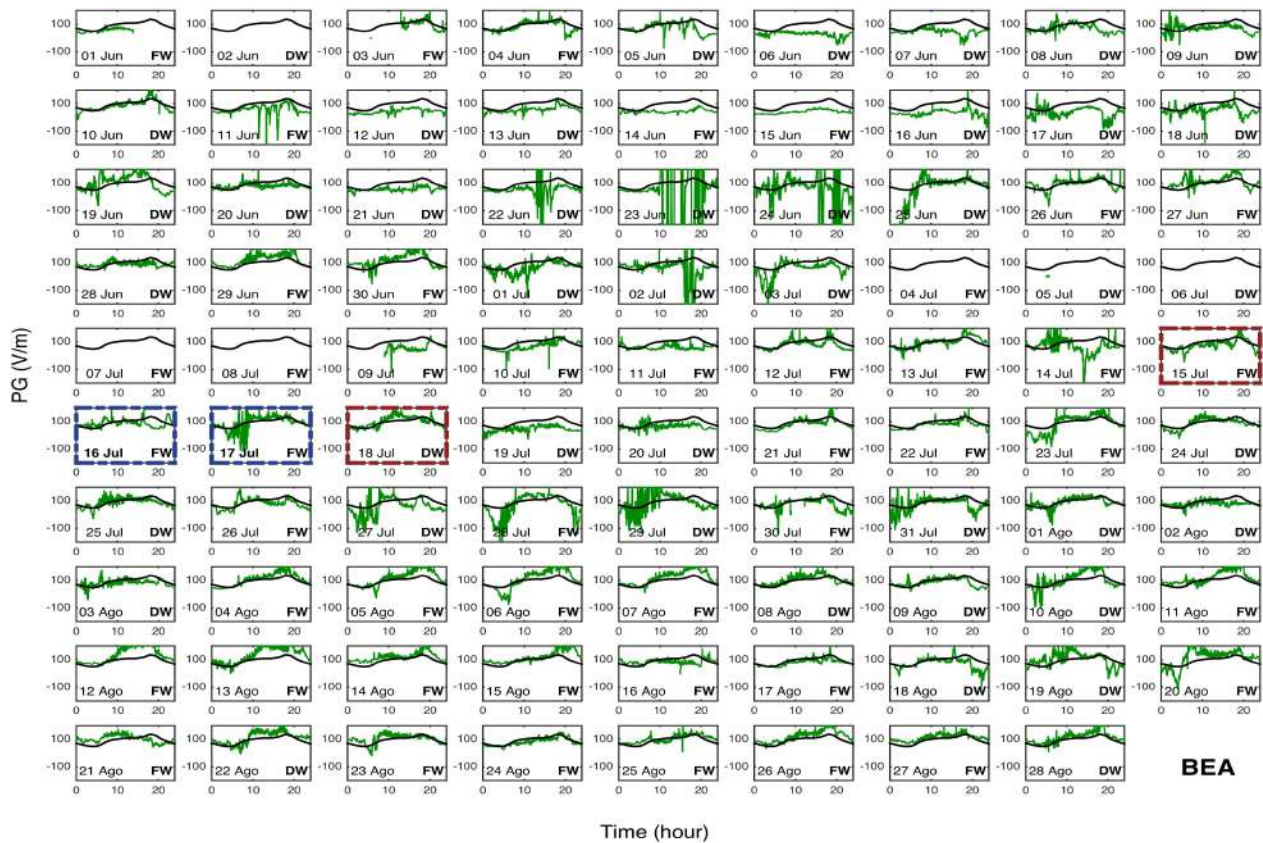


Figure C.4: Daily variation of the PG for the ALEX2014 campaign at BEA station. The thick black lines in the plots represent the lowest smoothed mean daily FW PG for the all campaign. The dust event starts on 16th July and ends on the 17th July (highlight by dark blue rectangles). Dark red rectangles mark the day before and after the dust event.

hypothesis that the PG oscillations observed on the 17th July can be attributed to the long-range dust transport. In line with this, the day following the dust event reveals that the PG, once again, follows the mean daily behavior.

Contrary to this observation, the AMI station does not show any considerable change in the PG behaviour during the dust event, 16th-17th July (dark blue rectangles), presented in Fig. C.5. This is surprising as it was demonstrated in Fig. C.3 that the dust during these dates covered the entire region of Southern Portugal; the region in which the three stations are located. There are several possible explanations for this, which include both horizontal and vertical variations in the dust concentration as well as variations in the charge distribution within the layer, which could lead to more noticeable effects on the PG at some sites than others. Another explanation includes a possible screening effect from charges generated by the Alqueva lake in the proximity of this station. Charging mechanisms affecting this station are discussed by the authors elsewhere [179] and could constitute a mechanism to suppress the short time-scale influence of the desert dust electrification. Interestingly, at mid time-scales the influence of the desert dust is perceived as will be shown below.

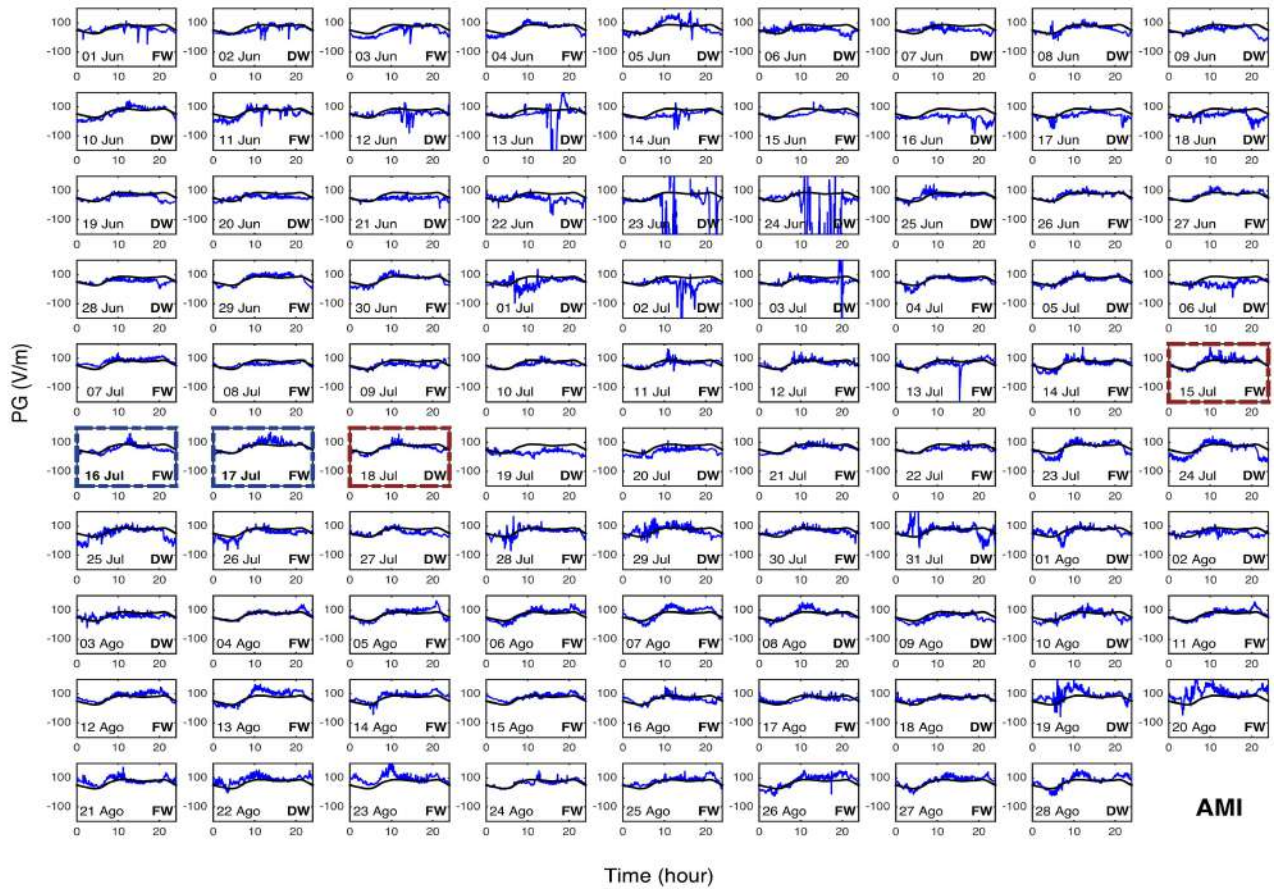


Figure C.5: Daily variation of the PG for the ALEX2014 campaign at AMI station. The thick black lines in the plots represent the lowest smoothed mean daily FW PG for the all campaign. The dust event starts on 16th July and ends on the 17th July (highlight by dark blue rectangles). Dark red rectangles mark the day before and after the dust event.

Finally, EVO station again evidences PG perturbations during the dust event, shown in Fig. C.6. On the day before the Saharan dust event, 15th July, the PG follows closely the mean daily behavior as anticipated (considering no dust has arrived at the station yet). During the following days significant variations in the PG are observed at the end of 16th July (≈ 22 UTC) and during all of the 17th July, with PG values reaching around -390 V/m, which is uncharacteristic of a normal FW day. On the day after the dust event, 18th July, the PG curve resumes its normal mean behavior again. To examine the likelihood of such negative PG excursions occurring during other FW days without dust, Fig. C.6 demonstrates that such behaviour does occur at EVO (e.g 27th June). In fact, on 22 out of 46 FW days ($\approx 50\%$) the PG is shown to go negative (potentially a result of variations in local aerosol concentration), although the magnitude of the excursions are typically smaller and less frequent than the ones on the 17th July shown in Fig. C.6.

To quantify the PG perturbations found at BEA and EVO on the 17th July in a statistical sense, two parameters have been estimated for the FW days of the ALEX2014 campaign: (i) Number of local minima – local minima of the smoothed PG daily curves (indicating PG negative inversions) – represented as blue

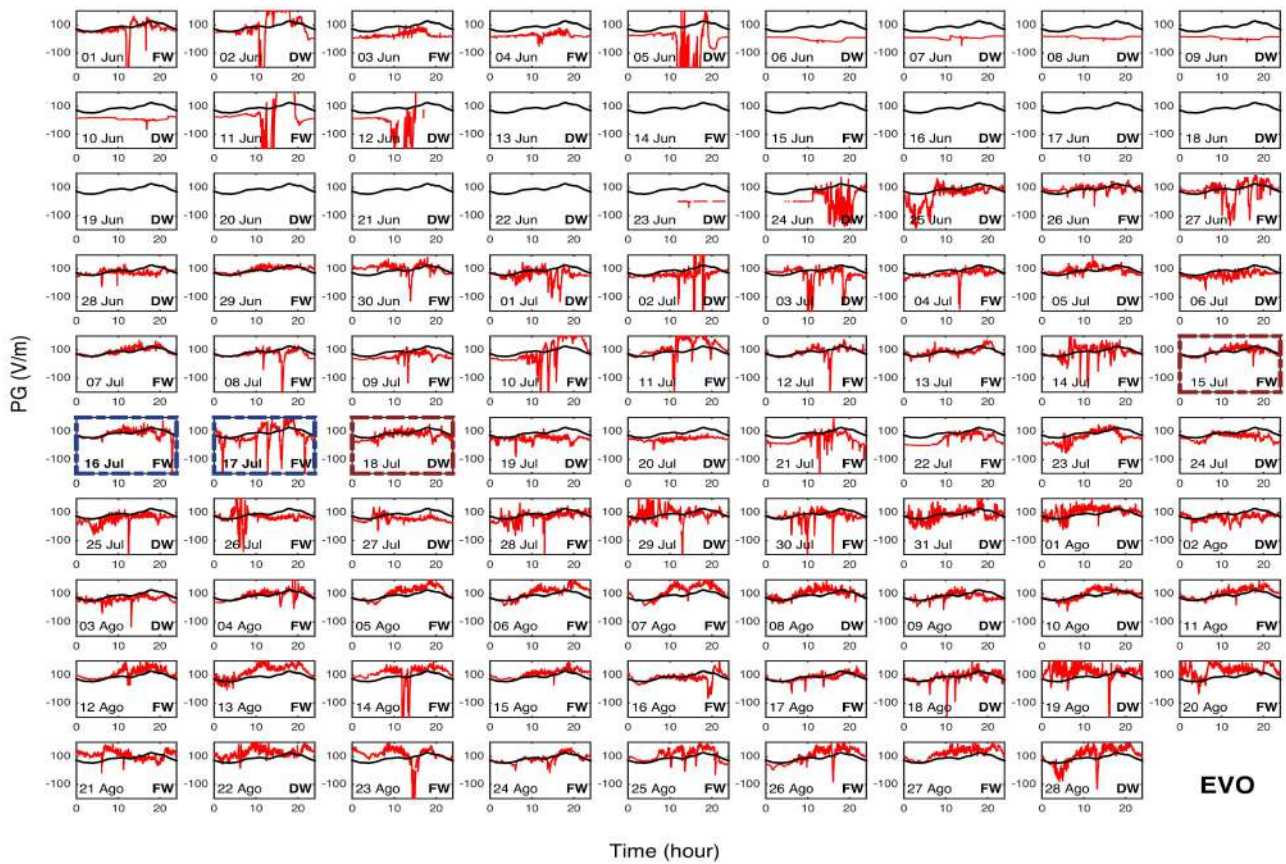


Figure C.6: Daily variation of the PG for the ALEX2014 campaign at EVO station. The thick black lines in the plots represent the lowest smoothed mean daily FW PG for the all campaign. The dust event starts on 16th July and ends on the 17th July (highlight by dark blue rectangles). Dark red rectangles mark the day before and after the dust event.

points and referred to the left y-axis of Fig. C.7; (ii) relative Std (%) – percentage of the daily standard deviation divided by the daily mean PG – represented as red points and referred to the right y-axis of Fig. C.7. The vertical black dashed line on Fig. C.7 marks the start of the dust event, 16th July, and the day of most interest, 17th July, is right after it. The analysis is also made for AMI (for consistency) though nothing worth mentioning is expected for this station for the reasons explained above. Two main features, related with the Saharan dust event, are observed: (i) the number of local minima is 15 during the day of the dust event on 17th July, for both BEA and EVO, which is larger than the ≈ 11 minima observed the previous day; only one FW day in BEA and three other FW days in EVO have the same number of minima. (ii) An increase in the relative Std from the day the dust event started, 16th July, to the following day when it was fully in progress on 17th July, is observed. At the BEA station the Relative Std increased from 30.6% to 63.7% (more than doubled) and in the EVO case from 38.4% to 92.4% (almost tripled); this reveals an increase of the PG variability during the dust event, in fact, only four FW days in BEA exceed the Relative Std of 17th July and only three in EVO.

Returning to the timing of the arrival of the dust, the BSC-DREAM8b maps (Fig. C.3a to Fig. C.3d)

depict that the desert dust event, 16th July, arrived at the two stations approximately at the same time, at least in the time scale of the dust plume transport (from hours to days), which means that the influence of the desert dust is a good candidate to explain these observations at a regional scale. The regional nature of this observation is a first highlight of the importance of using arrays of sensors instead of single sensors.

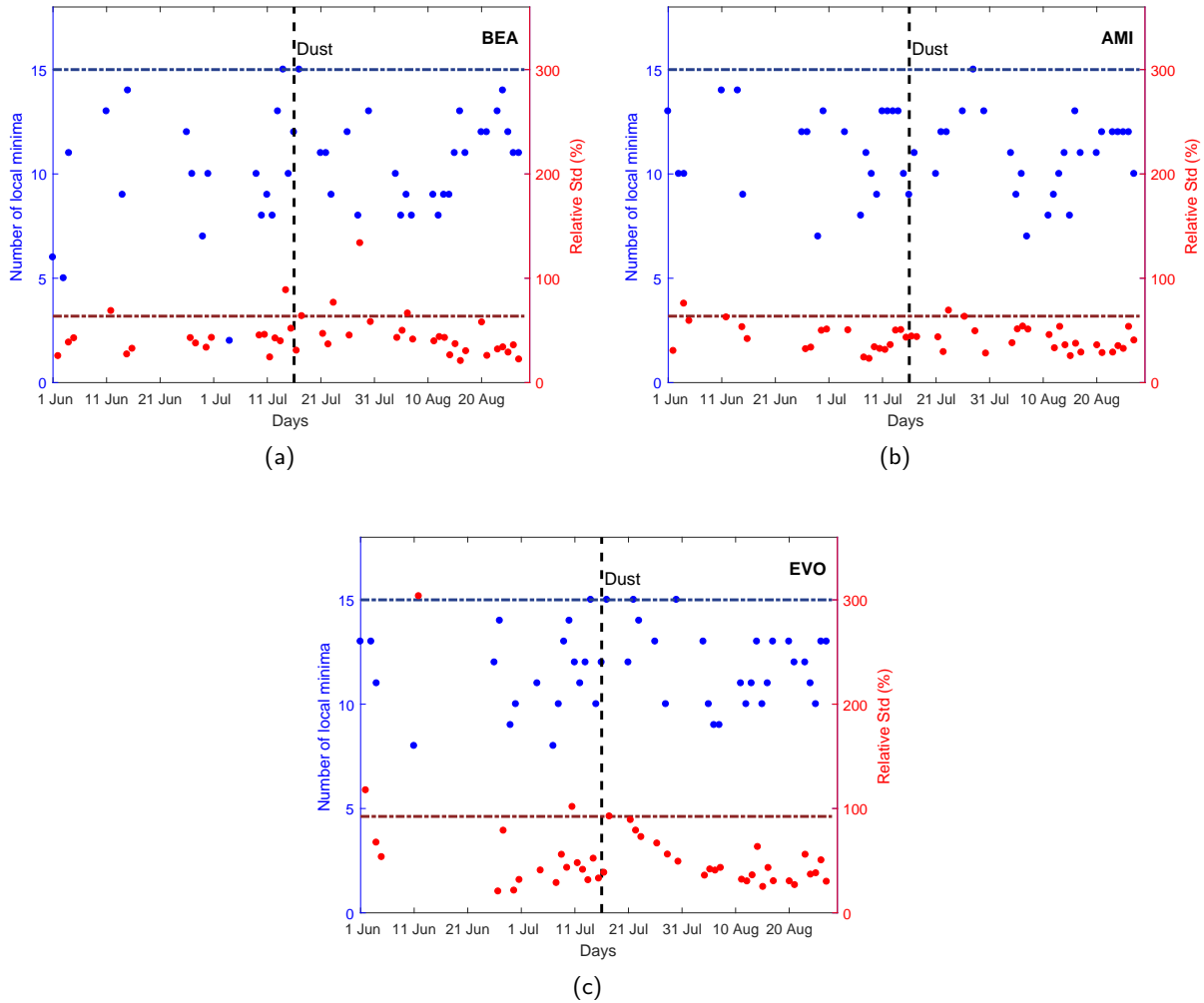


Figure C.7: Number of local minima of the PG daily curves, marked with red dots, and relative Std (%), marked with blue dots, respectively for: (a) BEA; (b) AMI; (c) EVO.

In this spirit, the BSC-DREAM8b maps (Fig. C.3a to Fig. C.3d) depict that the desert dust event, 16th-17th July, arrived at the two stations approximately at the same time, at least in the time scale of the dust plume transport (from hours to days), which means that the influence of the desert dust is a good candidate to explain these observations at a regional scale. The regional nature of this observation is a first highlight of the importance of using arrays of sensors instead of single sensors.

C.4.2 Robust lowess smoothing

To proceed with the analysis, the effect of the desert dust electrification at mid time-scales (above 1-day) are now explored. To that end lowess smoothed PG curves (black thick lines) are represented along with the PG raw data for BEA, AMI and EVO, respectively, in Fig. C.8a, Fig. C.9a, and Fig. C.10a, during the ALEX2014 campaign. A similar modulation of the lowess curves around the time of the dust event at the three stations sustain the occurrence of a regional process. The PG is also observed to reduce on the days following the dust event. Local minimum of the lowess curves are found at the mid-day of 19th July at BEA and AMI, 71.8 V/m and 49.1 V/m, respectively; while in EVO the minimum occurs ≈ 12 hours later reaching ≈ 50.1 V/m. If the mean PG value for the entire ALEX2014 campaign is used as reference, for each of the three stations, this represents a reduction of the PG of around 88.7 %, 82.6 %, 67.3 %, respectively for BEA, AMI and EVO. The percentage of reduction in the three stations is fairly similar and qualitatively confirms the influence of a regional process. A possible explanation for this reduction, two days after the on set of the Saharan desert dust on the region, is the dispersion of the negative charges that were accumulated on the bottom of the dust layer; occurring after the dust layer passed. Such charge suspended in the atmosphere would increase the atmospheric electric conductivity and through (quasi-static) Ohm's law it would imply a reduction of the PG. This possibility will be discussed below.

C.4.3 Wavelet analysis

Wavelet analysis is used to understand the evolution in time of the characteristic frequencies/periods composing the time-series. The interested reader is referred to the explanatory work in [180]; the basic technique behind wavelets is the Fourier transform, transforming the signal from the time domain to frequency (or period) domain, but instead of performing one transform for the entire the time-series, successive transforms are made by the use of a wavelet function, the so called mother function, to depict the evolution of those frequencies (or periods).

In fact, PG is affected by different periodicities, [59], but the one of most important is the 1-day periodicity, which is a result of the GEC. Thus monitoring the evolution of that periodicity can reveal the influence of local/regional processes on the PG, e.g. local pollution, which disguises the behavior imposed by the GEC. For this reason attention is given here to the 1 day periodicity. Wavelet analysis of the PG measurements at BEA is represented in Fig. C.8b and is generally similar to those observed in AMI and EVO, shown in Figures Fig. C.9b and Fig. C.10b, respectively. The colour gradient in the plots represents the isopower lines for a given frequency/period, lower powers appear in blue and higher powers in red.

The most significant information extracted from the wavelet periodogram for BEA and EVO is the persistence of the 1-day periodicity that appears to be diminished, in a more significant way at EVO, during the desert dust event; while for AMI no change is observed. Interestingly, a suppression of lower periodicities, below the 1/2-day periodicity, is observed after the dust event, around the 19th July. It reveals

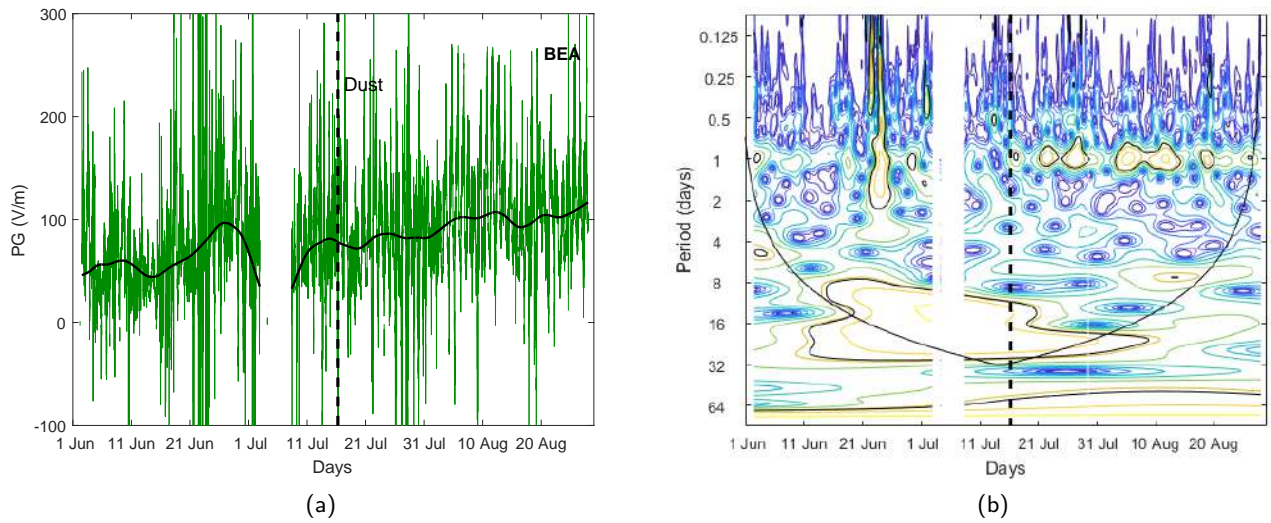


Figure C.8: PG at BEA: (a) raw data (back solid line represents a robust lowess smoothing); (b) wavelet periodogram (1-hour averaged). The vertical dashed line in both panels represents the 16th July 2014 desert dust event. Gaps correspond to missing data.

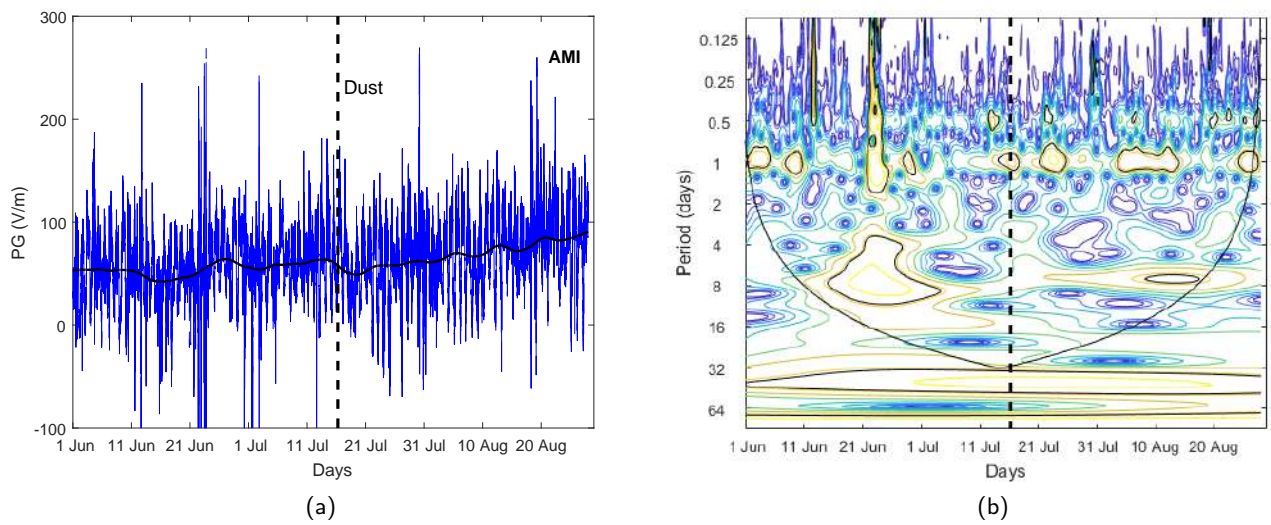


Figure C.9: PG at AMI: (a) raw data (back solid line represents a robust lowess smoothing); (b) wavelet periodogram (1-hour averaged). The vertical dashed line in both panels represents the 16th July 2014 desert dust event. Gaps correspond to missing data.

a lower influence of short time-scales phenomena, usually of local nature, and is another indication of the prevalence of a regional process (at mid time-scales) as revealed by the lowess analysis. With this view, the periodicity analysis is consistent with the observations described in previous sections. Revealing, in the frequency/period domain, that the desert dust affected more considerably the EVO station and also BEA (although slightly less significantly), while almost no effect is found at AMI.

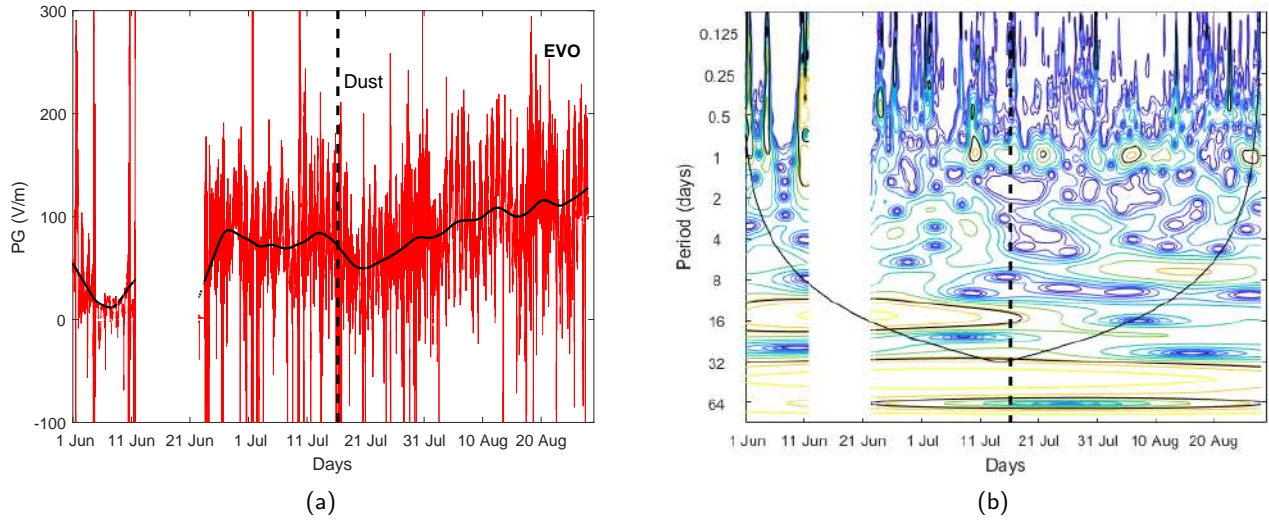


Figure C.10: PG at AMI: (a) raw data (back solid line represents a robust lowess smoothing); (b) wavelet periodogram (1-hour averaged). The vertical dashed line in both panels represents the 16th July 2014 desert dust event. Gaps correspond to missing data.

C.5 Dust charge model

To understand the influence of the Saharan dust electrification on the PG measurements a model is discussed in this section. Before considering the mathematical details of the model, it is worth discussing the electrification mechanism considered in the present model. Dust electrification is usually recognized to result from contact and triboelectric charging between particles being lofted from the surface. The basic mechanism for charge separation is commonly thought to be the fact that, during collisions, the smallest grains gain negative charge with respect to larger particles [181, 182, 183]. After this size dependent charging, the smallest particles are separated from the larger ones by gravitation inducing what might be called gravitational charge separation, which is consistent with the PG observations in the dust storms source region (e.g., [165, 166]).

Nevertheless, the contact and triboelectric charging depends strongly on the grain collision frequency and though high frequencies are expected in dust storms near to the source region to cause dust electrification, this is not the case for regions far away from it, as is the present case. The layers that reach distant locations have low dust concentrations; which corresponds to low collision frequencies which mean that contact and triboelectric charging are unlikely charging mechanisms. Assuming that dust charge decays on time-scales of minutes (based on the typical electrical relaxation time of air near the surface) a dust layer will lose its charge if a charging mechanism is absent. Consequently, the dust layers will no longer be charged when far from the source region. Thus, to explain long-range electrification, in the absence of other apparent mechanisms, it is reasonable to consider that the charging of the dust layers may be due to the action of the air-Earth electric current. In accordance to the discussion in [168], a layer of uncharged dust particles

will scavenge atmospheric ions by attachment to the large dust particles, reducing the air conductivity in that region. Such reduction in conductivity results in the creation of a space charge density (SCD) by the action of the air-Earth current, J_z as follows: air-Earth electric current, flowing from the Ionosphere to the Earth's surface, will bring to the upper part of the dust layer positive small ions which will attach to the dust particles. This accumulation of charge will create a positive SCD, at the top of the dust layer, while a similar but negative SCD will be formed at the bottom of the dust layer due to upward flow of negative ions in the air-Earth electric current.

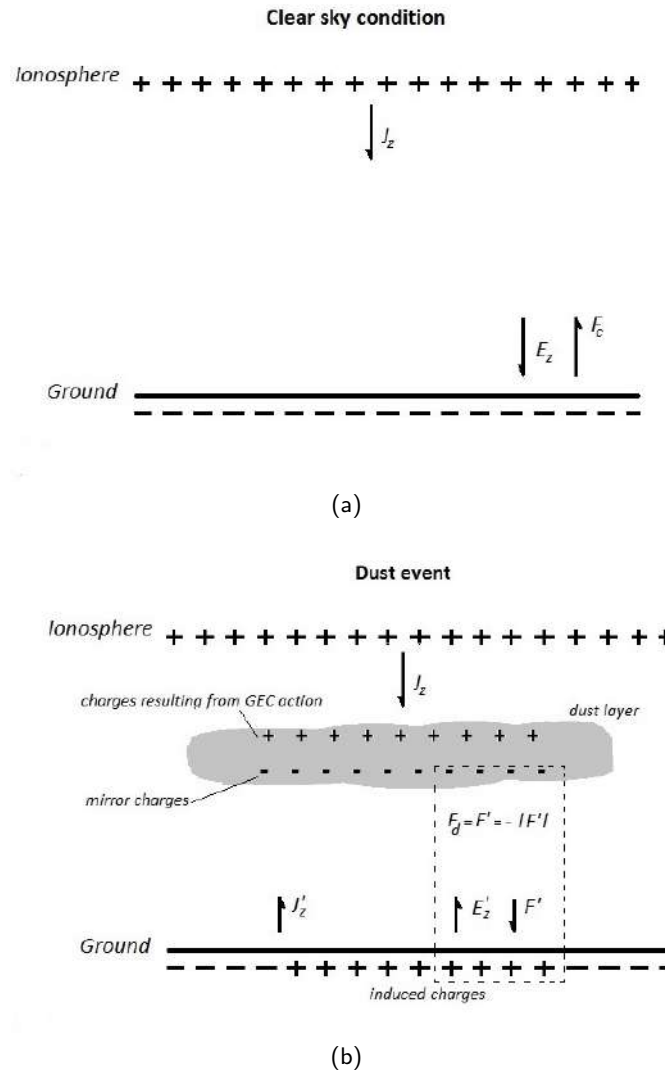


Figure C.11: Schematic diagram of the charge model to explain the observations: (a) diagram for clean aerosol conditions; (b) diagram for a desert dust event.

In Fig. C.11 it is shown a schematic diagram of the model which will be used to interpret the Southern Portugal PG data during the dust event. Basically two phenomena have been observed: (i) Short time-scale perturbations, below 1-day, of the PG at BEA and EVO, in which variations that reached ± 300 V/m were observed; (ii) Mid time-scale suppression, above 1-day, of the PG at the three stations, with reductions of $\approx 80\%$ in relation to the mean FW values. For FW days in clean sky conditions (i.e. low aerosol

concentration) the PG, represented in Fig. C.11 by F_c , points upwards from the ground and has the typical value for those conditions, ≈ 100 V/m. When a stable dust layer is interposed, theoretically, a bipolar charge distribution is formed by GEC action through the air-Earth current as described above., with positive space charge at the top of the dust layer and negative space charge at the base. Such negative space charge would then induce positive space charges near the ground (i.e. in the vicinity of the electric field mills) beneath. As a consequence of the distribution of charges between the bottom of the dust layer and ground, a downward pointing PG (F' in Fig. C.11) is generated below the dust layer. In such a situation the PG measured under the dust layer, F_d , is basically F' :

$$F_d = F' = -|F'|. \quad (\text{C.1})$$

In the case when F' is high (i.e. when the dust layer is sufficiently close to the ground and significant space charge accumulation occurs), F_d would evidence expressive negative excursions; this mechanism is suggested to explain the PG perturbations observed at both BEA and EVO during the Saharan dust event on 17th July. In normal FW conditions $F_c \approx 85.3$ V/m for BEA and $F_c \approx 99.7$ V/m for EVO (based on the mean daily behavior), however during the dust event on 17th July, the observed negative excursions reached $F_d \approx -119.5$ V/m for BEA and $F_d \approx -388.7$ for EVO demonstrating that significant space charge is likely to be present. Such space charge corresponds to a downward pointing PG generated by the dust layer of $|F'| \approx 119.5$ V/m for BEA and $|F'| \approx 388.7$ V/m for EVO. The observed oscillations are then a consequence of fast charge formation/recombination on even shorter time-scales, below 1-hour.

Returning to the model presented in Fig. C.11 it is expected that F' would depend on the SCD between the bottom of dust layer and the ground during the desert dust event. In fact, the steady-state F' can be estimated from Gauss' law, that relates the vertical variation of F' with SCD, usually represented by $\zeta(z)$, through the relation:

$$\frac{dF'}{dz} = \frac{\zeta(z)}{\varepsilon_0}, \quad (\text{C.2})$$

here ε_0 is the permittivity of vacuum and z the vertical altitude. To integrate this equation a region from the ground to the upper-limit of the SCD in the bottom of the dust layer needs to be defined; it is represented by a dashed line rectangle in Fig. C.11. Inside that region it is assumed that $\zeta(z)$ vertical profile is defined in terms of the Heaviside function $H(z)$:

$$\zeta(z) = \zeta_+ [H(z) - H(z - th_+)] - |\zeta_-| [H(z - he_-) - H(z - he_- - th_-)]. \quad (\text{C.3})$$

The Eq. C.3 assumes that the positive SCD is at the ground, thus its height is $he_+ \approx 0$, and has a thickness th_+ , that can be assumed to be $th_+ \approx 0$. Similarly, he_- and th_- stand for the height and thickness of the negative SCD at the bottom of the dust layer, respectively. The use of the Heaviside function assumes that the SCD is uniform inside the SCD thickness, th_- . Moreover, it is expected that ζ_+

$\approx |\zeta_-| \approx \zeta_0$ and for that reason Eq. C.3 can be simplified to:

$$\zeta(z) = -\zeta_d [H(z - he_-) - H(z - he_- - th_-)]. \quad (C.4)$$

It is important to mention that both the height, he_- , and thickness, th_- , of the space charge at the bottom of the dust layer are not necessarily equal to the height, he_d , and thickness, th_d , of the dust layer. Nevertheless, the space charge should be inside the dust layer and for that reason it is expected that: $he_d < he_- < he_d + th_d$ and $th_- < th_d$. According to the dust profile from BSC-DREAM8b model, Fig. C.3e, it is possible to estimate the height and thickness of the dust layer on the 17th July to be the $he_d \approx 2$ km and $th_d \approx 2$ km. With these parameters the space charge height and thickness can be approximated to: $he_- \approx 2$ km and $th_- \approx 0.1 - 1$ km. With the use of Eq. C.4, it is straightforward to integrate Eq. C.2 to estimate F' :

$$\int_0^{F'} dF' = \frac{1}{\varepsilon_0} \int_0^{he_-+th_-} \zeta(z) dz = -\frac{\zeta_d}{\varepsilon_0} \int_{he_-}^{he_-+th_-} dz. \quad (C.5)$$

After performing the integral, F' is simply given by: $F' = -\zeta_d th_- / \varepsilon_0$. This result can be used to estimate the SCD amplitude accumulated on the bottom of the dust layer from the F' values estimated above:

$$\zeta_d = \frac{\varepsilon_0}{th_-} |F'|. \quad (C.6)$$

For the BEA case, considering that th_- varies from 0.1 to 1 km, Eq. C.6 implies that the SCD amplitude varies around $\zeta_d \approx 1.0-10.6$ pC/m³. For the EVO case, using the same range for th_- the SCD estimated by Eq. C.6 is $\zeta_d \approx 3.4-34.4$ pC/m³. These are moderate SCD values, in reasonable agreement with the values observed experimentally [168]; which point towards a fair explanation, with the discussed model, of the PG perturbations found during the Saharan dust event of 16th and 17th July 2014. Nevertheless, it should be mentioned that this is a simplified model and for that reason it relies on many assumptions implying several limitations; one of which is related to Eq. C.5 where there is the assumption that the space charges occupy semi-infinite planes in the x and y coordinates. This simplification tends to overestimate the real SCD that is expected to have a disc like shape.

After the desert dust has passed the region where the three sensors were installed it is reasonable to admit that the positive space charges (carried by lighter dust particles) have been transported away; while negative space charges (carried by heavier dust particles) might have been dispersed in the atmosphere. Those charges would be suspended in the atmosphere for one or two days after the dust event increasing atmospheric electric conductivity and through (quasi-static) Ohm's law implying a reduction of the PG. With sufficient time, atmospheric mixing would make them recombine with positive atmospheric ions (becoming neutral) and both electric conductivity and PG would recover their normal values. The increase of the

electric conductivity under the influence of such negative space charge in relation to the normal case, where there are significantly less space charges, can be estimated by differentiating Ohm's law (assuming a constant air-Earth current, $J_z \approx 2 \text{ pA/m}^2$):

$$\Delta\sigma_t h = -J_z \frac{\Delta F}{F_n^2}. \quad (\text{C.7})$$

In this equation $F = F_s - F_n$, F_s corresponds to PG under the space charge and F_n the PG for the normal situation. If the mean PG for the entire ALEX2014 campaign is used to estimate $F_n \approx 81.0, 59.4$ and 74.4 V/m and the minimum of the lowest curves at the 19th July is used to estimate $F_s \approx 71.8, 49.1$ and 50.1 V/m , respectively for BEA, AMI and EVO, Eq. C.7 gives $\Delta\sigma_t \approx 2.8, 5.8, 8.8 \text{ fS/m}$ for BEA, AMI and EVO. According to [184] a typical estimation for atmospheric electric conductivity is $\sigma_t \approx 13.3 \text{ fS/m}$; what makes the estimations done for $\Delta\sigma_t$ reliable.

C.6 Conclusions

Evidence of long-range Saharan dust electrification is found in PG measurements carried out by a triangular array of stations in Southern Portugal. This occurred during the dust event of 16th-17th July 2014, which coincided with the ALEX 2014 campaign. Two signatures of dust electrification have been found in the PG data: (i) significant magnitude short time-scale oscillations of the PG at two of the stations; (ii) mid time-scale suppression of the PG at the three stations. A formulation was developed to explain these observations assuming that the air-Earth electrical current creates a bipolar space charge distribution inside of the dust layer. Values of space charge density amplitude are found to be around $\zeta \approx 20 \text{ pCm}^{-3}$; consistent with previously reported values in the literature. The importance of using arrays of PG sensors, instead of single site measurements, is hereby demonstrated.

The work in this appendix resulted in the following publication:

- H. G. Silva, F. M. Lopes, S. Pereira, K. Nicoll, S. M. Barbosa, R. Conceição, S. Neves, R. G. Harrison, M. Collares Pereira, Saharan dust electrification perceived by a triangle of atmospheric electricity stations in Southern Portugal, *J. Electrostat.* 84 (2016) 106–120.

It should be noted that in this work, a study about the long-range transport of Saharan dust was performed and the knowledge obtained, including the use of BSC forecasts, was used in other publications presented in this thesis, such as:

- R. Conceição, H.G. Silva, J. Mirão, M. Gostein, L. Fialho, L. Narvarte, M. Collares-Pereira, Saharan dust transport to Europe and its impact on photovoltaic performance: A case study of soiling in Portugal, *Sol. Energy.* 160 (2018) 94–102.

- R. Conceição, H.G. Silva, J. Mirão, M. Collares-Pereira, Organic Soiling: The Role of Pollen in PV Module Performance Degradation, *Energies*. (2018) 1–13.
- R. Conceição, A. Merrouni, D. Lopes, A. Alae, H. G. Silva, E. Bennouna, M. Collares-Pereira, A. Ghennioui, A Comparative Study of Soiling on Solar Mirrors in Portugal and Morocco: Preliminary Results for the Dry Season, *SolarPACES 2018*. Accepted for publication.

Bibliography

- [1] S. C. Costa, A. S. A. Diniz, and L. L. Kazmerski, "Dust and soiling issues and impacts relating to solar energy systems: Literature review update for 2012-2015," *Renew. Sustain. Energy Rev.*, vol. 63, pp. 33–61, 2016.
- [2] World Energy Council, "World Energy Resources: Solar 2016," tech. rep., 2016.
- [3] S. C. Costa, A. S. A. Diniz, and L. L. Kazmerski, "Solar energy dust and soiling R&D progress: Literature review update for 2016," *Renew. Sustain. Energy Rev.*, vol. 82, no. September, pp. 2504–2536, 2018.
- [4] W. J. Jamil, H. Abdul Rahman, S. Shaari, and Z. Salam, "Performance degradation of photovoltaic power system: Review on mitigation methods," *Renew. Sustain. Energy Rev.*, vol. 67, pp. 876–891, 2017.
- [5] M. N. Horenstein, M. K. Mazumder, R. C. Sumner, J. Stark, T. Abuhamed, and R. Boxman, "Modeling of trajectories in an electrodynamic screen for obtaining maximum particle removal efficiency," *IEEE Trans. Ind. Appl.*, vol. 49, no. 2, pp. 707–713, 2013.
- [6] T. Luo, R. Young, and P. Reig., "Aqueduct Projected Water Stress Country Rankings," Tech. Rep. August, 2015.
- [7] G. Marques, C. Martins, B. J, A. C, P. M, Caeiro E, and L.-P. P, "Pollen Counts Influence Web Searches for Asthma and Rhinitis," *J Investig Allergol Clin Immunol*, vol. 26, no. 3, pp. 192–194, 2016.
- [8] R. Xu, K. Ni, Y. Hu, J. Si, H. Wen, and D. Yu, "Analysis of the optimum tilt angle for a soiled PV panel," *Energy Convers. Manag.*, vol. 148, pp. 100–109, 2017.
- [9] H. Hottel and B. Woertz, "Performance of Flat Plate Solar Heat Collectors," *Trans. Am. Soc. Mech. Eng.*, vol. 64, pp. 91–104, 1942.

- [10] A. Dietz and . p. 59–86., *Diathermanous materials and properties of surfaces, in Introduction to the utilization of solar energy*. New York: McGraw-Hill, 1963.
- [11] O. Hamberg and F. Tomlinson, "Sensitivity of Thermal Surface Solar Absorptance to Particulate Contamination," tech. rep., 1971.
- [12] H. P. Garg, "Effect of dirt on transparent covers in flat-plate solar energy collectors," *Sol. Energy*, vol. 15, pp. 299–302, 1974.
- [13] K. Butti and J. Perlin, "A golden thread: 2500 years of solar architecture and technology," 1980.
- [14] B. Anderson, *Solar energy: fundamentals in building design*. New York: McGraw-Hill, 1977.
- [15] F. Kryza, *The Power of Light: The Epic Story of Man's Quest to Harness the Sun*. McGraw-Hill, 2003.
- [16] M. Collares-Pereira, "An Innovative, High Temperature and Concentration Solar Optical System at the Turn of the 19th Century: The Pyreheliophoro," in *Adv. Sol. Energy An Annu. Rev. Res. Dev. Renew. Energy Technol.* (Y. Goswami, ed.), ch. 12, pp. 465–486, 1 ed., 2005.
- [17] A. Meinel and M. Meinel, *Applied solar energy: an introduction*. Reading: Addison-Wesley, 1976.
- [18] C. Silvi, "The pioneering work on Linear Fresnel Reflector Concentrators (LFCs) in Italy," Available from (<http://www.mondosolare.it/pub/silvi-fresnel.pdf>), 2009.
- [19] J. Gretz, "Solar Thermal Electricity Generation EURELIOS, the 1 MW(el) Helioelectric Power Plant of the European Communities," *Int. J. Sol. Energy*, vol. 1, no. 1, pp. 3–19, 1982.
- [20] T. Mancini, "Solar-Electric Dish Stirling System Development," in *Eur. stirling forum, Osnabruck*, 1998.
- [21] B. Gallego, G. Cohen, T. Mancini, T. Wilkins, F. Morse, and D. Kearney, "The history of American CSP - A timeline," in *CSP Today*, pp. 1–10, 2012.
- [22] D. A. Baharoon, H. A. Rahman, W. Z. W. Omar, and S. O. Fadhl, "Historical development of concentrating solar power technologies to generate clean electricity efficiently – A review," *Renew. Sustain. Energy Rev.*, vol. 41, pp. 996–1027, 2015.
- [23] E. Becquerel, "Mémoire sur les effets électriques produits sous l'influence des rayons solaires," *C.R. Acad. Sci. Paris*, vol. 9, no. 561, 1839.
- [24] A. Einstein, "Ueber einen die Erzeugung und Verwandlung des Lichtes betreffenden heuristischen Gesichtspunkt," *Ann. Phys.*, vol. 17, pp. 132–148, 1905.
- [25] C. Fritts, "On a new form of selenium photocell," *Am. J. Sci.*, vol. 26, no. 465, 1883.

- [26] J. Perlin, *From Space to Earth – The Story of Solar Electricity*. London: Harvard University Press, 2002.
- [27] C. I. Calle, J. L. Mcfall, C. R. Buhler, S. J. Snyder, and E. E. Arens, “Dust Particle Removal by Electrostatic and Dielectrophoretic Forces with Applications to NASA Exploration Missions,” *ESA Annu. Meet. Electrostat.*, p. 1, 2008.
- [28] NREL, “Enabling Greater Penetration of Solar Power via the Use of CSP with Thermal Energy Storage,” *Nrel*, no. November, p. 28 p., 2011.
- [29] F. A. Mejia and J. Kleissl, “Soiling losses for solar photovoltaic systems in California,” *Sol. Energy*, vol. 95, pp. 357–363, 2013.
- [30] B. R. Paudyal, S. R. Shakya, D. P. Paudyal, and D. Das Mulmi, “Soiling-induced transmittance losses in solar PV modules installed in Kathmandu Valley,” *Renewables Wind. Water, Sol.*, vol. 4, no. 1, p. 5, 2017.
- [31] E. Urrejola, J. Antonanzas, P. Ayala, M. Salgado, G. Ramírez-Sagner, C. Cortés, A. Pino, and R. Escobar, “Effect of soiling and sunlight exposure on the performance ratio of photovoltaic technologies in Santiago, Chile,” *Energy Convers. Manag.*, vol. 114, pp. 338–347, 2016.
- [32] R. Conceição, H. Silva, J. Mirão, M. Gostein, L. Fialho, L. Narvarte, and M. Collares-Pereira, “Saharan dust transport to Europe and its impact on photovoltaic performance: A case study of soiling in Portugal,” *Sol. Energy*, vol. 160, pp. 94–102, 2018.
- [33] R. Conceição, H. G. Silva, J. Mirão, and M. Collares-Pereira, “Organic Soiling: The Role of Pollen in PV Module Performance Degradation,” pp. 1–13, 2018.
- [34] S. Dawson, N. Mardesich, B. Spence, and S. White, “Solar Array Panels With Dust-Removal Capability Inexpensive , low-power piezoelectric buzzers would be built in .,” tech. rep., NASA’s Jet Propulsion Laboratory, 2004.
- [35] S. You, Y. J. Lim, Y. Dai, and C. H. Wang, “On the temporal modelling of solar photovoltaic soiling: Energy and economic impacts in seven cities,” *Appl. Energy*, vol. 228, no. July, pp. 1136–1146, 2018.
- [36] M. Augusto, M. Lopes, D. Jesus, G. Timò, and C. Agustín-sáenz, “Solar Energy Materials and Solar Cells Anti-soiling coatings for solar cell cover glass : Climate and surface properties in fl uence,” *Sol. Energy Mater. Sol. Cells*, vol. 185, no. December 2017, pp. 1–7, 2018.
- [37] A. Sayyah, M. N. Horenstein, and M. K. Mazumder, “ScienceDirect Energy yield loss caused by dust deposition on photovoltaic panels,” vol. 107, pp. 576–604, 2014.
- [38] L. L. Kazmerski, A. Sonia, A. C. Diniz, C. Brasil, M. Machado, S. C. Costa, P. P. Brito, C. Dias, S. D. Morais, and L. R. D. Oliveira, “Soiling Particle Interactions on PV Modules: Surface and Inter - Particle Adhesion and Chemistry Effects,” *Pvsc*, pp. 2–4, 2016.

- [39] M. El-Shobokshy and F. M. Hussein, "Effect of dust with different physical properties on the performance of photovoltaic cells," *Sol. energy*, vol. 51, no. 6, pp. 505–511, 1993.
- [40] R. Appels, B. Lefevre, B. Herteleer, H. Goverde, A. Beerten, R. Paesen, K. De Medts, J. Driesen, and J. Poortmans, "Effect of soiling on photovoltaic modules," *Sol. Energy*, vol. 96, pp. 283–291, 2013.
- [41] J. Mallineni, K. Yedidi, S. Shrestha, B. Knisely, S. Tatapudi, J. Kuitche, and G. Tamizhmani, "Soiling losses of utility-scale PV systems in hot-dry desert climates: Results from four 4-16 years old power plants," *2014 IEEE 40th Photovolt. Spec. Conf. PVSC 2014*, pp. 3197–3200, 2014.
- [42] M. Šúri, T. A. Huld, E. D. Dunlop, and H. A. Ossenbrink, "Potential of solar electricity generation in the European Union member states and candidate countries," *Sol. Energy*, vol. 81, no. 10, pp. 1295–1305, 2007.
- [43] F. Lopes, H. Silva, R. Salgado, A. Cavaco, P. Canhoto, and M. Collares-Pereira, "Short-term forecasts of GHI and DNI for solar energy systems operation: assessment of the ECMWF integrated forecasting system in southern Portugal," *Sol. Energy*, vol. 170, no. May, pp. 14–30, 2018.
- [44] B. Thrasher, E. P. Maurer, C. McKellar, and P. B. Duffy, "Technical Note: Bias correcting climate model simulated daily temperature extremes with quantile mapping," *Hydrol. Earth Syst. Sci.*, vol. 16, no. 9, pp. 3309–3314, 2012.
- [45] J. Sheffield, G. Goteti, and E. F. Wood, "Development of a 50-year high-resolution global dataset of meteorological forcings for land surface modeling," *J. Clim.*, vol. 19, no. 13, pp. 3088–3111, 2006.
- [46] W. H. Smith, "Removal of Atmospheric Particulates By Urban Vegetation - Implications for Human and Vegetative Health," *Yale J. Biol. Med.*, vol. 50, no. 2, pp. 185–197, 1977.
- [47] H. Capdevila, V. Naidoo, and M. Graeber, "Soiling Forecast and Measurements for large PV Power Generation Projects in Desert Environments," *Pvsc*, no. February, pp. 2–6, 2016.
- [48] W. Javed, B. Guo, and B. Figgis, "Modeling of photovoltaic soiling loss as a function of environmental variables," *Sol. Energy*, vol. 157, no. August, pp. 397–407, 2017.
- [49] S. Pulipaka, F. Mani, and R. Kumar, "Modeling of soiled PV module with neural networks and regression using particle size composition," *Sol. Energy*, vol. 123, pp. 116–126, 2016.
- [50] S. Pulipaka and R. Kumar, "Power prediction of soiled PV module with neural networks using hybrid data clustering and division techniques," *Sol. Energy*, vol. 133, pp. 485–500, 2016.
- [51] F. V. Gutierrez-Corea, M. A. Manso-Callejo, M. P. Moreno-Regidor, and M. T. Manrique-Sancho, "Forecasting short-term solar irradiance based on artificial neural networks and data from neighboring meteorological stations," *Sol. Energy*, vol. 134, pp. 119–131, 2016.

- [52] A. Massi Pavan, A. Tessarolo, N. Barbini, A. Mellit, and V. Lughi, "The effect of manufacturing mismatch on energy production for large-scale photovoltaic plants," *Sol. Energy*, vol. 117, no. 5, pp. 282–289, 2015.
- [53] A. Sayyah, R. S. Eriksen, M. N. Horenstein, and M. K. Mazumder, "Performance Analysis of Electrodynamic Screens Based on Residual Particle Size Distribution," *IEEE J. Photovoltaics*, vol. 7, no. 1, pp. 221–229, 2017.
- [54] S. Masuda, K. Fujibayashi, K. Ishida, and H. Inaba, "Confinement and transportation of charged aerosol clouds via electric curtain," *Electr. Eng. Japan*, vol. 92, no. 1, pp. 43–52, 1972.
- [55] M. K. Mazumder, M. Horenstein, J. Stark, D. Erickson, A. Sayyah, S. Jung, and F. Hao, "Development of Self-Cleaning Solar Collectors for Minimizing Energy Yield Loss Caused by Dust Deposition," *Part. Sci. Technol.*, pp. 1–10, 2014.
- [56] R. Sharma, C. A. Wyatt, J. Zhang, C. I. Calle, N. Mardesich, and M. K. Mazumder, "Experimental evaluation and analysis of electrodynamic screen as dust mitigation technology for future Mars missions," *IEEE Trans. Ind. Appl.*, vol. 45, no. 2, pp. 591–596, 2009.
- [57] R. Conceição, M. Melgão, H. G. Silva, K. Nicoll, R. G. Harrison, and A. H. Reis, "Transport of the smoke plume from Chiado's fire in Lisbon (Portugal) sensed by atmospheric electric field measurements," *Air Qual. Atmos. Heal.*, vol. 9, no. 3, pp. 275–283, 2016.
- [58] R. Conceição, H. Silva, A. Bennett, R. Salgado, D. Bortoli, M. Costa, and M. Collares Pereira, "High-Frequency Response of the Atmospheric Electric Potential Gradient Under Strong and Dry Boundary-Layer Convection," *Boundary-Layer Meteorol.*, 2017.
- [59] H. Silva, R. Conceição, M. Melgão, K. Nicoll, P. Mendes, M. Tlemçani, A. Reis, and R. Harrison, "Atmospheric electric field measurements in urban environment and the pollutant aerosol weekly dependence," *Environ. Res. Lett.*, vol. 9, no. 11, 2014.
- [60] H. G. Silva, F. M. Lopes, S. Pereira, K. Nicoll, S. M. Barbosa, R. Conceição, S. Neves, R. G. Harrison, and M. Collares Pereira, "Saharan dust electrification perceived by a triangle of atmospheric electricity stations in Southern Portugal," *J. Electrostat.*, vol. 84, pp. 106–120, 2016.
- [61] H. Silva, R. Conceição, M. Khan, J. Matthews, M. Wright, M. Collares-Pereira, and D. Shallcross, "Atmospheric electricity as a proxy for air quality: Relationship between potential gradient and pollutant gases in an urban environment," *J. Electrostat.*, vol. 84, 2016.
- [62] A. Hassan, U. A. Rahoma, H. K. Elminir, and A. M. Fathy, "Effect of airborne dust concentration on the performance of PV modules," *J. Astron. Soc. Egypt*, vol. 13, no. 1, pp. 24–38, 2005.
- [63] M. R. Maghami, H. Hizam, C. Gomes, M. A. Radzi, M. I. Rezadad, and S. Hajighorbani, "Power Loss Due To Soiling on Solar Panel," *Renew. Sustain. Energy Rev.*, vol. 59, pp. 1307–1316, 2016.

- [64] B. Figgis, A. Ennaoui, S. Ahzi, and Y. Rémond, "Review of PV soiling particle mechanics in desert environments," *Renew. Sustain. Energy Rev.*, vol. 76, no. February, pp. 872–881, 2017.
- [65] B. Figgis, A. Ennaoui, B. Guo, W. Javed, and E. Chen, "Outdoor soiling microscope for measuring particle deposition and resuspension," *Sol. Energy*, vol. 137, no. November, pp. 158–164, 2016.
- [66] N. W. Alnaser, M. J. Al Othman, A. A. Dakhel, I. Batarseh, J. K. Lee, S. Najmaii, A. Alothman, H. Al Shawaikh, and W. E. Alnaser, "Comparison between performance of man-made and naturally cleaned PV panels in a middle of a desert," *Renew. Sustain. Energy Rev.*, vol. 82, no. September 2017, pp. 1048–1055, 2018.
- [67] B. Aïssa, R. J. Isaifan, V. E. Madhavan, and A. A. Abdallah, "Structural and physical properties of the dust particles in Qatar and their influence on the PV panel performance," *Sci. Rep.*, vol. 6, no. April, pp. 1–12, 2016.
- [68] D. Olivares, P. Ferrada, C. D. Matos, A. Marzo, E. Cabrera, C. Portillo, and J. Llanos, "Characterization of soiling on PV modules in the Atacama Desert," *Energy Procedia*, vol. 124, no. September, pp. 547–553, 2017.
- [69] E. Caeiro, R. Brandão, S. Carmo, L. Lopes, M. M. de Almeida, Â. Gaspar, J. F. Oliveira, A. Todo-Bom, T. Leitã, and C. Nunes, "Rede Portuguesa de Aerobiologia : Resultados da monitorização do pólen," *Rev Port Imunoalergologia*, vol. 15, no. December 2015, pp. 235–250, 2007.
- [70] L. Hamaoui-Laguel, R. Vautard, L. Liu, F. Solmon, N. Viovy, D. Khvorostyanov, F. Essl, I. Chuine, A. Colette, M. A. Semenov, A. Schaffhauser, J. Storkey, M. Thibaudon, and M. M. Epstein, "Effects of climate change and seed dispersal on airborne ragweed pollen loads in Europe," *Nat. Clim. Chang.*, vol. 5, no. 8, pp. 766–771, 2015.
- [71] H. Flentje, B. Briel, C. Beck, M. Collaud Coen, M. Fricke, J. Cyrys, J. Gu, M. Pitz, and W. Thomas, "Identification and monitoring of Saharan dust: An inventory representative for south Germany since 1997," *Atmos. Environ.*, vol. 109, pp. 87–96, 2015.
- [72] P. Horta, T. Osorio, J. Marcha, and M. Collares-Pereira, "ESCTP: Évora solar concentrators testing platform," *AIP Conf. Proc.*, vol. 1734, 2016.
- [73] H. K. Elminir, A. E. Ghitas, R. H. Hamid, F. El-Hussainy, M. M. Beheary, and K. M. Abdel-Moneim, "Effect of dust on the transparent cover of solar collectors," *Energy Convers. Manag.*, vol. 47, no. 18-19, pp. 3192–3203, 2006.
- [74] M. Gostein, T. Duster, and C. Thuman, "Accurately measuring PV soiling losses with soiling station employing module power measurements," *2015 IEEE 42nd Photovolt. Spec. Conf. PVSC 2015*, no. November, pp. 3–7, 2015.

- [75] A. Todo-bom, R. Brandão, C. Nunes, E. Caeiro, T. Leitão, J. F. Oliveira, and M. M. de Almeida, "Allergenic airborne pollen in Portugal 2002-2004," *Rev Port Imunoalergologia*, vol. 14 (1), no. 1, pp. 41 – 49, 2006.
- [76] P. Alcázar, C. Galán, P. Cariñanos, and E. Domínguez-Vilches, "Diurnal variation of airborne pollen at two different heights," *J. Investig. Allergol. Clin. Immunol.*, vol. 9, no. 2, pp. 89–95, 1999.
- [77] Grewling, P. Bogawski, and M. Smith, "Pollen nightmare: elevated airborne pollen levels at night," *Aerobiologia (Bologna)*, vol. 32, no. 4, pp. 725–728, 2016.
- [78] J. M. Albertine, W. J. Manning, M. Da Costa, K. A. Stinson, M. L. Muilenberg, and C. A. Rogers, "Projected carbon dioxide to increase grass pollen and allergen exposure despite higher ozone levels," *PLoS One*, vol. 9, no. 11, pp. 1–6, 2014.
- [79] T. Elias, A. M. Silva, N. Belo, S. Pereira, P. Formenti, G. Helas, and F. Wagner, "Aerosol extinction in a remote continental region of the Iberian Peninsula during summer," *J. Geophys. Res. Atmos.*, vol. 111, no. 14, 2006.
- [80] A. F. Stein, R. R. Draxler, G. D. Rolph, B. J. Stunder, M. D. Cohen, and F. Ngan, "Noaa's hysplit atmospheric transport and dispersion modeling system," *Bull. Am. Meteorol. Soc.*, vol. 96, no. 12, pp. 2059–2077, 2015.
- [81] M. Kanamitsu, "Description of the NMC Global Data Assimilation and Forecast System," *Weather Forecast.*, vol. 4, no. 3, pp. 335–342, 1989.
- [82] C. Pérez, K. Hausteine, Z. Janjic, O. Jorba, N. Huneus, J. M. Baldasano, T. Black, S. Basart, S. Nickovic, R. L. Miller, J. P. Perlwitz, M. Schulz, and M. Thomson, "Atmospheric dust modeling from meso to global scales with the online NMMB/BSC-Dust model – Part 1: Model description, annual simulations and evaluation," *Atmos. Chem. Phys.*, vol. 11, no. 24, pp. 13001–13027, 2011.
- [83] K. Hausteine, C. Pérez, J. M. Baldasano, O. Jorba, S. Basart, R. L. Miller, Z. Janjic, T. Black, S. Nickovic, M. C. Todd, R. Washington, D. Müller, M. Tesche, B. Weinzierl, M. Esselborn, and A. Schladitz, "Atmospheric dust modeling from meso to global scales with the online NMMB/BSC-Dust model - Part 2: Experimental campaigns in Northern Africa," *Atmos. Chem. Phys.*, vol. 12, no. 6, pp. 2933–2958, 2012.
- [84] F. Wagner, D. Bortoli, S. Pereira, M. J. Costa, A. M. Silva, B. Weinzierl, M. Esselborn, A. Petzold, K. Rasp, B. Heinold, and I. Tegen, "Properties of dust aerosol particles transported to Portugal from the Sahara desert," *Tellus, Ser. B Chem. Phys. Meteorol.*, vol. 61, no. 1, pp. 297–306, 2009.
- [85] D. Scheuven, L. Schütz, K. Kandler, M. Ebert, and S. Weinbruch, "Bulk composition of northern African dust and its source sediments - A compilation," *Earth-Science Rev.*, vol. 116, no. 1, pp. 170–194, 2013.

- [86] K. Kandler, N. Benker, U. Bundke, E. Cuevas, M. Ebert, P. Knippertz, S. Rodríguez, L. Schütz, and S. Weinbruch, "Chemical composition and complex refractive index of Saharan Mineral Dust at Izaña, Tenerife (Spain) derived by electron microscopy," *Atmos. Environ.*, vol. 41, no. 37, pp. 8058–8074, 2007.
- [87] A. U. Lewandowska and L. M. Falkowska, "Sea salt in aerosols over the southern Baltic. Part 1. The generation and transportation of marine particles," *Oceanologia*, vol. 55, no. 2, pp. 279–298, 2013.
- [88] L. Dunn, B. Littmann, J. R. Caron, and M. Gostein, "PV module soiling measurement uncertainty analysis," *2013 IEEE 39th Photovolt. Spec. Conf.*, no. June 2013, pp. 0658–0663, 2013.
- [89] L. Yalçın and R. Öztürk, "Performance comparison of c-Si, mc-Si and a-Si thin film PV by PVsyst simulation," *J. Optoelectron. Adv. Mater.*, vol. 15, no. 3-4, pp. 326–334, 2013.
- [90] M. Gostein, J. R. Caron, and B. Littmann, "Measuring soiling losses at utility-scale PV power plants," *2014 IEEE 40th Photovolt. Spec. Conf. PVSC 2014*, no. June, pp. 885–890, 2014.
- [91] R. G. Harrison, "Aerosol-induced correlation between visibility and atmospheric electricity," *J. Aerosol Sci.*, vol. 52, pp. 121–126, 2012.
- [92] D. Goossens and E. V. A. N. Kerschaeffer, "Aeolian Dust Deposition on Photovoltaic Solar Cells : the Effects of Wind Velocity and Airborne Dust Concentration on Cell Performance," *Sol. Energy*, vol. 66, no. 4, pp. 277–289, 1999.
- [93] D. Goossens, "The Effect of Surface Curvature on the Deposition of Loess : A Physical Model," *CATENA*, vol. 15, pp. 179–194, 1988.
- [94] J. J. John, S. Warade, G. Tamizhmani, and A. Kottantharayil, "Study of soiling loss on photovoltaic modules with artificially deposited dust of different gravimetric densities and compositions collected from different locations in India," *IEEE J. Photovoltaics*, vol. 6, no. 1, pp. 236–243, 2016.
- [95] E. P. Roth and R. B. Pettit, "The effect of soiling on solar mirrors and techniques used to maintain high reflectivity," *Sol. Mater. Sci.*, pp. 199–227, 1980.
- [96] R. Pettit and J. Freese, "Wavelength dependent scattering caused by dust accumulation on solar mirrors," *Sol. Energy Mater.*, vol. 3, no. 1-2, pp. 1–20, 1980.
- [97] D. J. Griffith, L. Vhengani, and M. Maliage, "Measurements of mirror soiling at a candidate CSP site," *Energy Procedia*, vol. 49, pp. 1371–1378, 2013.
- [98] A. A. Merrouni, F. Wolfertstetter, A. Mezrhah, S. Wilbert, and R. Pitz-Paal, "Investigation of Soiling Effect on Different Solar Mirror Materials under Moroccan Climate," *Energy Procedia*, vol. 69, pp. 1948–1957, 2015.

- [99] P. Bellmann, H. G. Silva, F. Wolfertstetter, and R. Conceicao, "Comparative modelling of optical soiling losses for CSP and PV devices in regard to gravimetric density," *Sol. Energy*, p. (to be submitted), 2019.
- [100] M. Torres-Ramírez, D. Elizondo, B. García-Domingo, G. Nofuentes, and D. L. Talavera, "Modelling the spectral irradiance distribution in sunny inland locations using an ANN-based methodology," *Energy*, vol. 86, pp. 323–334, 2015.
- [101] F. Wolfertstetter, K. Pottler, A. A. Merrouni, A. Mezrhah, and R. Pitz-paal, "A Novel Method for Automatic Real-Time Monitoring of Mirror Soiling Rates," *SolarPACES Conc. Sol. Power Chem. Energy Syst.*, no. September, pp. 2–5, 2012.
- [102] F. Wolfertstetter, K. Pottler, N. Geuder, R. Affolter, A. A. Merrouni, A. Mezrhah, and R. Pitz-Paal, "Monitoring of mirror and sensor soiling with TraCS for improved quality of ground based irradiance measurements," *Energy Procedia*, vol. 49, pp. 2422–2432, 2013.
- [103] H. G. Silva, R. Conceição, M. D. Wright, J. C. Matthews, S. N. Pereira, and D. E. Shallcross, "Aerosol hygroscopic growth and the dependence of atmospheric electric field measurements with relative humidity," *J. Aerosol Sci.*, vol. 85, pp. 42–51, 2015.
- [104] B. Guo, W. Javed, and B. Figgis, "Modeling of PV Soiling as A Function of Environmental Variables," *Soiling Eff. PV Modul. Dubai, April 5-7, 2016*, vol. 157, no. August, pp. 1–23, 2016.
- [105] A. K. Kamra, C. G. Deshpande, and V. Gopalakrishnan, "Effect of relative humidity on the electrical conductivity of marine air," *Q. J. R. Meteorol. Soc.*, vol. 123, pp. 1295–1305, 1997.
- [106] G. Hänel, "Influence of relative humidity on aerosol deposition by sedimentation," *Atmos. Environ.*, vol. 16, no. 11, pp. 2703–2706, 1982.
- [107] G. Ahmadi, S. Guo, and X. Zhang, "Particle adhesion and detachment in turbulent flows including capillary forces," *Part. Sci. Technol.*, vol. 25, no. 1, pp. 59–76, 2007.
- [108] B. Guo, W. Javed, B. W. Figgis, and T. Mirza, "Effect of dust and weather conditions on photovoltaic performance in Doha, Qatar," *2015 1st Work. Smart Grid Renew. Energy, SGRE 2015*, 2015.
- [109] B. Laarabi, O. May Tzuc, D. Dahlioui, A. Bassam, M. Flota-Bañuelos, and A. Barhdadi, "Artificial neural network modeling and sensitivity analysis for soiling effects on photovoltaic panels in Morocco," *Superlattices Microstruct.*, 2017.
- [110] S. A. Kalogirou, "Artificial neural networks in renewable energy systems applications: a review," *Renew. Sustain. Energy Rev.*, vol. 5, no. 4, pp. 373–401, 2001.
- [111] D. W. Marquardt, "An Algorithm for Least-Squares Estimation of Nonlinear Parameters," *J. Soc. Indust. Appl. Math.*, vol. 11, no. 2, 1963.

- [112] A. Avila, I. Queralt-Mitjans, and M. Alarcón, "Mineralogical composition of African dust delivered by red rains over northeastern Spain," *J. Geophys. Res. Atmos.*, vol. 102, no. D18, pp. 21977–21996, 1997.
- [113] F. Gassert, P. Reig, T. Luo, and A. Maddocks, "Aqueduct country and river basin rankings: a weighted aggregation of spatially distinct hydrological indicators," Tech. Rep. December, World Resources Institute, 2013.
- [114] R. Conceição, H. G. Silva, and M. Collares-Pereira, "CSP mirror soiling characterization and modeling," *Sol. Energy Mater. Sol. Cells*, vol. 185, no. March, pp. 233–239, 2018.
- [115] A. A. Hegazy, "Effect of dust accumulation on solar transmittance through glass covers of plate-type collectors," *Renew. Energy*, vol. 22, pp. 525–540, 2001.
- [116] B. Mondoc and F. Pop, "Factors Influencing the Performance of a Photovoltaic Power Plant," *3rd Int. Conf. Mod. Power Syst. MPS 2010*, pp. 18–21, 2010.
- [117] P. D. Burton and B. H. King, "Artificial soiling of photovoltaic module surfaces using traceable soil components," *Conf. Rec. IEEE Photovolt. Spec. Conf.*, pp. 1542–1545, 2013.
- [118] J. Lu and S. Hajimirza, "Optimizing sun-tracking angle for higher irradiance collection of PV panels using a particle-based dust accumulation model with gravity effect," *Sol. Energy*, vol. 158, no. April, pp. 71–82, 2017.
- [119] C. A. Gueymard, "From Global Horizontal To Global Tilted Irradiance: How Accurate Are Solar Energy Engineering Predictions in Practice?," ... *Conf., San Diego, CA, Am. Sol. Energy ...*, no. January 2008, 2008.
- [120] B. Y. Liu and R. C. Jordan, "The interrelationship and characteristic distribution of direct, diffuse and total solar radiation," *Sol. Energy*, vol. 4, no. 3, pp. 1–19, 1960.
- [121] M. Collares-Pereira and A. Rabl, "The average distribution of solar radiation-correlations between diffuse and hemispherical and between daily and hourly insolation values," *Sol. Energy*, vol. 22, no. 2, pp. 155–164, 1979.
- [122] T. Huld, R. Müller, and A. Gambardella, "A new solar radiation database for estimating PV performance in Europe and Africa," *Sol. Energy*, vol. 86, no. 6, pp. 1803–1815, 2012.
- [123] N. Martin and J. M. Ruiz, "Calculation of the PV modules angular losses under field conditions by means of an analytical model," *Sol. Energy Mater. Sol. Cells*, vol. 70, pp. 25–38, 2001.
- [124] M. García, L. Marroyo, E. Lorenzo, and M. Pérez, "Soiling and other optical losses in solar-tracking PV plants in navarra," *Prog. Photovoltaics Res. Appl.*, vol. 19, no. 2, pp. 211–217, 2011.

- [125] C. B. Eero Vartiainen, Gaëtan Masson, "The True Competitiveness of Solar PV: A European Case Study," tech. rep., European PV Technology and Innovation Platform Steering Committee PV LCOE and Competitiveness Working Group, 2017.
- [126] C. E. Kennedy, "Advances in concentrating solar power collectors: mirror and solar selective coatings," *Assoc. Ind. Met. Coaters Laminators (AIMCAL), Fall Technical Conf.*, vol. 6103, 2007.
- [127] H. Ennaceri, D. Erfurt, L. Wang, T. Köhler, A. Taleb, A. Khaldoun, A. El Kenz, A. Benyoussef, and A. Ennaoui, "Deposition of multifunctional TiO₂ and ZnO top-protective coatings for CSP application," *Surf. Coatings Technol.*, vol. 298, pp. 103–113, 2016.
- [128] E. Aranzabe, I. Azpitarte, A. Fernández-García, D. Argüelles-Arízcon, G. Pérez, J. Ubach, and F. Sutter, "Hydrophilic anti-soiling coating for improved efficiency of solar reflectors," *AIP Conf. Proc.*, vol. 2033, no. November, 2018.
- [129] R. Conceição, A. Merrouni, D. Lopes, A. Alae, H. G. Silva, G. Bennouna, M. Collares-Pereira, and A. Ghennioui, "Comparative Study of Soiling on Solar Mirrors in Portugal and Morocco: Preliminary Results for the Dry Season," in *SolarPACES (submitted)*, 2018.
- [130] A. A. Merrouni, A. Mezrhab, and A. Mezrhab, "PV sites suitability analysis in the Eastern region of Morocco," *Sustain. Energy Technol. Assessments*, vol. 18, pp. 6–15, 2016.
- [131] W. Hoppel, R. Anderson, and J. Willett, "Atmospheric electricity in the Planetary Boundary-layer," in *Earth's Electr. Environ.* (E. Krider and R. Roble, eds.), pp. 149–165, Washington D.C.: National Academy Press, 1896.
- [132] S. V. Anisimov, S. V. Galichenko, and N. M. Shikhova, "Space charge and aerelectric flows in the exchange layer: An experimental and numerical study," *Atmos. Res.*, vol. 135-136, no. February 2016, pp. 244–254, 2014.
- [133] R. Yaniv, Y. Yair, C. Price, and S. Katz, "Local and global impacts on the fair-weather electric field in Israel," *Atmos. Res.*, vol. 172-173, pp. 119–125, 2016.
- [134] R. Anderson, *Atmospheric Electricity in the Real World in: Electrical Processes in Atmospheres*. 1976.
- [135] H. D. Wright M.D., Holden N.K., Shallcross D.E., "Indoor and outdoor atmospheric ion mobility spectra, diurnal variation, and relationship with meteorological parameters," *J. Geophys. Res. Atmos.*, pp. 2109–2131, 2014.
- [136] J. A. Chalmers, *Atmospheric Electricity*. New York: Pergamon Press, 2 ed., 1967.
- [137] S. V. Anisimov, K. V. Afinogenov, and N. M. Shikhova, "Dynamics of undisturbed midlatitude atmospheric electricity: From observations to scaling," *Radiophys. Quantum Electron.*, vol. 56, no. 11-12, pp. 709–722, 2014.

- [138] M. J. Rycroft, K. A. Nicoll, K. L. Aplin, and R. G. Harrison, "Recent advances in global electric circuit coupling between the space environment and the troposphere," *J. Atmos. Solar-Terrestrial Phys.*, vol. 90-91, no. 1, pp. 198–211, 2012.
- [139] R. Conceição and H. G. Silva, "Simulations of the Global Electrical Circuit coupled to local Potential Gradient measurements," *J. Phys. Conf. Ser.*, vol. 646, no. 1, pp. 6–10, 2015.
- [140] R. G. Harrison, "The Carnegie Curve," *Surv. Geophys.*, vol. 34, no. 2, pp. 209–232, 2013.
- [141] I. M. Piper and A. J. Bennett, "Observations of the atmospheric electric field during two case studies of boundary layer processes," *Environ. Res. Lett.*, vol. 7, no. 1, 2012.
- [142] R. Stull, *An Introduction to Boundary Layer Meteorology*. New York City: Springer, 1988.
- [143] T. C. Marshall, W. D. Rust, M. Stolzenburg, W. P. Roeder, and P. R. Krehbiel, "A study of enhanced fair-weather electric fields occurring soon after sunrise," *J. Geophys. Res. Atmos.*, vol. 104, no. D20, pp. 24455–24469, 1999.
- [144] K. A. Nicoll, R. G. Harrison, H. G. Silva, R. Salgado, M. Melgão, and D. Bortoli, "Electrical sensing of the dynamical structure of the planetary boundary layer," *Atmos. Res.*, vol. 202, no. June 2017, pp. 81–95, 2018.
- [145] J. Chubb, "The measurement of atmospheric electric fields using pole mounted electrostatic fieldmeters," *J. Electrostat.*, vol. 72, no. 4, pp. 295–300, 2014.
- [146] J. Chubb, "Limitations on the performance of 'field mill' fieldmeters with alternating electric fields," *J. Electrostat.*, vol. 78, pp. 1–3, 2015.
- [147] M. J. Costa, D. Bortoli, S. Pereira, A. M. Silva, F. Wagner, N. Belo, J. L. Guerrero-Rascado, F. Navas-Guzman, and L. Alados-Arboledas, "Analysis of the measurements taken by a ceilometer installed in the south of Portugal," vol. 6745, p. 674523, 2007.
- [148] B. Holben, T. Eck, I. Slutsker, D. Tanré, J. Buis, A. Setzer, E. Vermote, J. Reagan, Y. J. Kaufman, T. Nakajima, F. Lavenue, I. Jankowiak, and A. Smirnov, "AERONET—A Federated Instrument Network and Data Archive for Aerosol Characterization," *Remote Sens. Environ.*, vol. 66, no. 1, pp. 1–16, 1998.
- [149] J. P. Lafore, J. Stein, N. Asencio, P. Bougeault, V. Ducrocq, J. Duron, C. Fischer, P. Hérel, P. Mascart, V. Masson, J. P. Pinty, J. L. Redelsperger, E. Richard, and J. Vilà-Guerau De Arellano, "The Meso-NH Atmospheric Simulation System. Part I: Adiabatic formulation and control simulations," *Ann. Geophys.*, vol. 16, no. 1, pp. 90–109, 1998.
- [150] J. Pergaud, V. Masson, S. Malardel, and F. Couvreux, "A parameterization of dry thermals and shallow cumuli for mesoscale numerical weather prediction," *Boundary-Layer Meteorol.*, vol. 132, no. 1, pp. 83–106, 2009.

- [151] V. Masson, P. Le Moigne, E. Martin, S. Faroux, A. Alias, R. Alkama, S. Belamari, A. Barbu, A. Boone, F. Bouyssel, P. Brousseau, E. Brun, J. C. Calvet, D. Carrer, B. Decharme, C. Delire, S. Donier, K. Essaouini, A. L. Gibelin, H. Giordani, F. Habets, M. Jidane, G. Kerdraon, E. Kourzeneva, M. Lafaysse, S. Lafont, C. Lebeau-pin Brossier, A. Lemonsu, J. F. Mahfouf, P. Marguinaud, M. Mokhtari, S. Morin, G. Pigeon, R. Salgado, Y. Seity, F. Taillefer, G. Tanguy, P. Tulet, B. Vincendon, V. Vionnet, and A. Voldoire, "The SURFEXv7.2 land and ocean surface platform for coupled or offline simulation of earth surface variables and fluxes," *Geosci. Model Dev.*, vol. 6, no. 4, pp. 929–960, 2013.
- [152] V. Masson, J. L. Champeaux, F. Chauvin, C. Meriguet, and R. Lacaze, "A global database of land surface parameters at 1-km resolution in meteorological and climate models," *J. Clim.*, vol. 16, no. 9, pp. 1261–1282, 2003.
- [153] C. Policarpo, R. Salgado, and M. J. Costa, "Numerical Simulations of Fog Events in Southern Portugal," *Adv. Meteorol.*, vol. 2017, no. 1989, 2017.
- [154] J. Tacza, J. P. Raulin, E. Macotela, E. Norabuena, G. Fernandez, E. Correia, M. J. Rycroft, and R. G. Harrison, "A new South American network to study the atmospheric electric field and its variations related to geophysical phenomena," *J. Atmos. Solar-Terrestrial Phys.*, vol. 120, pp. 70–79, 2014.
- [155] H. Israël, "Atmospheric electrical agitation," *Q. J. R. Meteorol. Soc.*, vol. 85, no. 364, pp. 91–104, 1959.
- [156] A. Chalmers, "The Ionisation in the Lowest Regions of the Atmosphere," no. 1939, 1946.
- [157] S. Engelstaedter, I. Tegen, and R. Washington, "North African dust emissions and transport," *Earth-Science Rev.*, vol. 79, no. 1-2, pp. 73–100, 2006.
- [158] A. I. Ette, "The effect of the Harmattan dust on atmospheric electric parameters," *J. Atmos. Terr. Phys.*, vol. 33, no. 2, pp. 295–300, 1971.
- [159] Z. Ulanowski, J. Bailey, P. W. Lucas, J. H. Hough, and E. Hirst, "Alignment of atmospheric mineral dust due to electric field," *Atmos. Chem. Phys.*, vol. 7, no. 24, pp. 6161–6173, 2007.
- [160] C. I. Calle, C. R. Buhler, J. L. McFall, and S. J. Snyder, "Particle removal by electrostatic and dielectrophoretic forces for dust control during lunar exploration missions," *J. Electrostat.*, vol. 67, no. 2-3, pp. 89–92, 2009.
- [161] T. Sarver, A. Al-Qaraghuli, and L. L. Kazmerski, "A comprehensive review of the impact of dust on the use of solar energy: History, investigations, results, literature, and mitigation approaches," *Renew. Sustain. Energy Rev.*, vol. 22, pp. 698–733, 2013.
- [162] G. T. Delory, W. M. Farrell, S. K. Atreya, N. O. Renno, A.-s. Wong, S. A. Cummer, D. D. Sentman, J. R. Marshall, S. C. R. Rafkin, and D. C. Catling, "Special Paper," *Astrobiology*, vol. 6, no. 3, 2006.

- [163] F. Esposito, S. Debei, C. Bettanini, C. Molfese, I. A. Rodríguez, G. Colombatti, and A.-m. Harri, "the Dreams Experiment on the Exomars 2016 Mission for the Study of Martian Environment During the Dust," pp. 249–255, 2016.
- [164] F. Esposito, R. Molinaro, C. I. Popa, C. Molfese, F. Cozzolino, L. Marty, K. Taj-Eddine, G. Di Achille, G. Franzese, S. Silvestro, and G. G. Ori, "The role of the atmospheric electric field in the dust-lifting process," *Geophys. Res. Lett.*, vol. 43, no. 10, pp. 5501–5508, 2016.
- [165] E. Williams, N. Nathou, E. Hicks, C. Pontikis, B. Russell, M. Miller, and M. J. Bartholomew, "The electrification of dust-lifting gust fronts ('haboobs') in the Sahel," *Atmos. Res.*, vol. 91, no. 2-4, pp. 292–298, 2009.
- [166] A. K. Kamra, "Measurements of the electrical properties of dust storms," *J. Geophys. Res.*, vol. 77, no. 30, p. 5856, 1972.
- [167] R. Reiter, *Phenomena in Atmospheric and Environmental Electricity. Developments in Atmospheric Sciences*. Elsevier, 1992.
- [168] K. A. Nicoll, R. G. Harrison, and Z. Ulanowski, "Observations of Saharan dust layer electrification," *Environ. Res. Lett.*, vol. 6, no. 1, 2011.
- [169] K. A. Nicoll and R. G. Harrison, "Experimental determination of layer cloud edge charging from cosmic ray ionisation," *Geophys. Res. Lett.*, vol. 37, no. 13, pp. 1–5, 2010.
- [170] W. A. D. Rudge, "Atmospheric Electrification during South African Dust Storms," *Nature*, vol. 91, no. 2263, pp. 31–32, 1913.
- [171] J. Preißler, F. Wagner, S. N. Pereira, and J. L. Guerrero-Rascado, "Multi-instrumental observation of an exceptionally strong Saharan dust outbreak over Portugal," *J. Geophys. Res. Atmos.*, vol. 116, no. 24, pp. 1–12, 2011.
- [172] M. A. Obregón, S. Pereira, V. Salgueiro, M. J. Costa, A. M. Silva, A. Serrano, and D. Bortoli, "Aerosol radiative effects during two desert dust events in August 2012 over the southwestern Iberian Peninsula," *Atmos. Res.*, vol. 153, pp. 404–415, 2015.
- [173] F. Lopes, H. G. Silva, S. Bárias, and S. M. Barbosa, "Preliminary results on soil-emitted gamma radiation and its relation with the local atmospheric electric field at Amieira (Portugal)," *J. Phys. Conf. Ser.*, vol. 646, no. 1, pp. 6–10, 2015.
- [174] A. Angström, "Solar and Terrestrial Radiation," *Int. Geophys.*, vol. 25, no. C, pp. 207–260, 1980.
- [175] D. M. Winker, W. H. Hunt, and M. J. McGill, "Initial performance assessment of CALIOP," *Geophys. Res. Lett.*, vol. 34, no. 19, pp. 1–5, 2007.

- [176] C. Pérez, S. Nickovic, J. M. Baldasano, M. Sicard, F. Rocadenbosch, and V. E. Cachorro, "A long Saharan dust event over the western Mediterranean: Lidar, Sun photometer observations, and regional dust modeling," *J. Geophys. Res. Atmos.*, vol. 111, no. 15, pp. 1–16, 2006.
- [177] C. Pérez, S. Nickovic, G. Pejanovic, J. M. Baldasano, and E. Özsoy, "Interactive dust-radiation modeling: A step to improve weather forecasts," *J. Geophys. Res. Atmos.*, vol. 111, no. 16, 2006.
- [178] S. Basart, C. Pérez, S. Nickovic, E. Cuevas, and J. M. Baldasano, "Development and evaluation of the BSC-DREAM8b dust regional model over northern Africa, the mediterranean and the middle east," *Tellus, Ser. B Chem. Phys. Meteorol.*, vol. 64, no. 1, 2012.
- [179] F. Lopes, H. G. Silva, R. Salgado, M. Potes, K. A. Nicoll, and R. G. Harrison, "Atmospheric electrical field measurements near a fresh water reservoir and the formation of the lake breeze," *Tellus, Ser. A Dyn. Meteorol. Oceanogr.*, vol. 68, 2016.
- [180] C. Torrence and G. Compo, "A practical guide to wavelet analysis," *Bull. Amer. Meteor. Soc.*, vol. 79, no. 1, pp. 61–78, 2016.
- [181] G. Freier, "The electric field of a large dust devil," *J. Geophys. Res.*, no. 10, p. 1960, 1960.
- [182] I. I. Inculet, G. S. P. Castle, and G. Aartsen, "Generation of bipolar electric fields during industrial handling of powders," *Chem. Eng. Sci.*, vol. 61, no. 7, pp. 2249–2253, 2006.
- [183] N. Duff and D. J. Lacks, "Particle dynamics simulations of triboelectric charging in granular insulator systems," *J. Electrostat.*, vol. 66, no. 1-2, pp. 51–57, 2008.
- [184] R. G. Harrison and K. S. Carslaw, "Ion-aerosol-cloud processes in the lower atmosphere," *Rev. Geophys.*, vol. 41, no. 3, 2003.
- [185] M. Naeem and G. Tamizhmani, "Climatological relevance to the soiling loss of photovoltaic modules," *2015 Saudi Arab. Smart Grid, SASG 2015*, pp. 1–5, 2016.
- [186] A. M. El-Nashar, "Effect of dust deposition on the performance of a solar desalination plant operating in an arid desert area," *Sol. Energy*, vol. 75, no. 5, pp. 421–431, 2003.
- [187] L. Boyle, H. Flinchpaugh, and M. P. Hannigan, "Natural soiling of photovoltaic cover plates and the impact on transmission," *Renew. Energy*, vol. 77, no. 1, pp. 166–173, 2015.
- [188] R. Conceição, H. G. Silva, L. Fialho, F. M. Lopes, and M. Collares-pereira, "PV system design with the effect of soiling on the optimum tilt angle," *Renew. Energy*, vol. 133, pp. 787–796, 2019.
- [189] B. Stridh, "Evaluation of economical benefit of cleaning of soiling and snow in PV plants at three European locations," *Conf. Rec. IEEE Photovolt. Spec. Conf.*, pp. 1448–1451, 2012.
- [190] S. Bouaddi, A. Ihlal, and A. Fernández-García, "Soiled CSP solar reflectors modeling using dynamic linear models," *Sol. Energy*, vol. 122, pp. 847–863, 2015.

- [191] F. A. Mejia and J. Kleissl, "Soiling losses for solar photovoltaic systems in California," *Sol. Energy*, vol. 95, pp. 357–363, 2013.
- [192] C. Perpiña, C. Batista, and S. Lavalle, "An assessment of the regional potential for solar power generation in EU-28," *Energy Policy*, vol. 88, pp. 86–99, 2016.
- [193] M. J. Adinoyi and S. A. Said, "Effect of dust accumulation on the power outputs of solar photovoltaic modules," *Renew. Energy*, vol. 60, pp. 633–636, 2013.
- [194] G. E. Cohen, D. W. Kearney, and G. J. Kolb, "Final report on the operation and maintenance improvement program for concentrating solar power plants," 1999.
- [195] F. Lopes, R. Conceição, H. Silva, R. Salgado, P. Canhoto, and M. Collares-Pereira, "Predictive Value of Short-term Forecasts of DNI for Solar Energy Systems Operation," in *SolarPACES (accepted Publ.*, 2018.
- [196] S. Bouaddi, A. Ihlal, and A. Fernández-García, "Comparative analysis of soiling of CSP mirror materials in arid zones," *Renew. Energy*, vol. 101, pp. 437–449, 2017.
- [197] D. M. Deffenbaugh, S. T. Green, and S. J. Svedeman, "The effect of dust accumulation on line-focus parabolic trough solar collector performance," *Sol. Energy*, vol. 36, no. 2, pp. 139–146, 1986.
- [198] F. Carapau and R. Conceição, "Three-dimensional velocity field for blood flow using the power-law viscosity function," *WSEAS Trans. HEAT MASS Transf.*, vol. 13, 2018.
- [199] D. Lopes, R. Conceição, H. Silva, J. Mirão, and G. Pérez, "Evaluating the use of an anti-soiling coating for reduction of the dirtiness effect on CSP mirrors," *Sol. Energy*, pp. 1–9, 2019.
- [200] S. A. Kalogirou, R. Agathokleous, and G. Panayiotou, "On-site PV characterization and the effect of soiling on their performance," *Energy*, vol. 51, pp. 439–446, 2013.
- [201] S. Nishimoto and B. Bhushan, "Bioinspired self-cleaning surfaces with superhydrophobicity, superoleophobicity, and superhydrophilicity," *RSC Adv.*, vol. 3, no. 3, pp. 671–690, 2013.
- [202] F. Lopes, R. Conceição, T. Fasquelle, H. Silva, R. Salgado, P. Canhoto, and M. Collares-Pereira, "Short-term Forecasts of DNI from the Integrated Forecasting System (ECMWF) for Optimized Operation Strategies of a Central Receiver System," *Energies*, 2019.
- [203] M. Rycroft, S. Israelsson, and C. Price, "The global atmospheric electric circuit, solar activity and climate change," *J. Atmos. Solar-Terrestrial Phys.*, vol. 62, no. 17-18, pp. 1563–1576, 2000.
- [204] K. Bergeron and J. Freese, "Cleaning Strategies for Parabolic-trough Solar-collector Fields; Guidelines for Decisions," tech. rep., Sandia National Labs, Albuquerque, 1981.

- [205] A. Fernández-García, L. Álvarez-Rodrigo, L. Martínez-Arcos, R. Aguiar, and J. M. Márquez-Payés, "Study of different cleaning methods for solar reflectors used in CSP plants," *Energy Procedia*, vol. 49, pp. 80–89, 2013.
- [206] F. Lopes, R. Conceição, T. Fasquelle, H. Silva, R. Salgado, P. Canhoto, and M. Collares-Pereira, "ECMWF Forecasts of DNI for Optimized Operation Strategies of Linear Focus Parabolic-trough Systems," *Appl. Energy*, 2019.
- [207] R. Conceição, A. Merrouni, D. Lopes, A. Alae, H. Silva, G. Bennouna, M. Collares-Pereira, and A. Ghennioui, "A Comparative Study of Soiling on Solar Mirrors in Portugal and Morocco: Preliminary Results for the Dry Season," in *SolarPACES (accepted Publ., AIP, 2018)*.
- [208] E. Cuddihy, "Surface soiling: Theoretical Mechanisms and Evaluation of Low-Soiling Coatings," *Proc. Flat-Plate Sol. Array Proj. ...*, pp. 379–396, 1983.



UNIVERSIDADE DE ÉVORA
INSTITUTO DE INVESTIGAÇÃO
E FORMAÇÃO AVANÇADA

Contacts:

University of Évora

Instituto de Investigação e Formação Avançada — IIFA

Palácio do Vimioso | Largo Marquês de Marialva, Apart. 94

7002 - 554 Évora | Portugal

Tel: (+351) 266 706 581

Fax: (+351) 266 744 677

email: iifa@uevora.pt